Universiteit Gent
Faculteit Ingenieurswetenschappen en Architectuur
Vakgroep Informatietechnologie

Tolerante Spectrale Filters met Behulp van Nanofotonische Golfgeleiders in Silicium

Tolerant Spectral Filters using Silicon Nanophotonic Waveguides

---

Sarvagya Paavan Dwivedi

Proefschrift tot het bekomen van de graad van
Doctor in de Ingenieurswetenschappen:
Fotonica
Academiejaar 2015-2016

Universiteit Gent
Faculteit Ingenieurswetenschappen en Architectuur
Vakgroep Informatietechnologie

Promotoren: Prof. Dr. Ir. Wim Bogaerts

Examencommisse:

Prof. Dr. Ir. Luc Taerwe (voorzitter)	Universiteit Gent, SE
Prof. Dr. Ir. Wim Bogaerts	Universiteit Gent, INTEC
Prof. Dr. Ir. Roel Baets	Universiteit Gent, INTEC
Prof. Dr. Ir. Peter Bienstman	Universiteit Gent, INTEC
Dr. Ir. Stephane Clemmen	Universiteit Gent, INTEC
Dr. Ir. Pieter Dumon	Luceda Photonics
Dr. Ir. Peter De Heyn	IMEC
Prof. Dr. Ir. Jeroen Beeckman	Universiteit Gent, ELIS

Universiteit Gent
Faculteit Ingenieurswetenschappen en Architectuur

Vakgroep Informatietechnologie
Sint-Pietersnieuwstraat 41, 9000 Gent, België

Tel.: +32-9-264 3324
Fax.: +32-9-264 3593

Acknowledgement

It all started way back in the early 2011 when I was working in Bangalore for Comsol as Application Engineer. Although I was enjoying the challenging job at Comsol working under Vineet, yet it was somehow always back in my mind to pursue something new and creative. I learnt a lot from you Vineet. Special thanks to my friend Harish, who inspired and guided me initially with his wonderful postdoc stories from Colorado, Boulder. Not many friends were happy with my decision of leaving my corporate career but my family stood by me firmly to pursue research career. My mother, father and my twin sisters Milie Di and Julie Di, were really happy proclaiming wow to my right decision in life. I am sure the happiest person at that time was my father as he himself a great researcher throughout his life. And my mother because she is happy with whatever makes me happy. My sisters have always been supportive and only because of them I feel like I am still a kid :). I am so fortunate to have a lovely niece Suhani and wonderful nephews Neel and Baby. This was a brief background.

Then I landed in this beautiful city of Ghent to start my career as a doctoral researcher on 13th October 2011. All credit goes to my promoter Wim. He is the one who always listened to me with my ideas, guided me in a way so that I get a confidence in whatever I do, answered my silliest possible questions and never got bored in answering them countless times. He supported me in all my failures and always said ”OK, if this is not working, we have at least learnt something from it.” I consider myself blessed to have him as my promoter. To all the professors in the group, Roel, Dries, Geert, Peter, Gunther, Nicolas and Bart, I cannot thank them enough for making this group so diverse at the same time like a big family and keeping its flag high as one of the best in the world. I am very fortunate to have worked in this wonderful group which provided me care, attention, affection and support in abundant measure. I am surely going to miss all this.

This long journey cannot be completed until without mentioning so many special people in this wonderful group. Starting from Bendix, how can I forget the number of cups of coffee we had in the last four years, on an average 3-4 per day (right?). Apart from this, it was a pleasure discussing all the research problems over the coffee. Special thanks to Floriane for inviting me so many times to make me realize how well is the French cuisine. I really enjoyed their wedding at south of France and my best wishes to lovely Kiya and Meline. Alfonso, we joined together, we deliberated almost every day even on trivial things and we are leaving almost at the same time, I am sure we miss all the fun. Best wishes for your postdoc new position in the US. Aditya, remember the very first day I joined; I came to your office and asked a few things. From the day one you have been a great friend and will always be. And, I think we should start our Starbucks coffee over the weekends again? It was nice to see and discuss about Ge-on-Si Mid IR framework you developed. I wish you and Kirti a happy married life. Ananth (Daddu), you have been there whenever I asked for any help as an elder brother. I think it would be very difficult for me in my next phase of life doing things without taking your lovely suggestions. Heartiest congratulations to Kamal (Bhabhi) and you for the new phase in your life.

Thank you, Hui Yu, for teaching me the design and characterization of silicon modulators. Muneeb, I have to learn the kind of patience you have as a person. You have been a great friend; I enjoyed discussing various research topics with you and the dinner we shared at the Indian place. Utsav, it was very nice sharing a flat with you. I enjoyed the spicy food you cooked and the long discussions we shared over the weekends on various topics whether it is movies, societal scenario, or even a bit of non-linear optics. Thomas, I guess you must be enjoying your stay in the US. It was great working with you on effective index extraction methods. Fredric, it was nice chatting with you along with Anton (Tawarish) almost every day in the evenings. Fredric, congrats for your future postdoc position and Tawarish many congrats for the new phase which is coming soon in your life. It was a pleasure meeting you guys. Shibnath you have always been helpful either for general suggestions or any specific design help. Michael, thanks for all your help with semi and fully automatic setup. I could not imagine measuring so many devices in due course of time without your help. Liesbet, thanks for all your help in taking SEM images on a short request. Amin (and Leila), you have been a nice colleague and a great friend. It was nice working with you on OCS lab course and then on various discussions on high speed measurements. I am missing our evening TT matches along with Ananth. Peter DH, it was nice working with you on CWDM and especially on designing wideband directional couplers. I hope the improved design will work on the system level and we can compete with IBM and others. Herbert, it was wonderful working with you for almost a year. I am sure your project is coming along well. Peter for helping me in all my doubts and keeping the plants alive in our wonderful office. Geert, I enjoyed working with you as a TA for the OCS course. I myself learned so many new things. Martin, many thanks for all your help Caphe, it gave me the flexibility to test my circuits quickly. Bart, you have always been helpful in sorting technical things out. Yanlu, thanks for your help with low reflection grating couplers.

The Brug food was not so enjoyable without you guys: Jesper, Antonio, Jan-Willem, Daan, Sren, Alejandro, Michael, Artur, Andrew, Ashim, Kasper, Paul, Koen, Peter Wuytens, Ali, Floris, Rodica, Alexandre and Stephanne. Andreas (thanks for your help in Dutch summary) and Sarah, many congratulations for the new phase coming into your life. Also, thanks to Jing, Chen, Weiqiang, Bin, Ruijun, Yunpeng and Zhechao for being so nice colleagues.

Special thanks to Thijs, Eva, Abdul and Antonio for the new simulation and design of experiment framework. I think it is going to help students in the future to minimize the obvious mistakes. Many thanks to Ilse VR, Ilse M, Kristien, Mike, Bert, Jeroen, Jelle and Peter Guns for providing all possible help whenever required.

On the professional note, I would like to thank our small design group led by Wim which includes Antonio, Alfonso, Ang, Yufei and myself. The weekly Monday morning Design meetings really helped me in prioritizing my work. Special thanks to Yufei and Antonio for helping me at the last minute in error analysis with the Monte Carlo. You guys are great. Ang, I am going to miss your funny jokes for sure.

My former colleagues Pieter, Shankar, Karel, Andrea, Samir, Rajesh, Sukumar, Adil, Amit, Youssef, Pauline, Sam, Elewout, Cristina and Yingtao many thanks to you guys for always been helpful and ready with suggestions when I joined this group. There are so many great friends I made here and I would like to say thanks for making the journey memorable. Paula and Else for wonderful food, movies and concert we shared. Manan, Namrata, Saurav, Sulakshna, Aditya, Kirti, Gaurav, Niharika, Ananth, Kamal, Utsav and Aswhin, it was great spending time with you guys on numerous Indian festivals and occasions. Manan and Namarata congratulations to your parenthood and welcome to Taashi. Shailesh, Sachin, Chetna, Ark, Vatsala, Abhishek and Karthik it was wonderful time spending with you guys. Manu, you have been a great friend and like a family back from our IIT days. It's great that you moved from Gttingen to Cologne so that we can visit each other more often. A special thanks to all my friends (Preeti Patil, Sarang and Gopal) from FOC Lab at IIT Bombay back in my master days and my Prof. R.K. Shevgaonkar who taught me Fiber Optics.

I would like to thank again, my parents, my twin sisters, my niece and nephews for being there for me and my fiance Shweta for her continuous support in the last days of my PhD. We didn't get any chance to spend some time together after our engagement, but from now on certainly we will.

I would like to thank again Wim for giving me this opportunity to work with him.

Finally, I would like to thank all my Jury members for providing valuable and constructive comments to improve my thesis. I hope you all will enjoy reading it.

Last, but certainly not the least, I am going to miss this wonderful city of Ghent in the future and the time I spent here as a PhD student at the world's best Photonics Research Group.

Ghent, February 2016
Sarvagya Dwivedi

Table of Contents

List of Figures

List of Tables

List of Acronyms

A

AWG	Array Waveguide Gratings
Au	Gold

B

BOX	Buried Oxide
BPM	Beam Propagation Method

C

CMOS	Complementary Metal-Oxide Semiconductor
CWDM	Coarse Wavelength Division Multiplexing

D

DBR	Distributed Bragg Reflector
DC	Directional Coupler
DWDM	Dense Wavelength Division Multiplexing

F

FEM	Finite Element Method

FDTD	Finite Difference Time Domain
FIB	Fcoused Ion Beam
FMM	Film Mode Matching
FPR	Free Propagation Region
FSR	Free Spectral Range

G

GbE	Gigabit Ethernet
Ge	Germanium
GC	Grating Coupler

I

ITU	International Telecommunication Union

K

K	Kelvin

M

MMI	Multimode Interference
MZI	Mach-Zehnder Interferometer

P

PCG	Planar Concave Grating
PIC	Photonic Integrated Circuit

R

RLMZI	Ring Loaded Mach-Zehnder Interferometer

S

SEM	Scanning Electron Microscope
Si	Silicon
SiN	Silicon Nitride
SiO	Silicon Oxide
SOI	Silicon on Insulator
SPR	Splitter Polarization Rotator
SK	Socket

T

TE	Transverse Electric
TM	Transverse Magnetic
Ti	Titanium
TDSEM	Top Down Scanning Electron Microscope
TO	Thermo Optic

W

WDM	Wavelength Division Multiplexing

Nederlandse samenvatting –Summary in Dutch–

Het voorbije decenium is siliciumfotonica een van de meestbelovende optische integratietechnieken geworden. De hoofdredenen hiervoor zijn:

1. Silicium is transparant voor de golflengtes die het meest gebruikt worden in optische communicatie systemen, de zogenaamde O-band (1310 nm) en C-band (1550 nm).

2. Silicium heeft een heel grote brekingsindex, wat zorgt voor golfgeleiders met een heel groot contrast in brekingsindex tussen de kern en de omgeving. Hierdoor kunnen de golfgeleiderdimensies geschaald worden naar sub-micrometer orde. Tevens kunnen bochten gemaakt worden met een straal van slechts enkele micrometer. Deze compacte basiscomponenten zorgen ervoor dat de totale oppervlakte van het volledige optische circuit in silicium een orde kleiner is dan die van andere technologin (vaak glasgebaseerd). Anders gesteld kunnen er meer functies gentegreerd worden op dezelfde oppervlakte, wat toelaat om de complexiteit te verhogen.

3. Silicium is ook het dominante material in electronische integratie. De voorbije 50 jaar heeft de CMOS industrie miljarden genvesteerd in fabricatietechnologie. Zowel het volume als de precisie werden geoptimaliseerd terwijl de kost per component steeds kleiner is geworden. Deze zelfde infrastructuur kan gebruikt worden voor siliciumfotonica, waardoor de fabricatiekwaliteit een stuk verder staat dan deze bij de concurrerende technologin.

4. Integratie van germanium met het silicium-op-isolator (SOI) platform laat toe om ook de detectoren te integreren. Aangezien de passieve componenten al van hoge kwaliteit kunnen zijn, is het laatste ontbrekende element de lichtbron. Door de indirecte bandkloof zijn efficinte bronnen rechtstreeks op silicium niet mogelijk. De hybride III-V integratie techniek op SOI wordt momenteel geoptimaliseerd om ook dit probleem uit de weg te helpen.

Siliciumfotonica wordt gezien als de oplossing voor goedkope verbindingen in datacenters, voor brede uitrol van *access networks* (*fiber-to-the-home*) en voor interconnecties tussen chips. Alle essentile componenten zijn reeds aangetoond op dit platform en de eerste siliciumfotonische producten zijn op de communicatiemarkt. Daarenboven worden andere markten zoals sensoren, spectroscopie en diagnose aangeboord.

Uitdagingen

Een aantal van de sterke punten van siliciumfotonica introduceren echter nieuwe zwakheden. We lijsten enkele van de nieuwe uitdagingen op:

1. Het hoge contrast in brekingsindex, dat om kleine golfgeleiders en scherpe bochten toelaat, zorgt er ook voor dat de structuur heel gevoelig wordt aan enige afwijking van de golfgeleiderdimensies. Hoewel de CMOS-fabricatietechnieken al nanometerschaal precisie haalt, is dit vaak niet goed genoeg voor functionaliteit die gevoelig is aan golflengte, zoals in een *wavelength-division multiplexing* (WDM) systemen. Om de laatste aanpassingen te brengen worden de golfgeleiders vaak getrimd voor of na de fabricatie.
2. De thermisch-optische (TO) cofficint van silicium is vrij groot. Dit wil zeggen dat de brekingsindex zal variren in functie van temperatuur. Indien je dit wil gebruiken om het circuit bewust te benvloeden is dit voordelig, maar dit zorgt tegelijk ook voor een groot energieverbruik en complexe logica. Passieve siliciumfotonische circuits gebruiken daarom meestal temperatuurstabilisatie. Een alternatief hiervoor is de introductie van materialen met een tegengestelde TO cofficint, zoals polymeren of titanium dioxide (TiO_2), maar dit verhoogt de complexiteit in fabricatie. Bovendien worden zo'n materialen niet altijd toegelaten in CMOS processen.
3. De effectieve brekingsindex is een van de belangrijkste parameters bij het ontwerpen van golflengtefilters. Dit bepaald immers wanneer er constructieve interferentie optreedt en bijgevolg de centrale golflengte van de filter. Door de hoge dispersie van siliciumgolfgeleiders zijn de groepsbrekingsindex n_g en de effectieve index n_{eff} zeer verschillend en sterk afhankelijk van golflengte. Als men de groepsindex kent, is het theoretisch gezien mogelijk om de effectieve index te berekenen, maar in praktijk is de data vaak niet goed genoeg.

1 Onze bijdrage en resultaten

Hierboven hebben we de fundamentele uitdagingen uiteen gezet van de hypergevoelig SOI golfgeleiders en golflengtefilters. We pakten deze niet aan via technologie, maar via slimmere ontwerptechnieken. Hieronder lijsten we onze belangrijkste resultaten op.

1. We stelden een nieuwe accurate methode voor om de effictieve brekingsindex (n_{eff}) en thermo-optische cofficint te meten van silicium-op-isolator

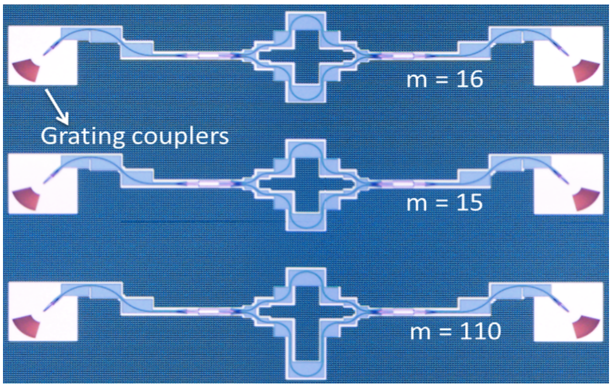

Figuur 1: Camerabeeld van gefabriceerde MZI's voor de extractie van de brekingsindex van een 600nm brede golfgeleider.

golfgeleider. Deze methode werkt in de volledige C-band en gebruikt drie Mach-Zehnder Interferometers (MZI). Ze laat toe om de golflengtedispersie accuraat te extraheren en houdt rekening met variaties in fabricatie. We gebruiken twee MZI's met een lage orde m, i.e. een grote spectraal bereik (FSR). Hierdoor kunnen we de orde van de filter correct schatten in de C-band. De derde MZI heeft een veel hogere orde en een kleine FSR, wat ons helpt om de golflengteafhankelijkheid van de groepsindex n_g te extraheren. Om de TO cofficint te bepalen, meten we ze dezelfde MZI's op verschillende temperaturen. De gefabriceerde componenten en de gesimuleerde en gemeten resultaten worden getoond in Fig. 1 en Fig. 2.

Om de golflengtefilters tolerant te maken aan fabricatiefouten en fluctuaties van temperatuur, hebben we de doorlaatband vlakker gemaakt. Met deze techniek hebben we verschillende SOI demultiplexers vergeleken, bijvoorbeeld *arrayed waveguide gratings* (AWG), *echelle gratings* en gecascadeerde MZI filters. Gecascadeerde MZI filters waren de beste keuze voor korte-afstandsinterconnecties, waar een laag energiebudget en lage kost van kritisch belang zijn.

We demonstreerden een vierkanaals demultiplexer voor de O-band, gebaseerd op een tweetraps gecascadeerde MZI, die zowel robuust is als lage verliezen heeft. De transferfunctie met vlakke doorlaatband werd gerealiseerd met een 4e orde gecascadeerde MZI filter. De kanalen van de gemeten component liggen 20nm uit elkaar, over een bereik van 80nm. Het spectrum is gecentreerd op 1301 nm met een vlakke doorlaatband over 60 % van de kanaalspatiering, en dit om fluctuaties in temperature tot 100 °C en de fabricatievariaties op te vangen. Karakterisatie over een volledige wafer toont dat het gemiddelde insertieverlies onder de 3dB ligt en dat de overspraak beer is dan -18dB. Deze brede doorlaatbanden maken de demultiplexer van nature uit thermisch robuust. Dit laat toe om ongekoelde lasers te gebruiken en maakt thermische controle overbodig, wat een positief gevolg heeft voor het vermogengebruik en de kost. De oppervlakte van de component is

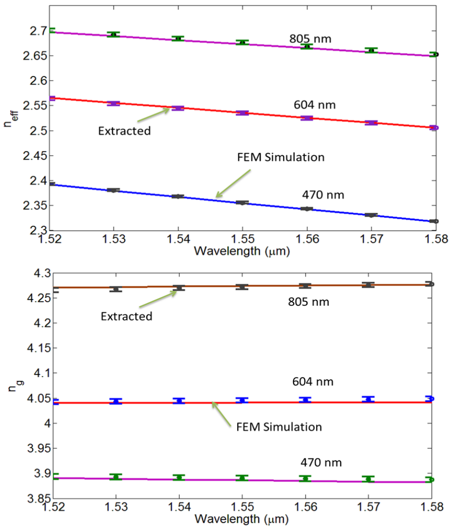

Figuur 2: (a) Gesimuleerde en geëxtraheerde effective brekingsindex n_{eff} van 470, 602 and 805 nm brede golfgeleiders en (b) gesimuleerde en gemeten groepsindex n_g over de C-band.

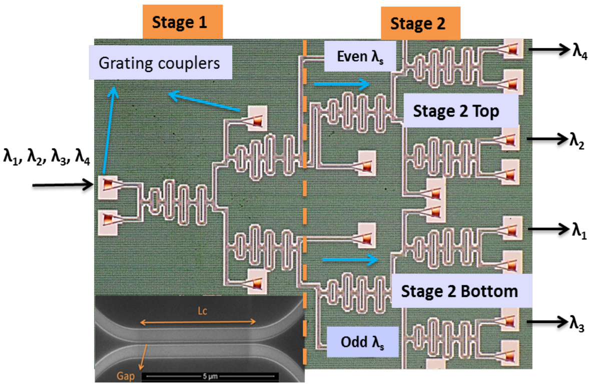

Figuur 3: Camerabeeld van een blok van een vierkanaals tweetraps gecascadeerde demultiplexer (detailbeeld: SEM-beeld van een directionele koppelaar)

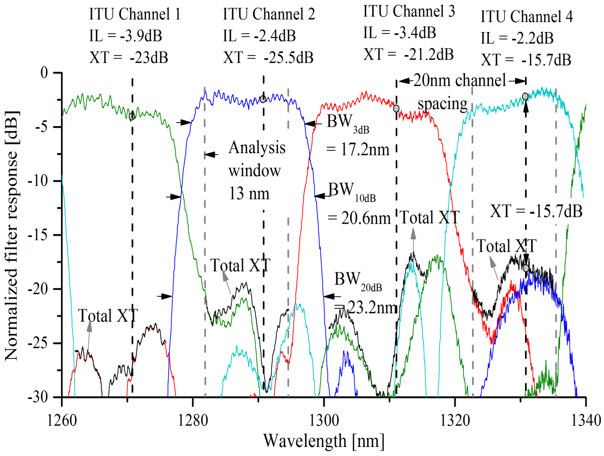

Figuur 4: Gemeen, genormalizeerde transmissie van de demultiplexer met aanduiding van de kanaalspatiering (CS), het verlies (IL) en de overspraak (XT) op de standaard ITU golflengtes.

$550 \times 650\mu m^2$. Het houdt de standaard intact, gesteld door andere platformen als silica *planar light-wave circuits* (PLC) waar de glasgolfgeleiders een kern hebben van enkele micrometers (hier is het controleren van de kanaalspatiering echter vrij eenvoudig door het lage brekingsindexcontrast). De gedemonstreerde component is een kandidaat voor 100Gb Ethernet en toekomstige 400GbE applicaties. De gefabriceerde en gemeten demultiplexer worden getoond in Fig. 3 en Fig. 4.

We stelden ook een nieuw ontwerp voor, gebaseerd op passieve compensatie technieken, om een golflengtefilter temperatuursongevoelig te maken. Door het gebruik van golfgeleiders van verschillende breedte of polarisatie kunnen we de opsluiting van de mode benvloeden. Dit heeft een direct effect op de TO-cofficint. In onze methode kunnen we dit gebruiken om het effect van de temperatuursgevoeligheid te onderdrukken in de filter. Hiervoor kiezen we verschillende golfgeleiders van een bepaalde lengte. We bewezen deze methode door middel van volledig in silicium gefabriceerde temperatuursongevoelige MZI filters en demultiplexers. Enkele gedemonstreerde componenten zijn:

1. Volledig silicium temperatuursongevoelige demultiplexer met vier kanalen: De kanaalspatiering was ontworpen op 5nm. Elke MZI is een combinatie van een nauwe (300 nm) en een brede (450 nm) golfgeleider. De gefabriceerde en gemeten componenten worden getoond in Fig. 5 en Fig. 6. De temperatuursgevoeligheid is minder dan 8pm/K, wat 10 keer lager is dan voor een niet-gecompenseerde component.

2. Volledig silicium temperatuurongevoelige *arrayed waveguide grating* (AWG) met vier kanalen: Om de AWG temperatuurstolerant te maken, hebben de golfgeleiders twee breedtes (in tegenstelling tot conventionele ontwerpen

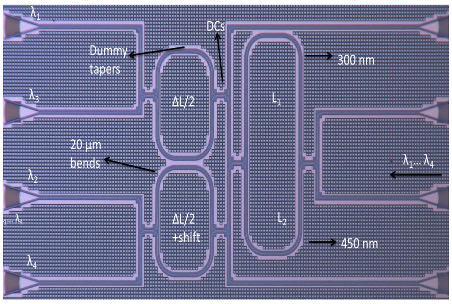

Figuur 5: Camerabeeld van een vierkanaals athermische demultiplexer.

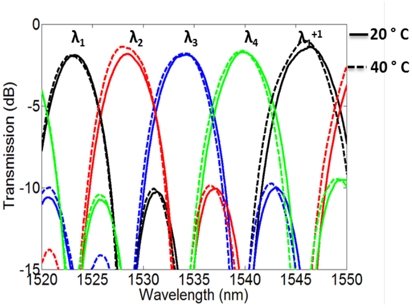

Figuur 6: Gemeten, genormalizeerde transmissie van ene vierkanaals athermische demultiplexer bij $20\,^{\circ}\mathrm{C}$ *en* $40\,^{\circ}\mathrm{C}$

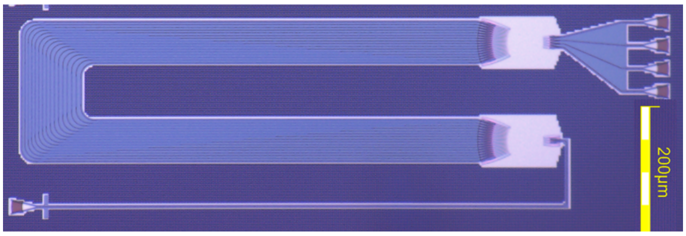

Figuur 7: Gefabriceerde vierkanaals athermische AWG in silicium.

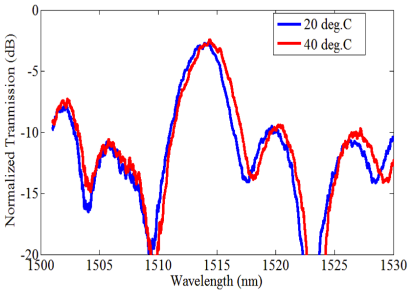

Figuur 8: Genormalizeerde transmissie van het eerste kanaal van de vierkanaals demultiplexer bij de temperatuur van 20 °C *en* 40 °C.

met een enkele breedte). De component gebruikt 300 nm en 800 nm brede volledige getst 220 nm dikke silicium golfgeleiders met silica als bovenliggende laag. Fig. 7 toont de gefabriceerde component. De genormaliseerde transmissie werd gemeten op twee verschillende temperaturen (20 °C en 40 °C) en wordt weergegeven in Fig. 8.

3. Compacte volledig silicium temperatuursongevoelige filter met een splitter-polarizatie sectie: We stellen een MZI voor die compact is, temperatuursongevoelig en volledig is silicium gedefinieerd is. De MZI maakt gebruik van polarizatieroterende directionele koppelaars. De temperatuursgevoeligheid is minder dan 8pm/K over een golflengtebereik van 30 nm. De oppervlakte van de component is gereduceerd door het gebruik van 2 polarizaties. De component wordt getoond in Fig. 9, de genormaliseerde transmissie op verschillende temperaturen in Fig. 10.

We gebruiken ook een gelijkaardige passieve compensatietechniek om de MZI filter fabricatietoleranter te maken. Deze componenten zijn 20 keer meer tolerant tegen variaties in de golfgeleiderbreedte, met een golflengteverschuiving van minder dan 60pm/nm breedteverschil.

De twee bovenstaande compensatietechnieken werden gecombineerd in 1 device. Dit is mogelijk door een orthogonale polarizatie te gebruiken in beide armen van de component. Indien men dezelfde polarizatie wil gebruiken kan men de

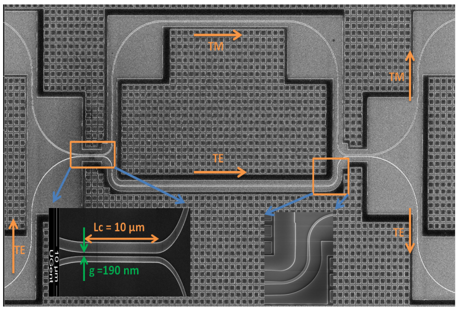

Figuur 9: SEM-beeld van een athermische MZI fiter met een detail van de splitter-polarizatiedraaier en de versmalling in the onderste arm.

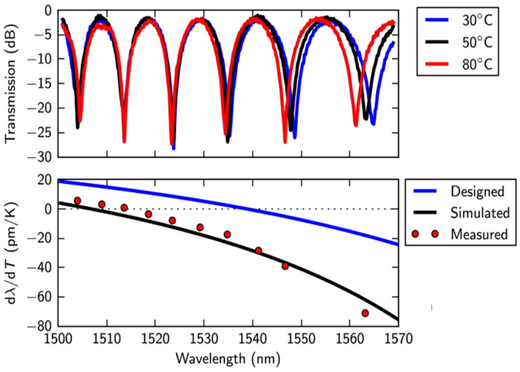

Figuur 10: (a) Gemeten transmissie van de gefabriceerde demultiplexer bij drie verschillende temperaturen. (b) De thermische gevoeligheid zoals ontworpen, zoals gesimuleerd op basis van het SEM-beeld, en zoals gemeten.

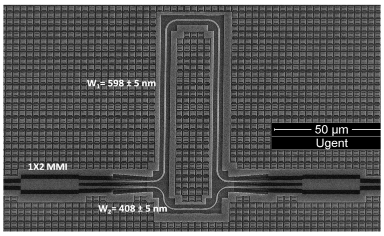

Figuur 11: SEM-beeld van de gefabriceerde MZI met ondiep geëtste MMI.

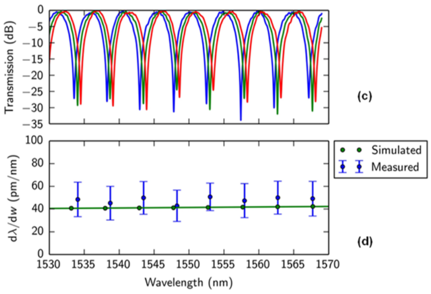

Figuur 12: (a) Genormaliseerde transmissie en (b) $\frac{d\lambda}{dw}$*-variatie als functie van golflengte*

golfgeleiderbreedte variren. Het ontwerp is zoals getoond in Fig. 10 met geoptimalizeerde breedte voor fabricagefouten. We meten een verschuiving van minder dan $\pm 65pm/nm$ en temperatuursgevoeligheid van $\pm 15pm/K$ over een golflengtebereik van 40 nm.

2 Conclusie

Van bovenstaande discussie kan geconcludeerd worden dat een slim ontwerp de fundamentele problemen van het SOI platform kan aanpakken. We namen de uitdaging aan om de effectieve brekingsindex van hoogdispersieve silicium golfgeleiders accurater te bepalen. We demonstreerden een robuuste demultiplexer met vlakke doorlaatband en kanaalspatiering van 20 nm voor 100 GbE applicaties. We hebben ook componenten gemaakt die compenseren voor fabricatie-imperfecties (vooral de golfgeleiderbreedte) en temperatuursgevoeligheid. Verschillende FIR filters werden aangetoond zoals AWG's en MZI's. De combinatie van deze ontwerpen met vlakke doorlaatband en compensatieschema's kunnen de performantie nog verder opkrikken, wat van belang is voor interconnecties op chip. Met deze gerealiseerde ontwerpen hebben we aangetoond dat enkele uitdagingen kunnen/-zullen opgelost worden zonder het fabricatieprocess verder te compliceren.

English summary

In the past decade, silicon photonics has rapidly become one of the most promising photonic integration technologies. This can be attributed to the following key factors:

1. Silicon is transparent at the wavelengths heavily used in present-day optical communications systems O-band (1310 nm) and C-band (1550 nm).

2. Silicon has a very high refractive index, enabling optical waveguides with a very high refractive index contrast. The consequence of this is that waveguide cross sections can be shrunk to sub-micrometer dimensions, and the waveguides can be bent with only a few micrometer bend radius. Therefore, photonic circuits in silicon can be orders of magnitude smaller than their predecessors made in low-contrast glass. Or conversely, a given chip area can accommodate more waveguide components, enabling more complex photonic circuits.

3. Silicon is also the material of choice for electronic integrated circuits. In the past 5 decades the CMOS industry has invested billions in a manufacturing infrastructure that has scaled up in volume and precision, while at the same time scaled down in cost per device. The same infrastructure can be used for silicon photonics, providing a fabrication platform that is far more advanced than that of competing photonic technologies.

4. Integration of Germanium with Silicon-On-Insulator (SOI) platform allows to fabricate integrated detectors. The only missing element is the light source. The indirect bandgap of silicon does not allow efficient light generation. One promising approach to tackle this problem is the hybrid integration of III-V materials on SOI platform.

Silicon photonics is expected to provide the solutions for low-cost data-center links, widespread deployment of access networks (fiber-to-the-home) and the chip-to-chip interconnect bottleneck. All the essential components have been demonstrated on this platform, and first silicon photonics communication products are entering the market. In additional, silicon photonics is finding applications in sensing, spectroscopy and diagnostics.

Challenges

Some of the strengths of silicon photonics also introduce weaknesses. Listed below are some key challenges of the silicon photonics that relate to the work in the manuscript:

1. The high refractive index contrast that allows the small waveguides and sharp bends also makes the waveguides highly sensitive to any variation in the cross section. While good process control already allows nanometer-level accuracy, this is often insufficient for wavelength selective functions in a wavelength-division multiplexing (WDM) system. Pre-fabrication or post-fabrication trimming of the components can be used to correct the effects of the last nanometer scale fabrication offsets.

2. Another issue is that silicon has a strong thermo-optic (TO) coefficient, meaning that there can be significant change in refractive index with temperature. This is beneficial if it is used for tuning circuit elements, but that also implies additional power consumption and complicated logic. A passive silicon photonic circuit will therefore need temperature stabilization, or a method is needed to compensate for the thermo-optic effect of silicon. One method for this is the introduction of materials with opposite TO coefficients, such as polymers or titanium dioxide (TiO_2), but this introduces additional process complexity and it is not always desirable to incorporate such materials in a CMOS-like process flow.

3. The effective refractive index is a very critical parameter in the design of wavelength filters. It determines the exact condition of constructive interference, and therefore the central operating wavelength of a filter. Because silicon wire waveguides are very dispersive, n_g and n_{eff} are very different, and highly wavelength dependent. Knowing the group index with the filter FSR measurements, it is theoretically possible to integrate the effective index. But this can result in an ambiguous solution because the order of the filter is unknown. Due to these constraints, measuring an absolute refractive index of the silicon photonic waveguide is non-trivial problem.

3 Our Contribution and Results

We addressed the above mentioned fundamental challenges of the extremely sensitive SOI waveguides and wavelength filters not at the technology level, but rather through smart design solutions. Listed below are our primary research contributions and results.

1. We proposed and demonstrated an accurate method of measuring the effective refractive index (n_{eff}) and thermo-optic coefficient of Silicon-On-Insulator waveguides in the entire C-band using three Mach-Zehnder Interferometers. The method allows for accurate extraction of the wavelength

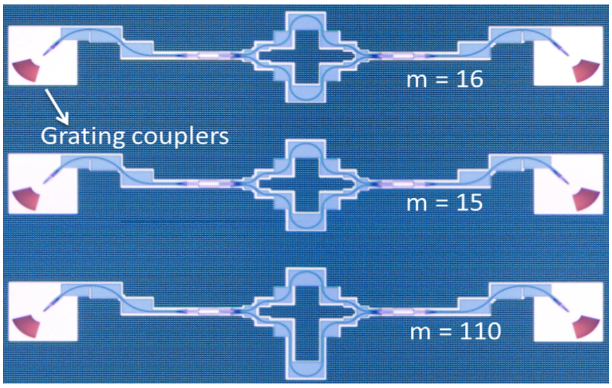

Figure 13: Camera image of set of fabricated devices for 600 nm wide waveguide.

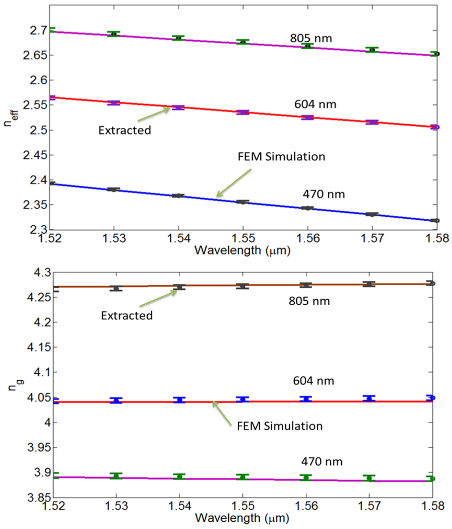

Figure 14: (a) Simulated and extracted n_{eff} of 470, 602 and 805 nm wide waveguides and (b) Simulated and extracted n_g over the C-band

dispersion and takes into account fabrication variability. We use two MZIs with a low order m, i.e. a large *free spectral range* (FSR), which allow us to estimate the order of the filter correctly within the C-band. The third MZI has a much higher order and a small FSR, which helps us to extract the wavelength dependence of the group index (n_g). To extract the TO coefficients, we measure the same MZIs at different temperatures and then extract the wavelength sensitivity of the spectrum with respect to temperature. The fabricated devices are shown in the Fig. 13. The simulated and extracted of $neff$ and n_g values are shown in Fig. 14.

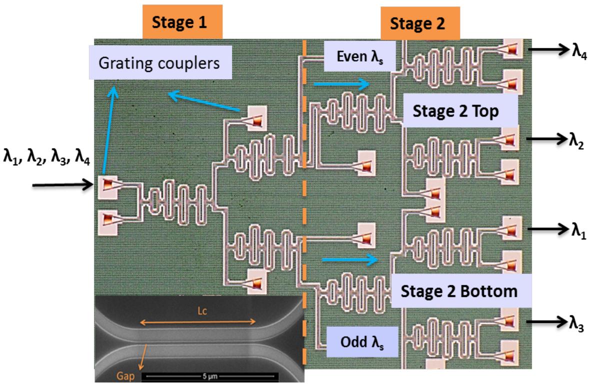

Figure 15: Camera image of fabricated single block and 4-channel dual stage cascaded MZI demultiplexing filter (Inset: SEM image of one of the directional coupler showing gap and coupling length).

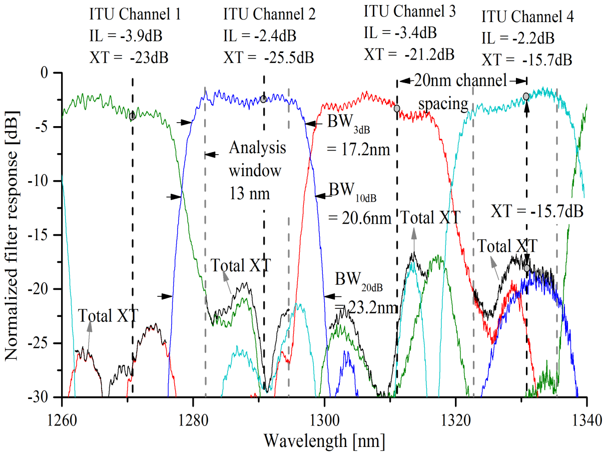

Figure 16: Normalized measured transmission of the demux filter showing channel spacing (CS), insertion loss (IL) and crosstalk (XT) at ITU grid wavelengths.

2. In order to make wavelength filters tolerant to fabrication process variations and environmental thermal fluctuations we flattened the pass band response of the channels. With this technique we compared different SOI de-multiplexers e.g. arrayed waveguide gratings, echelle gratings and cascaded MZI filters. In short reach optical inter-connects where low power budget and low cost is critical we found that cascaded MZI filters are the best choice.

   We demonstrate a low loss and robust four channel de-multiplexer for the O-band based on a dual stage cascaded Mach-Zehnder interferometer (MZI).

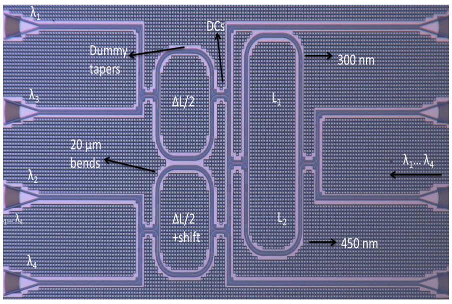

Figure 17: Camera image of fabricated 4-channel athermal demultiplexer

The flat top channel response is obtained by a fourth-order cascaded MZI filter design. The measured device has a 20 nm channel spacing, a span of over 80 nm, centered at 1301 nm with a flat pass band that spans over 60 % of the channel spacing, to mitigate temperature changes up to 100 °C and wafer-level waveguide dimensional variations. Full wafer-scale characterization of the device shows a mean insertion loss below 3 dB and cross talk below -18 dB. This wide band flatness makes the demultiplexer thermally robust in nature. This helps in direct usage of an uncooled laser and avoids thermal control, which results in a low power and low cost solution for a silicon based short reach optical interconnects. The footprint of the device is $550 \times 650 \mu m^2$. This is a critical demonstration on SOI platform due to the highly dispersive nature of silicon waveguides. Keeping the channel spacing intact for a platform such as silica *planar light-wave circuits* (PLC) where the glass waveguide cores are several μms across, is relatively straightforward due to the platform's low refractive index contrast. The demonstrated device is a potential candidate of 100 GbE and future 400 GbE applications. The fabricated and measured demultiplexer is shown in Fig. 15 and Fig. 16 respectively.

3. We proposed a novel design based passive compensation technique to make the wavelength filters temperature insensitive. By combining different waveguide widths or polarization we can change the mode confinements in their corresponding arms. The mode confinements are directly dependent on the waveguide thermo-optic (TO) coefficients. In our method the different arms of the filter have different waveguide width or polarization. By optimizing the arm lengths the thermal dependence of the output of the filter is nullified for a given FSR. With this method we demonstrated all-silicon athermal MZI filter and de-multiplexers. Some demonstrated devices are:

   (a) A four channel all-silicon athermal demultiplexer: The 4-channel athermal de-multiplexer is designed for 5 nm channel spacing. Each MZI is a combination of narrow (300 nm) and the wide (450 nm) waveguide. The fabricated and measured demultiplexer is shown in Fig. 17

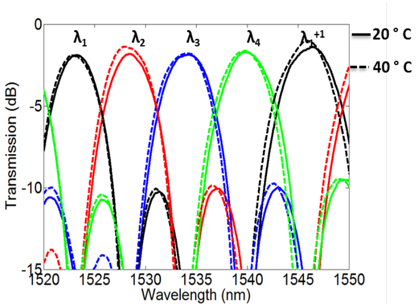

Figure 18: Measured normalized transmission of 4-channel athermal demultiplexer at 20 °C *and* 40 °C

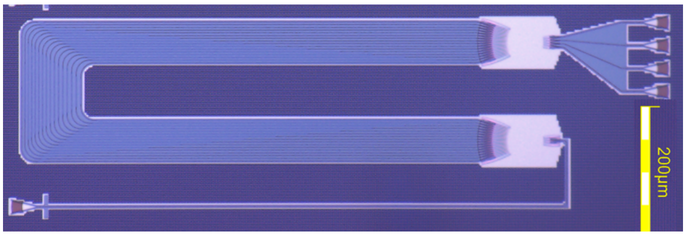

Figure 19: Fabricated all-silicon four channels athermal AWG

and Fig. 18 respectively. Temperature sensitivity of each channel is less than 8 pm/K which is a 10 times improvement with respect to a conventional MZI.

(b) A four channel all-silicon athermal AWG: In order to make the AWG thermal tolerant, individual waveguides in delay lines have two widths, unlike in a conventional one where the waveguides have single width. The device is composed of 300 nm and 800 nm wide fully etch 220 nm thick silicon waveguides with oxide top cladding. The fabricated device is shown in Fig. 19. The measured normalized transmission of an AWG at two different temperatures 20 °C and 40 °C is shown in Fig. 20.

(c) A compact all-silicon athermal filter using splitter-polarization rotator: We propose a compact, temperature-insensitive, all-silicon MZI filter that uses polarization-rotating asymmetrical directional couplers. The temperature sensitivity of the filter is less than 8 pm/K over a wavelength range of 30 nm. A reduce footprint of the device is made possible by using different poalrization. The fabricated device is shown in Fig. 21. measured normalized transmission at three different temperatures are shown in Fig. 22. This device has been the subject of a patent application.

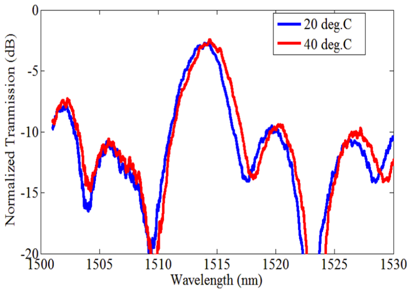

Figure 20: Normalized first channel response of all silicon athermal AWG at temperatures $20\,^\circ\mathrm{C}$ *and* $40\,^\circ\mathrm{C}$

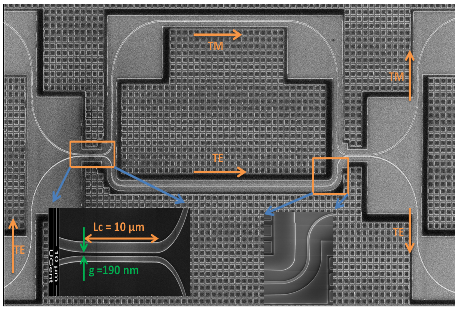

Figure 21: SEM image of fabricated athermal MZI filter with zoomed in SPR and waveguide tapering in the lower arm

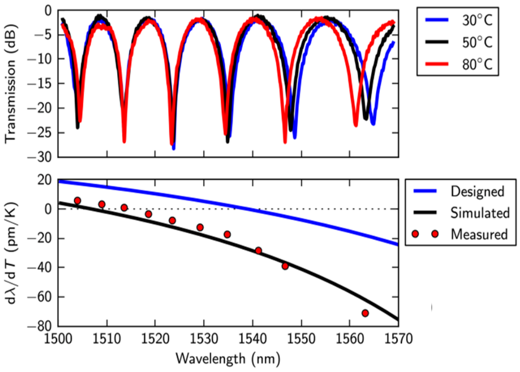

Figure 22: (a) Measured transmission of fabricated device at three different temperatures. (b) Thermal sensitivity designed, simulated (after SEM) and measured device .

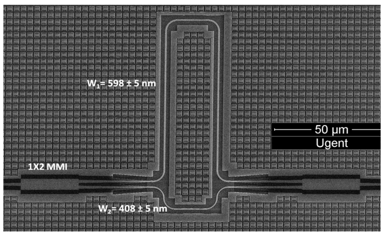

Figure 23: SEM image of fabricated MZI filter with shallow etch MMI

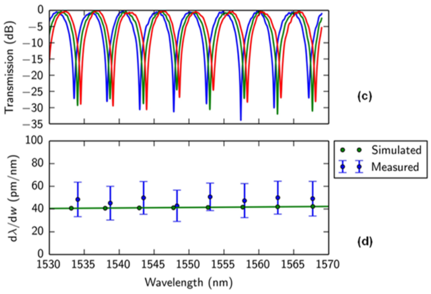

Figure 24: (a) Normalized measured transmission and (b) $\frac{d\lambda}{dw}$ *variation with wavelength.*

4. We also use a similar passive compensation technique to make the MZI filter fabrication tolerant in which we used different waveguide widths in the arms. Measurements show a 20-fold improved tolerance to systematic waveguide linewidth variations, with a wavelength shift of less than 60 pm/nm linewidth change over the entire C-band. The fabricated device is shown in Fig. 23. The normalized transmission, measured at three different widths, are shown in Fig. 24.

5. We have combined the temperature and linewidth tolerance in a single device. This is made possible by employing an orthogonal polarization in either arm of the device. For the same polarization can be done by using multiple waveguide widths. The device design is similar to the one shown in Fig. 22 with optimized width for linewidth tolerances. The fabricated device shows a shift of less than less than ±65 pm/nm and thermal sensitivity smaller than ±15 pm/ K over 40 nm of wavelength range.

4 Conclusion

A smart design approach can solve some of the fundamental issues of SOI platform. We demonstrated an accurate extraction of effective refractive index of highly dispersive silicon waveguides, a demonstration of flat band 20 nm spaced robust demultiplexer for 100 GbE applications and also the passive compensation

of various FIR filters like MZIs and AWGs. Combining the flat band approach and passive compensation techniques can further improve the performances of the demultiplexers which are critical for on chip optical interconnects. We have shown that without altering the fabrication process itself and with novel design approach some critical issues of silicon photonic devices can be resolved.

1

Introduction

”Tolerance always has limits - it cannot tolerate what is itself actively intolerant.”

– Sidney Hook

Tolerance and efficiency are among the most important measures of performance of any evolved technology ranging from space research to a hand-held electronic device. If we take an example of a mobile phone, it is designed to be efficient in operation and handle some extra stress, temperature, pressure and even interaction with water. If we take another example of an RF antenna attached to a satellite, it has to be efficient enough to receive or send signals in extreme environmental conditions.

The same kind of tolerance and efficiency are needed in the area of optical communications as well. Bandwidth demand is increasing day-by-day. Optical fiber links have been a huge success over the years for keeping up with the demand for the high-density data communications for long haul and metro network for more than a decade. Due to the massive data access between end users and the providers the energy consumption is huge. To keep up with this big data demand the data centers need to be extremely energy efficient [1]. However, the bulk optical devices consume a significant amount of power.

Silicon photonics is a recent technology which has been developed over the past decade and which is still developing to cater to the need of high speed low power interconnects for rack-to-rack and chip-to-chip communication [2–7].

Silicon is the most commonly used material for electronics. Since it is transparent to the heavily used present-day optical communication window (i.e. O and C-band), it is also a very interesting material for optics. Silicon has a very high refractive index, enabling optical waveguides with a very high refractive index contrast . As a consequence, the waveguide cross sections can be shrunk to sub-micrometer dimensions, and the waveguides can be bent with only a few μm bend radius [8]. Therefore, photonic circuits in silicon can be orders of magnitude smaller than their predecessors made in low-contrast glass. Conversely, a given chip area can accommodate more waveguide components, enabling more complex photonic circuits.

Silicon photonics uses the standard *complementary metal oxide semiconductor* (CMOS) integration technology and hence can be fabricated within the standard CMOS fab lines [9, 10]. In other terms, it reduces the overall cost due to mass production of the devices while maintaining high performance within the existing fab-lines with a proven technological track record.

1.1 Rationale

From some of the strengths of silicon photonics also emerge the weaknesses. The high refractive index contrast that allows the small waveguides and sharp bends also makes the waveguides highly sensitive to any variation in the cross section [11] and operating wavelength. While good process control already allows nanometer-level accuracy, this is often insufficient for wavelength-selective functions, such as channel drop filters in a wavelength-division multiplexing (WDM) system. Pre-fabrication or post-fabrication trimming of the components can be used to correct the effects of the last nanometer fabrication offsets [12, 13]. Since the light is confined in small cross-section silicon photonic waveguides are very dispersive in nature.

Silicon has a strong thermo-optic coefficient. This means that its refractive index changes as a function of temperature [14, 15]. This is beneficial if it is used for tuning circuit elements, but that also results in additional power consumption. A passive silicon photonic circuit will therefore, need temperature stabilization. Alternatively, a method is needed to compensate the thermo-optic effect of silicon.

One method involves the introduction of materials with opposite thermo-optic coefficients, such as polymers and titanium oxide (TiO_2), but this introduces additional process complexity and it is not always desirable to incorporate such materials in a CMOS-like process flow [16–23].

Typically in a filter design using a standard single mode Silicon-On-Insulator (SOI) waveguide ($220nm \times 450nm$), a change of 1 nm in the width of the waveguide corresponds to 1 nm of wavelength shift in the filter's response whereas a change of 1 nm in the SOI thickness leads to wavelength shift of 1.4 nm in the filter's response. The wavelength shift is around 80 pm/K due to the change in ambient temperature [24, 25]. This simulation is depicted in Fig. 1.1.

In a WDM optical link the total power consumption includes the electrical power needed for modulator and receiver operation, multiplexer and demultiplexer tuning and wavelength locking circuitry, as well as the laser source electrical power required to generate sufficient optical power to operate inter-chip links. For an example, the silicon photonic ring-resonator based WDM link running at the data rate of 12.5 Gbps consumes an average energy of 2.5 pJ/bit which is equivalent to 31.4 mW [26]. It includes total power consumption (electrical and optical) of transmitter side (laser, modulator and multiplexers), routing and transport, receiver side (de-multiplexers and photo-diodes) and total thermal tuning and control of the components. The thermal tuning and control itself consumes 6.4 mW of total power which is almost 20$\%$ of the full optical link [26–29]. Although these numbers are technology dependent and also depends upon kind of component used in the system but, they give a good idea of the contribution of tuning to the overall efficiency.

The goal is to lower down the link budget to 1 pJ/bit by 2020 predicted by Cisco and Oracle to meet the requirement of energy-efficient optical link that can work both for short chip-to-chip interconnects as well as capable of longer spans across intra-datacenter interconnects [26, 30, 31]. Hence, reducing thermo-optic related energy consumption is the key challenge in reaching this requirement.

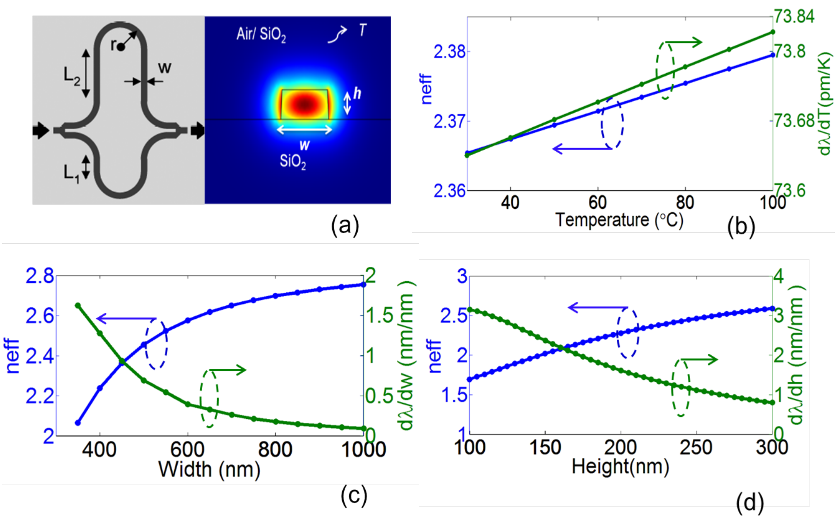

Figure 1.1: (a) Conventional Mach-Zehnder Interferometer (MZI) filter and simulated mode profile of the waveguide with width 450 nm and thickness 220 nm at a wavelength of 1550 nm. Simulated effective refractive index and sensitivity of the MZI spectrum position with (b) temperature, (c) width and (d) height variation respectively. The simulation is performed for the air cladding.

1.2 Goal

The goal of this work is to address the above mentioned issues of extremely sensitive silicon photonic waveguides and the wavelength filters not at the technology level, but rather through smart design solutions. The objective is to propose and demonstrate a method that does not involve any extra material or fabrication process.

In other words, the motivation of this work is to answer few fundamental questions like is it possible to make tolerant all-silicon demultiplexer which can be incorporated directly to an optical link just by design and it will lower down the energy consumption? Or, is it possible to make a wavelength filter just by design which is robust with respect to the fabrication and temperature variations?

1.3 Outline

Chapter 2 starts with an introduction to silicon photonic waveguides mainly developed on the Imec platform. It then deals with the study of a robust and accurate model of the highly dispersive SOI waveguides and their fundamental parameters like effective refractive index and thermo-optic coefficients, which should then be validated experimentally.

Chapter 3 deals with different SOI-based wavelength filters e.g, arrayed waveguide gratings, echelle gratings and cascaded Mach-Zehnder Interferometers (MZIs), mainly targeted at coarse wavelength division multiplexing (CWDM) applications for both C-band (center wavelength at 1550 nm and channel spacing of 6.4 nm) and the O-band (center wavelength at 1310 nm channel spacing of 20 nm). We have achieved the robust demultiplexers by flattening the channel pass band responses. The demonstrated cascaded MZI based demultiplexer for the O-band is a potential candidate for 100 Gigabit Ethernet (GBE), due to its low loss and wide flat band of 13 nm. The presented de-multiplexers does not require thermal tuning due to the wide flat pass band and hence contribute in lowering down the power budget of the optical link.

Chapter 4 gives an introduction to an all-silicon passive compensation technique to make wavelength filters insensitive to the thermal fluctuations. We apply the technique to various devices like MZIs, cascaded MZIs and arrayed waveguide gratings (AWGs).

Chapter 5 focuses on the implementation of a compact athermal MZI filter. The device achieves a reduced footprint by making use of both the TE and the TM polarization, compared to the TE-based design presented in the previous chapter. The device presented in this chapter is also the subject of a patent application [32].

Finally in chapter 6 we extend the concept of athermal filters and explore the possibility of addressing fabrication tolerances separately and also together with thermal tolerances. We also explore the possibilities of combination of flat pass band approach with passive compensation. Presented simulations shows that these wavelength filters are much more robust in terms of thermal tuning or fabrication variations.

1.4 Publications

1.4.1 Patent

1. **Sarvagya Dwivedi**, Wim Bogaerts, Integrated Photonic Devices with Reduced Sensitivity to External Influences, US9075251 B2, Dec. 2013

1.4.2 Publications in international journals

1. **S. Dwivedi**, P. De Heyn, A. Rahim, P. Absil, J. Van Campenhout, W. Bogaerts, " Flat-band Four-Channel Coarse Wavelength Division Multiplexer on Silicon-On-Insulator for the O-Band", submitted for publication in Journal of Lightwave Technology, IEEE/OSA.

2. **S. Dwivedi**, A. Ruocco, Michael Vanslembrouck, T. Spuesens, P. Bienstman, P. Dumon, T. Van Vaerenbergh, W. Bogaerts, " Experimental extraction of effective refractive index and thermo-optic coefficients of Silicon-On-Insulator waveguides using interferometers", Journal of Lightwave Technology, 33(21),IEEE/OSA, pp.4471 4477, Nov. 2015.

3. **S. Dwivedi**, H. D'heer, W. Bogaerts, "Maximizing fabrication and thermal tolerances of all-silicon FIR wavelength filtering devices", IEEE Photonics Technology Letters , vol. 27(8), IEEE, pp. 871-874, Apr. 2015.

4. A. Malik, **S. Dwivedi**, L. Van Landschoot, M. Muneeb, Y. Shimura, G. Lepage, J. Van Campenhout, W. Vanherle, T. Van Opstal, R. Loo, G. Roelkens, "Ge-on-Si and Ge-on-SOI thermo-optic phase shifters for the mid-infrared", Optics Express, vol. 22(23), Optical Society of America, pp. 28479-28488, Nov. 2014.

5. **S. Dwivedi**, H. D'heer, W. Bogaerts, "A compact all-silicon temperature insensitive filter for WDM and bio-sensing applications", IEEE Photonics Technology Letters , vol. 25(22), IEEE, pp. 2167 - 2170, Nov. 2013.

6. H. Yu, M. Pantouvaki, **S. Dwivedi**, P. Verheyen, G. Lepage, R. Baets, W. Bogaerts, P. Absil, J. Van Campenhout, "Compact, Thermally Tunable Silicon Racetrack Modulators Based on an Asymmetric Waveguide", IEEE Photonics Technology Letters, vol. 25(2), IEEE, pp. 159 - 162, Jan. 2013.

1.4.3 Publications in international conferences

1. **S. Dwivedi**, P. De Heyn, P. Absil, J. Van Campenhout, W. Bogaerts, "Coarse Wavelength Division Multiplexer on Silicon-On-Insulator for 100 GbE", 12th International Conference on Group IV Photonics (GFP), IEEE, Vancouver, Canada, p.WC2, Aug. 2015.

2. **S. Dwivedi**, T. Van Vaerenbergh, A. Ruocco, T. Spuesens, P. Bienstman, P. Dumon, W. Bogaerts, "Measurements of Effective Refractive Index of SOI Waveguides using Interferometers", Integrated Photonics Research, Silicon and Nano Photonics, Boston, United States, p.IM2A.6, 2015.

3. W. Bogaerts, S. Pathak, A. Ruocco, **S. Dwivedi**, "Silicon photonics non-resonant wavelength filters: comparison between AWGs, echelle gratings and cascaded Mach-Zehnder filters." (invited), Proc. SPIE 9365, Integrated Optics: Devices, Materials, and Technologies XIX, SPIE, Sin Francisco, United States, Feb. 2015.

4. **S. Dwivedi**, H. D'heer, W. Bogaerts, ”Fabrication and Thermal Tolerant all-Silicon Wavelength Filtering Devices”, IEEE Photonics Society Benelux, IEEE , Enschede, Netherlands, Nov. 2014.

5. **S. Dwivedi**, H. D'heer, W. Bogaerts, ”Fabrication tolerant silicon MZI filter”, 11th International Conference on Group IV Photonics (GFP), IEEE, Paris, France, pp. 147-148, Aug. 2014.

6. **S. Dwivedi**, H. D'heer, W. Bogaerts, ”A compact temperature insensitive filter using splitter polarization-rotating section”, 10th International Conference on Group IV Photonics (GFP), IEEE, Seoul, South Korea, p. WC6, Aug. 2013.

7. **S. Dwivedi**, W. Bogaerts, ”Compact Athermal Filter in Silicon Waveguides for WDM and bio-sensing applications”, Fiber Optics and Photonics 2012, vol. p.M.2.B.3, Optical Society of America, Chennai, India, Dec. 2012.

References

[1] K. Hinton, J. Baliga, M.Z. Feng, R.W.A. Ayre, and RodneyS. Tucker. *Power consumption and energy efficiency in the internet*. Network, IEEE, 25(2):6–12, March 2011.

[2] C. Gunn. *CMOS Photonics for High-Speed Interconnects*. Micro, IEEE, 26(2):58–66, March 2006.

[3] B. Jalali and S. Fathpour. *Silicon Photonics*. Lightwave Technology, Journal of, 24(12):4600–4615, Dec 2006.

[4] D.A.B. Miller. *Device Requirements for Optical Interconnects to Silicon Chips*. Proceedings of the IEEE, 97(7):1166–1185, July 2009.

[5] S. Assefa, S. Shank, W. Green, M. Khater, E. Kiewra, C. Reinholm, S. Kamlapurkar, A. Rylyakov, C. Schow, F. Horst, Huapu Pan, T. Topuria, P. Rice, D.M. Gill, J. Rosenberg, T. Barwicz, Min Yang, J. Proesel, J. Hofrichter, B. Offrein, Xiaoxiong Gu, W. Haensch, J. Ellis-Monaghan, and Y. Vlasov. *A 90nm CMOS integrated Nano-Photonics technology for 25Gbps WDM optical communications applications*. In Electron Devices Meeting (IEDM), 2012 IEEE International, pages 33.8.1–33.8.3, Dec 2012.

[6] Y.A. Vlasov. *Silicon CMOS-integrated nano-photonics for computer and data communications beyond 100G*. Communications Magazine, IEEE, 50(2):s67–s72, February 2012.

[7] Frederic Boeuf, Sebastien Cremer, Enrico Temporiti, Massimo Fere', Mark Shaw, Nathalie Vulliet, bastien orlando, Delia Ristoiu, Alexis Farcy, Thierry Pinguet, Attila Mekis, Gianlorenzo Masini, Peng Sun, Yuemeng Chi, Herve Petiton, Sebastien Jan, Jean-Robert Manouvrier, Charles Baudot, Patrick Le-Maitre, Jean Francois CARPENTIER, Laurent Salager, Matteo Traldi, Luca Maggi, Danilo Rigamonti, Chiara Zaccherini, Carolina Elemi, Bernard Sautreuil, and Luigi Verga. *Recent Progress in Silicon Photonics R&D and Manufacturing on 300mm Wafer Platform*. In Optical Fiber Communication Conference, page W3A.1. Optical Society of America, 2015.

[8] S.K. Selvaraja, P. Jaenen, W. Bogaerts, D. Van Thourhout, P. Dumon, and R. Baets. *Fabrication of Photonic Wire and Crystal Circuits in Silicon-on-Insulator Using 193-nm Optical Lithography*. Lightwave Technology, Journal of, 27(18):4076–4083, Sept 2009.

[9] `http://http://www.st.com/web/en/press/cn/t3279`.

[10] `http://www.intel.com/content/www/us/en/research/intel-labs-silicon-photonics-research.html`.

[11] S.K. Selvaraja, P. Jaenen, W. Bogaerts, D. Van Thourhout, P. Dumon, and R. Baets. *Fabrication of Photonic Wire and Crystal Circuits in Silicon-on-Insulator Using 193-nm Optical Lithography*. Lightwave Technology, Journal of, 27(18):4076–4083, Sept 2009.

[12] Shankar Kumar Selvaraja, Wim Bogaerts, Dries VanThourhout, and Marc Schaekers. *Thermal trimming and tuning of hydrogenated amorphous silicon nanophotonic devices*. Applied Physics Letters, 97(7):–, 2010.

[13] J. Schrauwen, D. Van Thourhout, and R. Baets. *Trimming of silicon ring resonator by electron beam induced compaction and strain*. Opt. Express, 16(6):3738–3743, Mar 2008.

[14] Francesco G. Della Corte, Maurizio Esposito Montefusco, Luigi Moretti, Ivo Rendina, and Giuseppe Cocorullo. *Temperature dependence analysis of the thermo-optic effect in silicon by single and double oscillator models*. Journal of Applied Physics, 88(12):7115–7119, 2000.

[15] Joris Van Campenhout, William M. J. Green, Solomon Assefa, and Yurii A. Vlasov. *Integrated NiSi waveguide heaters for CMOS-compatible silicon thermo-optic devices*. Opt. Lett., 35(7):1013–1015, Apr 2010.

[16] Jie Teng, Pieter Dumon, Wim Bogaerts, Hongbo Zhang, Xigao Jian, Xiuyou Han, Mingshan Zhao, Geert Morthier, and Roel Baets. *Athermal Silicon-on-insulator ring resonators by overlaying a polymer cladding on narrowed waveguides*. Opt. Express, 17(17):14627–14633, Aug 2009.

[17] Vivek Raghunathan, Tomoyuki Izuhara, Jurgen Michel, and Lionel Kimerling. *Stability of polymer-dielectric bi-layers for athermal silicon photonics*. Opt. Express, 20(14):16059–16066, Jul 2012.

[18] Jong-Moo Lee, Duk-Jun Kim, Hokyun Ahn, Sang-Ho Park, and Gyungock Kim. *Temperature Dependence of Silicon Nanophotonic Ring Resonator With a Polymeric Overlayer*. Lightwave Technology, Journal of, 25(8):2236–2243, Aug 2007.

[19] Biswajeet Guha, Jaime Cardenas, and Michal Lipson. *Athermal silicon microring resonators with titanium oxide cladding*. Opt. Express, 21(22):26557–26563, Nov 2013.

[20] Stevan S. Djordjevic, Kuanping Shang, Binbin Guan, Stanley T. S. Cheung, Ling Liao, Juthika Basak, Hai-Feng Liu, and S. J. B. Yoo. *CMOS-compatible, athermal silicon ring modulators clad with titanium dioxide*. Opt. Express, 21(12):13958–13968, Jun 2013.

[21] Jock Bovington, Rui Wu, Kwang-Ting Cheng, and John E. Bowers. *Thermal stress implications in athermal TiO2 waveguides on a silicon substrate*. Opt. Express, 22(1):661–666, Jan 2014.

[22] Feng Qiu, Andrew M. Spring, Feng Yu, and Shiyoshi Yokoyama. *Complementary metaloxidesemiconductor compatible athermal silicon nitride/titanium dioxide hybrid micro-ring resonators*. Applied Physics Letters, 102(5), 2013.

[23] Shaoqi Feng, Kuanping Shang, Jock T. Bovington, Rui Wu, Binbin Guan, Kwang-Ting Cheng, John E. Bowers, and S. J. Ben Yoo. *Athermal silicon ring resonators clad with titanium dioxide for 1.3* μm *wavelength operation*. Opt. Express, 23(20):25653–25660, Oct 2015.

[24] K. Okamoto. *Wavelength-Division-Multiplexing Devices in Thin SOI: Advances and Prospects*. Selected Topics in Quantum Electronics, IEEE Journal of, 20(4):248–257, July 2014.

[25] S. Dwivedi, H. D'heer, and W. Bogaerts. *Maximizing Fabrication and Thermal Tolerances of All-Silicon FIR Wavelength Filters*. Photonics Technology Letters, IEEE, 27(8):871–874, April 2015.

[26] A. V. Krishnamoorthy, H. Schwetman, X. Zheng, and R. Ho. *Energy-Efficient Photonics in Future High-Connectivity Computing Systems*. J. Lightwave Technol., 33(4):889–900, Feb 2015.

[27] Xuezhe Zheng, Ivan Shubin, Guoliang Li, Thierry Pinguet, Attila Mekis, Jin Yao, Hiren Thacker, Ying Luo, Joey Costa, Kannan Raj, John E. Cunningham, and Ashok V. Krishnamoorthy. *A tunable 1x4 silicon CMOS photonic wavelength multiplexer/demultiplexer for dense optical interconnects*. Opt. Express, 18(5):5151–5160, Mar 2010.

[28] Xuezhe Zheng, Eric Chang, Philip Amberg, Ivan Shubin, Jon Lexau, Frankie Liu, Hiren Thacker, Stevan S. Djordjevic, Shiyun Lin, Ying Luo, Jin Yao, Jin-Hyoung Lee, Kannan Raj, Ron Ho, John E. Cunningham, and Ashok V. Krishnamoorthy. *A high-speed, tunable silicon photonic ring modulator integrated with ultra-efficient active wavelength control*. Opt. Express, 22(10):12628–12633, May 2014.

[29] Zhiping Zhou, Bing Yin, Qingzhong Deng, Xinbai Li, and Jishi Cui. *Lowering the energy consumption in silicon photonic devices and systems [Invited]*. Photon. Res., 3(5):B28–B46, Oct 2015.

[30] *Cisco Visual Networking Index: Forecast and Methodology, 2014-2019*.

[31] Yu Li, Yu Zhang, Lei Zhang, and Andrew W. Poon. *Silicon and hybrid silicon photonic devices for intra-datacenter applications: state of the art and perspectives [Invited].* Photon. Res., 3(5):B10–B27, Oct 2015.

[32] S. Dwivedi and W. Bogaerts. *Integrated photonic devices with reduced sensitivity to external influences*, July 7 2015. US Patent 9,075,251.

2

Silicon-On-Insulator Waveguides

2.1 Introduction

Optical waveguides need to confine light along a path on chip, so it can be used to transport a signal between two points. The most straightforward way to construct a waveguide is to use a core with a high refractive index surrounded by a lower refractive index. A well-known example of such a waveguide is an optical fiber, consisting of two types of glass with a slight difference in refractive index.

In this chapter SOI waveguides are studied. The focus of the first part of the chapter is to have an accurate model of the SOI waveguides and their fundamental parameters like effective refractive index (n_{eff}), group index (n_g) and thermo-optic (TO) coefficients. The second part discusses the novel method which is developed to validate these parameters experimentally.

2.2 SOI platform

The silicon-on-insulator (SOI) platform is gaining prominence for industrial production of integrated photonics devices since it can use the well established and existing infrastructure of complementary metal-oxide-semiconductor (CMOS) process technology for fabrication. This offers a scaling avenue to large-volume production at an affordable cost. SOI can be used to define waveguides with a high refractive index contrast between the core and the cladding. This enables dense integrated photonic circuits with sub-micron waveguide cores and sharp bends. This

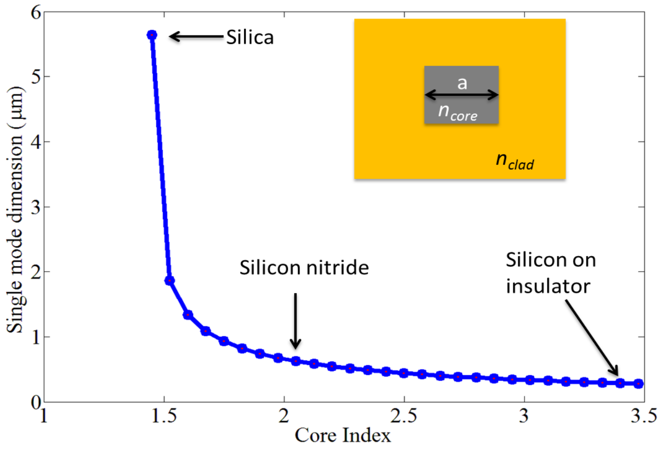

Figure 2.1: Size (a) of the square core for single mode operation for different platforms: Silica, Silicon nitride and Silicon-on-Insulator in the C-band.

is because in the photonic scaling laws, it all depends upon the index contrast. It is an approximation of parameter *V-number* in optical fibers which determines the cutoff condition for all possible guided modes [1]. The maximum core size (a) for a single mode operation for a square core embedded in a uniform cladding can be estimated by:

$$a \approx \frac{\lambda}{2.\sqrt{(n_{core}^2 - n_{cladding}^2)}} \tag{2.1}$$

The comparison of the single mode operation for SOI with other standard platforms operating at conventional band (C-band) with center wavelength of 1550 nm is shown in Fig. 2.1. It can be easily seen that for the SOI platform $a < 300\ nm$ (we assume a square waveguide in this plot, but the scaling is similar for other core geometries).

The cross section of a typical SOI material stack is shown in Fig. 2.2. The SOI material stack consists of 220 nm thick crystalline Silicon (Si) core and 2 μm of buried oxide (SiO_2). The thickness is chosen as 220 nm for several reasons. First, with this thickness, the optical mode is smallest for a width of 450 nm at wavelength of 1550 nm, hence with such waveguides it is possible to make bends with 2-3 μm bend radius without significant bending losses. Second, it provides a single mode behavior of the waveguide. As the optical waveguides get larger they can support more higher order modes [2]. The 2 μm box is chosen to avoid the leakage loss into the substrate. This stack is based on IMEC silicon photonics passives platform.

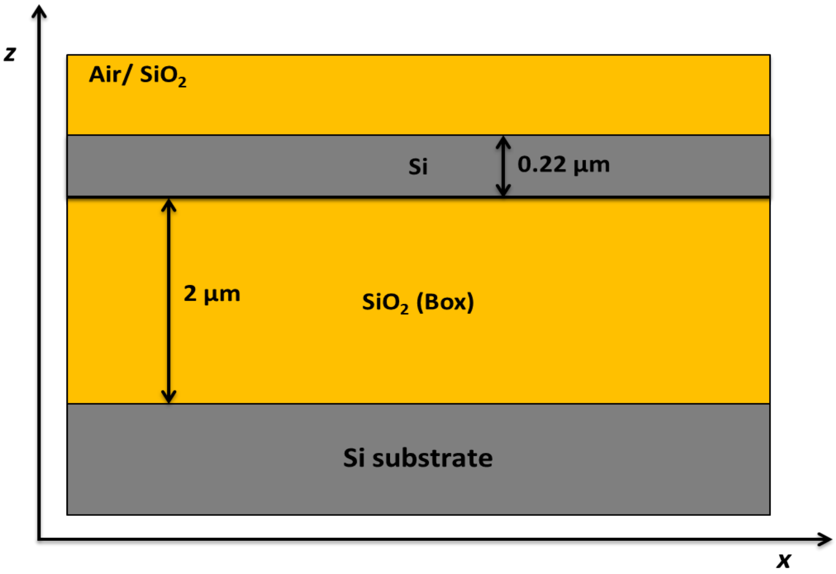

Figure 2.2: Cross sectional drawing of an SOI wafer.

Material properties of Si and SiO_2 at 1550 nm		
Parameter	Si	SiO_2
n	3.477	1.444
$\frac{dn}{dT}$	$1.86 \times 10^{-4}\ K^{-1}$	$1.0 \times 10^{-5}\ K^{-1}$

Table 2.1: Material properties of Si and SiO_2

The wavelength and temperature dependent refractive index material model of silicon and oxide at room temperature is given by the Sellmeier equation [3–5]:

$$n_{\lambda,T}^2 - 1 = \sum_{i=1}^{3} \frac{S_i(T)\lambda^2}{\lambda^2 - \lambda_i^2(T)} \tag{2.2}$$

where $S_i(T)$ are the temperature dependent Sellmeier coefficients. At $\lambda =$ 1550 nm and room temperature, the value of n_{Si} is 3.4777 and for n_{SiO2} it is 1.4440. The thermo-optic coefficient ($\frac{dn}{dT}$) at 1550 nm is $1.86 \times 10^{-4}\ K^{-1}$ for silicon and $1.0 \times 10^{-5}\ K^{-1}$ for oxide, here T is the temperature in Kelvin (K). The material parameter of SOI platform at 1550 nm is summarized in the table 2.1.

2.2.1 Introduction to SOI waveguides

This work is largely based on the IMEC silicon photonics platform (we usually call it SOI platform in this report) which offers Multi Project Wafer (MPW) runs and is available through euro-practice [6]. The SOI platform allows for different waveguide cross sections as shown in Fig. 2.3, which are useful for different applications. The most standard ones are *Strip waveguides* and *Rib waveguides*. The strip waveguide, which consists of a fully-etched silicon line, is the most widely used one for different on chip interconnect functions like routing, connections between components and for different passive circuit functionality like wavelength filtering etc. [7].

Ribs, or shallow etched waveguides, have a partial etch of 70 nm of rib section followed by 150 nm of slab section. This waveguide is mainly used for active components like carrier injection or depletion modulators where slab section is used for doping and metal connection [8]. This partial step is also used in grating couplers [9–13] for coupling light in and out of the photonic chip and wavelength filtering devices like arrayed waveguide gratings (AWGs) and echelle gratings [14]. The propagation loss of rib waveguides are lower than the strip waveguides so they are mostly used for long delay lines [15].

A Socket waveguide is a bit of compromise between strip and a rib waveguide where the etch step is increased to 150 nm and the slab section is just 70 nm. Increasing the etch depth helps in smaller bend radius and lower loss than a strip waveguide. Hence, there is a possibility of compact ring modulators with similar functionality like rib waveguides [16].

In a slot waveguide, the mode is confined in the low index region either air or oxide i.e. in the slot section. Slot waveguide is quite useful for various applications like low power modulators and sensing due to an efficient mode overlap in a slot area either by liquid crystals for modulators [17] or with any sensing element [18, 19].

The propagation inside the waveguide can be described in terms of eigenmodes: a field distribution in and around the core that propagates as a single entity at a fixed velocity. Such an eigenmode is characterized by a propagation vector β or an effective refractive index n_{eff}. The propagation speed of the mode in the waveguide is given by $\frac{c}{n_{eff}}$, with c the speed of light in vacuum. Depending on their dimensions, waveguide can support multiple eigenmodes, that is propagate independently with their own n_{eff}.

Finally, there is the issue of polarization. Modes in optical waveguides can be classified according to their polarization, i.e the orientation of electric field (E-field) components. This classification is done with respect to the plane of the chip. The Transverse Electric (TE) mode is the one in which the E-field is in-plane of the chip, while for the Transverse Magnetic (TM) mode, it is perpendicular to the plane (in vertical direction). A strip waveguide always supports both TE and

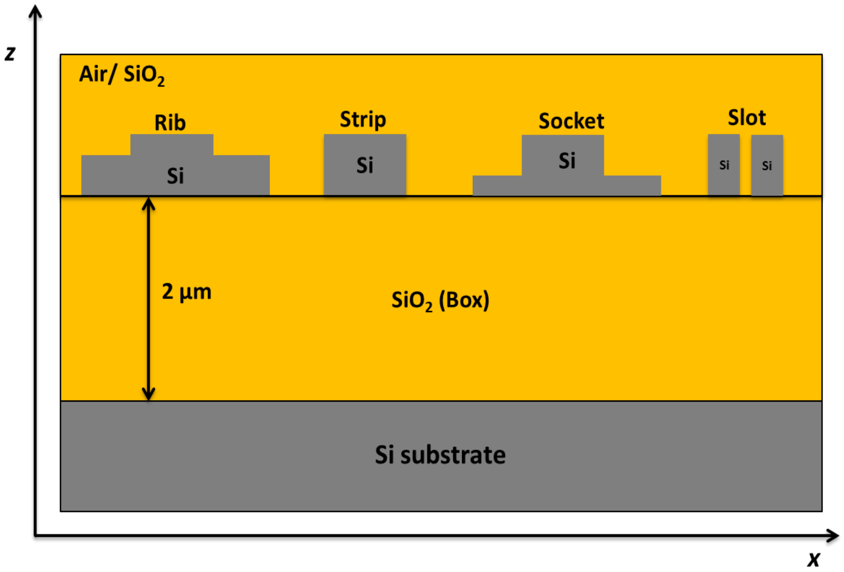

Figure 2.3: Cross section of some standard SOI waveguides: Rib, Strip, Socket and Slot.

TM fundamental modes but they are fully decoupled from each other as long as the vertical symmetry is maintained (waveguide completely surrounded by oxide). Normally, the photonic waveguides have a larger width than height, due to easier in fabrication (printing wider lines, and etching less deep). For this reason the TE is being a fundamental mode in these waveguides. For square waveguides, the TE and TM modes become degenerate [2]. Because of their small feature size, the properties of SOI waveguides are fairly wavelength dependent: the n_{eff}, as well as the exact mode profile, changes as function of wavelength. This dispersion has as a result that signals in the waveguide will travel at a group velocity (v_g) that is considerably smaller that the speed of light. The ratio of speed of light in vacuum to this group velocity $(\frac{c}{v_g})$ is called the group index n_g of the waveguide. In SOI waveguides group index is almost double than the effective index due to its highly wavelength dependent nature.

In this chapter we mainly study strip waveguides. However, all presented methods for measurements and analysis are equally applicable to other waveguide geometries and TM polarization.

2.2.2 Modelling of SOI waveguides

There are different numerical methods proposed in literature to model the optical properties of waveguides e.g. Finite Element Method (FEM) [20, 21], Finite

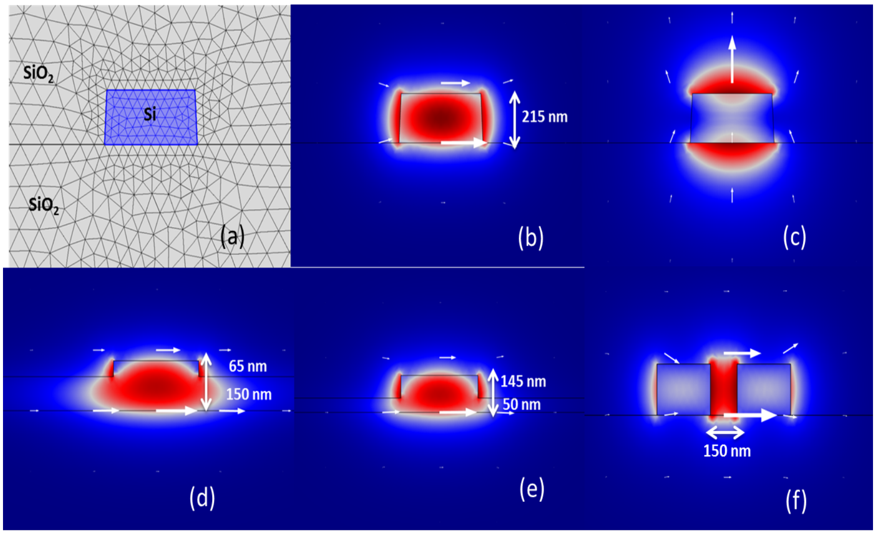

Figure 2.4: (a) Finite element mesh of the strip waveguide (b) TE mode profile and (c) TM mode profile of strip waveguide. TE mode profiles of (d) Rib, (e) Socket and (f) Slot waveguide. Arrows are electric field lines

Difference Time Domain (FDTD) [22, 23], Beam Propagation Method (BPM) [24, 25] and Film Mode Matching (FMM) [26, 27] are the few most common used ones.

The n_{eff} of a guided mode of an SOI waveguide at a given wavelength is a function of the material, the waveguide cross-sectional geometry and environmental temperature. We can conceptually simplify this as

$$n_{eff}(\lambda) = f(w, h, T) \tag{2.3}$$

where w and h are waveguide width and thickness respectively and T is the environment temperature.

The wave equation for mode analysis is given by:

$$\nabla \times (\nabla \times E) - k_0^2 \epsilon_r E = 0 \tag{2.4}$$

In the mode analysis we solve mainly for propagation constant: $\alpha + j\beta$, where α is attenuation and β is propagation constant. In Eq. 2.4, ϵ_r is a material parameter given by $(n - jk)^2$, where n is real part and jk is the imaginary part of the bulk refractive index.

In this work, most of the eigen mode simulations of the SOI waveguide mode are performed by the finite element method (FEM) from COMSOL, taking a wavelength and temperature dependent material model as given in Eq. 2.2. Fig. 2.4

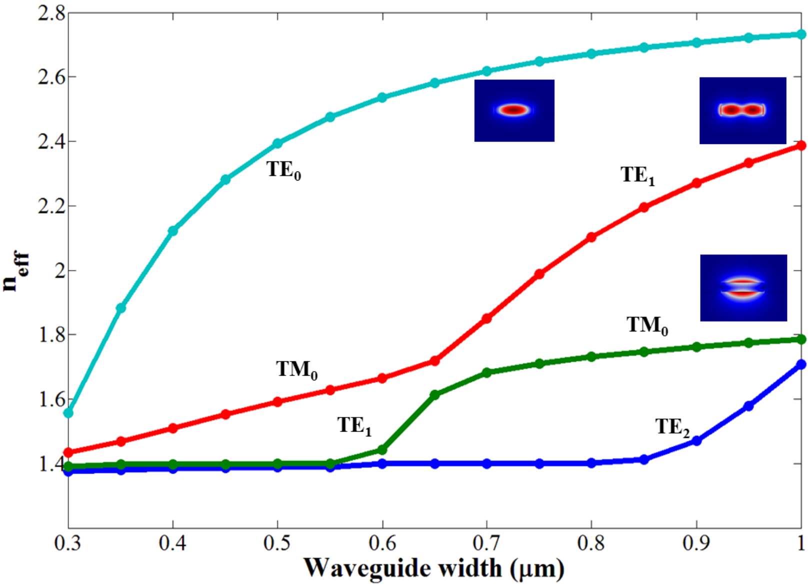

Figure 2.5: Simulated n_{eff} of strip waveguide with waveguide width for air cladding with core thickness = 220 nm

shows the finite element mesh, the transverse electric (TE) and transverse magnetic (TM) mode profile for a strip waveguide with width of 450 nm and thickness of 220 nm at 1550 nm. The simulated mode profile for the Rib, Socket and Slot waveguides are also shown. The mesh size is fine enough to resolve the wavelengths in all media being modelled. A minimum of two elements per wavelength is necessary to solve the problem, it is fundamentally similar to Nyquist frequency in signal processing. Two elements per wavelength is a coarse mesh and resulted in poor accuracy, so we have used minimum 10 elements for our simulations [21].

The simulated n_{eff} with waveguide core width and thickness for strip waveguide with air as top cladding are shown in Fig. 2.5 and Fig. 2.6 respectively.

2.2.3 SOI waveguide sensitivity

The high index contrast and small waveguide dimensions can translate small variations in waveguide width and thickness into a large fluctuations in the n_{eff} [7]. This sensitivity affects the performance of wavelength filters made out of these waveguides. If we consider the wavelength sensitivity of any filtering device to a

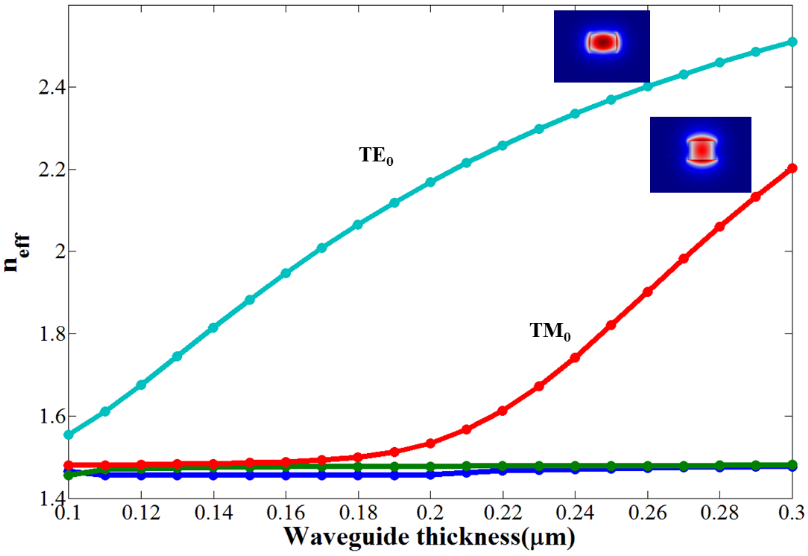

Figure 2.6: Simulated n_{eff} of strip waveguide with waveguide thickness for air cladding with core width = 450 nm

parameter X, this can be expressed as:

$$\frac{d\lambda}{dX} = \frac{\lambda_m}{n_g} \cdot \frac{dn_{eff}}{dX} \tag{2.5}$$

where X can be waveguide width (w), height (h), temperature (T) or any other influence. λ_m is the wavelength of operation, n_{eff} and n_g are the effective refractive index and group index of the waveguide respectively.

2.2.3.1 Sensitivity to waveguide geometry

The n_{eff} and sensitivity of spectral position of wavelength filter due to waveguide width is shown in Fig. 2.7. The n_{eff} and sensitivity of spectral position of wavelength filter due to waveguide thickness is shown in Fig. 2.8.

The wider the waveguide width becomes the smaller is the variation of n_{eff}. It is because the mode confinement inside the core of the waveguide increases with the waveguide. As a result, its overlap with the sidewall decreases and hence the variation of n_{eff} also decreases. Similar argument holds true for the variation of n_{eff} with SOI thickness. However, compared to the width variation, the variation in the thickness leads to the greater n_{eff} variation as shown in Fig. 2.8. Typically in a designed filter using a standard single mode SOI wire (220 nm×450 nm),

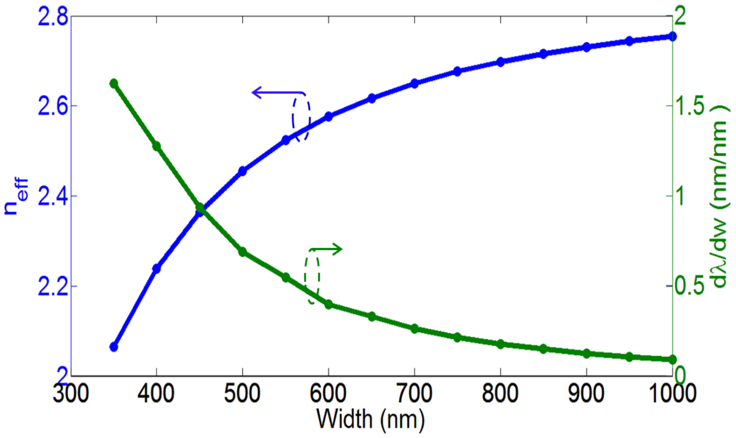

Figure 2.7: Simulated n_{eff} of strip waveguide and sensitivity of spectrum position for any wavelength filter with increasing waveguide core width. Here, h = 220 nm and T = $20\,^{\circ}\mathrm{C}$

a change of 1 nm in the width of the waveguide leads to 1 nm wavelength shift in the filter's response whereas a change of 1 nm in the SOI thickness leads to a wavelength shift of 1 nm in the filter's response.

2.2.3.2 Sensitivity to environmental temperature

Silicon has a high thermo-optic (TO) coefficient of $1.86 \times 10^{-4}\ K^{-1}$, which can result in a filter shift of around 80 pm/K. The n_{eff} and sensitivity of spectral position for any wavelength filter due to environmental temperature is shown in Fig. 2.9.

In order to deal with the effect of environmental temperature fluctuations, there are different available techniques. The most common one is the active tuning by heaters. There are different heaters on SOI platform. The most common one in the use is metallic resistors [28], among others, like silicon doped heaters or silicides are sitting adjacent to the waveguide [29], and some others with the substrate undercut for insulation and higher efficiency [30, 31].

2.2.3.3 Sensitivity to wavelength

As the light is confined in a sub-micron core area with a high index contrast, the waveguide behavior is very dispersive with wavelength. The dispersive nature of the waveguide greatly affect the behavior of wavelength filters over a wide wavelength range. Maintaining a constant *free spectral range* (FSR): the difference between two consecutive peaks of the filter is challenging task, as it is inversely proportional to n_g of the waveguide. The simulated n_g with waveguide core width

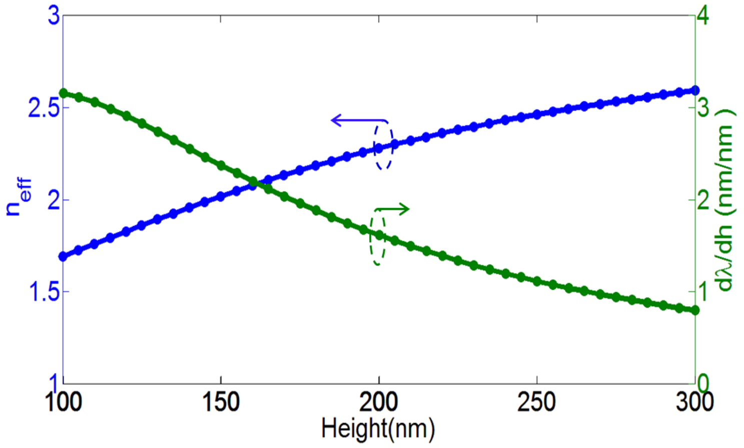

Figure 2.8: Simulated n_{eff} of strip waveguide and sensitivity of spectrum position for any wavelength filter with increasing waveguide core thickness. Here, w = 450 nm and T = 20 °C

for air and oxide as top cladding is shown in Fig. 2.10. It clearly shows how dispersive the SOI waveguides are, as the n_g is almost twice that of n_{eff} as plotted in Fig. 2.5.

2.3 Fabrication of SOI photonic integrated circuits

The fabrication of microelectronics is one of the most advanced manufacturing technologies over past couple of decades. The fabrication technology has been optimized to integrate dense *complementary metal-oxide semiconductor* (CMOS) functionality on a very small area in high volumes with extremely high repeatability. CMOS scaling has been extremely successful over the years with companies like Intel, TSMC, ST Microelectronics, Micron taking the lead in the fabrication of transistors with ever smaller features. Recently Intel has demonstrated a 14 nm node technology, which can pack again more transistors in the same area [32].

Similar fabrication technology can be used for the realization of SOI photonic integrated circuits. The material compatibility allows piggy-backing onto the existing manufacturing and research infrastructures. Today, we see silicon photonics being fabricated in several pilot lines [33–36]. Future migration to standard CMOS production line will enable mass production which will lower the over cost of fabrication. At IMEC, we make use of such a CMOS pilot line to fabricate these circuits. The overview of this fabrication process is shown in Fig. 2.11. The fabrication process uses 193 nm optical lithography to define the waveguide patterns. The process starts with commercially available 200 mm SOI wafer which has 2

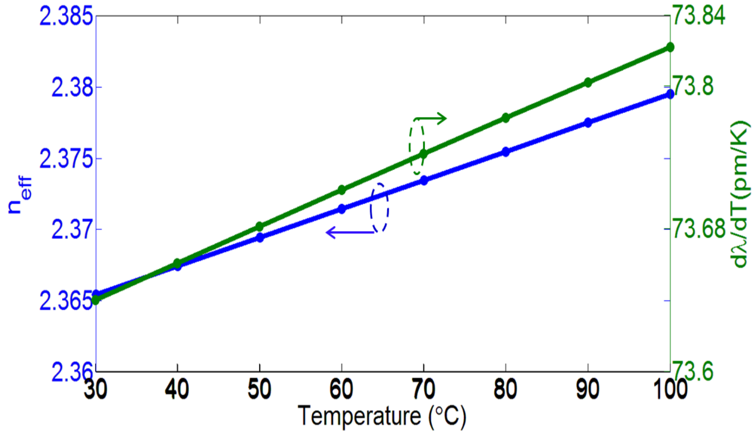

Figure 2.9: Simulated n_{eff} of strip waveguide and sensitivity of spectrum position for any wavelength filter with increasing temperature. Here, w = 450 nm and h = 220 nm

μm of buried oxide and 220 nm of thick crystalline silicon layer on top. To start, the wafer is coated with an anti-reflection coating and photoresist. Addition of an anti-reflective layer at the top or bottom of photoresist helps in suppressing the reflection from substrate which generates a standing wave pattern in photoresist, when illuminated. This standing wave pattern causes a variation in line width. The optimum thickness of photoresist and anti-reflective coating is found to be 330 nm and 77 nm respectively. The wafer is then baked at the optimum temperature and for the optimum time to evaporate the solvents. The resist coated wafers are then exposed with the image of the mask using 193 nm ArF laser in a scanner. The intensity of the illumination in the photoresist, also called the *exposure dose*, defines the sidewall angle and the line width of the developed photoresist. In *post-exposure baking* (PEB), the protons are generated as a result of exposure react with the polymer to form a soluble product. Precise temperature control is required in this process to avoid underdevelopment of the photoresist, which would result in an increased line width. In the *development* process the exposed areas are removed with a selective solvent.

After this lithography process, the structures patterned in the photoresist are ready for dry etching. In the IMEC process, there are etching recipes optimized for 220 nm deep etch (strip waveguide), 70 nm shallow etch (grating couplers and rib waveguide) and 150 nm shallow etch (socket waveguide) respectively. A proper etching recipe is required to achieve low sidewall roughness. The sidewall roughness contributes to the loss and phase errors of the waveguides. The sidewall roughness is seen by the propagating mode of the waveguide, which leads to the phase error accumulation in the wavelength filters. This results in higher cross

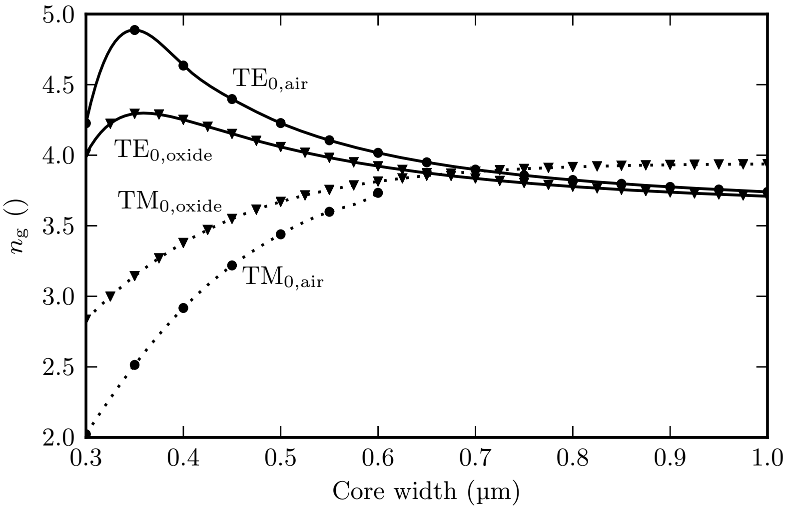

Figure 2.10: Simulated n_g *of strip waveguide with air/ oxide as top cladding with increasing core width*

talk in their performance. The detailed process is discussed in the thesis of S. K. Selvaraja [37]. The fabricated strip waveguide and spiral are shown in Fig. 2.12.

2.4 Characterization

In order to characterize the optical properties of SOI waveguides and other wavelength filtering devices, the light needs to be coupled with the fiber into the photonic chip and then out of the chip to another fiber. Normally, we measure the transmission of the device as a function of operating wavelength. There are different coupling methods. The most common ones are either vertical coupling by using a fiber grating couplers or horizontal coupling (also called edge coupling) in which one has a cleaved chip and light is coupled horizontally via fiber. In this work, we have characterized our all devices via vertical coupling through fiber grating couplers. The vertical coupling via grating couplers has a number of advantages over other methods: For instance, it does not require any post-processing, it has good alignment tolerances, the coupling structure is compact in size, and it is possible to achieve high coupling efficiency . However, they have limited bandwidth, back-reflection problems and work for only one polarization at a time [9, 10, 38]. There has been extensive research in the past few years to improve the efficiency, reduce the back-reflection and couple light through both the polarization [11, 12, 39].

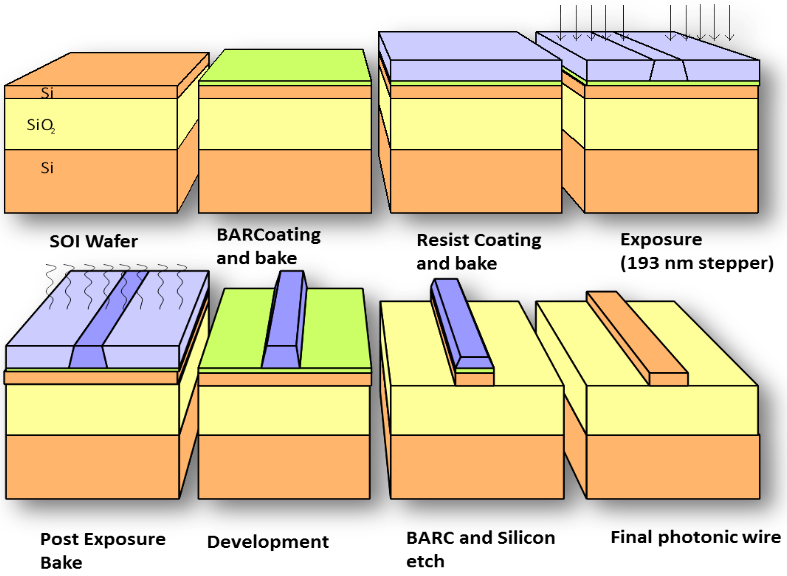

Figure 2.11: Overview of the fabrication process of SOI photonic waveguide using 193 nm optical lithography

2.4.1 Vertical coupling

The light couples from the laser to the waveguide by positioning the fiber vertically over the grating coupler [9, 10, 38]. The silicon waveguides are highly birefringent, so these grating couplers need to be designed accordingly i.e. either for the TE or the TM polarization. 1-D grating couplers are specially designed to serve this purpose. Since these 1-D grating coupler couples to only one selected polarization and rejects the other one, it is necessary to have the light at the output of the fiber with the desired polarization. To achieve this, a polarization controller is used between laser and input fiber. Similarly, the output grating coupler couples light to the output fiber which is connected to the power meter for read out. The grating couplers are designed in such a way as to get the maximum efficiency and minimum back reflections at a particular wavelength band (normally in our case it is C-band with center wavelength of 1550 nm). The fibers are at 10 ° with respect to vertical axis to get the optimum performance of grating coupler. The alignment of fiber with respect to the gratings are done manually with the help of X-Y-Z movable stage as shown in Fig. 2.13. The manual alignment is done in a way so that the output power received from output fiber is maximum at a particular wavelength and is noted at the power meter. There is also an automatic vertical alignment method by more advanced controllable stages. It will be discussed later

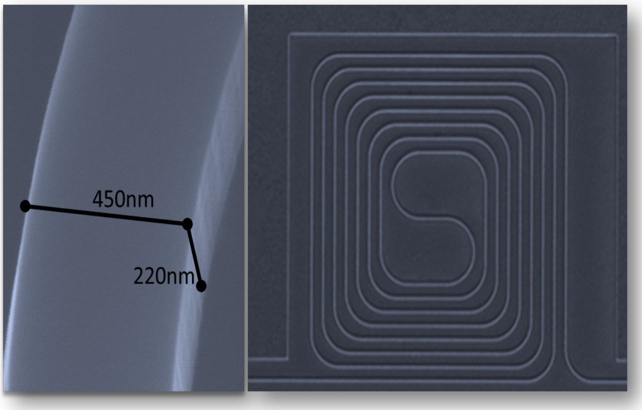

Figure 2.12: Fabricated waveguides, SEM image of (a) the strip waveguide and (b) waveguide spiral

in this section 2.5.4.1.

2.4.2 Waveguide loss measurements

To characterize the waveguide losses, we have measured the transmission through several spirals of different lengths. The spiral consists of photonic waveguides of 450 nm width for full-etch (strip) waveguide and 600 nm width for shallow-etch (rib) waveguide with oxide top cladding. The light is coupled through the vertical grating couplers (GCs) for the TE polarized mode at 1550 nm wavelength as mentioned in the previous section. The measurement uses a *continuous-wave* (CW) laser for sweeping the wavelength across the C-band. We measure the transmission of the spirals of different lengths i.e 1.1,1.6, 2.7 and 4.7 cm is used from which the propagation losses are extracted by a linear fit. The bend radius in spirals is taken as 15 μm and 50 μm for full-etch waveguides and shallow-etch waveguides respectively, to have negligible loss in the bends. One of the standard spirals suit for loss extraction SEM image, which is shown in Fig. 2.14. The plot of absolute transmission vs waveguide spiral length for the loss extraction is shown in Fig. 2.15. At 1550 nm, the measured loss of the fully etch waveguide and shallow etch waveguide are 1.45 dB/cm and 0.85 dB/cm respectively. The other losses mainly comes from bends and GCs when the waveguide length is zero which are very low.

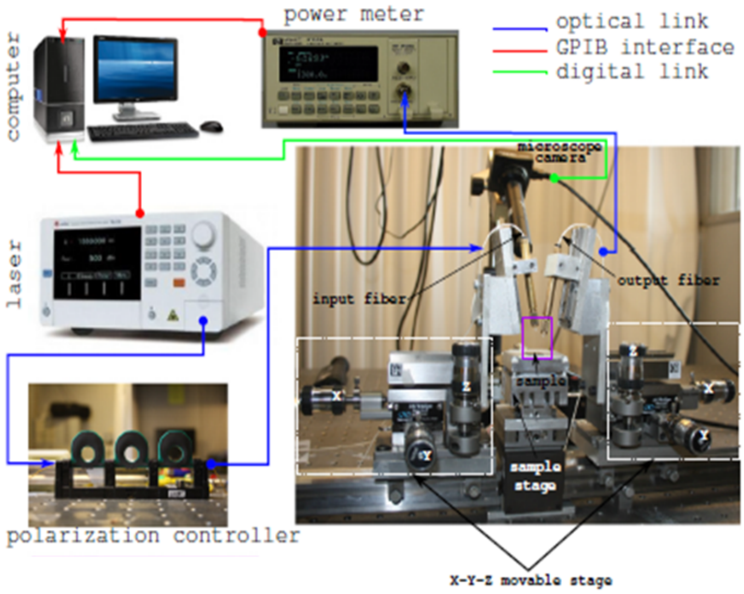

Figure 2.13: The measurement setup for vertical coupling

2.5 Experimental extraction of effective index of the SOI photonic waveguides

In order to design components effectively on the SOI waveguide platform, the exact value of the optical properties should be known, including their wavelength dependence and the statistics of their variability. Many optical properties, such as waveguide loss, can be collected from the optical measurements on fabricated devices as mentioned in the previous section. But this is not straightforward for the *effective refractive index* (n_{eff}) of the waveguide.

The effective refractive index is a very critical parameter in the design of wavelength filters [40, 41]. It determines the exact condition of constructive interference, and therefore the central operating wavelength of a filter.

Given the extreme sensitivity of a silicon wire waveguide to the exact geometry and environmental temperature fluctuations as mentioned in section 2.2.3, it is important to accurately characterize the effective index, including its dispersion, without perturbing the actual waveguide geometry, or the fabrication process.

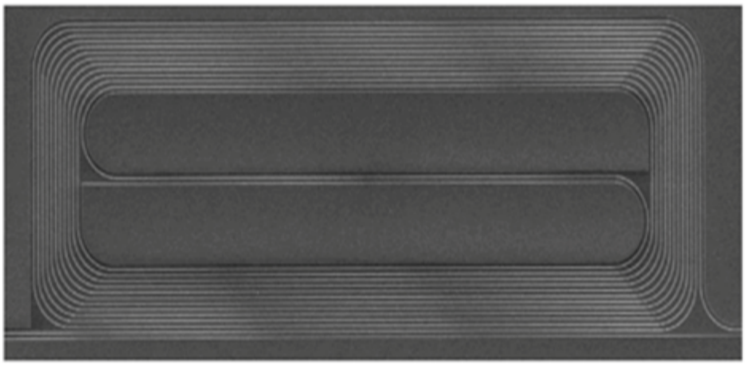

Figure 2.14: One of the standard spiral used for loss measurement

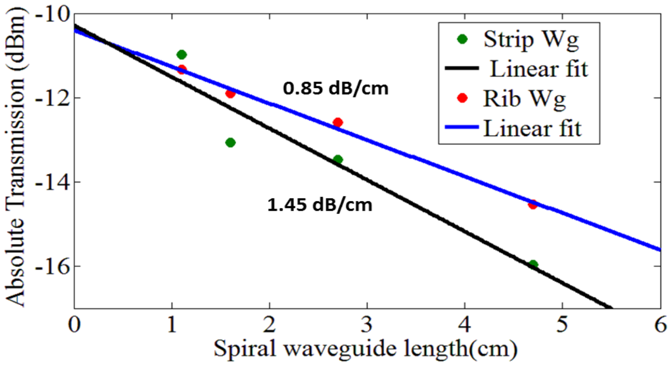

Figure 2.15: Propagation loss extraction of 450 nm wide strip and 600 nm wide rib waveguide at 1550 nm

2.5.1 Existing methods to (not) characterize the effective index

2.5.1.1 Prism coupling

The prism coupling technique has been used for measuring the film thickness and refractive index. In this technique, the laser beam is directed through a side of the prism, bent, and is normally reflected back from the opposite side into a photo detector. However, at certain values of the incident angle theta, the beam does not reflect back. Instead, it is transmitted through the base into the film sample.These angles are called *mode angles*. The first mode angle determines the refractive index, and the angle difference from one mode to the next determines the sample thickness [42, 43]. This technique has the following problems:

1. It needs a very-high-index prism to couple light with silicon waveguide.

2. Hard to couple into narrow line (better for sheets/slabs).
3. Film thickness information is needed for the refractive index measurements.

2.5.1.2 Fourier-space imaging

Fourier space imaging is another method in which the phase information of propagating mode is transferred into far-field by linear probe grating sitting close to waveguide and hence can measure the dispersion accurately [44]. But, this technique faces the following problems:

1. It perturbs the waveguide optical properties.
2. It perturbs the waveguide patterning during fabrication (proximity effects, loading).

Techniques using scattering with weak higher-order periodic perturbations effectively not only perturb the waveguide, but also change the local pattern density, and thus could even influence the fabrication process [7].

2.5.1.3 Ellipsometry

Ellipsometry is another technique which consists of the measurement of the change in polarization state of the light upon reflection from the sample of interest. It is used for characterizing the dielectric properties of thin films like refractive index, composition, roughness, doping concentration etc [45]. However, it faces the following problems:

1. It is useful for the slab but not easy to use on narrow waveguides.
2. It loses accuracy in multilayer stacks.

2.5.1.4 On-chip interferometers

Methods which rely on the relative features in the transmission spectrum of the interferometric devices, measure n_g rather than n_{eff} [46]. Silicon strip waveguides are very dispersive, n_g and n_{eff} are very different, and highly wavelength dependent. Estimating the group index, it is theoretically possible to integrate the effective index, but this can result in an ambiguous solution. An integration needs a constant which is nothing but the exact interference order of the measured filter at a particular wavelength.

Therefore, a method is needed to extract the effective index (as well as the group index) unambiguously and including their wavelength dispersion and temperature dependence.

2.5.1.5 Simulation

Simulation of a waveguide cross section to extract the waveguide mode properties is also possible, but at best it gives a good estimate of the effective index. In practice, the geometry of a buried silicon waveguide is hard to measure experimentally, even with high-resolution SEM. Also, boundary effects in the material properties can also affect the effective index but cannot be perceived by visual or SEM inspections. However, simulations provide a first estimate which we use in our method as a starting point to improve the accuracy.

2.5.2 Our method to extract the effective Index

We present a simple approach to accurately measure the n_{eff} of a silicon photonics waveguide that overcomes the problems described in the previous section. Our method uses three Mach-Zehnder interferometers (MZI) designed with the same photonic wire located as close as possible to each other. MZIs are good candidates as they are simple in design, linear in phase response and flexible in choosing the filter order. Also, an MZI can be designed with symmetric bend sections, enabling delay to be entirely in the straight waveguide sections.

In contrast, while using ring resonators, the measurements must be done at sufficiently low power levels to avoid nonlinear effects [47–49]. Also, the resulting measurement will be a weighted average of the bends, the straight sections and the coupling sections. The measurement is even more complicated because in achieving the highest accuracy the ring needs to be critically coupled, requiring precise control of the waveguide to ring gap dimension.

In our method, we use two MZIs with a low order m, i.e. a large *free spectral range* (FSR), which allow us to estimate the order of the filter correctly within the C-band. The third MZI has a much higher order and a small FSR, which helps us to extract the wavelength dependence of the group index (n_g). To extract the TO coefficients, we measure the same MZIs at different temperatures and then extract the wavelength sensitivity of the spectrum with respect to temperature. Since individual device parameter extraction does not give much information, we also perform and present wafer-scale measurements for three different waveguide widths of 450 nm, 600 nm and 800 nm respectively. Our method is generic in nature and should work for all the integrated waveguide platforms.

2.5.2.1 Extracting the effective index from a single MZI

In any given wavelength filter, as in our MZI, we get constructive interference at the output when

$$m.\lambda_m = n_{eff}(\lambda_m).\Delta L \tag{2.6}$$

where, λ_m is a wavelength where constructive or destructive interference occurs for a given filter order m, $n_{eff}(\lambda_m)$ is the n_{eff} of the waveguide at that wavelength and ΔL is the physical path length difference.

From Eq. 2.6, if we know the wavelength where constructive interference occurs and the filter order, we can extract the effective index at that wavelength. In normal practice, we have designed the filter with a known order m, using a prior estimate of n_{eff}. If the possible deviations in n_{eff} from our design estimate become too large, we cannot be sure about the order. Identifying the order of a filter response is essential, as it gives us an absolute reference for the calculation of the effective index. Consider a simple case where the effective index is changing from n_{eff} to n'_{eff} by increasing the order from m to $m+1$ and by keeping the path length ΔL. Using Eq. 2.6, the largest change Δn_{eff} that we can allow to successfully identify the same order m of the fabricated design can be calculated as

$$\begin{aligned}\Delta n_{eff} &= \frac{n'_{eff} - n_{eff}}{(n'_{eff} + n_{eff})/2} \\ &= \frac{2}{2m+1}\end{aligned} \tag{2.7}$$

We can assume that in first order, Δn_{eff} is due to a change in width Δw and height Δh:

$$\Delta n_{eff} = \frac{dn_{eff}}{dw}.\Delta w + \frac{dn_{eff}}{dh}.\Delta h \tag{2.8}$$

Here, dn_{eff}/dw and dn_{eff}/dh is the change in n_{eff} due to waveguide width and thickness respectively at a given temperature. These parameters can be extracted from simulations. The maximum allowed Δn_{eff} for a wavelength filter of a given order is shown in Fig. 2.16. We see that for higher-order filters, it becomes difficult to estimate the interference order unless the fabrication process is very precise.

Fig. 2.16 also shows the maximum Δn_{eff} for three different waveguides widths, i.e. 450 nm , 600 nm and 800 nm for a fabrication process with a variation of ±20 nm on the waveguide linewidth and ±5 nm on the waveguide thickness. These values are realistic upper limits based on Imec 200 mm platform [7, 33]. As is expected, the wider waveguides suffer less from the small absolute linewidth variations than the narrow waveguides. For the 450 nm wide waveguide the field strength of the fundamental TE mode is much stronger on the side wall boundaries than the 600 nm and 800 nm wide waveguides. The specified variation of ±5 nm on the waveguide thickness does not affect the TE mode as such, but it does have a much stronger impact on the TM mode. For this work we focus on the fundamental TE mode but the same method can be extended to the TM mode as well.

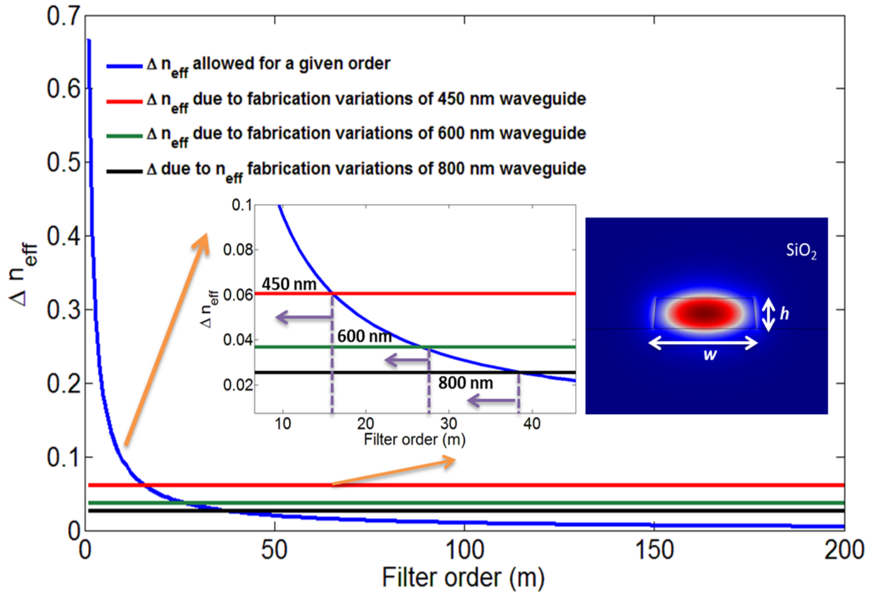

Figure 2.16: The estimated Δn_{eff} allowed and maximum fabrication variations for three different waveguides 450, 600 and 800 nm for increasing filter order m. Inset 1: Zoomed plot showing the region of operation of which order to choose when their maximum fabrication in a different waveguides. Inset 2: Simulated 2D TE mode profile of 800 nm wide and 220 nm SOI waveguide with oxide as top cladding at room temperature.

The intersection of the 3 horizontal traces with the blue trace gives us the maximum order of a wavelength filter where we can still identify the order m with confidence. For 450, 600 and 800 nm, the values of m are 17, 27 and 38 respectively. When designing a filter to use for refractive index extraction, we should pick an order m below these values. Just to give some more insight, we have simulated the transmission of a filter with some order m and then added n_{eff} variation due to fabrications as given by Eq. 2.8. The similar simulation is repeated with sufficiently low order filter as shown in Fig. 2.17. This transmission simulation confirms that low order filter is pretty robust in terms of extracting the n_{eff} at an interference wavelength even if the waveguide dimensions are off with respect to the designed one due to fabrication.

Also, when we design our filter with a sufficiently low order m, the possible changes in the refractive index will be low enough such that

$$n_{eff}^{(m-1)} + \Delta n_{eff} < n_{eff}^{(m)} - \Delta n_{eff} \tag{2.9}$$

$$n_{eff}^{(m)} + \Delta n_{eff} < n_{eff}^{(m+1)} - \Delta n_{eff} \tag{2.10}$$

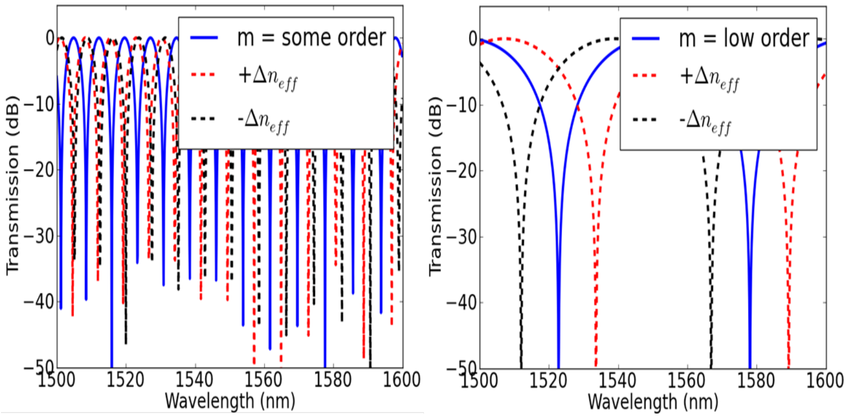

Figure 2.17: (a) Simulated transmission of a filter with some order m and added the fabrication variations and, (b) Simulated transmission of a filter with sufficiently low order m and added the fabrication variations.

This means that we can unambiguously associate each λ_m of constructive interference with an order m. This is shown in Fig. 2.18, where we have simulated an MZI (with 450 nm wide waveguide) case for $m = 15$ (middle curve). The error bars indicate our initial uncertainty on the n_{eff}. The top and bottom curves show the extracted index given an error of ± 1 in the order m. It is clear that the curves do not overlap, even after taking into account the uncertainty. This means that we can confidently use a filter with this order for the waveguides in this fabrication process.

2.5.2.2 Using high-order MZI

A low-order MZI allows us to accurately identify the order of interference at λ_m and thus the effective index at that wavelength. However, in the typical wavelength range of the C-band around 1550 nm, this will result in at most two peaks and valleys in the transmission spectrum. This makes it difficult to extract an accurate model for the wavelength dispersion.

In order to compensate this, we introduce another MZI with a much higher interference order M. From this we can get a large number of peaks and valleys in the wavelength band. The FSR of the filter is the difference between two consecutive peaks of the filter:

$$FSR = \lambda^2 / n_g . \Delta L \tag{2.11}$$

From this device, extraction of $n_g(\lambda)$ of the waveguide is possible by extract-

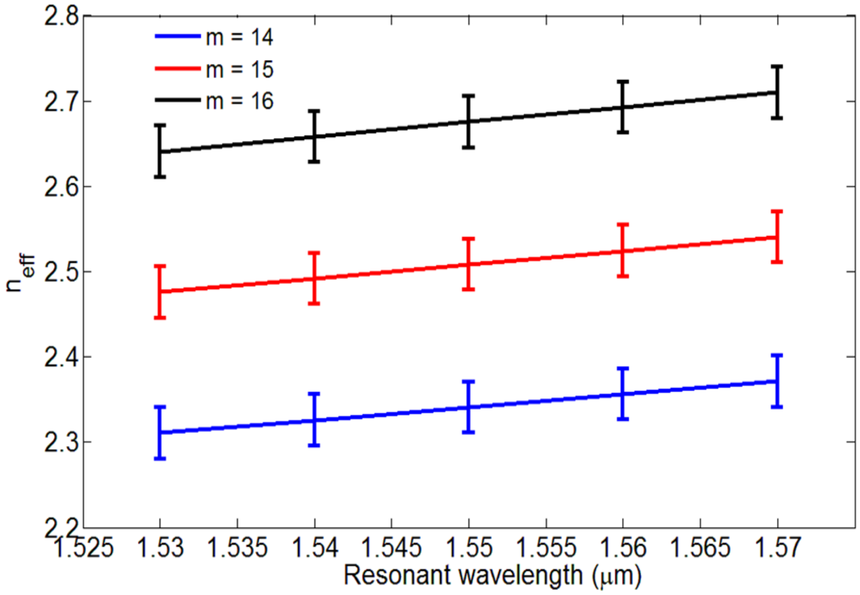

Figure 2.18: Simulated effective index for neighboring order at resonant wavelengths for 450 nm waveguide. Shown error margin is due to the maximum fabrication variations

ing the wavelength dependent FSR from the transmission measurements.

The relation between effective index and group index is given by:

$$n_g(\lambda) = n_{eff}(\lambda) - \lambda(\frac{dn_{eff}}{d\lambda})|_{\lambda} \tag{2.12}$$

With the above information we can extract the coefficients of modified Taylor expansion in $n_{eff}(\lambda)$ and $n_g(\lambda)$. It is based on the reference of the known $n_{eff}(\lambda_0)$ and Eq. 2.12 which is given by:

$$n_{eff}(\lambda) = a + b\Delta\lambda + c(\Delta\lambda)^2 \tag{2.13}$$

$$n_g(\lambda) = a - b\lambda_0 - 2c(\lambda_0.\Delta\lambda) \tag{2.14}$$

where $a = n_{eff}(\lambda_0)$, $b = \frac{dn_{eff}}{d\lambda}|_{\lambda_0}$ and $c = \frac{1}{2}\frac{d^2n_{eff}}{d\lambda^2}|_{\lambda_0}$.

For the TE waveguide, we can ignore the higher order terms of the Taylor expansion, since they are comparable to the fitting error for the designed TE-polarized waveguide. For TM waveguides, the higher-order terms cannot be neglected because of its high dispersive nature compared to the TE mode. From low order MZI, coefficient a can be extracted. The b and c coefficients are extracted accurately by higher order filter. Combining these two, we have all the coefficients and accurate extraction of $n_{eff}(\lambda)$ and $n_g(\lambda)$.

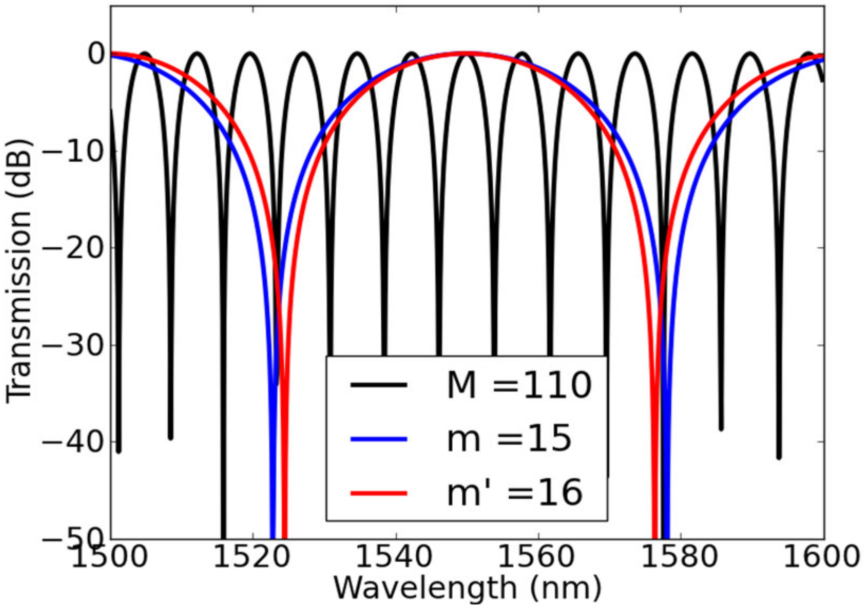

Figure 2.19: Simulated circuit transmission of an MZI filter made out of 450 nm wide and 215 nm thick SOI waveguide with $m = 15$, $m' = 16$ and $M = 110$ respectively

2.5.2.3 A second low-order MZI

Keeping in view that we use two different devices for extracting a single effective index, there is always the possibility of local variability between the two devices introducing errors in our extraction procedure. To reduce this error, we introduce a second low-order MZI, with an order $m' > m$, but still lower than the maximum allowed order needed to identify it unambiguously. We design this second MZI to have the same resonance wavelength as the original MZI:

$$\frac{\Delta L}{m} = \frac{\Delta L'}{m'} \tag{2.15}$$

We can now estimate the local variations of the effective index Δn_{eff} from the shifts of the two resonances λ_m and λ'_m, which ideally should be zero.

$$\Delta n_{eff} = 2.\frac{m'.\lambda'_m.\Delta L - m.\lambda_m.\Delta L'}{m'.\lambda'_m.\Delta L + m.\lambda_m.\Delta L'} \tag{2.16}$$

For our experiments, we have chosen two MZIs with low order $m = 15$ and $m' = 16$, to satisfy the condition for fabrication variations mentioned in Eq. (2.7-2.10) and $M = 110$ to get the $n_g(\lambda)$ in the wavelength of interest. For this, we have used a simulated model of n_{eff}, calculated using a finite-element fully vectorial mode solver, and using a geometry extracted from a cross-sectional SEM

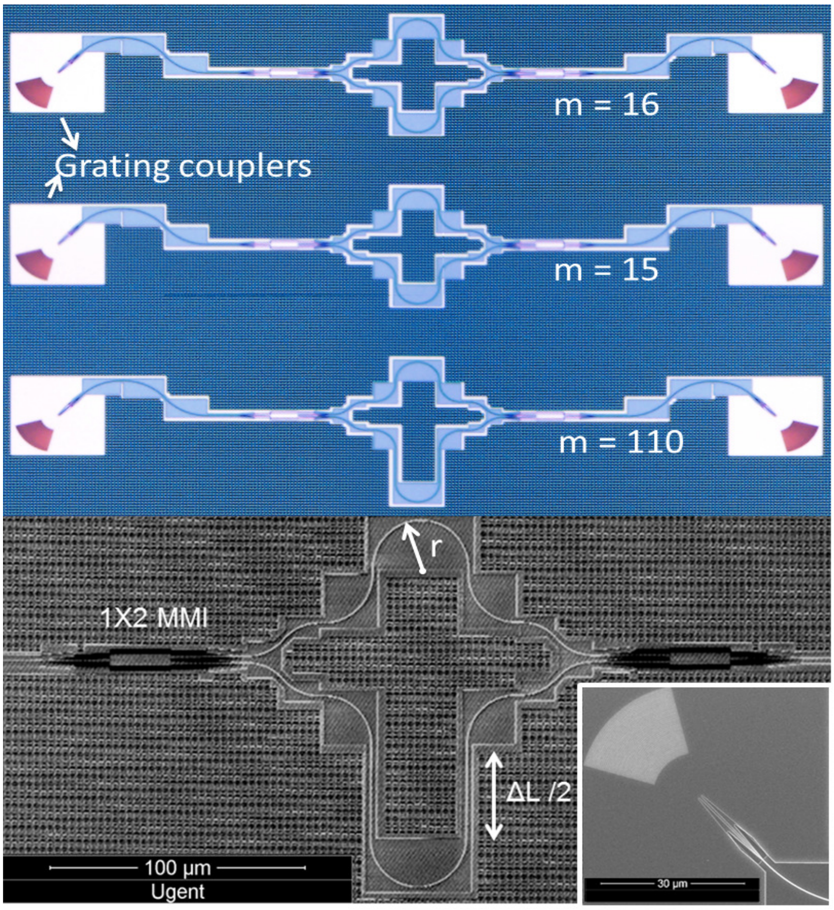

Figure 2.20: (a). Camera image of set of fabricated devices for 600 nm wide waveguide and (b) SEM image of fabricated MZI with $M = 110$ showing the MMI, bend radius r and path length difference ΔL. Inset: Low reflection compact grating coupler.

image. With these parameters, even with a significant deviation from the model, we are able to identify the peaks of the right order.

2.5.2.4 Extraction of thermo-optic coefficient

For the extraction of the thermo-optic (TO) coefficient of a waveguide, the wavelength sensitivity with respect to the temperature needs to be measured which is given by [50] :

$$\frac{dn_{eff}}{dT}|_{\lambda_m} = \frac{n_g}{\lambda_m}\frac{d\lambda}{dT} \tag{2.17}$$

The TO coefficient of the waveguide is extracted after extracting the n_g at a given wavelength λ_m and the filter transmission at different temperatures T.

An alternative method to extract the TO coefficient is to extract $n_{eff}(\lambda_m)$ from the low order MZIs for different temperatures and then use equation (2.6) directly at a given wavelength.

2.5.3 Design and fabrication

The MZIs are simulated and designed for three different waveguides, i.e. 450 nm, 600 nm and 800 nm wide respectively and with 215 nm thick silicon wires for values $m = 15$, $m' = 16$ and $M = 110$ respectively. The full eigenmode solutions as discussed in section 2 are fed to the circuit solver CAPHE to get the transmission response at fixed room temperature [51, 52]. The simulated transmission of the three 450 nm MZI filters for $m = 15$, $m' = 16$ and $M = 110$ is shown in Fig. 2.19. As they have been designed for that condition, the three simulations show constructive interference at λ_m of 1550 nm.

Devices are designed using IPKISS, a designed framework by Luceda Photonics, which generates the layouts directly from a parametric description of the MZI [52].

Since the quality of the transmission trace is essential for an accurate extraction, we have designed the test circuits to minimize reflections. There are different sources of contribution towards reflection in the SOI based wavelength devices. The major contributions to reflection are from the grating couplers to and from the chip. Therefore, we use compact off-axis grating couplers with reduce back reflections [13]. They are designed at an angle of $45\,\mathrm{deg}$ to the in-plane fiber axis, and they direct backreflections away from the input waveguide. This reduces back-reflection of curved grating couplers from -20 dB to -50 dB.

The arms of the MZI are designed with a relatively large bend radius of 20 μm to avoid reflections from the straight-bend interface and to minimize the loss. The arms are symmetric except for the vertical straight section which incorporates the actual delay ΔL. This cancels out possible effects of bend-radius dependence of n_{eff}. Our device focuses on measuring and extracting the n_{eff} of straight photonic wires. It can be extended to extract the bend mode waveguide refractive index by incorporating the delay line in the bend sections.

The side wall roughness of the waveguide is unavoidable which depends upon the fabrication. This effect is prominent in 450 nm wide waveguides which gradually decreases for wider waveguides i.e for 600 and 800 nm.

For equal splitting and combining the light, the device uses wide band 1×2 multimode interference (MMI) based splitter. By using a symmetric splitter and combiner, we reduce the effect of wavelength dependence in directional couplers, noting that the couplers do not inherently introduce a phase delay between the

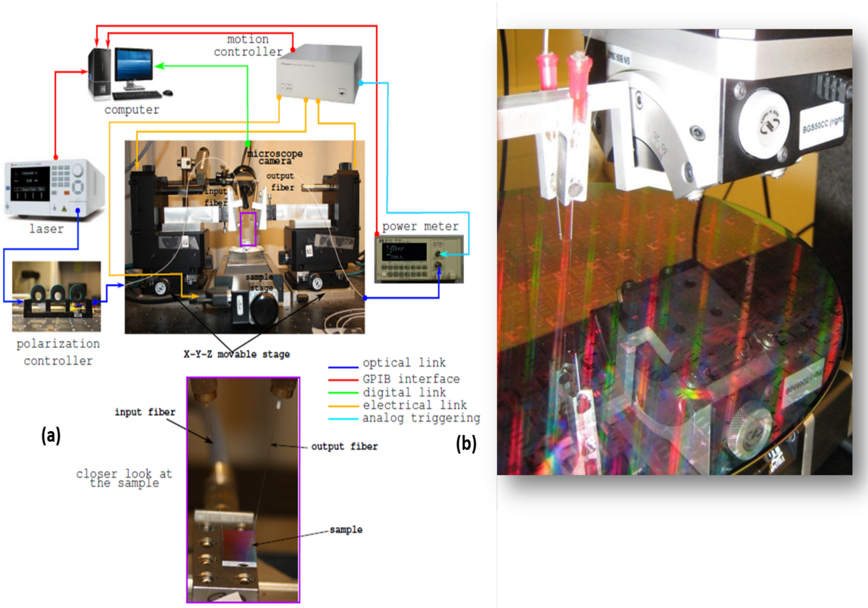

Figure 2.21: The automatic setup using vertical coupling for (a) photonic dies and (b) wafer

arms.

Camera images of all three MZIs designed with 600 nm wide waveguide and SEM image of one of the fabricated MZI with $M = 110$ are shown in Fig. 2.20.

2.5.4 Measurements and analysis

2.5.4.1 Automatic vertical alignment

Using motion controller having X-Y-Z movable stages for fiber and sample, the vertical setup (which is discussed in the section 2.4.1) can be automated to make it highly accurate. These setups are available in the group for both die based or for the full wafer measurements, as shown in Fig. 2.21. The zoom in image of semi-automatic setup is shown in Fig. 2.22. In die scale setup, the sample stage can move in one direction while in wafer scale setup, the wafer stage is capable of not only X-Y-Z movement but also rotations. The combination of a motion controller and the X-Y-Z stages allows aligning the fibers with an accuracy of 0.01 μm in X, Y, Z directions. First we perform the manual alignment as discussed in section 2.4.1. After that, the grating coupler locations of the devices are measured which is provided from designed mask layout. These relative positions help the motion controller to move the fibers to the correct fiber grating couplers. At this position, with the help of the external triggering of the power meter, the motion

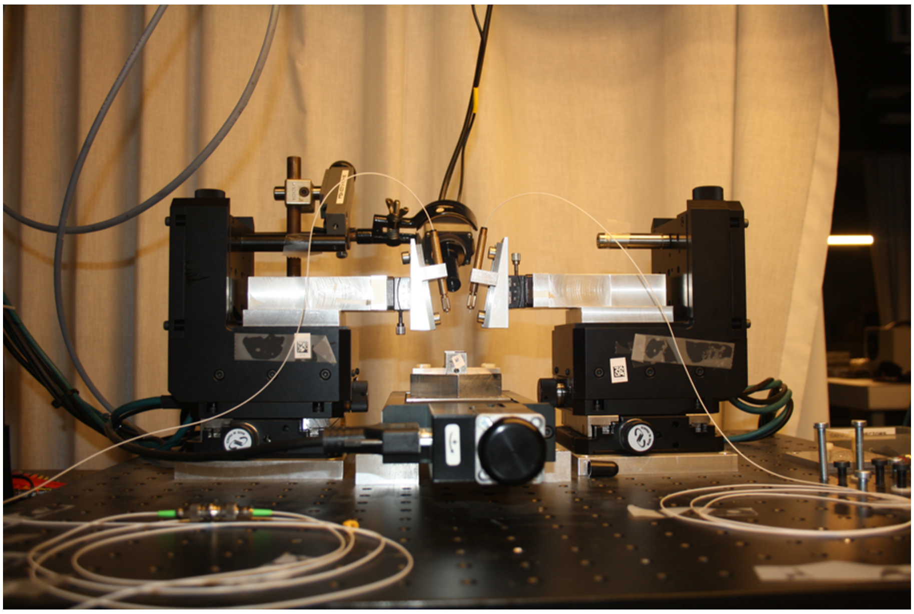

Figure 2.22: The zoom in image of semi-automatic setup

controller aligns the fibers at the maximum coupling positions by moving the fibers in X and Y direction simultaneously. The coupling is not optimized by moving the fibers in Z direction as this can result a collision with the sample. The relative positions are further optimized for small rotations of the sample during placement of the sample on the sample stage. Both the setups are available with nicely built graphical user interface with python backend developed mainly by Wim Bogaerts, Karel Van Acoleyen and Michael Vanslembrouck. Also, it can be controlled remotely after setting up the chip or the wafer.

2.5.4.2 Device measurements

The measurements were performed on the fully automatic vertical setup as mentioned in the section 2.5.4.1 which is located in our clean room. The transmission measurements are performed in a thermally controlled environment to eliminate the effect of the high TO coefficient of silicon, which can induce a wavelength peak shift of about 80 pm/K. The wavelength sweep are performed using CW Santec TSL 510 laser. The output of the laser goes to polarization controller through the input fiber to select one polarization. The output of the polarization controller then go to the input grating couplers which is designed specifically for one polarization (TE). The device transmission is first normalized to that of a straight waveguide to eliminate the grating coupler spectrum. The 10 dB bandwidth of the

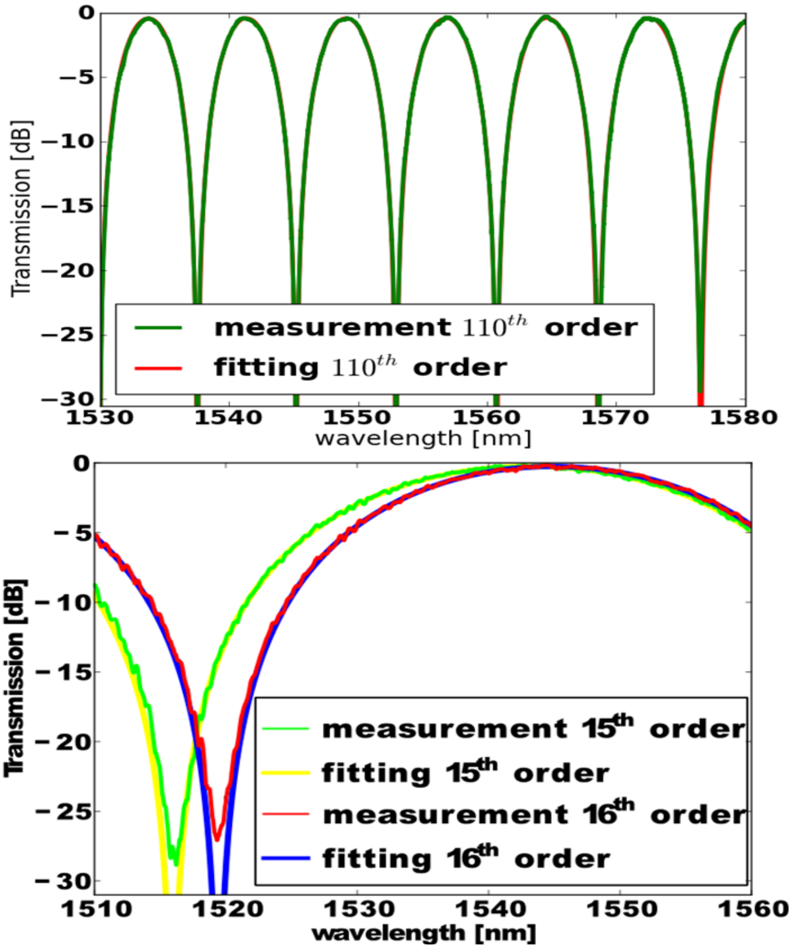

Figure 2.23: Measured and fitted normalized spectrum of MZI designed with 450 nm wide and 215 nm thick silicon waveguide (a) higher filter order and (b) lower filter order.

grating coupler is around 80 nm from 1505 nm to 1585 nm. The on-chip insertion loss of the MZI is less than 0.3 dB.

2.5.4.3 Fitting

For fitting the normalized spectrum we have used non-linear least square method and cosine square interferometric model as a base function. The optical parameter of this model is given in Eq. (2.13-2.14). The fitting procedure minimizes the RMS error between the measured and theoretical transmission trace.

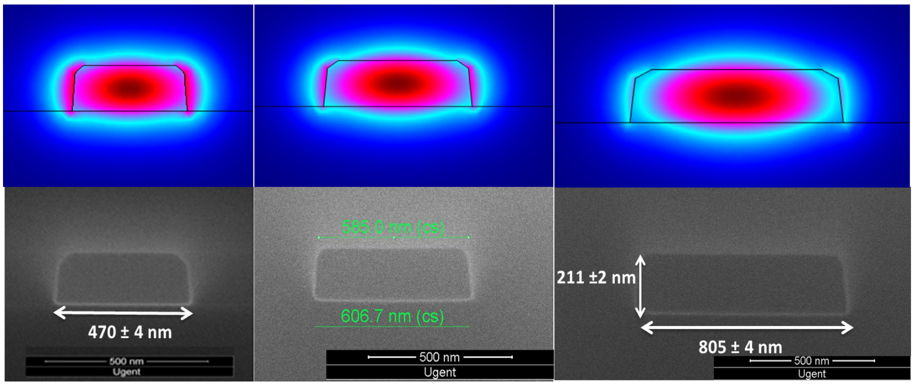

Figure 2.24: Simulated mode profile and XSEM image of 470 nm, 604 and 805 nm wide and 211 nm thick waveguides. Side wall angles of the trapezoidal waveguides can be easily seen in the SEM. Silicon corner rounding in the waveguide is due to the passive short loop specific process; which involves oxide deposition after the hardmask removal.

The measured and fitted the transmission spectra of the 3 MZIs designed for 450 nm are shown in Fig. 2.23. However, the measured width and thickness of the waveguide are closer to 470±4 nm and 211±2 nm respectively, as extracted from SEM inspection. The other two waveguides, designed at 600 nm and 800 nm, are closer to the designed width, as shown in the SEM images. The local variability can be estimated by extracting the n_{eff} from $m' = 16$ as well and compare with $m = 15$. The variation of Δn_{eff} for 470 nm wide wire due to this is around ±0.0015.

The cross-section SEM (XSEM) of the waveguide, the simulated mode profile of all the three waveguides i.e. 470, 604 and 805 nm are shown in Fig. 2.24.

For a proper statistical analysis we have used two different techniques: resampling based on the Bootstrapping method [53] and Monte Carlo simulations [54].

2.5.4.4 Error analysis: Bootstrapping method

The RMS of the first fitting iteration is used as standard deviation for the Gaussian distribution describing the single point measurements fluctuation. This Gaussian is fed to a random number generator with zero mean. The random noise generation is used for a bootstrapping process. Now the fitting is performed to fit the measurement with this additional random noise. This procedure is reiterated 1000 times to obtain a statistical relevant data set. The results of these fittings are used to define the standard deviations of the a, b and c coefficients used in Eq. (2.13-2.14) to define $n_{eff}(\lambda)$ and $n_g(\lambda)$.

The simulated (after taking SEM) and extracted n_{eff} and n_g for all three

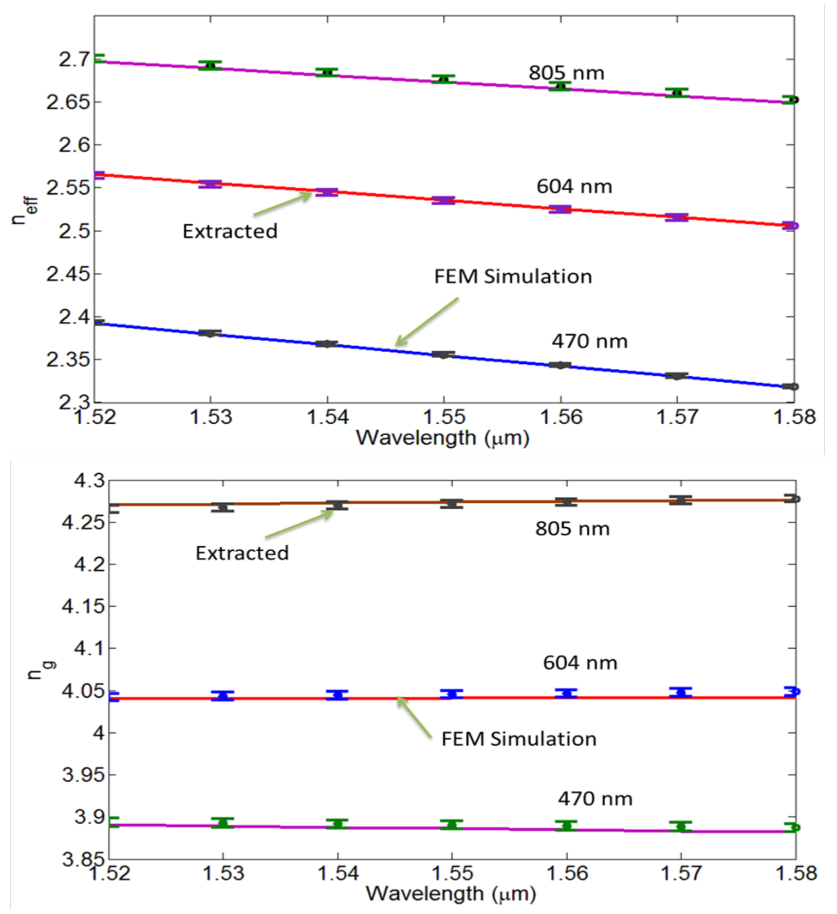

Figure 2.25: (a) Simulated and extracted n_{eff} of 470, 602 and 805 nm wide waveguides and (b) Simulated and extracted n_g over the C-band

waveguides over the entire C-band is shown in Fig. 2.25.

The extracted n_g from the higher order filter and then the n_{eff} from the low order filter of the different waveguide widths at 1550 nm is shown in the table 2.2.

In the table 2.2, the n_{eff} and n_g extracted value and their error contributions are mentioned. The first and third column is the extracted n_{eff} and n_g values and the measurement error which is due to the local variability, the absolute laser accuracy and the shift in grating couplers. The σ of fitting is reported after the re-sampling. The total error on n_{eff} is the addition the measurement error and the fitting error on the initial extraction. For example the error on the extracted value of n_{eff} of 470 nm waveguide by our method is 2.355±0.003.

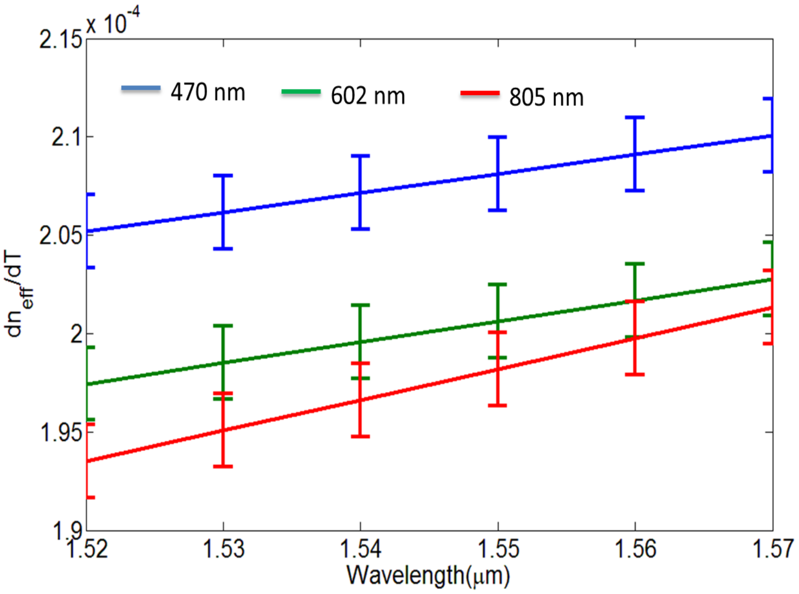

Figure 2.26: Extracted $\frac{dn_{eff}}{dT}$ *of 470, 602 and 805 nm wide waveguides*

Waveguide	n_{eff}	n_{eff} fitting σ	n_g	n_g fitting σ
470 nm	2.355 $\pm$ 0.002	$\pm$0.0013	4.2739 $\pm$ 0.0042	$\pm$0.0063
602 nm	2.534 $\pm$ 0.0035	$\pm$0.0020	4.0453 $\pm$ 0.0045	$\pm$0.0064
805 nm	2.67 $\pm$ 0.004	$\pm$0.0028	3.8902 $\pm$ 0.005	$\pm$0.0066

Table 2.2: Table showing the extracted n_{eff} *and* n_g

2.5.4.5 Error analysis: Monte Carlo simulations

The procedure of this error analysis is as follows:

1. The non-linear least square fitted value of measurements i.e. a, b and c used as the input of the circuit model.
2. The circuit model is build using Caphe from Luceda Photonics. This model generates a circuit of both the low and higher order MZIs, but including the incoupling and outcoupling waveguides and grating couplers.
3. To this model we add different error contributions from measurements as a Gaussian distribution.

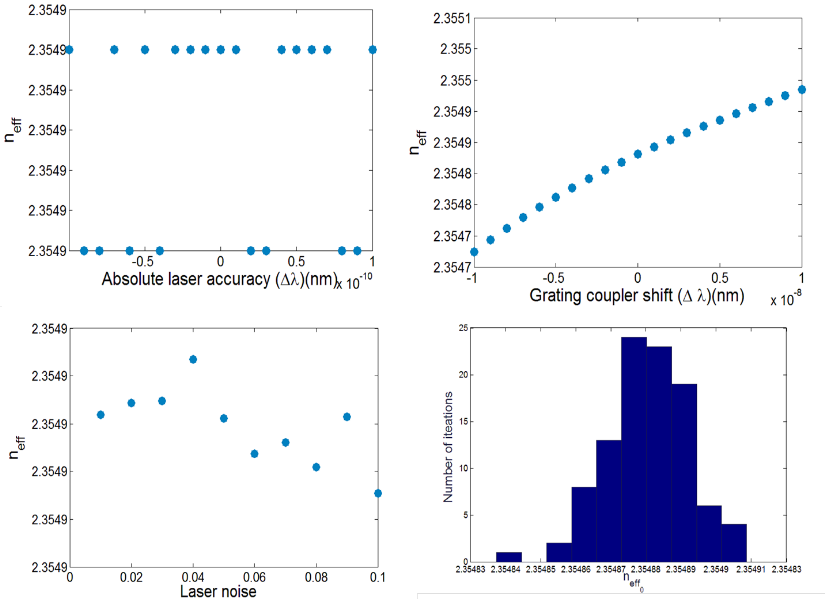

Figure 2.27: Extracted n_{eff} when an error is introduced on (a) the absolute laser accuracy, (b) the grating coupler peak wavelength, (c) the laser output power, (d) Histogram of n_{eff0} after 100 iterations with stochastic variations on these three error contributions using Monte Carlo simulations

4. After adding these error contributions we fit the new transmission spectrum using our fitting algorithm. This fit gives a new value and we can call as a', b' and c'.

5. The error can be estimated by taking the difference between the initial fitted value on measurement and this new fitted value of circuit simulation i.e. error on $\epsilon(a) = a' - a$ and similarly for estimating $\epsilon(b)$ and $\epsilon(c)$.

6. We re-iterate this process 100 times to generate a reliable value for the error on a, b and c.

When measuring the MZIs, we identified different contributions to include in the circuit model:

1. Absolute laser accuracy: This parameter is defined as the variations in the laser actual wavelength and the wavelength it shows during the measurements. For Santec TSL-510 (C-band) it is ±2.5 pm.

2. Laser output power or laser noise: This is basically the output power fluctuations from laser. For the laser used this is ±0.2 dB.

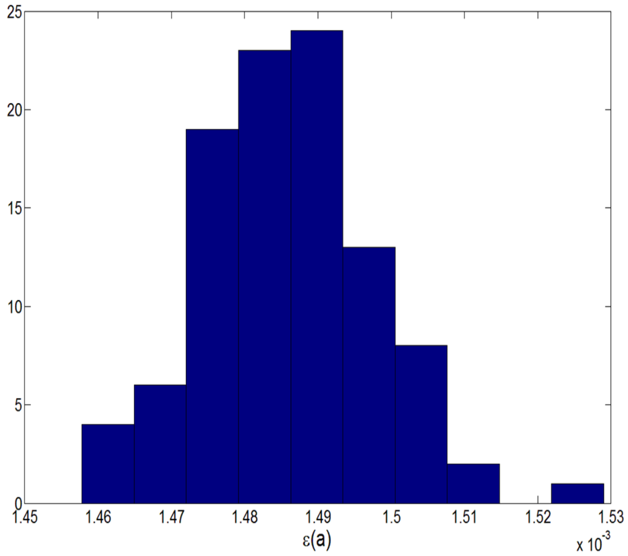

Figure 2.28: Error extraction $\epsilon(a)$ on 470 nm waveguide after 100 iterations through Monte Carlo simulations

3. Grating coupler shift: We are using reference waveguide to normalize the grating couplers. Every set of gratings is unique and its performance depends upon how uniform the fabrication is within a die. This we can call as local variability in the gratings. Due to this local variability every set of gratings spectrum has unique peak position. If process variations is large it causes an error on the normalization and henceforth the extracted effective index. We vary the peak position of the reference waveguide by ($\pm$)10 nm deliberately to check if it affects the extraction.

The individual errors on the extracted effective index contributed to the absolute laser accuracy, laser output power and grating coupler shift on n_{eff} at 1550 nm for 450 nm wide waveguide are shown in the Fig. 2.27(a-c). The histogram in Fig. 2.27(d) is n_{eff0} after taking random contributions of these errors, iterated for 100 times using Monte Carlo. The histogram plot shows that the variation of n_{eff} is only at the 5th decimal place. The absolute extracted error $\epsilon(a)$ from Monte Carlo and the original least square fitted value is only at 3rd decimal and the value is around 0.001 and is plotted in the Fig. 2.28. As can be seen this comparable to the one extracted from Bootstrapping method. This experiment shows that the extraction method is quite robust against the measurement fluctuations.

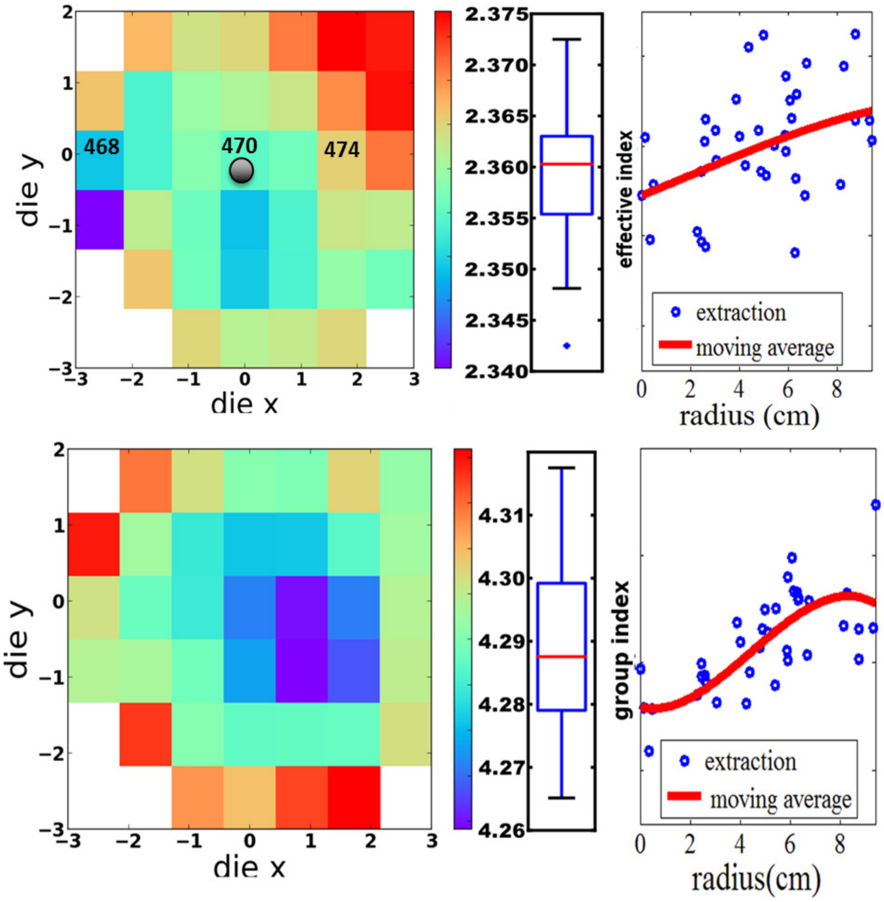

Figure 2.29: Wafer map, distribution and radial plot of 470 nm wide fabricated waveguide at 1550 nm. Thickness variation is 211±2 nm and σ of linewidth variation is 5 nm. Top-down SEM in nm at 3 locations. (a) n_{eff} and (b) n_g

The mismatch between the extracted value and the simulations of the waveguide according to XSEM (with SEM width, taking into account the uncertainty of the SEM measurement itself) mainly comes from local environmental variations, and fabricated waveguide geometrical non-idealities.

2.5.4.6 Thermo-optic coefficient measurements

For the measurements of the TO coefficient ($\frac{dn}{dT}$) we placed the fabricated chip on a thermally controlled chuck with a resistive heater and temperature sensor. The MZIs transmission are characterized at a different temperatures. The spectrum gets red shifted with an increase in the temperature due to positive TO coeff. of

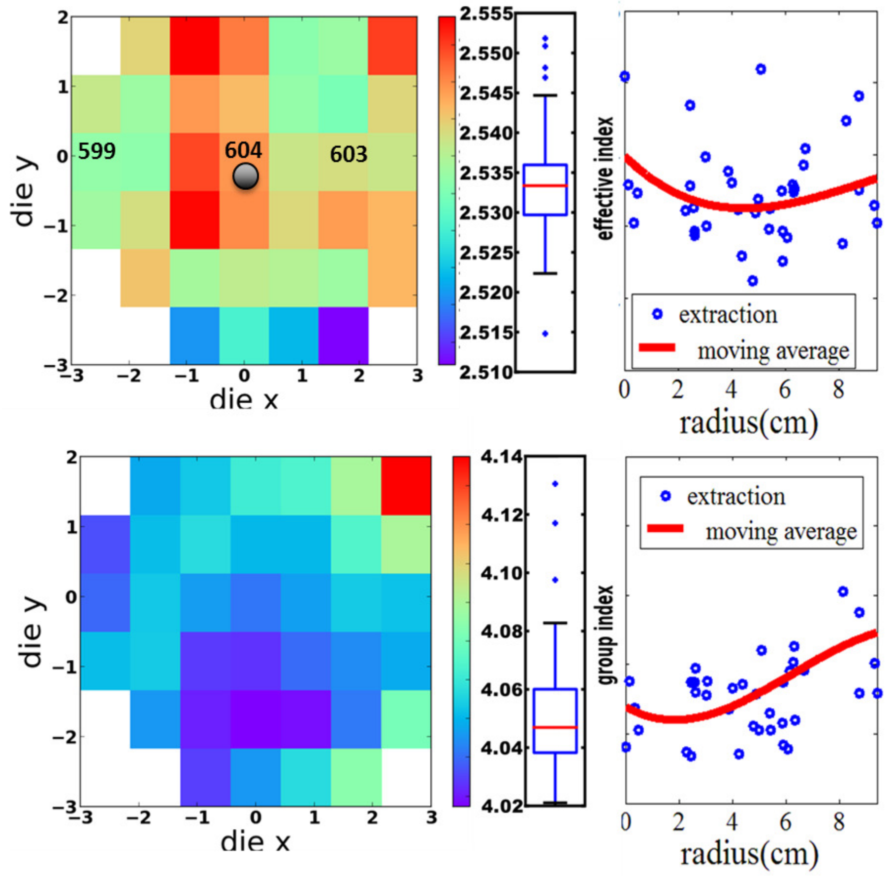

Figure 2.30: Wafer map, distribution and radial plot of 604 nm wide fabricated waveguide at 1550 nm. Thickness variation is 211±2 nm and σ of line width variation is 4 nm. Top-down SEM in nm at 3 locations. (a) n_{eff} and (b) n_g

silicon. The shifted spectrum is fitted in the similar way as explained in previous section and by Eq. (2.17) the TO coefficients of the waveguides can be extracted. The extracted TO coefficients for all the three waveguides are shown in Fig. 2.26.

The error contribution in TO coefficient extraction can be mainly attributed to the small thermal fluctuations in the chuck.

2.5.4.7 Wafer scale measurements

We have characterized these devices over an entire wafer using a fully automatic optical probe station. The wafer map and distribution plot of extracted n_{eff} and n_g for 470 nm, 600 nm and 800 nm wide and 211 nm thick waveguides at 1550 nm

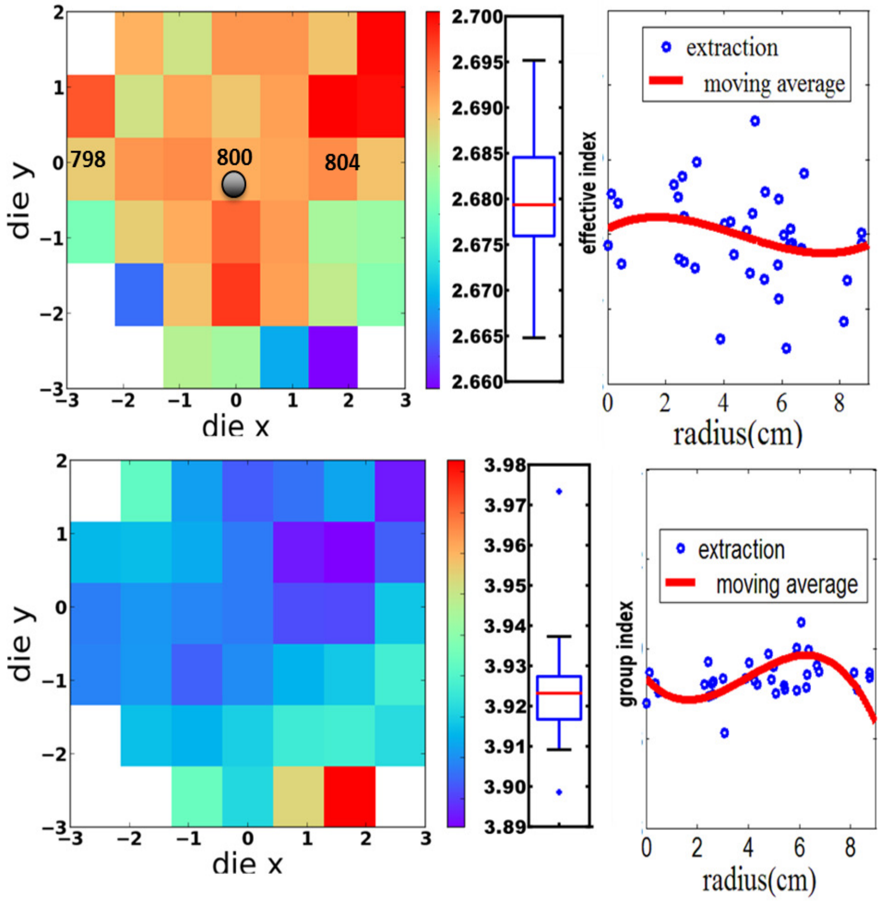

Figure 2.31: Wafer map, distribution and radial plot of 805 nm wide fabricated waveguide at 1550 nm. Measured thickness is 211±2 nm and σ of line width variation is 4 nm. Top-down SEM in nm at 3 locations. (a) n_{eff} *and (b)* n_g

are shown in Figs. 2.29, 2.30, and 2.31 respectively. Wafer scale measurements are important to know the statistical variation of the n_{eff}. Also, the method needs to be tested and automated in such a way as to ensure that it can work over a wafer scale since the X-SEM is both a destructive and an expensive process.

Across the wafer, for 470 nm waveguide at 1550 nm, the mean value and standard deviation of n_{eff} is 2.360 and 0.008 and for n_g is 4.287 and 0.018 respectively. For the 600 nm waveguide the mean value and standard deviation of n_{eff} is 2.533 and 0.006 and for n_g is 4.045 and 0.02. And, for the 800 nm wide waveguide, the mean value and standard deviation of n_{eff} is 2.679 and 0.008 and for n_g is 3.924 and 0.01. The line width was measured using top-down SEM (TDSEM) provided by the foundry at 3 different locations of the wafer and is shown on the wafer maps.

The deviation of the extracted effective and group indices is mainly influenced by two effects: the thickness and the line width variation over the wafer. Thickness variation is due to the SOI polishing and can be considered to be slow across the wafer. As provided by the foundry it is only a few nm over the entire wafer. The line width is correlated to lithographic process and it is performed using die based stepping which introduces discrete variations. The effect of the line width is therefore more pronounced than the effect of the thickness. As a result, we see a slow variation which is superimposed with a faster variation on the wafer maps.

2.6 Conclusion and discussion

In this chapter we have discussed the SOI platform, its material stack and fabrication process, in particular the most fundamental component of the platform i.e. the SOI photonic waveguide. We have shown the mode simulations of different types of SOI waveguides, their geometrical, wavelength and thermal sensitivities. The waveguide loss has been measured using grating couplers.

We have then proposed and demonstrated a novel method for measuring the refractive index of dispersive SOI waveguides. Combining 3 MZIs of low and high order, we can extract the wavelength and temperature dependent effective index and the group index unambiguously. We also obtain an estimate for the local variability of the effective index accurately. It does not perturb the waveguide of local pattern density, which is essential in a high-contrast waveguide platform such as silicon photonics.

This method can be applied to the TM polarization, different types of waveguides and can also be extended to other waveguide platforms. This method can be further extended i.e. extraction might well be possible just by cascading two MZIs in series in which one is with the lower order and another with higher order. In that case, the fitting of the transmission envelope gives the n_{eff} at that wavelength while fitting the full transmission spectrum extracts the higher order terms of n_{eff} i.e. n_g of the waveguide.

References

[1] Gerd Keiser. *Optical fiber communication*. NY: McGraw-Hill, 2000.

[2] Wim Bogaerts, Liu Liu, and Gunther Roelkens. *Technologies and Building Blocks for On-Chip Optical Interconnects*. In Ian O'Connor and Gabriela Nicolescu, editors, Integrated Optical Interconnect Architectures for Embedded Systems, Embedded Systems, pages 27–78. Springer New York, 2013.

[3] Berge Tatian. *Fitting refractive-index data with the Sellmeier dispersion formula*. Appl. Opt., 23(24):4477–4485, Dec 1984.

[4] G. Ghosh, M. Endo, and T. Iwasaki. *Temperature-dependent Sellmeier coefficients and chromatic dispersions for some optical fiber glasses*. Lightwave Technology, Journal of, 12(8):1338–1342, Aug 1994.

[5] Bradley J. Frey, Douglas B. Leviton, and Timothy J. Madison. *Temperature-dependent refractive index of silicon and germanium*, July 2006.

[6] `http://www.europractice-ic.com/SiPhotonics_general.php`.

[7] S.K. Selvaraja, W. Bogaerts, P. Dumon, D. Van Thourhout, and R. Baets. *Subnanometer Linewidth Uniformity in Silicon Nanophotonic Waveguide Devices Using CMOS Fabrication Technology*. Selected Topics in Quantum Electronics, IEEE Journal of, 16(1):316–324, Jan 2010.

[8] Hui Yu, Marianna Pantouvaki, Joris Van Campenhout, Dietmar Korn, Katarzyna Komorowska, Pieter Dumon, Yanlu Li, Peter Verheyen, Philippe Absil, Luca Alloatti, David Hillerkuss, Juerg Leuthold, Roel Baets, and Wim Bogaerts. *Performance tradeoff between lateral and interdigitated doping patterns for high speed carrier-depletion based silicon modulators*. Opt. Express, 20(12):12926–12938, Jun 2012.

[9] Dirk Taillaert, Peter Bienstman, and Roel Baets. *Compact efficient broadband grating coupler for silicon-on-insulator waveguides*. Opt. Lett., 29(23):2749–2751, Dec 2004.

[10] D. Vermeulen, S. Selvaraja, P. Verheyen, G. Lepage, W. Bogaerts, P. Absil, D. Van Thourhout, and G. Roelkens. *High-efficiency fiber-to-chip grating couplers realized using an advanced CMOS-compatible Silicon-On-Insulator platform*. Opt. Express, 18(17):18278–18283, Aug 2010.

[11] D. Vermeulen, Y. De Koninck, Y. Li, E. Lambert, W. Bogaerts, R. Baets, and G. Roelkens. *Reflectionless grating couplers for Silicon-on-Insulator photonic integrated circuits*. Opt. Express, 20(20):22278–22283, Sep 2012.

[12] Yanlu Li, Lianyan Li, Bin Tian, G. Roelkens, and R.G. Baets. *Reflectionless Tilted Grating Couplers With Improved Coupling Efficiency Based on a Silicon Overlay*. Photonics Technology Letters, IEEE, 25(13):1195–1198, July 2013.

[13] Yanlu Li, Diedrik Vermeulen, Yannick De Koninck, Gunay Yurtsever, Günther Roelkens, and Roel Baets. *Compact grating couplers on silicon-on-insulator with reduced backreflection*. Opt. Lett., 37(21):4356–4358, Nov 2012.

[14] S. Pathak, P. Dumon, D. Van Thourhout, and W. Bogaerts. *Comparison of AWGs and Echelle Gratings for Wavelength Division Multiplexing on Silicon-on-Insulator*. Photonics Journal, IEEE, 6(5):1–9, Oct 2014.

[15] Shankar K. Selvaraja, Gustaf Winroth, Sabrina Locorotondo, Gayle Murdoch, Alexey Milenin, Christie Delvaux, Patrick Ong, Shibnath Pathak, Weiqiang Xie, Gunther Sterckx, Guy Lepage, Dries Van Thourhout, Wim Bogaerts, Joris Van Campenhout, and Philippe Absil. *193nm immersion lithography for high-performance silicon photonic circuits*, 2014.

[16] Marianna Pantouvaki, Peter Verheyen, Guy Lepage, Jeroen De Coster, Hui Yu, Peter De Heyn, Adil Masood, Wim Bogaerts, Philippe Absil, and Joris Van Campenhout. *8x14Gb/s Si Ring WDM Modulator Array with Integrated Tungsten Heaters and Ge Monitor Photodetectors*. In Optical Fiber Communication Conference, page Th1C.5. Optical Society of America, 2014.

[17] Yufei Xing, T. Ako, J.P. George, D. Korn, Hui Yu, P. Verheyen, M. Pantouvaki, G. Lepage, P. Absil, A. Ruocco, C. Koos, J. Leuthold, K. Neyts, J. Beeckman, and W. Bogaerts. *Digitally Controlled Phase Shifter Using an SOI Slot Waveguide With Liquid Crystal Infiltration*. Photonics Technology Letters, IEEE, 27(12):1269–1272, June 2015.

[18] Carlos A. Barrios, Kristinn B. Gylfason, Benito Sánchez, Amadeu Griol, H. Sohlström, M. Holgado, and R. Casquel. *Slot-waveguide biochemical sensor*. Opt. Lett., 32(21):3080–3082, Nov 2007.

[19] Francesco Dell'Olio and Vittorio M. Passaro. *Optical sensing by optimized silicon slot waveguides*. Opt. Express, 15(8):4977–4993, Apr 2007.

[20] Jianming Jin. *The Finite Element Method in Electromagnetics*. Wiley-IEEE Press, 3rd edition, 2014.

[21] `http://www.comsol.com/`.

[22] R.M. Joseph and Allen Taflove. *Spatial soliton deflection mechanism indicated by FD-TD Maxwell's equations modeling*. Photonics Technology Letters, IEEE, 6(10):1251–1254, Oct 1994.

[23] `http://www.lumerical.com/`.

[24] J. Van Roey, J. van der Donk, and P. E. Lagasse. *Beam-propagation method: analysis and assessment*. J. Opt. Soc. Am., 71(7):803–810, Jul 1981.

[25] `http://optiwave.com/category/products/component-design/optibpm/`.

[26] P. Bienstman, E. Six, M. Roelens, M. Vanwolleghem, and R. Baets. *Calculation of bending losses in dielectric waveguides using eigenmode expansion and perfectly matched layers*. Photonics Technology Letters, IEEE, 14(2):164–166, Feb 2002.

[27] `http://www.photond.com/`.

[28] F. Gan, T. Barwicz, M.A. Popovic, M.S. Dahlem, C.W. Holzwarth, P.T. Rakich, H.I. Smith, E.P. Ippen, and F.X. Kartner. *Maximizing the Thermo-Optic Tuning Range of Silicon Photonic Structures*. In Photonics in Switching, 2007, pages 67–68, Aug 2007.

[29] Joris Van Campenhout, William M. J. Green, Solomon Assefa, and Yurii A. Vlasov. *Integrated NiSi waveguide heaters for CMOS-compatible silicon thermo-optic devices*. Opt. Lett., 35(7):1013–1015, Apr 2010.

[30] Po Dong, Wei Qian, Hong Liang, Roshanak Shafiiha, Dazeng Feng, Guoliang Li, John E. Cunningham, Ashok V. Krishnamoorthy, and Mehdi Asghari. *Thermally tunable silicon racetrack resonators with ultralow tuning power*. Opt. Express, 18(19):20298–20304, Sep 2010.

[31] A. Masood, M. Pantouvaki, G. Lepage, P. Verheyen, J. Van Campenhout, P. Absil, D. Van Thourhout, and W. Bogaerts. *Comparison of heater architectures for thermal control of silicon photonic circuits*. In Group IV Photonics (GFP), 2013 IEEE 10th International Conference on, pages 83–84, Aug 2013.

[32] `http://www.intel.com/content/www/us/en/silicon-innovations/intel-14nm-technology`.

[33] Philippe P. Absil, Peter Verheyen, Peter De Heyn, Marianna Pantouvaki, Guy Lepage, Jeroen De Coster, and Joris Van Campenhout. *Silicon photonics integrated circuits: a manufacturing platform for high density, low power optical I/O's*. Opt. Express, 23(7):9369–9378, Apr 2015.

[34] `https://www.a-star.edu.sg/ime/RESEARCH/NANO-PHOTONICS-PROGRAMME.aspx`.

[35] T. Mogami, T. Horikawa, K. Kinoshita, H. Sasaki, K. Morito, and K. Kurata. *A 300mm Si photonics platform for optical interconnection*. In Interconnect Technology Conference and 2015 IEEE Materials for Advanced Metallization Conference (IITC/MAM), 2015 IEEE International, pages 273–276, May 2015.

[36] Frederic Boeuf, Sebastien Cremer, Enrico Temporiti, Massimo Fere', Mark Shaw, Nathalie Vulliet, bastien orlando, Delia Ristoiu, Alexis Farcy, Thierry Pinguet, Attila Mekis, Gianlorenzo Masini, Peng Sun, Yuemeng Chi, Herve Petiton, Sebastien Jan, Jean-Robert Manouvrier, Charles Baudot, Patrick Le-Maitre, Jean Francois CARPENTIER, Laurent Salager, Matteo Traldi, Luca Maggi, Danilo Rigamonti, Chiara Zaccherini, Carolina Elemi, Bernard Sautreuil, and Luigi Verga. *Recent Progress in Silicon Photonics R&D and Manufacturing on 300mm Wafer Platform*. In Optical Fiber Communication Conference, page W3A.1. Optical Society of America, 2015.

[37] S.K. Selvaraja. Wafer-Scale Fabrication Technology for Silicon Photonic Integrated Circuits., PhD thesis, Ghent University, 2011.

[38] F. Van Laere, T. Claes, Jonathan Schrauwen, S. Scheerlinck, W. Bogaerts, D. Taillaert, L. O'Faolain, D. Van Thourhout, and R. Baets. *Compact Focusing Grating Couplers for Silicon-on-Insulator Integrated Circuits*. Photonics Technology Letters, IEEE, 19(23):1919–1921, Dec 2007.

[39] S. Pathak, M. Vanslembrouck, P. Dumon, D. Van Thourhout, and W. Bogaerts. *Compact SOI-based polarization diversity wavelength de-multiplexer circuit using two symmetric AWGs*. Opt. Express, 20(26):B493–B500, Dec 2012.

[40] W. Bogaerts, S.K. Selvaraja, P. Dumon, J. Brouckaert, K. De Vos, D. Van Thourhout, and R. Baets. *Silicon-on-Insulator Spectral Filters Fabricated With CMOS Technology*. Selected Topics in Quantum Electronics, IEEE Journal of, 16(1):33–44, Jan 2010.

[41] Wim Bogaerts, Shibnath Pathak, Alfonso Ruocco, and Sarvagya Dwivedi. *Silicon photonics non-resonant wavelength filters: comparison between AWGs, echelle gratings, and cascaded Mach-Zehnder filters*. volume 9365, pages 93650H–93650H–12. SPIE, April 2015.

[42] Hidetoshi Onodera, Ikuo Awai, and Jun ichi Ikenoue. *Refractive-index measurement of bulk materials: prism coupling method*. Appl. Opt., 22(8):1194–1197, Apr 1983.

[43] M. R. Shenoy, Sukhdev Roy, and K. Thyagarajan. *Simple prism coupling technique to measure the refractive index of a liquid and its variation with temperature*. Review of Scientific Instruments, 61(3), 1990.

[44] J. Jágerská, N. Le Thomas, R. Houdré, J. Bolten, C. Moormann, T. Wahlbrink, J. Ctyroký, M. Waldow, and M. Först. *Dispersion properties of silicon nanophotonic waveguides investigated with Fourier optics*. Opt. Lett., 32(18):2723–2725, Sep 2007.

[45] L Lvesque. *Refractive index determination of materials on thin transparent substrates using ellipsometry*. Physics Education, 35(5):359, 2000.

[46] Eric Dulkeith, Fengnian Xia, Laurent Schares, William M. J. Green, and Yurii A. Vlasov. *Group index and group velocity dispersion in silicon-on-insulator photonic wires*. Opt. Express, 14(9):3853–3863, May 2006.

[47] Xi Chen, Zheng Li, Moustafa Mohamed, Li Shang, and Alan R. Mickelson. *Parameter extraction from fabricated silicon photonic devices*. Appl. Opt., 53(7):1396–1405, Mar 2014.

[48] Amir Arbabi and Lynford L. Goddard. *Measurements of the refractive indices and thermo-optic coefficients of Si3N4 and SiOx using microring resonances*. Opt. Lett., 38(19):3878–3881, Oct 2013.

[49] W. Bogaerts, P. De Heyn, T. Van Vaerenbergh, K. De Vos, S. Kumar Selvaraja, T. Claes, P. Dumon, P. Bienstman, D. Van Thourhout, and R. Baets. *Silicon microring resonators*. Laser and Photonics Reviews, 6(1).

[50] S. Dwivedi, H. D'heer, and W. Bogaerts. *Maximizing Fabrication and Thermal Tolerances of All-Silicon FIR Wavelength Filters*. Photonics Technology Letters, IEEE, 27(8):871–874, April 2015.

[51] Martin Fiers, Thomas Van Vaerenbergh, Ken Caluwaerts, Dries Vande Ginste, Benjamin Schrauwen, Joni Dambre, and Peter Bienstman. *Time-domain and frequency-domain modeling of nonlinear optical components at the circuit-level using a node-based approach*. J. Opt. Soc. Am. B, 29(5):896–900, May 2012.

[52] `http://www.lucedaphotonics.com/`.

[53] Christopher Z Mooney, Robert D Duval, and Robert Duval. *Bootstrapping: A nonparametric approach to statistical inference*. Number 94-95. Sage, 1993.

[54] Christopher Z Mooney. *Monte carlo simulation*, volume 116. Sage Publications, 1997.

3

Silicon Photonic Based Flat-band Wavelength Filters

In this chapter, we present different SOI based wavelength filters, which are mainly targeted at coarse wavelength division multiplexing (CWDM) applications for both the C-band (center wavelength at 1550 nm) and the O-band (center wavelength at 1310 nm). For the C-band we have targeted for a 30 nm wide wavelength band while for O-band it is 80 nm wide to match the CWDM ITU grid specification [1]. We compare finite impulse response (FIR) filters, such as *arrayed waveguide gratings* (AWG), *echelle gratings* (also called *planar concave gratings* or PCG) and *cascaded Mach-Zehnder* filters. We discuss their operation principles, design criteria and different performance metrics (e.g. insertion loss or cross talk). We derive the strengths and weaknesses the operation principles and confirm those with the experimental data from fabricated devices.

3.1 Introduction

The *International Technology Roadmap for Semiconductors* (ITRS) has projected the bandwidth requirement for I/O communications to reach the level of TB/s in the near future [2]. Silicon photonics is a potentially attractive technology to meet the growing bandwidth demand [3]. Since it can be fabricated with CMOS technology, it has the potential to scale to higher volume production with a high process yield.

To scale the bandwidth of silicon optical interconnects, *wavelength division* *multiplexing* (WDM) is a way forward where individual channel high speed signals are modulated on different wavelength carriers. This can range from coarse WDM with a few widely spaced channels to ultra dense WDM with over thousand closely packed wavelength channels. To effectively multiplex and demultiplex these communication channels, good wavelength filters are required, with sufficiently low insertion and a high rejection ratio of the other communication channels. In addition, wavelength filters can be useful for sensing applications. Many optical sensors rely on spectral information. For instance, a wavelength shift is related to a specific quantity (e.g. concentration of biomarkers in a biosensor, or strain in a fiber Bragg grating sensor), or it can be spectroscopic information, such as spectral fingerprints of gases and complex molecules. The requirements for these applications can differ significantly from those of WDM communications.

There are different techniques to make wavelength filters, but almost all of them rely on interference of two of more light paths. In this chapter, we discuss different implementations of finite impulse response (FIR) filters. These filters are based on a finite set of interfering optical delay lines in a feed-forward architecture. The main examples of such filters in an integrated circuit include Mach-Zehnder interferometers (MZI), arrayed waveguide gratings (AWG) and echelle gratings [4, 5]. In contrast to FIR filters, it is also possible to make infinite impulse response (IIR) filters in a PIC. These include a feed-back mechanism, with optical delay paths coupling back on themselves. This will cause multiple self-interferences of light waves, which will lead to resonances. The feedback cavity can be based on a travelling wave such as in ring resonators, or on a standing wave, such as a Fabry-Perot cavity. IIR wavelength filters have a significant advantage (compared to FIR filters) in the sense that they use the same delay line multiple lines. Therefore they have less problems in matching the delay lengths, and the device footprint is usually very compact. It is also relatively easy to obtain narrow filter line widths. However, a key drawback of the resonant filters is that the multiple rounds also introduce a higher optical peak power in the filter. Therefore, IIR filters can suffer from nonlinear effects, even at a low power [6].

In this chapter, we first give an overview of the functionality of FIR filters and then discuss SOI based wavelength filters. We have already discussed the SOI waveguide and wavelength filter sensitivities in the chapter 2, so we focus on the methods to make the filters tolerant to fabrication process variations and environmental thermal fluctuations. We also compare the different types of filters and select the one which suits the best for the coarse wavelength division multiplexing (CWDM) at O-band where low cost and high speed (preferably 100 GbE-400 GbE) is a primary requirement.

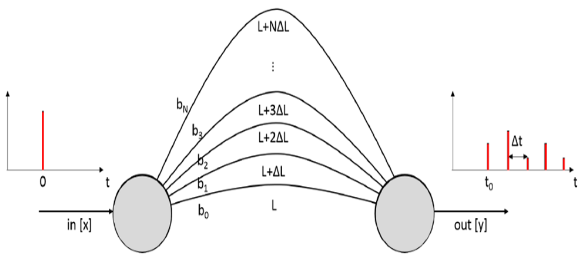

Figure 3.1: Finite impulse response filter based on constant delay lines (from [7])

3.2 FIR Wavelength Filters

Interferometric FIR wavelength filters are based on optical delay lines. The unfiltered light is split over two or more paths with a different optical path lengths, and the different contributions are recombined. This is illustrated in Fig. 3.1. An input impulse is split over the multiple delay lines, and at the the output this results in a finite series of impulses, one for each delay lines.

If the path difference between the delay lines is a constant ΔL, the time difference between the impulses is $\Delta t = \Delta L \frac{n_g}{c}$, with $\frac{c}{n_g}$ the group velocity of the pulses. If we ignore the common delay t_0, the output $y(t)$ can be written as a function of the input $x(t)$:

$$y(t) = b_0 x(t) + b_1 x(t - \Delta t) + b_2 x(t - 2.\Delta t) + ... + b_N x(t - N.\Delta t) \tag{3.1}$$

In the Z-domain we can write this as a polynomial expansion:

$$\begin{aligned} y[z] &= b_0 + b_1 z + b_2 z^2 + ... + b_N z^N \\ &= (z - q_1)(z - q_2)...(z - q_N) \end{aligned} \tag{3.2}$$

where q_i are the zeros of the filter. In contrast, IIR filters have a feedback loop, which results in an impulse response which never completely dies out. In the Z-domain this translates into a series of zeros and poles [8].

In the frequency (or wavelength) domain, the repeating patterns of pulses will also result in a periodic response, with a free spectral range (FSR) equal to:

$$FSR[Hz] = \frac{1}{\Delta t} = \frac{c}{ng\Delta L} \tag{3.3}$$

$$FSR[nm] = \frac{\lambda^2}{n_g.\Delta L} \tag{3.4}$$

around a central operating wavelength λ_0.

In the wavelength domain, we can see that the optical delay lines introduce a wavelength dependent phase shift $\Delta\phi(\lambda)$=$2\pi n_{eff}(\lambda)\Delta L/\lambda$. When the optical path length difference $n_{eff}\Delta L$ is exactly a whole number m of wavelengths, the phase difference $\Delta\phi$ between contributions is a multiple of 2π, and they will interfere constructively. Otherwise we will get only partial constructive interference. When the delay lines are properly chosen, all contributions will add up for the desired wavelength channel $\Delta\lambda$, resulting in a high transmission. However, outside the channel they will cancel out, resulting in a low transmission.

Note that the absolute filter wavelength depends on the effective index n_{eff} of the delay line, while the channel bandwidth and the FSR depends upon the group index n_g, which includes the wavelength dependence of n_{eff}. In highly dispersive silicon waveguides, the group index is almost twice to that of the effective index [9].

The performance of the channel filter can be expressed by different metrics, which is illustrated in Fig. 3.2. The bandwidth of a channel is usually expressed as a full-width-half maximum (FWHM) or 3 dB bandwidth. However, 1 dB bandwidth and 10 dB bandwidth is often used. To characterize the flatness of the spectral response we introduce aspect ratio: $\frac{\lambda_{1dB}}{\lambda_{1dB}}$ where λ_{1dB} and λ_{10dB} are the 1dB and 10dB of the spectral response of the channel as shown in Fig. 3.2. It is also used to describe the roll-off of the filter. The closer the ratio of 1dB/10dB equal to one, the more the filter approaches the box-like edge. The *crosstalk* indicates the maximum power collected from the outside the channel i.e. the rejection of light with wavelengths outside the channel. There are different types of cross talk e.g. neighbor channel cross talk and phase error cross talk as indicated in the Fig. 3.2. The *insertion loss* indicates the transmission efficiency of the wavelength inside the channel. If one considers crosstalk as optical power which is not directed into the correct channel, and is therefore lost.

Normally for the MZI lattice filters, the filter synthesis coefficients can be calculated based on techniques used in digital filter design, to define Butterworth, Chebyshev, Elliptical or other filter profiles with specific objective functions such as pass-band shape, roll-off and crosstalk [8].

3.3 SOI Based Wavelength Filters

Different delay-based filters are illustrated in Fig. 3.3. A Mach-Zehnder interferometer splits the light over two arms, effectively introducing a single delay stage, and which be cascaded to multiple delay stages. An arrayed waveguide grating (AWG) distributes light over many delay lines using a star coupler, while an echelle grating implements the optical delays by positions reflecting facets at different distances of inputs and outputs.

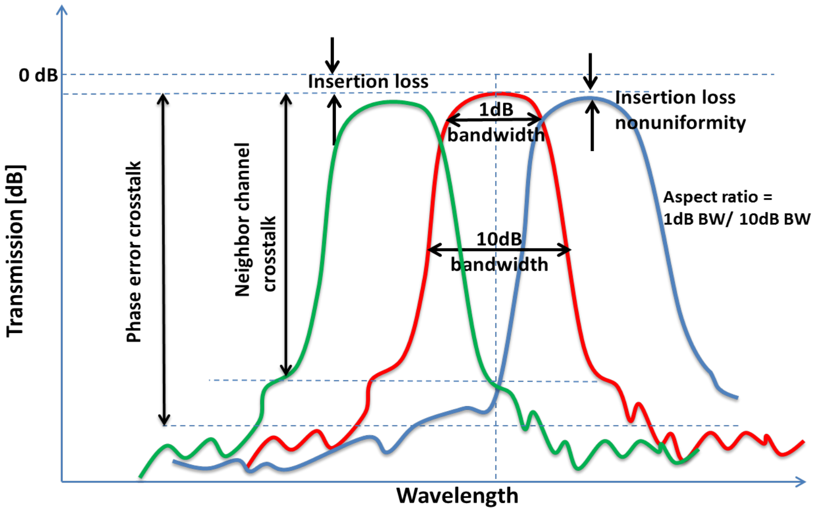

Figure 3.2: Schematic representation of performance metrics of a wavelength filter: insertion loss, insertion loss non-uniformity, neighbor channel crosstalk, phase error crosstalk, 1dB and 10dB channel bandwidth. Passband aspect ratio is 1dB/10 dB channel bandwidth (from [7]).

The key differences between the filters are how the light is distributed over the different delays and how the contributions are recombined, i.e, the b_i coefficients. As we will discuss further, MZI lattice filters allow, in principle, better control of the b_i coefficients than an AWG or echelle grating. In actual waveguides, the actual phase and amplitude of each b_i contribution depends on the exact geometric definition of the delay, as well as the optical properties of the medium in which the delay is implemented. And this is where the differences between silicon photonics FIR filters lie.

Silicon photonic waveguides are typically quite dispersive. This means that the optical phase delay, and even the group delay, are not constant over a wide wavelength range. This is not necessarily a problem for filters that operate in a narrow wavelength band. But, for filters that operate in a broad spectrum like coarse wavelength division multiplexers, the dispersion could become a problem.

Also, the high refractive index contrast of silicon waveguides makes them very sensitive to small geometry variations, or changes in temperature. This means that the exact optical length of each delay line cannot be precisely controlled [10]. When multiple lines with a supposedly identical delay are used, the phase errors will manifest as a higher insertion loss and a higher crosstalk [7]. It is evident that the effect of these stochastic errors increases with longer delay lines and is strongly dependent on the quality of the fabrication technology. Also, global changes in

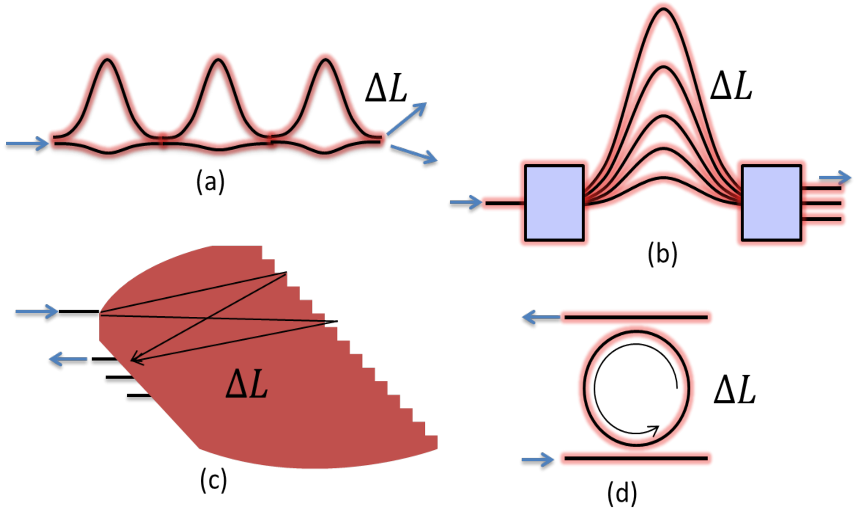

Figure 3.3: Different implementations of optical filters based on delay lines. (a) a Mach-Zehnder lattice filter, (b) an Arrayed Waveguide Grating, (c) an Echelle Grating and (d) a Ring Resonator. (a-c) are finite impulse response filters, consisting only of feed forward delay lines. The ring resonator (d) introduces a feed-back loop, making an infinite impulse response filter. Figure is from [7].

the waveguide geometry (linewidth and thickness) or environmental conditions (temperature) can affect the optical length of the waveguide in a stochastic way.

Due to the large thermo-optic coefficient of silicon ($1.86 \times 10^{-4}\ K^{-1}$) the spectral response of these filters will be red-shifted by approximately 80 pm/K, depending on the exact waveguide geometry. Similarly, the reproducibility of the fabrication process can also induce a wavelength shift. Variations in silicon waveguide width and thickness induce a wavelength shift of almost 1-1.5 nm/ nm in the filter response [11]. Even though the fabrication of silicon waveguides is done using advanced silicon processing techniques, there will always be some variability in the process, within wafer, between wafers in the same fabrication batch and between batches [12].

Different methods have been proposed to maximize the fabrication and thermal tolerances of these filters:

1. Active compensation either with thermo-optic tuning by applying heaters or electro-optic tuning by doping the waveguide geometry (mainly used for modulators). But, this being a power hungry process that results in complexity [13–20].

2. Passive compensation which we will discuss in the following chapters (4-5).

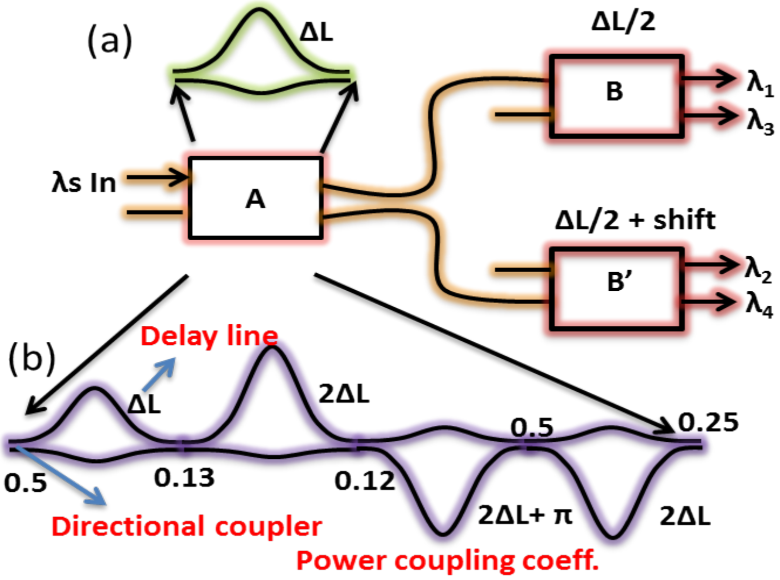

Figure 3.4: Schematic for a 1×4 demultiplexer. (a) Single MZI in each stage and, (b) 4 MZIs cascaded in each stage with directional couplers with a power coupling coefficients to get flat band response.

3. Flattening the channel pass bands. This method is the focus of this chapter. We have implemented four channel de-multiplexer at C-band to demonstrate this concept for different FIR filters.

3.4 MZI Cascaded Filters

3.4.1 Introduction and Design

A simple MZI is a 2×2 filter with a single delay path. These single MZIs connected in cascaded fashion can work as a demultiplexer or a channel selector. The demultiplexer can also be used as a multiplexer since it is a reciprocal device. For demultiplexer with M stages, there are 2^M outputs. The architecture is referred to as a log_2N filter because of its number of stages $M = log_2N$ where N is number of channels [8]. The wavelength selector is similar to the demultiplexer where only one output port is used. The transfer function for any input and output port is the product of the transfer functions for the individual stages.

The schematic of the $M = log_2N$ filter based on 2 stages MZI 4-channel demultiplexer is shown in Fig. 3.4. As shown in Fig. 3.4(a), the desired filter response of each channel is sinusoidal because every stage is single delay line.

While in Fig. 3.4(b) we have designed every stage in such a way so that each channel gets box shape like response. It is made possible by coupling 4 MZIs as a lattice filter in every stage. The coupling coefficients between MZIs are calculated based on the optical half band filters [21]. This concept comes from digital filter techniques which was first introduced by [22]. Later it was implemented with MZI lattice filters and demonstrated in different platforms like silica based planar lightwave circuits [23–26] and also on silicon [27–30].

The simulation is performed in two steps. In the first step, the waveguide and directional coupler parameters, such as the effective refractive index, group index and coupling lengths are simulated with a full wave FEM solver. In the second step, these parameters are fed into the circuit solver Caphe from Luceda photonics [31]. The directional couplers are considered to be wavelength dependent in simulations. Every channel is designed for a 5 nm channel spacing. It means that the FSR of the MZI of stage 1 (block A) is designed for 10 nm and for the second stage the FSR is doubled. The FSR of the individual MZIs in a block is inversely proportional to the delay length which is given by:

$$FSR = \frac{\lambda^2}{n_g.\Delta L} \tag{3.5}$$

where λ is the center wavelength of interest, ΔL is the physical path length difference between longer and shorter arm of the MZI and n_g is the group index of the designed waveguide around the center wavelength. In order to adjust the center wavelengths of output channels, we provide the phase shift of $\pi/2$ or one-fourth of FSR in the B'-block design. This shift can be calculated as:

$$\Delta L' = \Delta L + \frac{\lambda}{4.n_{eff}} \tag{3.6}$$

The circuit simulation for 4-channel demultiplexer with single MZI in each stage and with cascaded MZIs in each stage is shown in Fig. 3.5(a) and Fig. 3.5(b) respectively.

3.4.2 Fabrication and Measurements

The waveguides in the delay lines and in DCs are 450 nm wide. The gap in the DCs are designed as 180 nm wide. The bend radius is $5\mu m$ to make the devices small in footprint. The two stage device is fabricated in IMEC's standard passive platform [32]. This process uses 200 mm SOI wafers and 130 nm CMOS technology node with 220 nm of silicon and 2 μm of buried oxide (BOX). The device is connected to compact grating couplers that are etched 70 nm into silicon, to couple light from fiber to chip. The waveguides and directional couplers (DCs) are fabricated in fully etched 220 nm thick silicon. During the full process flow, approximately 5 nm of

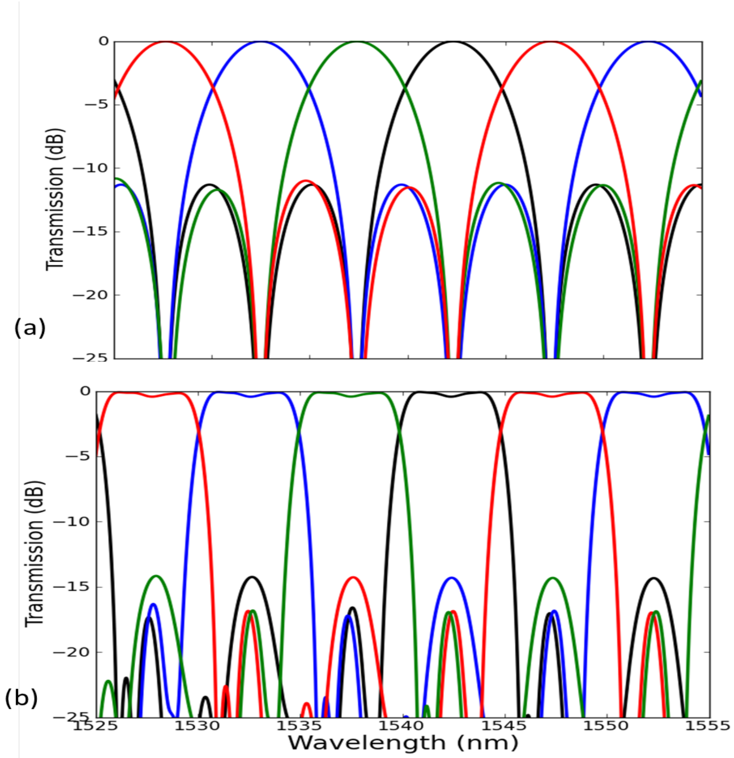

Figure 3.5: Circuit simulation of (a) Single MZI in each stage and, (b) with a 4-MZIs lattice filter in each stage

silicon is removed, resulting in a waveguide core thickness of 215 nm. The details of this process have been discussed in chapter 2.

Measurements of the devices are performed with a continuous-wave Agilent laser with 4 mW of input power using semi-automatic setup discussed in section 2.5.4.1. First, the reference waveguide sitting beside the demultiplexer is aligned at the channel wavelengths and then the corresponding channels of the device are measured to get a maximum transmission.

The camera image of fabricated demultiplexer with single MZI in every stage and measured transmission of all four channels are shown in Fig. 3.6(a) and Fig. 3.6(b) respectively.

The measured insertion loss of all the four channels of the two stages MZI demultiplexer is better than 0.5 dB, while the channel cross talk values are below -10 dB for all the channels. 1 dB bandwidth is considered to evaluate the channel cross talk. The measured channel spacing is 5 nm which matches very well with the circuit simulation. This is measured using the center of the 1 dB channel

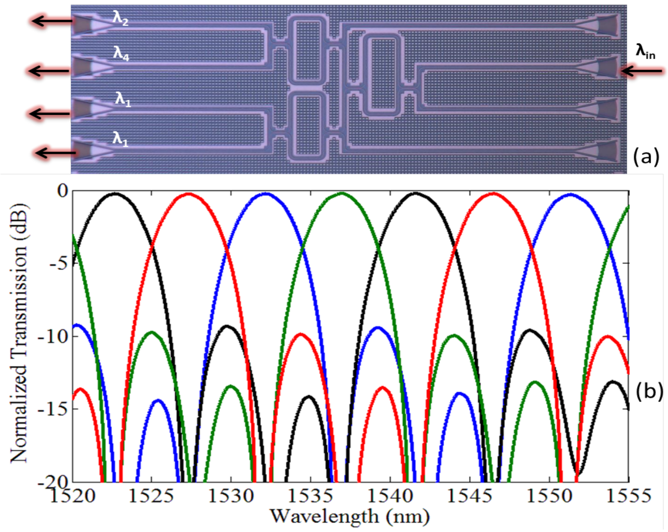

Figure 3.6: MZI based 4-channel demultiplexer (a) fabricated device, (b) normalized measure transmission

bandwidth.

The camera image of fabricated demultiplexer with cascaded MZIs in every stage and measured transmission of all four channels are shown in Fig. 3.7(a) and Fig. 3.7(b) respectively. The total footprint of the device is 280 × $260\mu m^2$.

The measured insertion loss of all the four channels of the two stages cascaded MZI demultiplexer is better than 1.2 dB, while the channel cross talk values are below -11 dB. The channel cross talk is calculated using 1 dB bandwidth as analysis window and then adding all the power contribution from other channels in that analysis window. Due to cascading of the MZI filters, the insertion loss of the demultiplexer increases but as expected from simulation we achieve the box-type rectangular pass band response and also a better roll-off than the previous demultiplexer. The side lobes of the filter can be further improved by adding number of stages. The design can be improved by using the wider waveguide section instead of 450 nm in the delay lines which will further suppress the phase errors [30, 33]. The 1 dB bandwidth of the demultiplexer is almost 3 nm wide which is 60% of the channel spacing. The flattened pass band makes the demultiplexer robust for the fabrication and thermal tolerant but comes with a price of larger footprint, more insertion losses and phase errors due to longer waveguide sections in number of cascade stages.

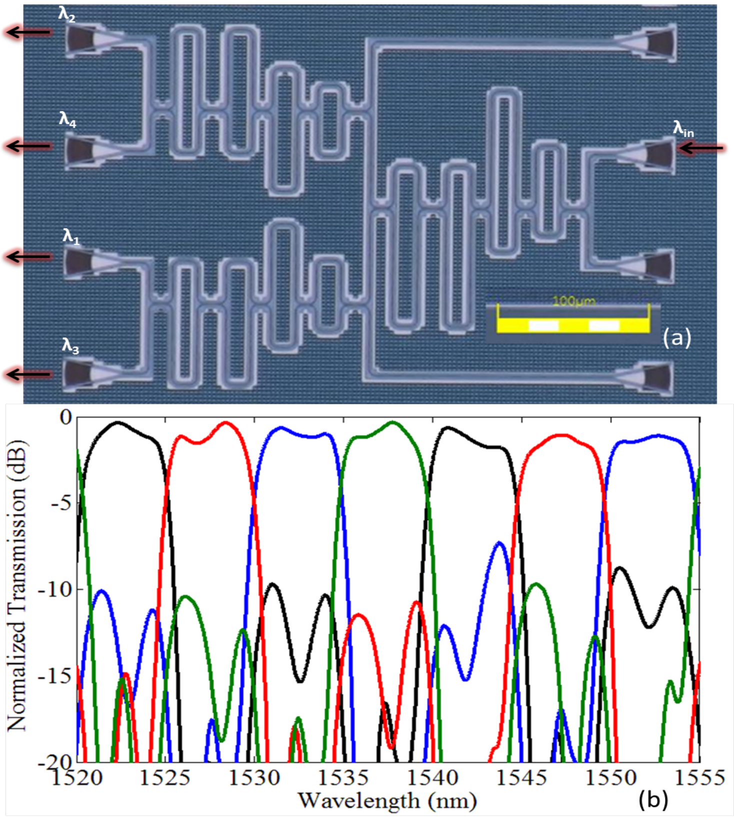

Figure 3.7: Cascaded MZI based 4-channel demultiplexer (a) fabricated and, (b) normalized measure transmission

3.5 Arrayed Waveguide Gratings

Arrayed waveguide gratings are another mechanism to implement the interference of multiple delay lines. The principle is illustrated in Fig. 3.8(a) Incoming light is distributed over many lines in a star coupler. The individual contributions are then recombined in a star coupler. However, the recombination mechanism is significantly different from MZI cascaded filter. The star couplers function as an imaging system. When all the contributions of the delay lines are in phase, the field profile of the input aperture is imagined in the plane of the output apertures. The quality of this image depends on the number of contributions (delay lines), but it is never perfect. When the wavelength changes, there will be a constant phase difference between every two arms, and this will tilt the phase front in the output star coupler. This, in turn, will shift the image. Therefore, there is a one-to-one

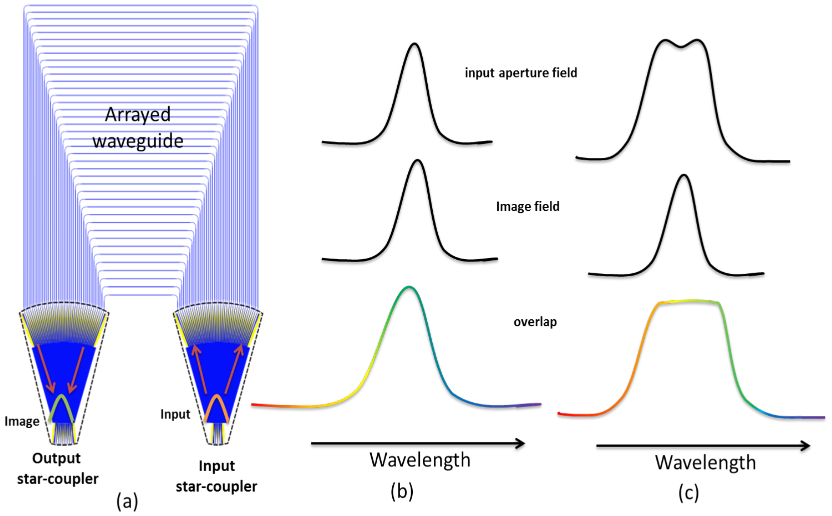

Figure 3.8: Array Waveguide Gratings (a) operation principle, (b) the overlap of the image field profile with the aperture mode gives rise to a wider wavelength response (c) Flat band response which can be obtained by using MMI as an input aperture

mapping of the position in the image plane to the wavelength within a single FSR. The mode-to-mode response of input to output is determined by the overlap of the image field profile with the mode profile of the output aperture. As shown in Fig. 3.8(b), the imaging and resulting overlap broadens the wavelength response of the filter, to approximately twice the bandwidth. Consequently, an AWG which needs to select 1 channel out of N, needs about twice the number of arms than an equivalent MZI lattice filter.

An advantage of the AWG is that the imaging principle makes it possible to create a wavelength demultiplexer, instead of a single filter. When positioning multiple waveguides apertures in the output star coupler, different wavelengths are coupled to different output waveguides. However, the channels will have an uneven insertion loss. The transmission from the center input to the center output is highest, while the transmission between an input and an output both at the edge of the star coupler (or the edge of the FSR in the spectrum) could be 3-6 dB lower. A way to overcome this is to increase the number of channels within the FSR without use the outer channels. This requires additional delay lines.

3.5.1 Flat band AWGs

A flat band spectral response can be achieved using an MMI as an input aperture of the AWG as shown in Fig. 3.8(c). This concept has already been demonstrated

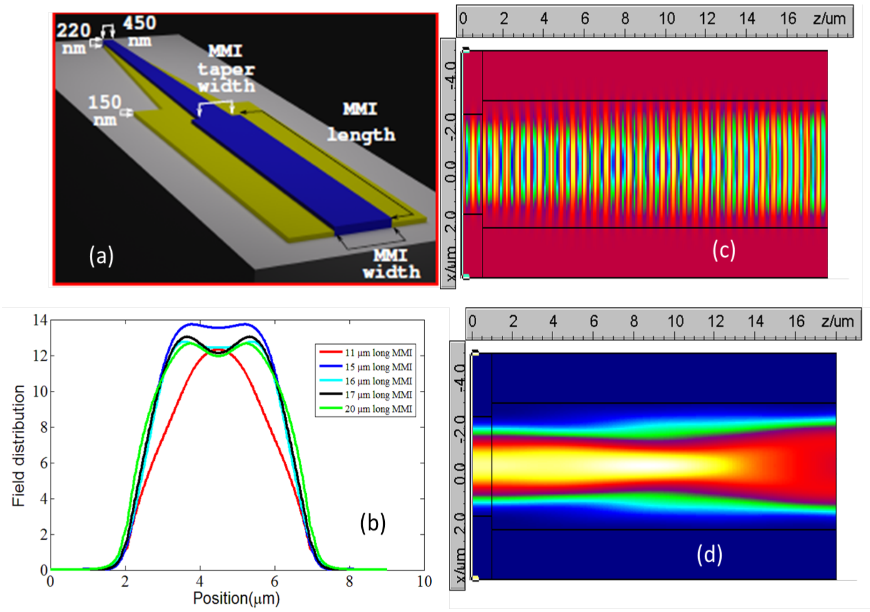

Figure 3.9: MMI (a) schematic (from [36]) , (b) simulated field distribution at the end of MMI of width 5μm for different lengths (c) simulated E-field and (d) intensity field with length of MMI as 17μm

in different platforms [34, 35] including silicon [33]. In order to get the flattop response, the design of MMI is very critical. The primary design parameters are: MMI width, MMI length, taper width, taper length and position. With optimization of these parameters, we can tailor the input aperture field and obtain a broader, more uniform pass band at the output. The detailed design, simulation and optimization of these types of devices is explained in the PhD thesis of Shibnath Pathak [36].

We have designed four channel flat band AWGs for 800 GHz (6.4 nm) of channel spacing. The input MMI aperture is optimized using Fimmprop from photon design [37] (can be done in CAMFR as well [38]). The width of the MMI aperture is first optimized which is found to be 5μm wide. The length is then swept to get the desired input aperture field. The schematic of MMI, the simulated field and intensity profile, and the field distribution at the end of the MMI for different lengths are shown in Fig. 3.9.

The optimized length has been obtained by simulation between 16 to 20 μm, the one we have already used in the design i.e. 17 μm.

The simulation of the AWG is performed using IPKISS from Luceda photonics [31]. The model is based on the integration of different tools which handle the parts of an AWG. It includes input star coupler, delay lines and output star cou-

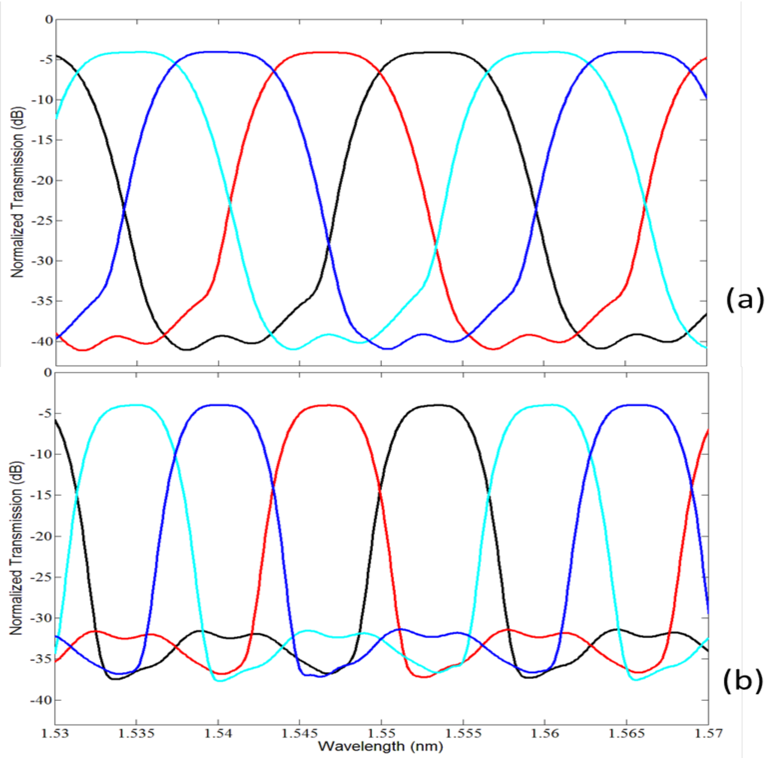

Figure 3.10: Flat band 4 channel AWG simulation (a) with 16 delay lines, the designed one and, (b) with 24 delay lines. As we increase the number of delay lines the roll-off becomes steep at the same time phase errors increase.

pler. The input, output and arms aperture field profiles are solved by eigen mode expansion from CAMFR. These field profile are used as an input of the Fresnel diffraction model [33] that generates the matrix which contains the amplitude and phase response of the couplings of the input and arm aperture of the input star coupler. The same procedure is followed for the output star coupler. The waveguide array is modelled by theoretical propagation model of the waveguide which includes dispersion and effective index of the waveguide cross section. The simulated AWG with varying delay lines are shown in Fig. 3.10.

All devices have been designed to be fabricated on the imec 200 mm pilot line SOI platform. A shallow etch process has been used for defining all star coupler apertures, including the MMIs, to reduce reflections at the transitions. The output apertures are 2 μm wide and are connected to a 450 nm wide photonic wire through a 25 μm long adiabatic taper. The input apertures of the MMI-AWGs consist of a 43 μm long taper having a width of 4 μm coupled to an MMI with length and

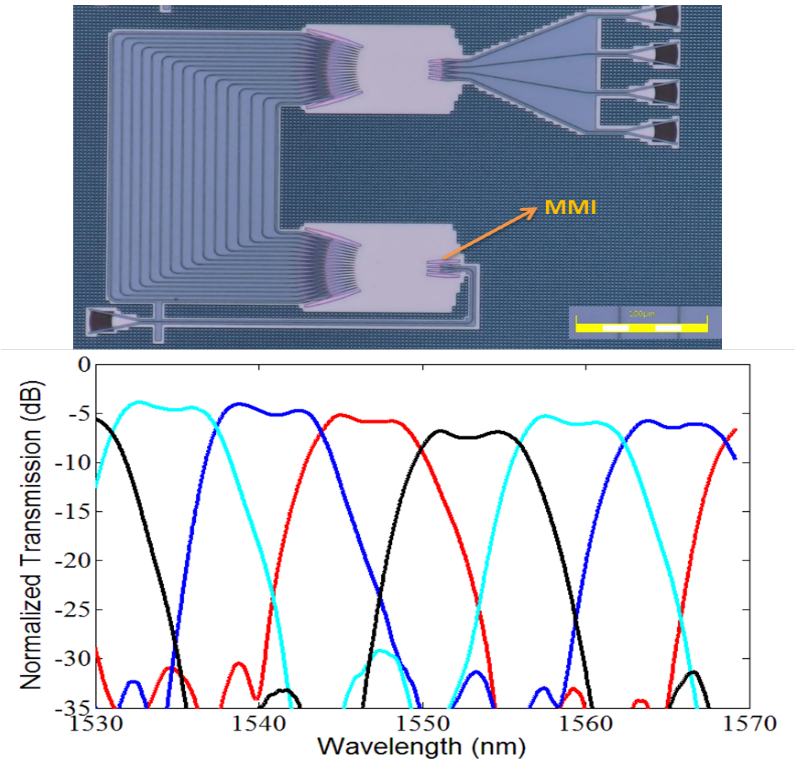

Figure 3.11: (a) Camera image of fabricated MMI-AWG and, (b) measured normalized transmission response

width of 17 μm and 5 μm as simulated above. The fabricated flat band AWG are shown in Fig. 3.11(a). The total footprint of the device is $270 \times 270 \mu m^2$.

Measurements of the AWG are performed with a continuous-wave Agilent laser with 4 mW of input power using semi-automatic setup discussed in section 2.5.4.1. First, the reference waveguide sitting beside the AWG is aligned at the channel wavelengths and then the corresponding channels of the device are measured to get a maximum transmission. The measured response is shown in Fig. 3.11(b).

The measured insertion loss of all the four channels is better than 6.0 dB, while the channel cross talk values below -20 dB. 1 dB bandwidth has been used to analyze the channel cross talk. The nearest neighbor crosstalk is high due to unoptimized roll-off. The reason for this is that only 16 delay lines has been used in the waveguide array, it can get improved with additional delay lines, but comes with a cost of additional phase errors [39]. We have confirmed this in the simulation where we used 16 delay lines and 24 delay lines. The MMI based AWG intrinsi-

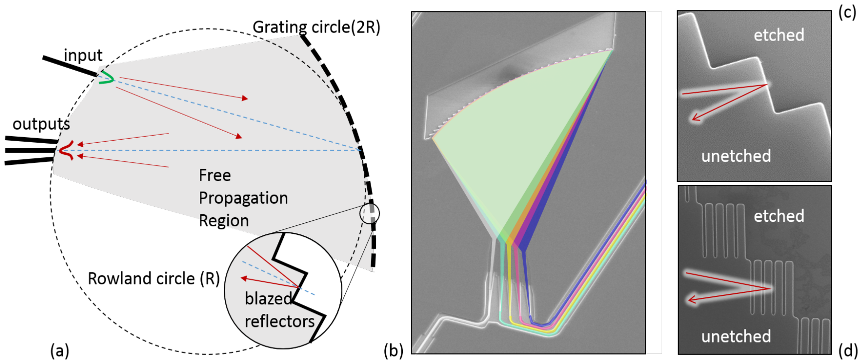

Figure 3.12: (a) Echelle grating (from [7]. Basic design of the echelle grating where the input and output apertures are located on the Rowland circle. (b) Fabricated echelle gratings [4]. (c) Etch gratings facets [40] and (d) Bragg mirror grating facets [41]

cally has a higher insertion loss than the conventional AWG because of the shape mismatch in the image plane of the AWG, and it is due to the fact that the power in the image is now wide spread over a wider area to obtain the flat-top wavelength response.

3.6 Echelle Gratings

Echelle gratings operate in a similar way as AWGs, by combining a number of optical delays with a free-space imaging system [40]. The key difference with AWGs is that echelle gratings implement the delay lines as distance in the free propagation region (FPR) set by the location of an array of reflecting facets. As shown in Fig. 3.12, light traverses the same free propagation region twice. The exact phase delay is therefore not dependent on the linewidth of the patterned waveguides. This makes echelle gratings more fabrication tolerant, because the optical delay length now depends only on the guiding layer, rather than the exact geometry of waveguide cross section. However, thickness variations of the silicon can still introduce phase errors.

The fabrication-critical detail of echelle gratings are the reflector facets. Etch facets only have a reflection of 30-40%, which immediately introduce a 5 dB insertion loss [41]. Better solutions involve the use of corner reflectors or distributed Bragg mirrors which can reduce the reflection loss by 1 dB or even less. Just having a high reflection of the grating is not sufficient: it is important that the edges of the reflectors do not scatter too much light, because that gives rise to to imagining errors and therefore distortion. So, while the image quality generally improves by using the more reflectors (or grating elements), the reflectors should be suffi-

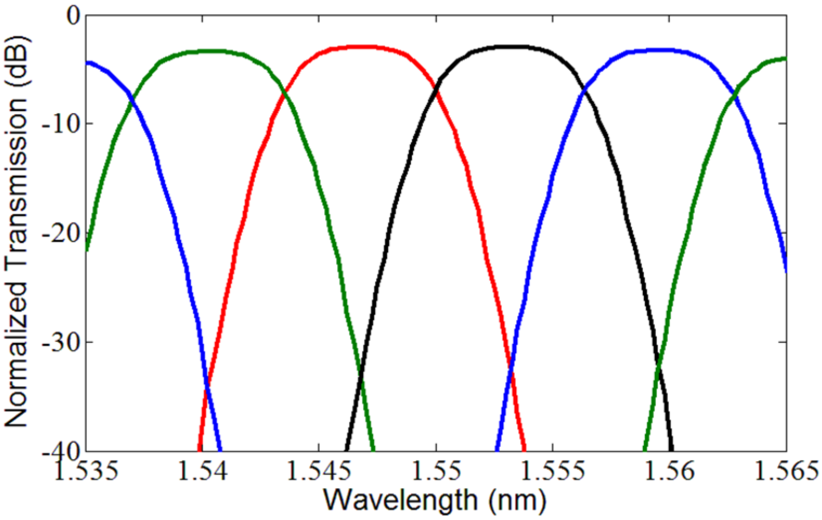

Figure 3.13: (Simulated transmission of MMI-echelle grating

ciently large to make sure that the edge effects do not dominate the main body of reflectors.

3.6.1 Flat band Echelle Gratings

For getting the flat band response we have designed the echelle gratings in a similar way as of MMI based AWG. We have used the same MMI width and length as used in the AWG i.e. 5 μm wide and 17 μm long. We have designed echelle gratings with the FSR of 50 nm and a channel spacing of 800 GHz (6.4 nm). The channel spacing is the same as the AWG demonstrated above, but with a larger FSR to optimize the performance [42]. The detailed design procedure of echelle gratings is mentioned in [40]. Simulation of the echelle gratings are performed are also in a similar way as AWG. The eigen mode profile and the group index are calculated through CAMFR or fimmwave and then free propagation region is semi-analytically calculated through the Fresnel diffraction model. The assumption is made for the distributed Bragg reflectors (DBRs) that they reflect 90% light. The simulated transmission of the designed echelle grating is shown in Fig. 3.13.

The fabricated MMI-echelle grating is shown in Fig. 3.14(a). The total footprint of the device is $610 \times 310 \mu m^2$.

Measurements of the echelle gratings are performed with a continuous-wave Agilent laser with 4 mW of input power using semi-automatic setup discussed in section 2.5.4.1. First, the reference waveguide sitting beside the AWG is aligned at the channel wavelengths and then the corresponding channels of the device are

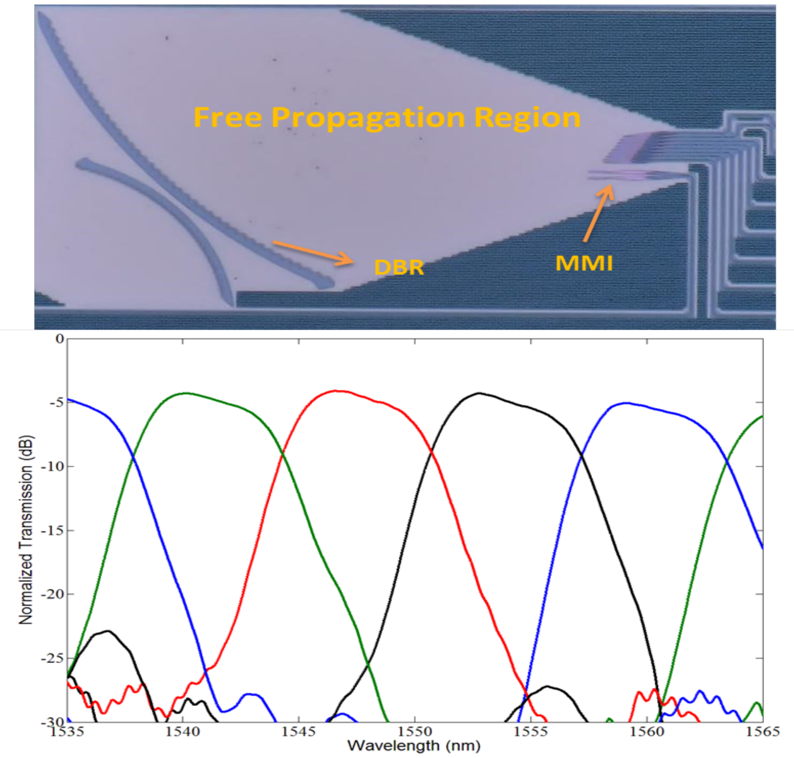

Figure 3.14: (a) Camera image of fabricated device MMI - echelle grating and, (b) measured normalized transmission response

measured to get a maximum transmission. The measured response is shown in Fig. 3.14(b).

The measured insertion loss of all the four channels is better than 6.0 dB, while the channel cross talk values below -20 dB. 1 dB bandwidth window has been used to analyze the channel cross talk.

3.7 Comparison

We have compared all the three above mentioned devices in terms of insertion loss, channel cross talk, 1 dB/10 dB bandwidth in table 3.1.

We can see that the MZI cascaded filters are most appropriate in terms of insertion loss and the roll-off or aspect ratio (1dB/ 10dB ratio) and is due to engineered pass band. In terms of channel crosstalk AWG and echelle gratings are better. As we have seen from the simulations the roll-off of an AWG can be improved by adding more delay lines. It certainly improves the nearest neighbor crosstalk.

Device	Insertion loss (dB)	Crosstalk (dB)	1dB/10dB	Footprint (μm^2)
Cascaded MZI	1.2	-11	0.9	280×260
MMI-AWG	5.0	-20	0.6	270×270
MMI-Echelle Gratings	5.2	-21	0.44	610×310

Table 3.1: Flat band four channel demultiplexers

However, at the same time the phase error increase as well. For echelle gratings the nearest neighbor crosstalk and phase error crosstalk is quite close. All these demonstrations are for four channels coarse wavelength demultiplexers and it changes when number of channel increases or the channel spacing decreases. One such comparison, we can find in [7]. If we compare in this particular analysis about the footprint, MZI cascaded filters and AWGs are competing.

3.8 Coarse Wavelength Division Multiplexer for the O-band: Need

There are different types of WDM filters depending on the application: Dense-WDM (DWDM) channels are usually spaced between 12.5 GHz to 100 GHz while in Coarse WDM (CWDM) the channel spacing is 20 nm as proposed by International Telecom Union (ITU) [1, 43]. Due to this wide wavelength spacing, the transmitters deployed in CWDM applications do not require expensive control mechanism, which is favourable for inexpensive short reach optical interconnects.

Keeping the channel spacing intact over the entire wavelength range of the filter, is fairly easy in a platform such as silica *planar light-wave circuits* (PLC), where the glass waveguide cores are several μms across and have a low refractive index contrast and dispersion [25, 26]. But this low contrast also requires centimeter-scale waveguide components. Due to the high material index contrast on the *silicon-on-insulator* (SOI) platform, it is possible to keep the waveguide cross section in the submicrometer range with waveguide bends that can be shrunk down to the order of μms. However, this also makes the waveguide properties very dispersive with wavelength. As a result, it is difficult to keep the channel performance intact over a wide wavelength range, as essential parameters such as waveguide effective index and coupling strengths of *directional couplers* (DC) change significantly.

To achieve the key requirement of power efficiency of 1 pJ/bit [44] for short reach and on-chip optical link in CWDM applications, CWDM (de-)multiplexers need to have: (1) to keep the channel spacing of 20 nm intact over a wide bandwidth, (2) to have a low insertion loss and low cross talk, (3) be compact in size, (4) be manufacturable with standard CMOS processes, and (5) robust against fabrication and environmental thermal fluctuations.

Channel band flattening in pass bands is possible in the different FIR based filters as discussed in the previous section. In filters with an imaging-based star coupler, such as AWGs and PCGs as demonstrated above, a flat passband usually incurs the cost of additional insertion losses [33, 45].

Ring-based IIR filters are not ideally suited for CWDM due to their inherently narrow bandwidth [46]. Increasing the overall bandwidth and free spectral range would require the use of smaller, lower-quality rings, and these can become very lossy for small bend radii.

There have been various demonstrations of different demultiplexers on SOI demonstrated for CWDM applications , based on PCGs and AWGs [42, 47, 48] and contra-directional couplers [49] but these either suffer from thermal and fabrication tolerance issues or limited by the fabrication technology.

The challenges for silicon based CWDM transceiver is to have a minimum channel insertion loss, without the use of a *thermo-electric cooler* (TEC). This latter aspect should reduce the cost, enable the use of an uncooled DFB laser array, and reduce the operational power consumption.

Considering all the above discussed parameters, cascaded MZI based de-multiplexers appear to be the best suited option for a passive filter designed for the CWDM wavelength grid. By cascading multiple MZIs using correct coupling coefficients, the pass band can be engineered while keeping the device quite compact. Such an approach for WDM channels with narrower spacing has been proposed before [30] but here it is extended to a wider wavelength range (with the correspondingly larger dispersion between channels) to meet the ITU-T CWDM grid [1]. Our proposed design is a dual stage cascaded MZI de-multiplexing filter with flat band response and channels centered at ITU grid wavelengths of 1271 nm, 1291 nm, 1311 nm and 1331 nm. We have also used the measured results to test the device in a 100 GbE system simulation with every channel carrying 28 Gb/s data.

3.9 Design and Simulation

The building block of the demultiplexer (demux) is a set of four cascaded MZIs designed to get a maximally flat response for a given FSR. Coupling coefficient calculations are based on FIR optical half-band filters [21]. The FSR of the individual MZIs in a building block is inversely proportional to the delay length and is given by Eq. 3.5.

The demux is divided into two stages, and each stage consists of two cascaded MZI blocks (schematic in Fig. 3.15). The first block is designed as an interleaver, and splits the odd and even wavelength channels. Outputs are then sent to a second block that enhances the suppression of unwanted wavelengths. The first stage is centered in the O-band (i.e. at 1301 nm), and each MZI at this stage is designed for an FSR of 40 nm. The second stage is designed in a similar fashion as the first

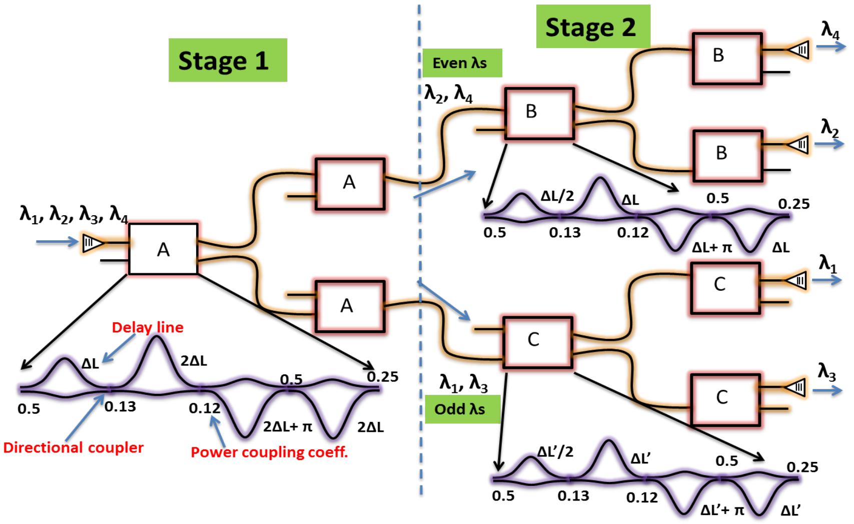

Figure 3.15: Schematic of the cascaded dual stage cascaded MZI de-multiplexing filter. Stage 1 constitutes the tree-like structure of block A. Similar structures in stage 2 carry even and odd wavelengths. Each block is a set of four cascaded MZIs. Cascaded MZI parameters: path length difference ΔL, directional coupler and power coupling coefficients K are shown.

stage, but with an FSR of 80 nm and therefore the designed delay ΔL is half that of the first stage. The 2 second stage filters split the 2×2 interleaved wavelength channels into four separate waveguides.

The design of each stage is tuned to the respective channels, using the properties of the waveguide and directional couplers for that wavelength. As shown in Fig. 3.15, the first stage must support all four wavelengths, and therefore its building block (A in this case) is targeted to the center of the entire band, i.e.

$$\lambda_A = \frac{\lambda_1 + \lambda_2 + \lambda_3 + \lambda_4}{4} \tag{3.7}$$

Here, $\lambda_A = 1301$ nm is the center wavelength and $\lambda_1, \lambda_2, \lambda_3, \lambda_4$ are the ITU grid wavelengths i.e. 1271 nm, 1291 nm, 1311 nm and 1331 nm respectively.

For stage 2-top (B blocks) and 2-bottom (C blocks), the wavelengths are split in even and odd channels. These stages are designed on the center of these wavelengths which are given by:

$$\lambda_B = \lambda_3 = \frac{\lambda_2 + \lambda_4}{2} \tag{3.8}$$

$$\lambda_C = \lambda_2 = \frac{\lambda_1 + \lambda_3}{2} \tag{3.9}$$

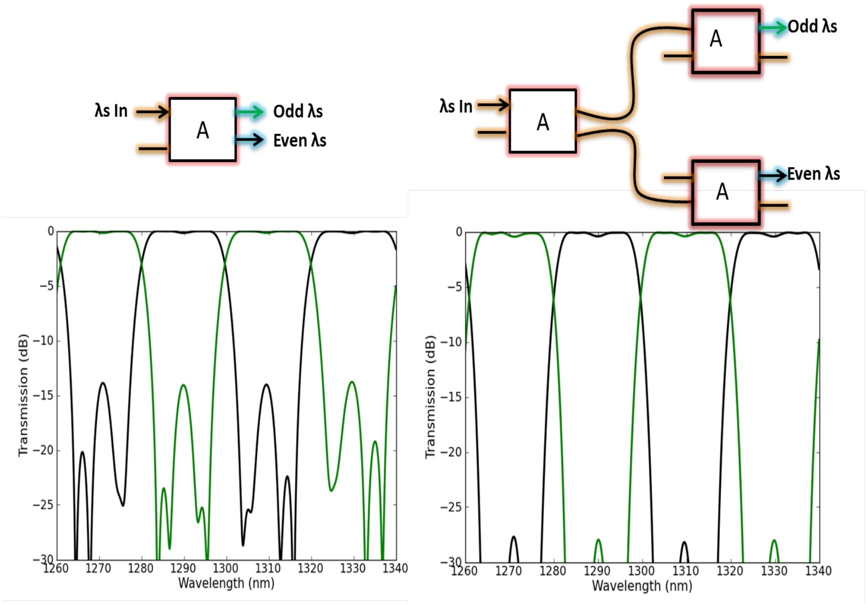

Figure 3.16: Simulation of (a) the individual block splitting odd and even wavelengths and, (b) Tree-like structure showing the improved channels suppression and band flatness.

Here, $\lambda_B = 1311$ nm and $\lambda_C = 1291$ nm which are equivalent to λ_3 and λ_2 respectively.

The coupling coefficients are designed to be the same for all stages, but the center wavelengths are tuned for each individual stage. Physically this means that the directional couplers (DC) are adjusted by changing the coupling length with a fixed gap. The π phase shift in the building block is given by:

$$L_\pi = \frac{\lambda_c}{2.n_{eff}} \tag{3.10}$$

where n_{eff} is the waveguide's effective index of the waveguide at λ_c .

In order to adjust the center wavelengths of output channels, similar calculations are performed to provide the phase shift of $\pi/2$ or one-fourth of FSR in the C-block in design. As shown in Fig. 3.15, the $\Delta L'$ is then given by :

$$\Delta L' = \Delta L + \frac{\lambda_c}{4.n_{eff}} \tag{3.11}$$

The device design layout is done in the IPKISS parametric design framework from Luceda photonics [31]. The device is designed for TE polarized light with oxide as the top cladding. To ensure single mode operation over the O-band, the

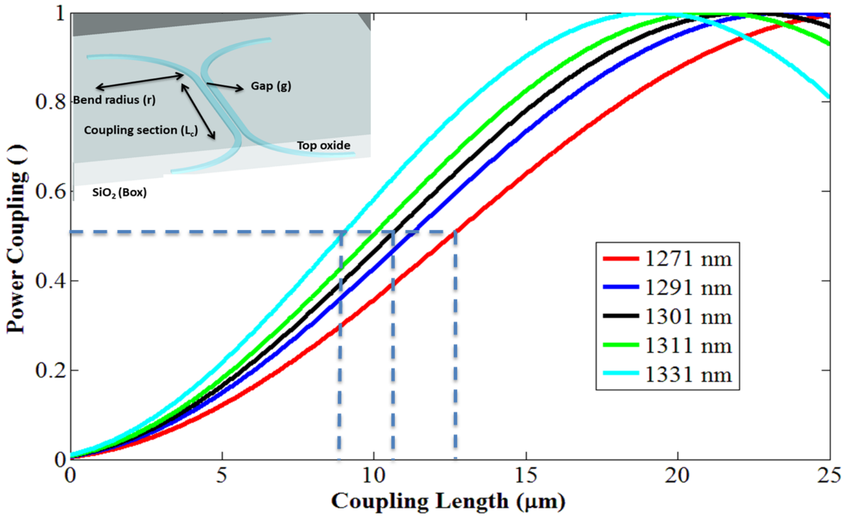

Figure 3.17: Full wave simulation of the power coupling with coupling length of directional couplers at their respective center wavelengths and at ITU grid. Dotted lines show 50 % coupling at 1271 nm, 1301 nm and 1331 nm wavelengths. Inset: directional coupler sketch showing the straight, bend section and gap.

delay lines are fabricated with 380 nm wide waveguides and 215 nm thick silicon. The same widths are used in the directional couplers, with a gap of 150 nm.

The waveguide and directional coupler simulations are performed in a *finite element method* (FEM) solver. Full device simulations are performed in circuit simulator Caphe from Luceda Photonics [51] taking waveguide dispersion and wavelength dependence of the directional couplers into account. The coupling contributions from the waveguide bends are also taken into account. The bend radius is kept as 5 μm in the DCs and the same in the delay lines to make the device footprint small while at the same time not incurring excessive bend losses.

The simulated transmission of individual block A and Stage 1 is shown in Fig. 3.16. The simulation clearly shows cascading the stages significantly improves the band flatness and channel suppression of drop channels.

The full wave simulation of the directional couplers showing the power coupling with coupling length (L_c) at designed wavelengths is shown in Fig. 3.17. It can be seen that for a given power coupling (k) at different ITU grid wavelengths, the (L_c) varies in a significant amount. For example, for 50 % coupling the (L_c) changes from 8 to 12.5 μm for wavelength variation of 60 nm i.e from 1331 to 1291 nm. The gap is fixed and bend radius is kept constant throughout.

The full demux device simulation is shown in Fig. 3.18. The simulated transmission of the demux shows a 20 nm of channel spacing with center wavelength

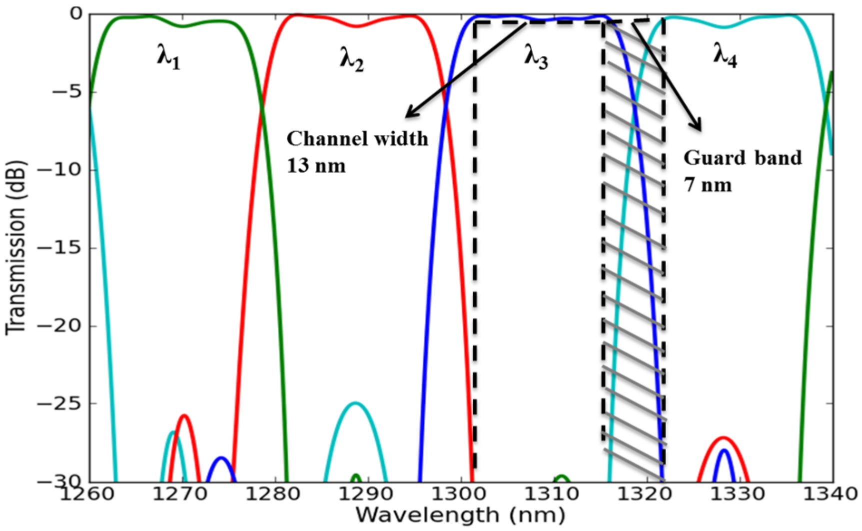

Figure 3.18: Simulated transmission of the demux filter showing the channel width and guard band according to [50].

at 1301 nm. The simulated cross-talk is around -25 dB and the insertion loss is around 1 dB. The pass band channel width and guard band are 13 nm and 7 nm respectively which matches with specifications of the ITU [50].

3.10 Fabrication

The fabrication of the device is briefly discussed in section 3.4.2. The details of this process have been discussed in chapter 2. The grating coupler uses the same 70 nm etch process but the periods are set in such a way as the efficiency of the coupling of light to the chip is maximum at the O-band.

The camera image of fabricated single block, demultiplexer and the SEM image of one of DCs are shown in Fig. 3.19. The length of the DCs for 50 $\%$ of power coupling at 1301 nm is around 10.3 μm. The total footprint of the device is $550 \times 650 \mu m^2$. This can be further reduced by folding the stages.

3.11 Measurements and Analysis

3.11.1 Device measurements

The transmission measurements of the device are performed with a continuous-wave O-band tunable laser. First, the reference waveguide sitting beside the demux filter is aligned at ITU grid wavelengths and then the corresponding channels

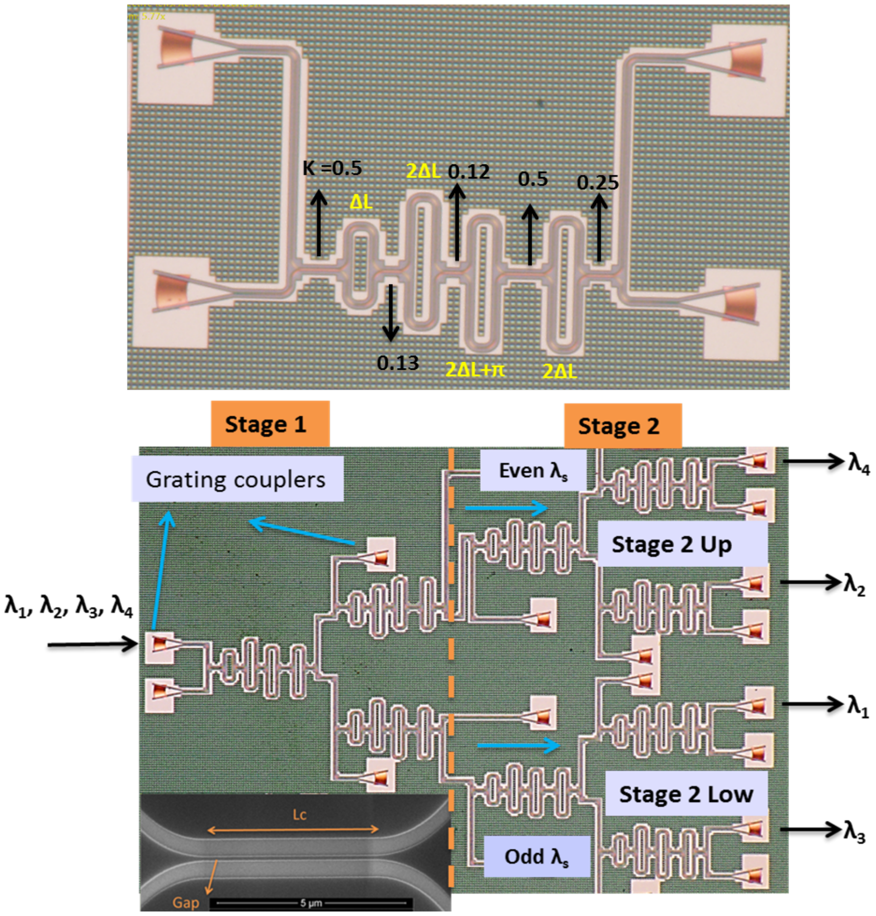

Figure 3.19: Camera image of fabricated single block and 4-channel dual stage cascaded MZI demultiplexing filter (Inset: SEM image of one of the directional coupler showing gap and coupling length).

of the filter are measured. The measured waveguide loss at 1310 nm is 3 dB/cm. The alignment waveguide at the ITU grid wavelengths is shown in Fig. 3.20. The spectral response of the fiber grating coupler at the input and output of filter is normalized out of the measured spectrum using a reference waveguide in order to analyze the filter response. The normalized spectrum of the demux is shown in Fig. 3.21. The channel spacing (CS) matches well with the 20 nm specifications; the ITU wavelengths are indicated by a dashed line. The measured 1 dB channel bandwidth of all channels is more than 12 nm, or over 60 % of the channel spacing. This band flatness helps in handling the temperature changes of 100 °C at the transmitter and receiver side. On-chip device insertion loss (IL) is calculated by

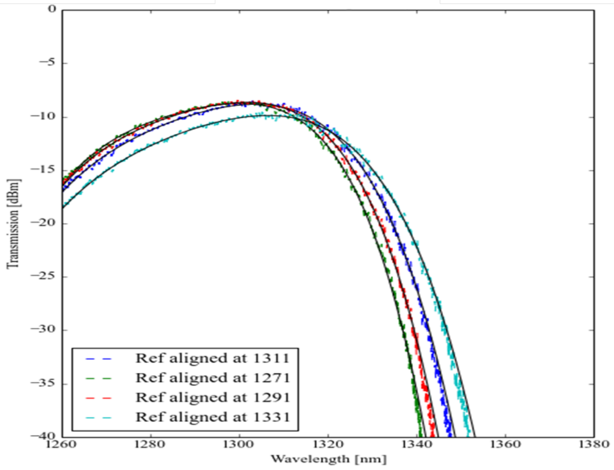

Figure 3.20: Reference waveguide at ITU grids

normalizing the spectrum to that of a reference grating coupler. The IL for all channels is better than 4dB.

The channel cross talk is calculated using 13 nm bandwidth as analysis window and then adding all the power contribution from other neighboring channels in that analysis window. From Fig. 3.21, one can find that channels 1, 2 and 3 are performing with a very low XT values i.e. below -20 dB. Channel 4 is the worst performing with XT below -15.7 dB. We attribute this increasing XT towards longer wavelengths to the strong wavelength dependence of the directional couplers, which have been insufficiently corrected in the design. More tolerant directional couplers for a wider wavelength band can certainly improve the performance [52]. The 3, 10 and 20 dB bandwidth of channel 2 is respectively 17.2 nm, 20.6 nm and 23.2 nm.

Also from Fig. 3.21, one can find that the actual XT varies considerably within the 13 nm window of each pass band. This can be visualized by grey dashed lines in Fig. 3.21. Within this window, the XT in channel 3 rises from -21.2 dB evaluated at ITU grid to -15 dB at slightly longer wavelengths. This is possibly due to accumulated phase errors. This effect can be reduced by using wider waveguide sections in the delay lines. On the other hand, this requires tapered transition from the single mode to the multimode section, which increases the overall size of device. Phase errors and IL of the device can certainly be improved by improved process technology, e.g. by migrating from a 200 mm to a 300 mm processing line [53].

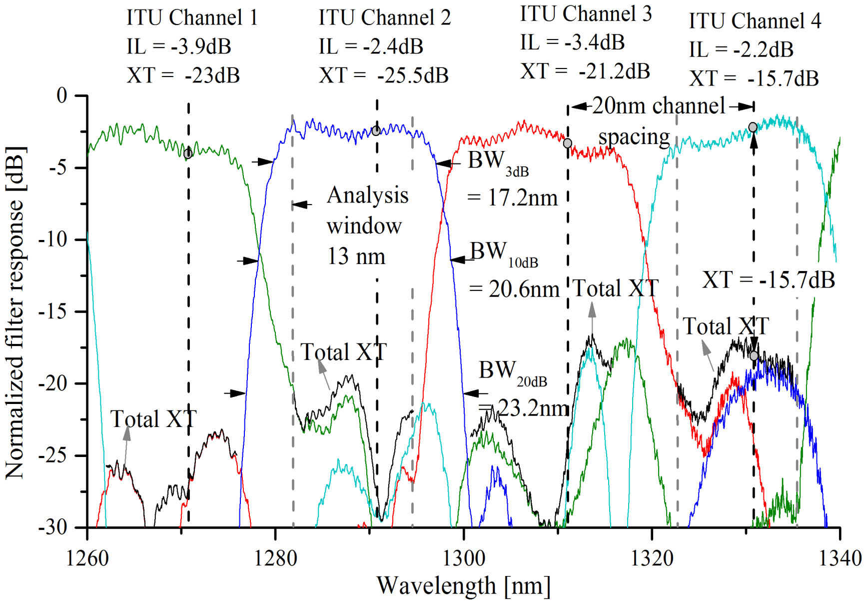

Figure 3.21: Normalized measured transmission of the demux filter showing channel spacing (CS), insertion loss (IL) and crosstalk (XT) at ITU grid wavelengths.

Wafer scale performance			
Parameter	Mean	Std Dev	N
Mean IL ITU [dB]	-3.015	0.4820	22
Mean XT ITU [dB]	-18.7282	2.442985	22
Center Wavelength [nm]	1306	1.77	22
Channel Spacing [nm]	20.35	0.08	22

Table 3.2: Wafer scale performance of the demux.

3.11.2 Wafer scale measurements

Our filter has been characterized at 22 positions over a 200 mm wafer. The device-mean IL and XT performance evaluated at ITU grid is used as performance metric and its distribution and contour plots are shown in Fig. 3.22.

The device-mean IL and XT over the wafer, evaluated at ITU grid, is -3.01 dB and -18.7 dB with a standard deviation of 0.48 dB and 2.4 dB respectively. The wafer scale performance is shown in table 3.2.

The center wavelength of each channel is determined by the center of 10 dB bandwidth wavelengths as indicated with arrows in Fig. 3.21. The center wavelength of the third channel around 1311 nm is tracked over the wafer as shown in Fig. 3.23 which can be understood as an effect of the varying mean n_{eff} the light

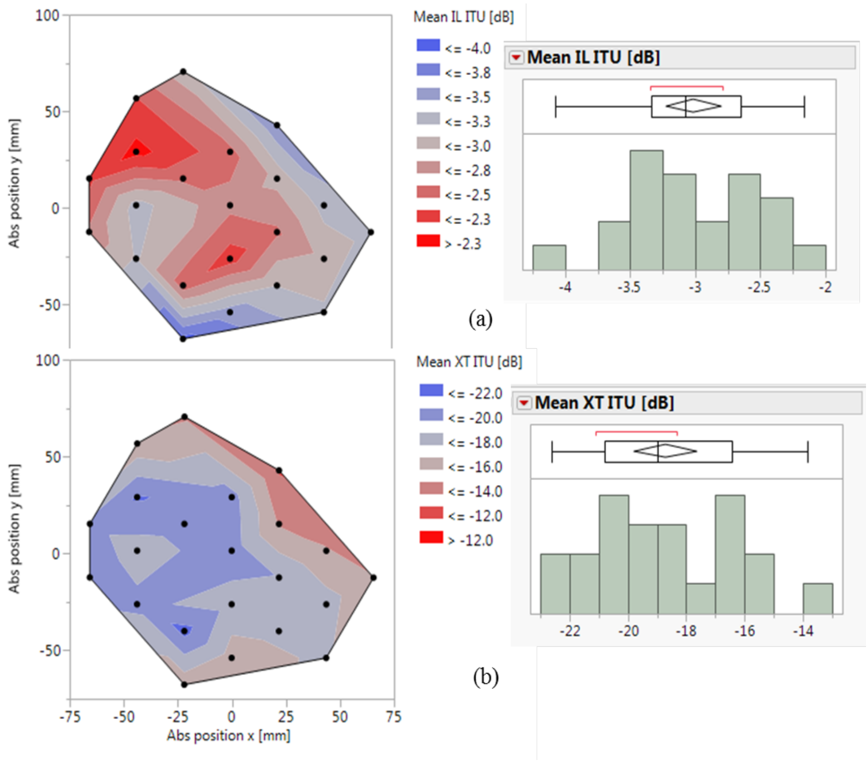

Figure 3.22: Wafer scale distribution and contour plots showing mean IL and XT at ITU grids.

experiences coming from small dimensional waveguide variation. On the average, the center wavelength of the channel is at 1306 nm with a within-wafer standard deviation of 1.77 nm. The first channel around 1271 nm is only partly registered due to the limited range of the used O-band laser. The channel spacing is, therefore, determined by the center wavelengths of the remaining three channels. On the average, the channel spacing is 20.3 nm with a tight within-wafer standard deviation of 0.085 nm. Tweaking the underlying waveguide model based on experimental data could pre-compensate the mean value of both the absolute center wavelength and channel spacing. The wafer scale performance of the channel centers is also listed in table 3.2.

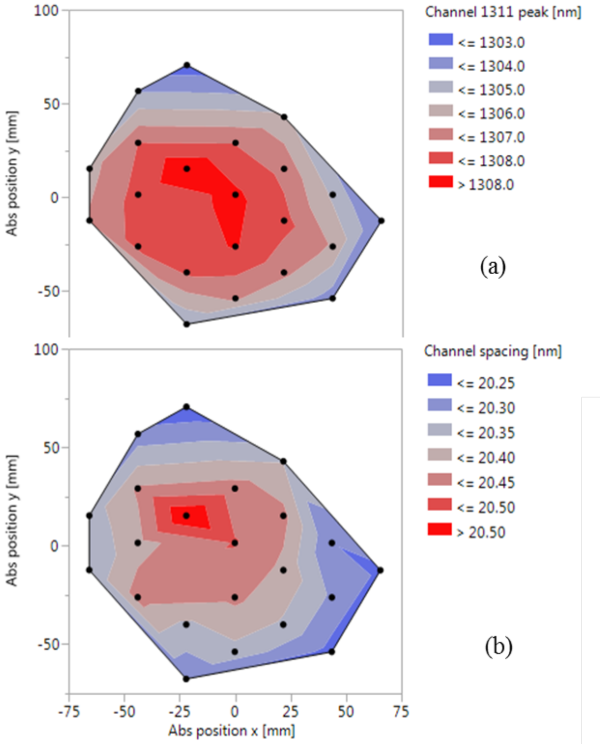

Figure 3.23: Wafer scale contour plots showing (a) the center wavelength of channel 3 around 1311 nm and (b) the channel spacing over the wafer.

3.11.3 Thermal simulation and measurements

The wavelength sensitivity of any filtering device with temperature is given by [11, 54]:

$$\frac{d\lambda}{dT} = \frac{\lambda_c}{n_g(T)}\frac{dn_{eff}}{dT} \tag{3.12}$$

Here T is the temperature, $\frac{dn_{eff}}{dT}$ is the thermo-optic coefficient (TO) of the waveguide and λ_c is the operating wavelength. The simulated shifts for the demux filter in the O-band is around 70 pm/K. The simulated spectral shift for $20\,^\circ$C, $60\,^\circ$C and $170\,^\circ$C are shown in Fig. 3.24.

For thermal measurements of the demux filter, we have placed the fabricated chip on a thermally controlled stage with a resistive heater and a temperature sensor. All four channels are aligned at ITU grid and the temperature is varied from $10\,^\circ$C to $60\,^\circ$C, which is the limit of our test setup. All the channels are red shifted but still within the 1 dB bandwidth line. The $50\,^\circ$C variation corresponds to 4 nm

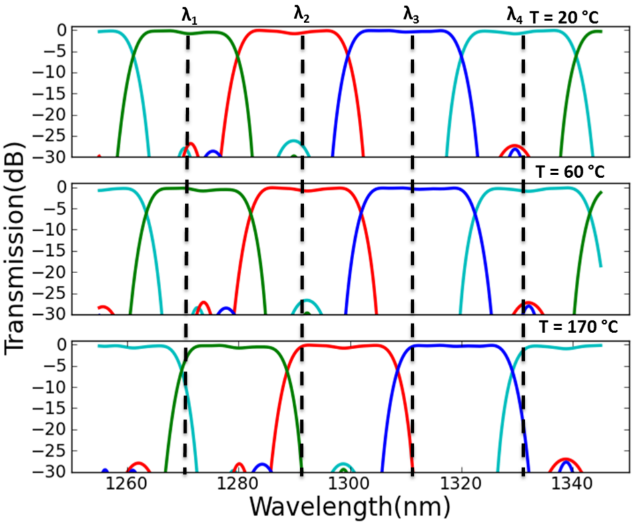

Figure 3.24: Simulated spectral shift at 20 °C, 60 °C *and* 170 °C.

of wavelength shift. Since the channel bandwidth is close to 13 nm which corresponds to ±6.5 nm on either side of the center wavelength, we extrapolate that the demux is thermally robust up to ±85 °C.

3.11.4 Performance estimation of CWDM demultiplexer using system simulation

Because it was not possible, within the time frame of the PhD, to package and test the fabricated CWDM demultiplexer in a system, the performance is estimated by using the emulation environment of VPI TransmissionMaker version 9.3. A block level representation of the emulation setup is shown in Fig. 3.26.

It comprises an ideal 112 Gbps transmitter with 4 channels. For each channel, the CW laser is modulated at 28 Gbps using *on-off keying* (OOK) by a Mach-Zehnder modulator. The four channels are 20 nm apart and are operating at 1271 nm, 1291 nm, 1311 nm and 1331 nm respectively. A sequence of 2^{13} pseudo random bits is transmitted by each channel of the CWDM transmitter. After ideal multiplexing of the four channels, the de-multiplexing is performed using the measurement results shown in Fig. 3.21. The de-multiplexed signal is then fed to the four ideal OOK receivers for detection. Fig. 3.27 shows the open eye diagram for channel 2 after 2 km of single mode fiber (SMF) and the performance is similar for all other three channels.

Furthermore, the power penalty of the fabricated filter is estimated by comparing the *bit error rate* (BER) vs input power of the *continuous wave* (CW) laser for

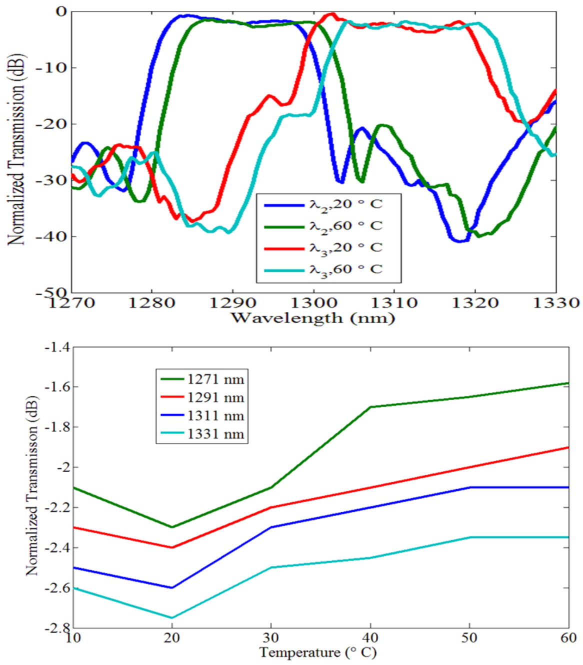

Figure 3.25: a) Measured spectral shift of two center channels at 20 °C *and* 60 °C *and b) insertion loss or the normalized transmission with respect to reference waveguide showing the channel pass-bands with increasing temperature. The fact that all the channels are within the 1 dB BW demonstrates the thermal tolerance of de-mux filter*

the simulated and fabricated filters. The dotted and solid lines in Fig. 3.28 show the BER vs. input CW power for the designed and fabricated filter. The small variation in the BER vs. input power for the designed filter originates from the different transmission response of the four channels of the filter due to the wavelength dependence in the designed filter. For the fabricated filter, channel 2 shows the lowest penalty while channel 4 shows the highest penalty due to its degraded crosstalk of only -15.7 dB.

In order to verify the thermal tolerant behavior of the filter, the BER vs input power for Channel 2 is determined at four different temperatures of 20 °C, 70 °C, 120 °C and 170 °C respectively. Due to very high transmission uniformity of 1dB in the flat top region of the filter, almost no additional power penalty is introduced. A comparable trend is observed for other channels as well. For channel 2, the channel detuning versus BER is plotted to observe the tolerant behavior of the demux if there is thermal drift and laser drift together. In the case of on chip III-V integrated laser the nominal shift is 0.1 nm/K [55].

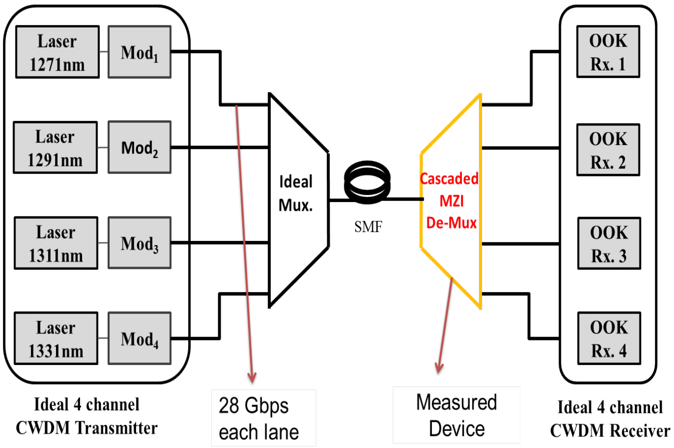

Figure 3.26: Simulation setup to determine the system evaluation of demultiplexer

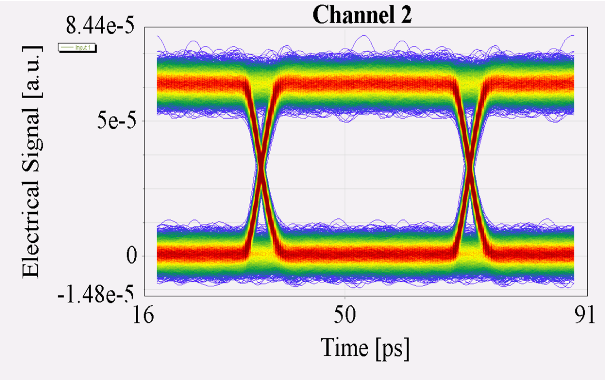

Figure 3.27: Simulated eye diagram of channel 2 with input power of 0 dBm and 2 km of single mode fiber

3.12 Conclusion and Discussion

In this chapter, we have presented a systematic study of the silicon photonic wavelength filters. We compare the performances of FIR filters, such as *arrayed waveguide gratings* (AWG), *echelle gratings* (also called *planar concave gratings* or PCG) and *cascaded Mach-Zehnder* filters. We have discussed their operating principles, design criteria and different performance metrics (e.g. insertion loss and cross talk). We have found that for the low loss CWDM applications, cascaded MZIs filters are the best choice because their low insertion loss and engineered pass band.

Then we have demonstrated a silicon-on-insulator four-channel demux filter

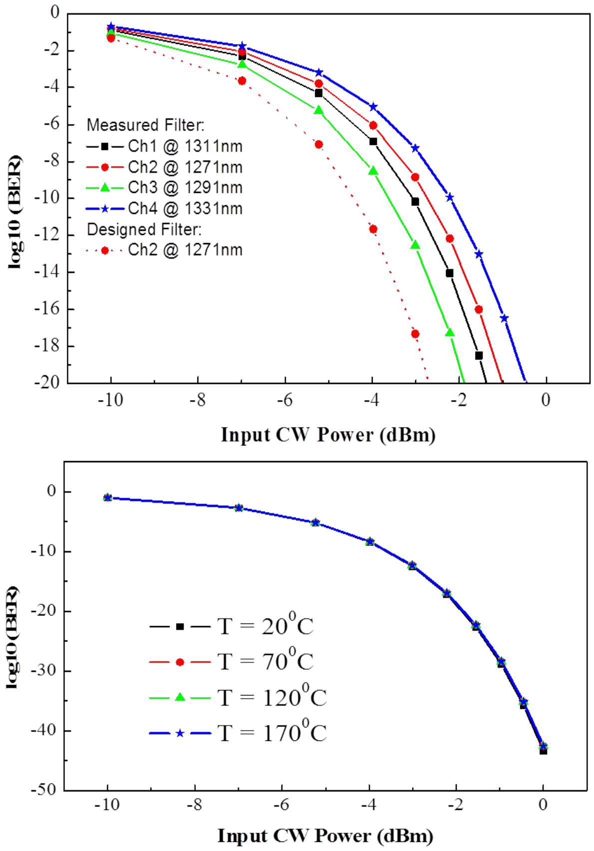

Figure 3.28: Simulated BER of 4 CWDM channels with different input power of the CW laser.

with 20 nm channel spacing designed to match the CWDM ITU grid in the O-band. The measured band-flatness of the demux is more than 60 % of the channel spacing and the mean IL and XT is below 3 dB and -18 dB respectively.

This wide band flatness makes the demux filter thermally robust in nature. This will enable the direct usage of uncooled laser and avoid thermal control, which results in turn whole lead to a low power and low cost solution for a CWDM transceiver. System emulation based on the measured demux filter characteristic shows that it is a possible candidate for 100 GbE and future 400 GbE applications.

The comparison of different CWDM on SOI technology is shown in the table 3.3.

As shown in the table 3.3 only the Intel [47] has been able demonstrate the device in the 12.5 Gbps link, but we do not have much information about it. The

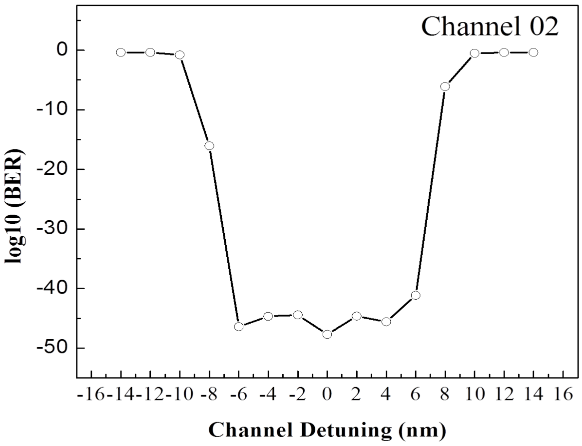

Figure 3.29: Simulated BER of channel 2 with channel de-tuning.

Reference	Device/Technology	IL(dB)/ XT (dB)	BW (1dB)	Footprint
Kotura [56]	Echelle Gratings\ e-beam	2.5 /-22	13nm	9×5 mm^2
Intel [47]	Echelle Gratings\ e-beam	-	-	-
UBC [49]	Contra-directional couplers (C-band) e-beam	2.5 /-15	13 nm	1200 μm^2
UGhent-Imec	Cascaded MZIs\ 193 nm Optical	3/-15	13 nm	550×650 μm^2

Table 3.3: CWDM comparison, IL: Insertion loss, XT: Crosstalk

shown de-mux response is not flat band in this case hence, an external thermal control is required to stabilize it. If we compare with demonstration from Kotura [56], the insertion loss and crosstalk was better than our device. However, the device was fabricated with thicker silicon waveguides as a result of that their footprint is 1000 times bigger compared to our demonstration. If we compare the demonstration from UBC [49] then we find that their performance is comparable to ours but, it is not easily mass producible due to the feature size of their contra-directional couplers.

As we have seen only flat band is not enough to provide the complete robustness to the SOI wavelength filter. So, we need to have compensation technique which is low power and aligned with standard CMOS fabrication process, and allows a compensation on both transmitter and receiver side as their temperature can change independently without affecting the link performance.

References

[1] *G.695: Optical interfaces for coarse wavelength division multiplexing applications* . `https://www.itu.int/rec/T-REC-G.695-201501-I/`. [Online].

[2] D.A.B. Miller. *Device Requirements for Optical Interconnects to Silicon Chips*. Proceedings of the IEEE, 97(7):1166–1185, July 2009.

[3] Y.A. Vlasov. *Silicon CMOS-integrated nano-photonics for computer and data communications beyond 100G*. Communications Magazine, IEEE, 50(2):s67–s72, February 2012.

[4] W. Bogaerts, S.K. Selvaraja, P. Dumon, J. Brouckaert, K. De Vos, D. Van Thourhout, and R Baets. *Silicon-on-Insulator Spectral Filters Fabricated With CMOS Technology*. Selected Topics in Quantum Electronics, IEEE Journal of, 16(1):33–44, Jan 2010.

[5] K. Okamoto. *Wavelength-Division-Multiplexing Devices in Thin SOI: Advances and Prospects*. Selected Topics in Quantum Electronics, IEEE Journal of, 20(4):248–257, July 2014.

[6] W. Bogaerts, P. De Heyn, T. Van Vaerenbergh, K. De Vos, S. Kumar Selvaraja, T. Claes, P. Dumon, P. Bienstman, D. Van Thourhout, and R. Baets. *Silicon microring resonators*. Laser Photonics Reviews, 6(1):47–73, 2012.

[7] Wim Bogaerts, Shibnath Pathak, Alfonso Ruocco, and Sarvagya Dwivedi. *Silicon photonics non-resonant wavelength filters: comparison between AWGs, echelle gratings, and cascaded Mach-Zehnder filters*. volume 9365, pages 93650H–93650H–12. SPIE, April 2015.

[8] Christi K. Madsen and Jian H. Zhao. *Optical Filter Design and Analysis*, pages 1–17. John Wiley Sons, Inc., 2001.

[9] Eric Dulkeith, Fengnian Xia, Laurent Schares, William M. J. Green, and Yurii A. Vlasov. *Group index and group velocity dispersion in silicon-on-insulator photonic wires*. Opt. Express, 14(9):3853–3863, May 2006.

[10] T. Goh, S. Suzuki, and A. Sugita. *Estimation of waveguide phase error in silica-based waveguides*. Lightwave Technology, Journal of, 15(11):2107–2113, Nov 1997.

[11] S. Dwivedi, H. D'heer, and W. Bogaerts. *Maximizing Fabrication and Thermal Tolerances of All-Silicon FIR Wavelength Filters*. Photonics Technology Letters, IEEE, 27(8):871–874, April 2015.

[12] S.K. Selvaraja, W. Bogaerts, P. Dumon, D. Van Thourhout, and R. Baets. *Subnanometer Linewidth Uniformity in Silicon Nanophotonic Waveguide Devices Using CMOS Fabrication Technology*. Selected Topics in Quantum Electronics, IEEE Journal of, 16(1):316–324, Jan 2010.

[13] F. Gan, T. Barwicz, M.A. Popovic, M.S. Dahlem, C.W. Holzwarth, P.T. Rakich, H.I. Smith, E.P. Ippen, and F.X. Kartner. *Maximizing the Thermo-Optic Tuning Range of Silicon Photonic Structures*. In Photonics in Switching, 2007, pages 67–68, Aug 2007.

[14] Joris Van Campenhout, William M. J. Green, Solomon Assefa, and Yurii A. Vlasov. *Integrated NiSi waveguide heaters for CMOS-compatible silicon thermo-optic devices*. Opt. Lett., 35(7):1013–1015, Apr 2010.

[15] Po Dong, Wei Qian, Hong Liang, Roshanak Shafiiha, Dazeng Feng, Guoliang Li, John E. Cunningham, Ashok V. Krishnamoorthy, and Mehdi Asghari. *Thermally tunable silicon racetrack resonators with ultralow tuning power*. Opt. Express, 18(19):20298–20304, Sep 2010.

[16] A. Masood, M. Pantouvaki, G. Lepage, P. Verheyen, J. Van Campenhout, P. Absil, D. Van Thourhout, and W. Bogaerts. *Comparison of heater architectures for thermal control of silicon photonic circuits*. In Group IV Photonics (GFP), 2013 IEEE 10th International Conference on, pages 83–84, Aug 2013.

[17] Qianfan Xu, Sasikanth Manipatruni, Brad Schmidt, Jagat Shakya, and Michal Lipson. *12.5 Gbit/s carrier-injection-based silicon micro-ring silicon modulators*. Opt. Express, 15(2):430–436, Jan 2007.

[18] F. Y. Gardes, D. J. Thomson, N. G. Emerson, and G. T. Reed. *40 Gb/s silicon photonics modulator for TE and TM polarisations*. Opt. Express, 19(12):11804–11814, Jun 2011.

[19] L. Alloatti, D. Korn, R. Palmer, D. Hillerkuss, J. Li, A. Barklund, R. Dinu, J. Wieland, M. Fournier, J. Fedeli, H. Yu, W. Bogaerts, P. Dumon, R. Baets, C. Koos, W. Freude, and J. Leuthold. *42.7 Gbit/s electro-optic modulator in silicon technology*. Opt. Express, 19(12):11841–11851, Jun 2011.

[20] Hui Yu, M. Pantouvaki, S. Dwivedi, P. Verheyen, G. Lepage, R. Baets, W. Bogaerts, P. Absil, and J. Van Campenhout. *Compact Thermally Tunable Silicon Racetrack Modulators Based on an Asymmetric Waveguide*. Photonics Technology Letters, IEEE, 25(2):159–162, Jan 2013.

[21] K. Jinguji and Manabu Oguma. *Optical half-band filters*. Lightwave Technology, Journal of, 18(2):252–259, Feb 2000.

[22] J.H. McClellan, T.W. Parks, and L. Rabiner. *A computer program for designing optimum FIR linear phase digital filters*. Audio and Electroacoustics, IEEE Transactions on, 21(6):506–526, Dec 1973.

[23] M. Kawachi. *Recent progress in silica-based planar lightwave circuits on silicon*. Optoelectronics, IEE Proceedings -, 143(5):257–262, Oct 1996.

[24] A. Kaneko, T. Goh, H. Yamada, T. Tanaka, and I. Ogawa. *Design and applications of silica-based planar lightwave circuits*. Selected Topics in Quantum Electronics, IEEE Journal of, 5(5):1227–1236, Sep 1999.

[25] Qian Wang and Sailing He. *Optimal design of planar wavelength circuits based on Mach-Zehnder Interferometers and their cascaded forms*. Lightwave Technology, Journal of, 23(3):1284–1290, March 2005.

[26] T. Mizuno, M. Oguma, T. Kitoh, Y. Inoue, and H. Takahashi. *Lattice-form CWDM interleave filter using silica-based planar lightwave circuit*. Photonics Technology Letters, IEEE, 18(15):1570–1572, Aug 2006.

[27] Koji Yamada, Tetsufumi Shoji, Tai Tsuchizawa, Toshifumi Watanabe, Jun ichi Takahashi, and Sei ichi Itabashi. *Silicon-wire-based ultrasmall lattice filters with wide free spectral ranges*. Opt. Lett., 28(18):1663–1664, Sep 2003.

[28] Pieter Dumon, Gino Priem, Luis Romeu Nunes, Wim Bogaerts, Dries Van Thourhout, Peter Bienstman, Tak Keung Liang, Masahiro Tsuchiya, Patrick Jaenen, Stephan Beckx, Johan Wouters, and Roel Baets. *Linear and Nonlinear Nanophotonic Devices Based on Silicon-on-Insulator Wire Waveguides*. Japanese Journal of Applied Physics, 45(8S):6589, 2006.

[29] S.S. Djordjevic, L.W. Luo, S. Ibrahim, N.K. Fontaine, C.B. Poitras, Binbin Guan, L. Zhou, K. Okamoto, Zhi Ding, M. Lipson, and S.J.B. Yoo. *Fully Reconfigurable Silicon Photonic Lattice Filters With Four Cascaded Unit Cells*. Photonics Technology Letters, IEEE, 23(1):42–44, Jan 2011.

[30] Folkert Horst, William M.J. Green, Solomon Assefa, Steven M. Shank, Yurii A. Vlasov, and Bert Jan Offrein. *Cascaded Mach-Zehnder wavelength filters in silicon photonics for low loss and flat pass-band WDM (de-)multiplexing*. Opt. Express, 21(10):11652–11658, May 2013.

[31] `http://www.lucedaphotonics.com/`.

[32] Philippe P. Absil, Peter Verheyen, Peter De Heyn, Marianna Pantouvaki, Guy Lepage, Jeroen De Coster, and Joris Van Campenhout. *Silicon photonics integrated circuits: a manufacturing platform for high density, low power optical I/O's*. Opt. Express, 23(7):9369–9378, Apr 2015.

[33] S. Pathak, M. Vanslembrouck, P. Dumon, D. Van Thourhout, and W. Bogaerts. *Optimized Silicon AWG With Flattened Spectral Response Using an MMI Aperture*. Lightwave Technology, Journal of, 31(1):87–93, Jan 2013.

[34] J.B.D. Soole, M.R. Amersfoort, H.P. Leblanc, N.C. Andreadakis, A. Rajhel, C. Caneau, R. Bhat, M.A. Koza, C. Youtsey, and I. Adesida. *Use of multimode interference couplers to broaden the passband of wavelength-dispersive integrated WDM filters*. Photonics Technology Letters, IEEE, 8(10):1340–1342, Oct 1996.

[35] Daoxin Dai, Weiquan Mei, and Sailing He. *Using a tapered {MMI} to flatten the passband of an {AWG}*. Optics Communications, 219(16):233 – 239, 2003.

[36] Shibnath Pathak. Silicon Nano-Photonics Based Arrayed Waveguide Gratings, PhD thesis, Ghent University, 2014.

[37] `http://www.photond.com/`.

[38] urlhttp://camfr.sourceforge.net/.

[39] M.K. Smit and C. Van Dam. *PHASAR-based WDM-devices: Principles, design and applications*. Selected Topics in Quantum Electronics, IEEE Journal of, 2(2):236–250, Jun 1996.

[40] J. Brouckaert, W. Bogaerts, P. Dumon, D. Van Thourhout, and R. Baets. *Planar Concave Grating Demultiplexer Fabricated on a Nanophotonic Silicon-on-Insulator Platform*. Lightwave Technology, Journal of, 25(5):1269–1275, May 2007.

[41] J. Brouckaert, W. Bogaerts, S. Selvaraja, P. Dumon, R. Baets, and D. Van Thourhout. *Planar Concave Grating Demultiplexer With High Reflective Bragg Reflector Facets*. Photonics Technology Letters, IEEE, 20(4):309–311, Feb 2008.

[42] S. Pathak, P. Dumon, D. Van Thourhout, and W. Bogaerts. *Comparison of AWGs and Echelle Gratings for Wavelength Division Multiplexing on Silicon-on-Insulator*. Photonics Journal, IEEE, 6(5):1–9, Oct 2014.

[43] *G.694.1 : Spectral grids for WDM applications: DWDM frequency grid* . `http://www.itu.int/rec/T-REC-G.694.1-201202-I/`. [Online].

[44] A.V. Krishnamoorthy, H. Schwetman, X. Zheng, and R. Ho. *Energy-Efficient Photonics in Future High-Connectivity Computing Systems*. Lightwave Technology, Journal of, 33(4):889–900, Feb 2015.

[45] C. Sciancalepore, R.J. Lycett, J.A. Dallery, S. Pauliac, K. Hassan, J. Harduin, H. Duprez, U. Weidenmueller, D.F.G. Gallagher, S. Menezo, and B. Ben Bakir. *Low-Crosstalk Fabrication-Insensitive Echelle Grating Demultiplexers on Silicon-on-Insulator*. Photonics Technology Letters, IEEE, 27(5):494–497, March 2015.

[46] P. De Heyn, J. De Coster, P. Verheyen, G. Lepage, M. Pantouvaki, P. Absil, W. Bogaerts, J. Van Campenhout, and D. Van Thourhout. *Fabrication-Tolerant Four-Channel Wavelength-Division-Multiplexing Filter Based on Collectively Tuned Si Microrings*. Lightwave Technology, Journal of, 31(16):2785–2792, Aug 2013.

[47] Andrew Alduino, Ling Liao, Richard Jones, Michael Morse, Brian Kim, Wei-Zen Lo, Juthika Basak, Brian Koch, Hai-Feng Liu, Haisheng Rong, Matthew Sysak, Christine Krause, Rushdy Saba, Dror Lazar, Lior Horwitz, Roi Bar, Stas Litski, Ansheng Liu, Kevin Sullivan, Olufemi Dosunmu, Neil Na, Tao Yin, Frederick Haubensack, I wei Hsieh, John Heck, Robert Beatty, Hyundai Park, Jock Bovington, Simon Lee, Hat Nguyen, Hinmeng Au, Katie Nguyen, Priya Merani, Mahtab Hakami, and Mario Paniccia. *Demonstration of a High Speed 4-Channel Integrated Silicon Photonics WDM Link with Hybrid Silicon Lasers*. In Integrated Photonics Research, Silicon and Nanophotonics and Photonics in Switching, page PDIWI5. Optical Society of America, 2010.

[48] J. Brouckaert, G. Roelkens, S.K. Selvaraja, W. Bogaerts, P. Dumon, S. Verstuyft, D. Van Thourhout, and R. Baets. *Silicon-on-Insulator CWDM Power Monitor/Receiver With Integrated Thin-Film InGaAs Photodetectors*. Photonics Technology Letters, IEEE, 21(19):1423–1425, Oct 2009.

[49] Wei Shi, Han Yun, Charlie Lin, Mark Greenberg, Xu Wang, Yun Wang, Sahba Talebi Fard, Jonas Flueckiger, Nicolas A. F. Jaeger, and Lukas Chrostowski. *Ultra-compact, flat-top demultiplexer using anti-reflection contra-directional couplers for CWDM networks on silicon*. Opt. Express, 21(6):6733–6738, Mar 2013.

[50] *IEEE P802.3bm 40Gb/s and 100Gb/s Ethernet Task Force*. `http://www.ieee802.org/3/bm/public/nov12/vlasov_01a_1112_optx.pdf`. [Online].

[51] Martin Fiers, Thomas Van Vaerenbergh, Ken Caluwaerts, Dries Vande Ginste, Benjamin Schrauwen, Joni Dambre, and Peter Bienstman. *Time-domain and frequency-domain modeling of nonlinear optical components at the circuit-level using a node-based approach*. J. Opt. Soc. Am. B, 29(5):896–900, May 2012.

[52] Zeqin Lu et al. *Broadband silicon photonic directional coupler using asymmetric-waveguide based phase control*. Opt. Express, 23(3):3795–3808, Feb 2015.

[53] S.K. Selvaraja, P. De Heyn, G. Winroth, P. Ong, G. Lepage, C. Cailler, A. Rigny, K.K. Bourdelle, W. Bogaerts, D. Van Thourhout, J. Van Campenhout, and P. Absil. *Highly uniform and low-loss passive silicon photonics devices using a 300mm CMOS platform*. In Optical Fiber Communications Conference and Exhibition (OFC), 2014, pages 1–3, March 2014.

[54] Jie Teng, Pieter Dumon, Wim Bogaerts, Hongbo Zhang, Xigao Jian, Xiuyou Han, Mingshan Zhao, Geert Morthier, and Roel Baets. *Athermal Silicon-on-insulator ring resonators byoverlaying a polymer cladding on narrowed-waveguides*. Opt. Express, 17(17):14627–14633, Aug 2009.

[55] Shahram Keyvaninia, Gunther Roelkens, Dries Van Thourhout, Christophe Jany, Marco Lamponi, Alban Le Liepvre, Francois Lelarge, Dalila Make, Guang-Hua Duan, Damien Bordel, and Jean-Marc Fedeli. *Demonstration of a heterogeneously integrated III-V/SOI single wavelength tunable laser*. Opt. Express, 21(3):3784–3792, Feb 2013.

[56] Dazeng Feng, Wei Qian, Hong Liang, Cheng-Chih Kung, J. Fong, B.J. Luff, and M. Asghari. *Novel fabrication tolerant flat-top demultiplexers based on etched diffraction gratings in SOI*. In Group IV Photonics, 2008 5th IEEE International Conference on, pages 386–388, Sept 2008.

4

All-Silicon Athermal Wavelength Filters

In the previous chapter we have seen that we can develop wavelength filters more tolerant to fabrication and temperature variations by flattening the pass band. But due to the high thermo-optic coefficient of silicon these pass bands are still red or blue shifted as the operating temperature fluctuates. In this chapter, we present an all-silicon passive compensation technique to make wavelength filters insensitive to thermal fluctuations by design. We apply this technique to demonstrate different FIR filters like MZIs and AWGs to make them temperature insensitive.

4.1 Introduction

The spectral response of a silicon photonic filter depends on the effective index of the delay line, which is determined by the waveguide geometry and by the temperature, and other less pronounced effects such as stress or irradiation [1]. Any change in these parameters will change the effective index, and as a consequence, the spectral response of the device will shift accordingly. For many applications, drift due to the ambient temperature is the most problematic issue. To compensate for this effect, different techniques have been proposed to make silicon wavelength filters thermally insensitive:

1. The introduction of materials with a negative thermo-optic coefficient as a cladding, such as polymers [2]. In this case a part of the waveguide mode feels the negative thermo-optic material. A temperature change will affect

an opposite shift of polymer cladding and silicon core, balancing out the change in modal effective index. However, such materials are not always easy to incorporate in a CMOS-like process flow. Also, the accurate balance between the materials and the optical confinement is delicate to achieve.

2. Titanium oxide (TiO_2), recently gained attention for being CMOS-like material and with a negative thermo-optic (TO) coefficient [3]. Ring resonator based filters with TiO_2 cladding on top of the waveguide made temperature insensitive by canceling the positive TO of Si with negative TO of TiO_2. Number of demonstrations has been shown e.g. TM polarization based athermal ring resonator [4] and narrow rib waveguide based ring modulators [5]. However, this material is still in testing phase for its CMOS compatibility and integration with Back-end-of-line (BEOL) processes [6, 7].

3. Local heaters can be used to dynamically stabilize the device. This approach consumes power and requires supporting logic [8–11].

Therefore, there is a need for a method which does not required any usage of extra material or active tuning. In this chapter, we propose the method of passive compensation and then demonstrate the technique with a number of devices e.g. MZIs, cascaded MZIs, AWGs.

4.2 Thermal Sensitivity of Silicon Photonic Wavelength Filters

Silicon photonic waveguide components are inherently sensitive to temperature. Temperature can change due to ambient temperature variations, which are generally uniform over the chip. But temperature on the chip can also change locally, due to integrated electronics, lasers, or even due to neighboring active heaters. Both global and local temperature variations can be time-dependent. A consequence of temperature variations is that the spectrum position changes with temperature, as shown in Fig. 4.1. The sensitivity of the spectrum position to temperature for a conventional MZI, AWG is given by:

$$\frac{d\lambda_m}{dT} = \frac{\lambda_m}{n_g}(\alpha.n_{eff} + \frac{dn_{eff}}{dT}) \tag{4.1}$$

where α is the thermal expansion coefficient of the substrate ($\alpha = \frac{1}{L}\frac{dL}{dT}$). The expansion coefficient ($\alpha = 3 \times 10^{-6} K^{-1}$) is two orders of magnitude smaller than the ($TO = 2 \times 10^{-4} K^{-1}$) and will be neglected in the remainder of this work. However, all the techniques used in this chapter could also be extended to include the effect of substrate expansion.

As can be seen in Fig. 4.2, a conventional MZI, AWG, and ring resonator with the TE polarization, has a temperature sensitivity of $75pm/K$ for a core width of

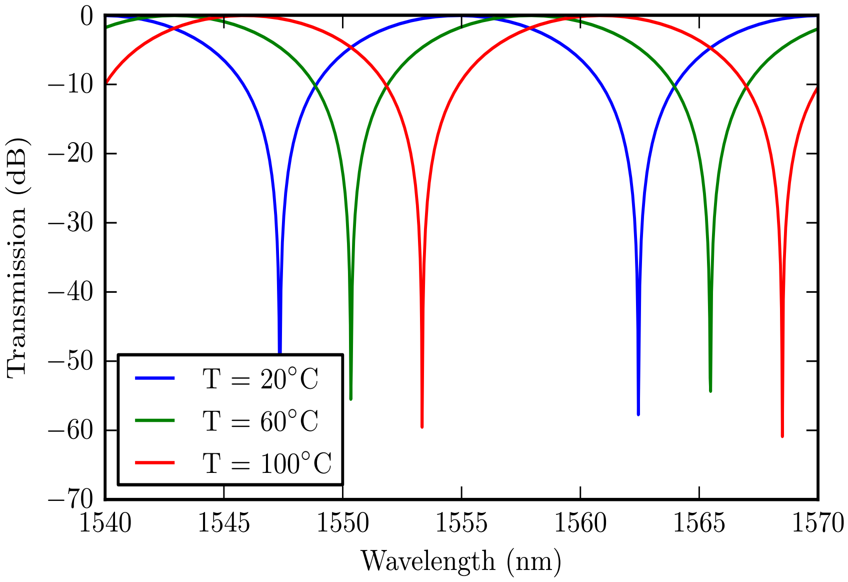

Figure 4.1: Transmission of a conventional MZI for different temperatures; oxide top cladding, core width is 450 nm

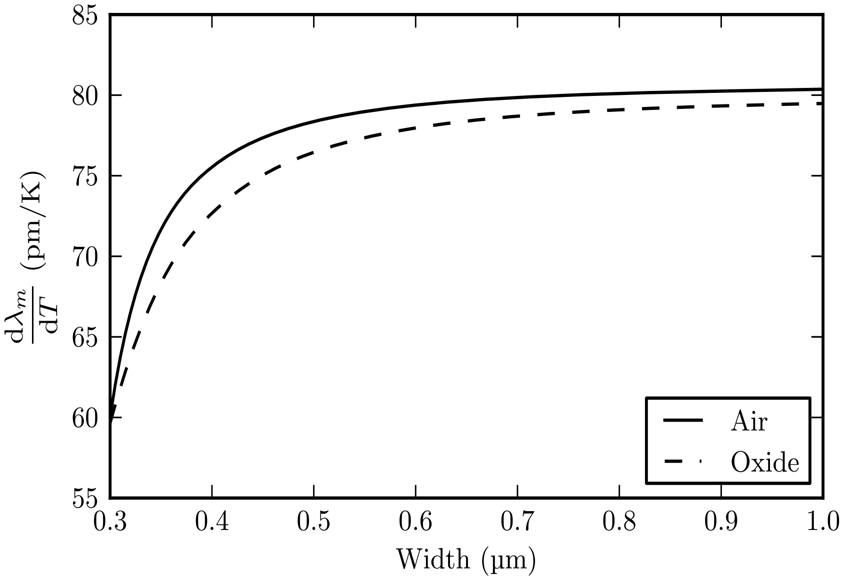

Figure 4.2: Sensitivity of spectrum position to temperature of a conventional MZI, AWG, and ring resonator with the air and oxide top-cladding at $\lambda = 1550$ nm

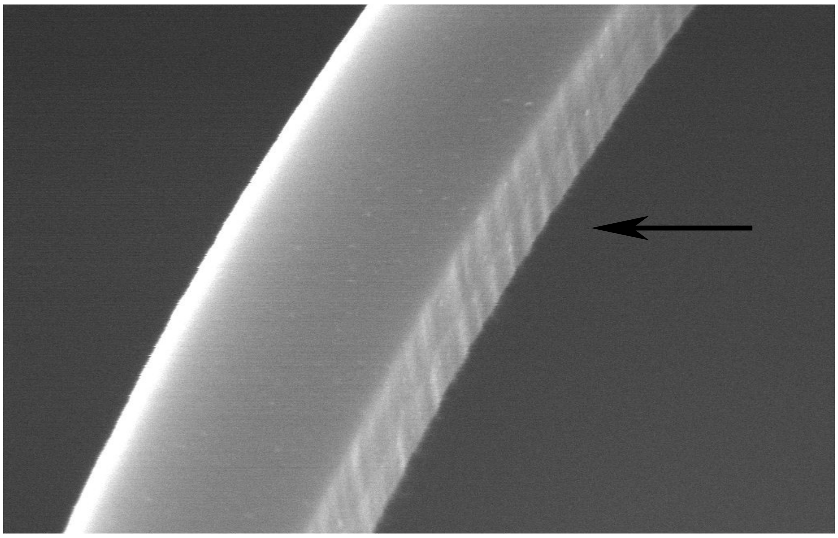

Figure 4.3: SEM picture of a waveguide where the corrugated sidewall is visible; width of waveguide is 400 nm

450 nm and at wavelength of 1550 nm. The transmission is redshifted as a function of wavelength.

The spectrum is not only influenced by the temperature variations, but also by deviations in physical dimensions of the waveguides such as the linewidth and thickness, because of the tolerance of the fabrication process. The fabrication tolerance can be handled by making channel pass band flat as already noted in the previous chapter. Also, fabrication tolerant filters will be discussed in chapter 6 . For a conventional wavelength filter such as an MZI, AWG, or ring resonator, Eq. 4.1 can be modified as:

$$\frac{d\lambda_m}{dX} = \frac{\lambda_m}{n_g}\frac{dn_{eff}}{dX} \tag{4.2}$$

The position of the spectrum not only depends on uniform waveguide width deviations due to fabrication tolerances, but also depends on the phase errors (difference between target and actual phase) introduced by the corrugated sidewall of the waveguide. The corrugated side wall is clearly visible in Fig. 4.3.

The variance of the phase error is given by [12, 13] :

$$\sigma^2(\delta\phi) = 2\left(\frac{\partial\beta}{\partial w}\right)^2 \sigma^2_{sidewall} L_c L, \tag{4.3}$$

where $\sigma_{sidewall}$ is the standard deviation of the sidewall position with respect to waveguide center; L_c is the correlation length, and L is the length of the waveguide. The standard deviation of the phase error is proportional to $\frac{\partial\beta}{\partial w}$ or $\frac{\partial n_{eff}}{\partial w}$. This

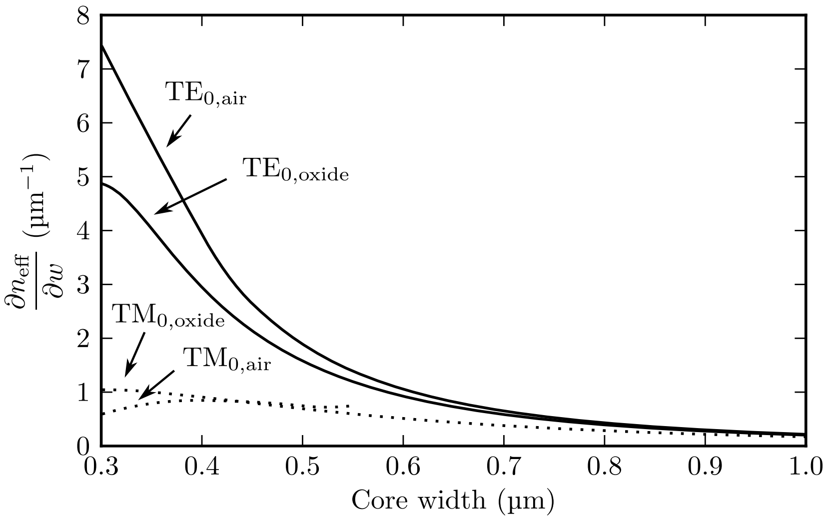

Figure 4.4: Variation of n_{eff} with respect to width for TE and TM polarization, for air and oxide top-cladding; $\lambda = 1.55\mu m$

factor decreases with increasing waveguide width as shown in Fig. 4.4. Therefore, for a certain L_c and $\sigma_{sidewall}$ it is better to use broader waveguides.

4.3 Passive compensation of FIR Filters

Let us assume a wavelength filter f to be a conventional filter which consists of some zeros and poles with amplitude response A and phase response ϕ . Its transmission with respect to wavelength drifts with ambient temperature and fabrication variations. On the other side, filter g with amplitude response A' and phase response ϕ', could be the same or larger order wavelength filter with minimized temperature and fabrication variations. We can treat this as an optimization problem with target function $\frac{d\lambda}{dT}$ to be minimized. In this chapter we discuss only the thermal compensation aspect and in chapter 6 we will discuss about fabrication tolerant filters as well with this technique.

We apply this technique to a number of filters e.g. MZI, lattice filter and AWG.

4.4 Athermal MZI

4.4.1 Method

Before getting into the athermal MZI, we briefly revisit the workings of a conventional MZI filter. As we know in any given wavelength filter, as in our MZI, we

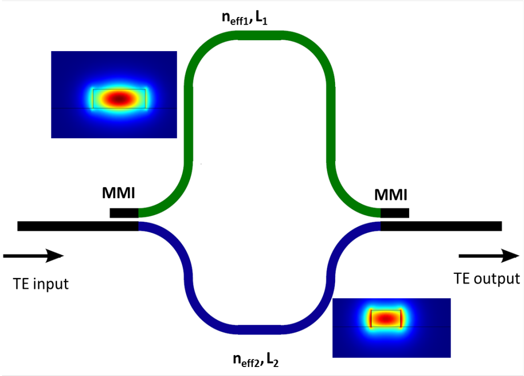

Figure 4.5: Schematic of MZI filter with modes in each arm

get constructive or destructive interference at the output when:

$$m\lambda_m = n_{eff}(\lambda_m, T)\Delta L \tag{4.4}$$

Instead of using the same waveguide, we can now use different waveguides in the two arms. As a result, the propagating mode in each arm will have a different effective index. In that case, the constructive interference condition changes to:

$$m\lambda_m = n_{eff1}(\lambda_m, T)L_1 - n_{eff2}(\lambda_m, T)L_2 \tag{4.5}$$

where m is the interference order of the filter and T is the operating temperature. Here, m should be integer or half integer in order to have a constructive or destructive interference at λ_m.

If we take the first order expansion of the Eq.(4.5) with T, we have:

$$\frac{d\lambda_m}{dT}\left(m - \left(L1\frac{dn_{eff1}}{d\lambda} - L2\frac{dn_{eff2}}{d\lambda}\right)\right) = L1\frac{dn_{eff1}}{dT} - L2\frac{dn_{eff2}}{dT} \tag{4.6}$$

The schematic of such an MZI with different modes in each arm is shown in Fig. 4.5.

We can call the multiplier term on the left hand side as M which is modified interference order, which taking into account dispersion. If we write it separately:

$$M = (m - (L1\frac{dn_{eff1}}{d\lambda} - L2\frac{dn_{eff2}}{d\lambda})) \tag{4.7}$$

From Eq. (4.6 -4.7) the change in wavelength with respect to temperature T is given by:

$$\frac{d\lambda_m}{dT} = \frac{1}{M}(L1\frac{dn_{eff1}}{dT} - L2\frac{dn_{eff2}}{dT}) \tag{4.8}$$

To minimize the sensitivity to temperature, the last two terms should cancel out at the wavelength of interest, and for a given FSR of the designed filter.

The free spectral range (FSR) of the output spectrum is given by

$$\Delta\lambda_{FSR} = |\lambda_{m+1} - \lambda_m| \approx \frac{\lambda}{|M|} \tag{4.9}$$

The modified interference order M can be derived from Eq. (4.9). The sensitivity of FSR is related to the sensitivity of spectrum position. For a sufficiently small FSR ($n_{eff}(\lambda_m) \approx n_{eff}(\lambda_{m+1})$), the sensitivity is given by

$$\frac{d\Delta\lambda_{FSR}}{dT} = \frac{\Delta\lambda_{FSR}}{\lambda}\frac{d\lambda_m}{dT} \tag{4.10}$$

The modified FSR of the athermal MZI is given by

$$FSR = \frac{\lambda^2}{n_{g1}.L_1 - n_{g2}.L_2} \tag{4.11}$$

As can be easily seen, reducing the sensitivity of the spectrum position also reduces the sensitivity of the FSR. This means that for an interferometric device such as an MZI, it is possible to obtain temperature insensitivity by combining wide and narrow waveguides in different arms. The two arms of the MZI have different TO coefficients which directly depend upon the confinement in the silicon core. The TO coefficient of the silicon strip waveguide with air and oxide as top cladding at wavelength of 1550 nm is shown in Fig. 4.6.

By choosing appropriate arm lengths, the temperature dependence of both the arms can be made to cancel each other out.

4.4.2 Design and Simulation

The device is designed for the TE polarization. The width of wider waveguide is 1000 nm while narrower one is 450 nm. The width is chosen in such a way as to make the difference in thermo-optic coefficient maximum, as shown in Fig. 4.6. Also, it is possible to eliminate the temperature dependence of the designed filter with appropriate combination of L_1 and L_2.

The device is designed for an order $m = 200$. The modified interference order M and $\frac{d\lambda}{dT}$ with respect to length of the wider waveguide is shown in Fig. 4.7.

The simulated length for athermal operation of the wider waveguide is 393 μm while the path length difference between the arms is 22 μm.

4.4.3 Fabrication and Measurements

The device is fabricated in IMEC's standard passive platform which is already in the chapter 2. This process uses 200 mm SOI wafers and 130 nm CMOS technology node with 220 nm of silicon and 2 μm of buried oxide (BOX). The device uses compact grating couplers that are etched 70 nm into silicon, to couple light from

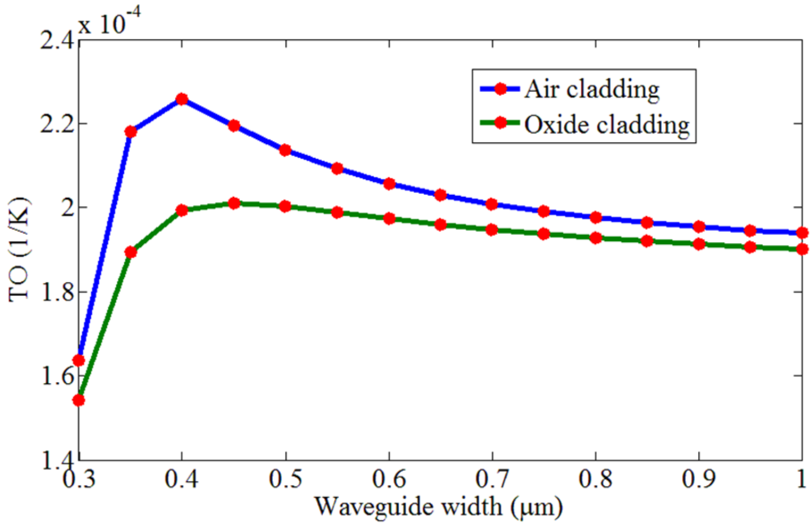

Figure 4.6: Thermo-optic coefficient of fully etch silicon waveguide of 220 nm thickness at λ = 1550 nm

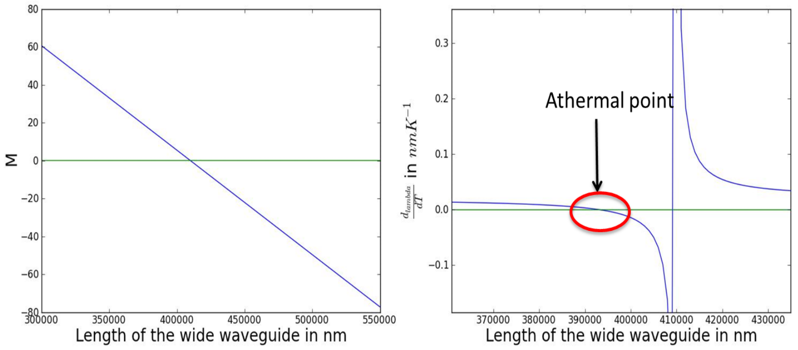

Figure 4.7: (a) Modified interference order M and (b) $\frac{d\lambda}{dT}$ with wide waveguide

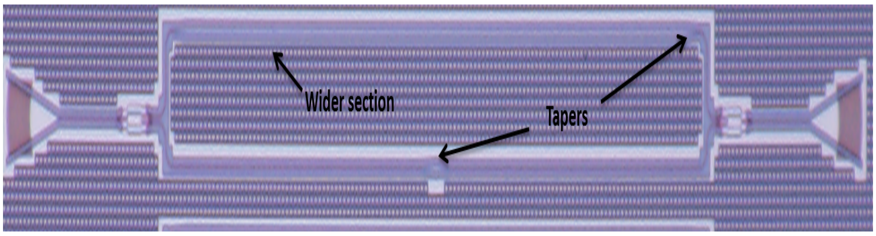

Figure 4.8: Camera image of fabricated all-silicon athermal MZI with wider and narrower waveguide section. The taper section is clearly seen in both arms.

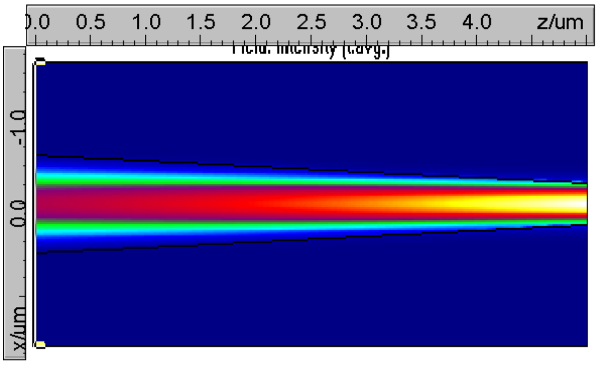

Figure 4.9: Simulated $5\mu m$ long taper section showing the field intensity

fiber to chip. The fabricated device is shown in Fig. 4.8. The tapers are designed in such a way so that there will be no excitation of the higher order modes, and to keep the loss to a minimum. The tapers are added in both the arms to avoid any differential phase addition. The full wave simulation of the field intensity of $5\mu m$ taper is shown in Fig. 4.9 from a 1000 nm wide waveguide to a 450 nm narrow waveguide section. In the designed filter, we have used $10\mu m$ tapers from narrow to wide waveguides. The equal dummy tapers are added in the lower arm of the MZI to avoid any phase or thermal shift in the device due to them.

For transmission measurements of the filter with thermal variations, we placed the fabricated chip on a thermally controlled stage with a resistive heater and a temperature sensor. The setup is explained in the section 2.5.4.1, but now the thermal chuck is placed on the semi-automatic setup. The wavelength sweep from 1501 nm to 1569 nm has been performed by CW Agilent laser with input power of 4 mW. The thermal chuck is shown in Fig. 4.10.

The normalized measured transmission at different temperatures of $30\,^{\circ}\mathrm{C}$ and $50\,^{\circ}\mathrm{C}$ is shown in Fig. 4.11. The insertion loss is measured by first aligning the fibers with a reference waveguide and normalizing the filter spectrum with respect to this reference waveguide. The measured FSR is 14 nm, insertion loss is less

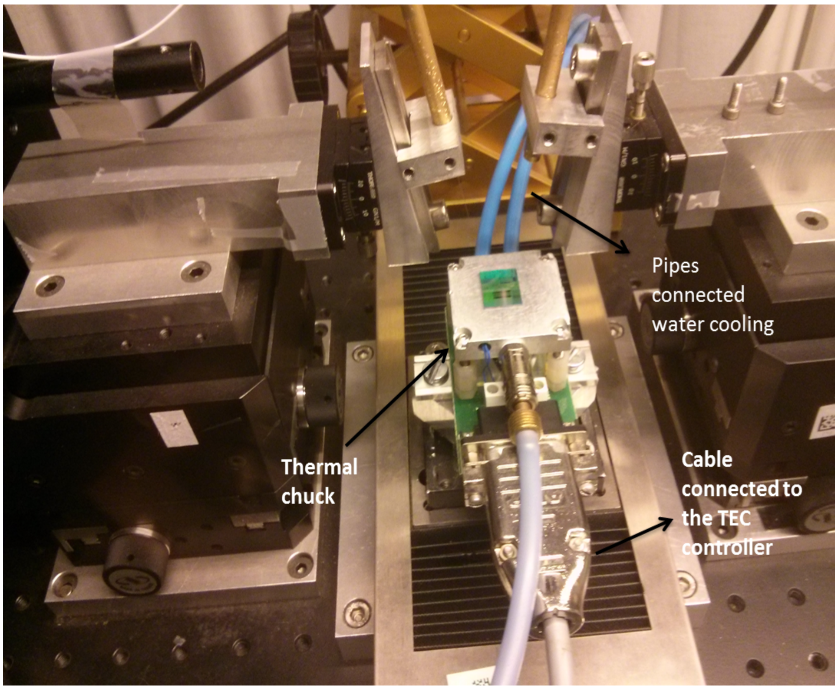

Figure 4.10: Thermally controlled chuck placed on the semi-automatic setup.

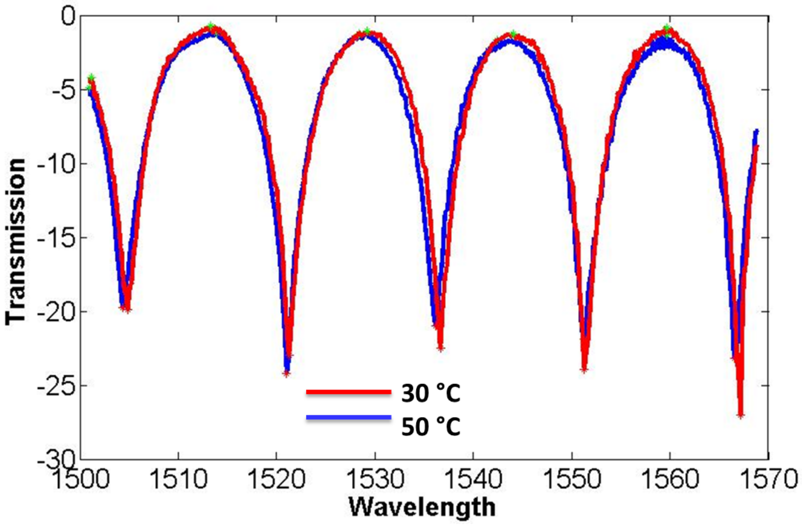

Figure 4.11: Normalized transmission of athermal MZI filter at $30\,^{\circ}\mathrm{C}$ *and* $50\,^{\circ}\mathrm{C}$*. The thermal sensitivity of the MZI is less than 10 pm/K in entire C-band*

than 1 dB and the extinction ratio is more than 20 dB. The high extinction ratio is caused due to the good splitting balance in the MMI which acts as input and output coupler. The measured thermal sensitivity of the MZI is less than 10 pm/K in the entire C-band. The improvement is more than 8 times than the conventional MZI.

4.5 Athermal Four Channel De-multiplexer

As we have seen by using different mode confinements in either arms we can make a thermally insensitive MZI filter. In this section, this concept is extended to higher order filters like 4-channel demultiplexers. The scheme is shown in Fig. 4.12.

4.5.1 Design and Simulation

The four channel athermal de-multiplexer is based on two stages of cascaded MZIs. It is designed for oxide cladding and for TE polarization. As mentioned in chapter 3, the FSR of the normal wavelength filter is given by

$$FSR = \frac{\lambda^2}{n_g \Delta L} \tag{4.12}$$

The modified FSR of the athermal MZI is given by Eq. 4.11.

From Eqs. (4.8-4.9), the wavelength shift due to temperature which needs to

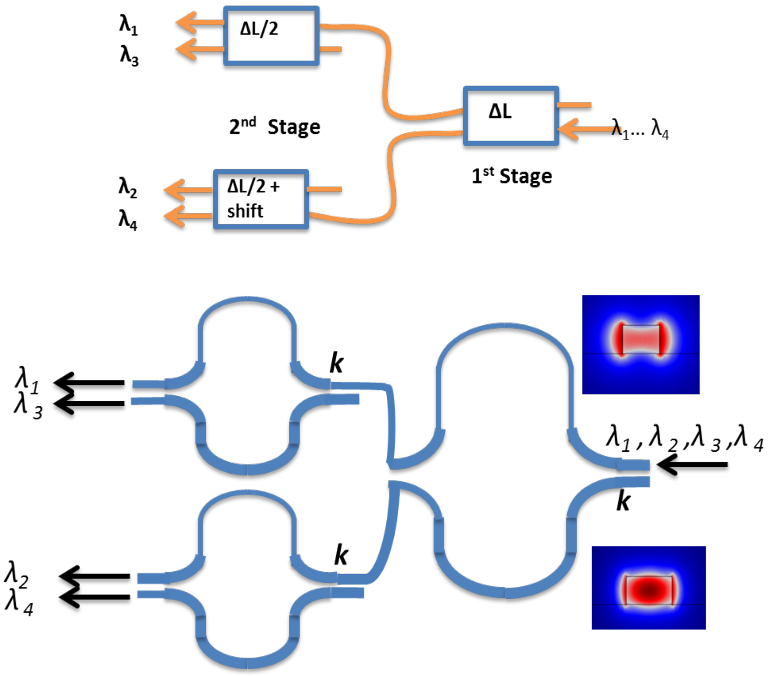

Figure 4.12: Schematic of a four channel a-thermal demultiplexer, a) block diagram and b) cascaded MZI stages. Each MZI is combination of 300 nm and 450 nm waveguide, K is power coupling coefficient

minimized is given by:

$$\frac{d\lambda}{dT} = \frac{\lambda}{n_{g1}.L_1 - n_{g2}.L_2}.(\frac{dn_{eff1}.L_1}{dT} - \frac{dn_{eff2}.L_2}{dT}) \tag{4.13}$$

Here, n_{eff1}, n_{g1} and n_{eff2}, n_{g2} are the effective refractive index and group index of the corresponding waveguides. The $\frac{dn_{eff1}}{dT}$,L_1, $\frac{dn_{eff2}}{dT}$, L_2 corresponds TO coefficients and waveguide lengths respectively. For athermal operation of the demultiplexer, $\frac{d\lambda}{dT}$ should be minimized.

The 4-channel athermal de-multiplexer is designed for 5 nm of channel spacing. The first stage MZI is designed for the 10 nm of channel spacing and the second stage MZI is designed for 20 nm.

The arm lengths can be calculated from Eq. (4.11- 4.13) and is given by

$$L_1 = \frac{\lambda^2}{(n_{g1} - n_{g2}\frac{TO_1}{TO_2})FSR} \tag{4.14}$$

$$L_2 = \frac{\lambda^2}{(n_{g1}\frac{TO_2}{TO_1} - n_{g2})FSR} \tag{4.15}$$

Here TO_1 and TO_2 are thermo-optic coefficients of narrow and wider waveguides.

The length required for π phase shift is given by:

$$L_\pi = \frac{\lambda}{2 * n_{eff1}} \tag{4.16}$$

The shift of $\pi/2$ length is added in the longer arm of the 2nd stage lower MZI as shown in Fig. 4.12 in order to adjust the center wavelength of the channels. The modified length is given by:

$$L_1' = L_1 + \frac{\lambda}{4 * n_{eff1}} \tag{4.17}$$

The narrow designed waveguide is 300 nm wide and the wider one is 450 nm. The TO coefficients are obtained from the full wave FEM solver COMSOL as plotted in Fig. 4.6. The TO coefficent of 300 nm is $1.4 \times 10^{-4}/K$ and for 400 nm it is $2 \times 10^{-4}/K$.The widths are chosen in such way so that the difference in TO coefficients is maximum and hence the footprint of the device become minimum. The calculated lengths for 300 nm and 450 nm wide waveguide for first stage MZI are designed for 10 nm FSR is 224.76 μm and 159.88 μm respectively. The directional couplers are designed for 50 $\%$ coupling at both stages. The circuit simulation is performed by Caphe. Full device simulations are performed in circuit simulator Caphe from Luceda Photonics [14] taking into account waveguide dispersion and thermal effect. The simulated transmission at $20\,^{\circ}$C and $40\,^{\circ}$C is shown in Fig. 4.13.

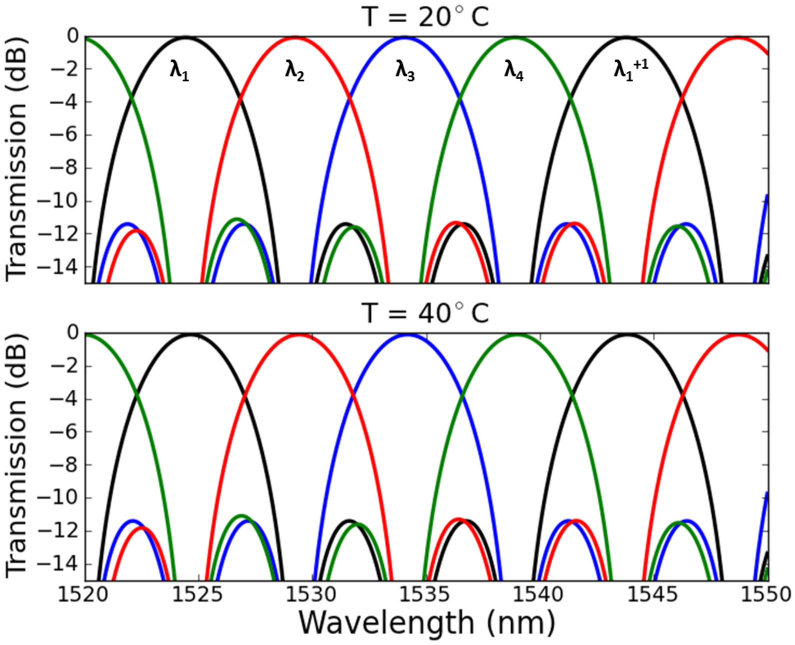

Figure 4.13: Simulated circuit transmission of 4-channel athermal demultiplexer at $20\,^\circ\mathrm{C}$ *and* $40\,^\circ\mathrm{C}$

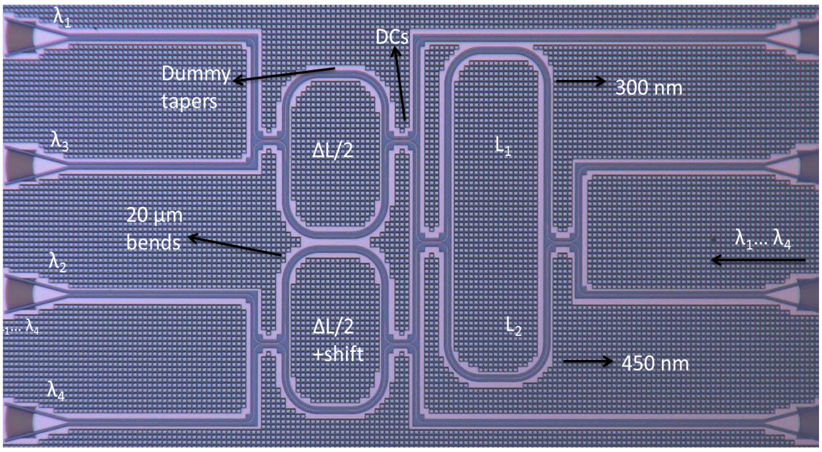

Figure 4.14: Camera image of fabricated 4-channel athermal demultiplexer

4.5.2 Fabricated De-multiplexer and Measurements

The device is fabricated in IMEC's standard passive platform which is described in the chapter 2. The waveguides are fully etched into a 220 nm thick silicon-on-insulator layer with oxide as top cladding. The fabricated device is shown in Fig. 4.14. The bend radius in the delay lines in the individual MZIs is chosen to be 20 μm to avoid reflection and losses due to narrow waveguides. Adiabatic tapers are used in the longer arm of MZI for a smooth mode transition from 450 nm wide waveguide to 300 nm waveguide. The dummy tapers are added in the straight shorter arm to avoid any phase or thermal shift. The tapers are 10 μm long. The directional couplers are designed as 450 nm wide waveguides with a bend radius of 5 μm. The directional couplers are 9.038 μm long for 50$\%$ of power coupling with a gap of 180 nm at 1530 nm. The total footprint of the device is $500 \times 250 \mu m^2$.

The device is measured using a CW Agilent laser with output power of 4 mW. The measurement setup is explained in Fig. 4.10. The chip is kept on a thermally controlled chuck. All the channels are sequentially measured by aligning a fiber to the respective grating coupler. A reference transmission between two grating couplers is used to normalize the transmission of the filter at different temperatures. The normalized transmission at two different temperatures $20\,^{\circ}\mathrm{C}$ and $40\,^{\circ}\mathrm{C}$ is shown in the Fig. 4.15. The measured insertion loss is less than 2 dB. The channel cross talk is measured by taking 1 dB channel bandwidth and the channel spacing is measured by taking the center position of this 1 dB bandwidth. The measured channel cross talk is better than -10 dB for all the channels and the measured channel spacing is 5 nm. The measurement matches very well with the circuit simulation. The side lobes of the measured spectrum is due to the single MZIs in each stage which is evident in the simulations as well. This can be further improved by replacing single MZI to lattice MZIs in every stage. The measured thermal

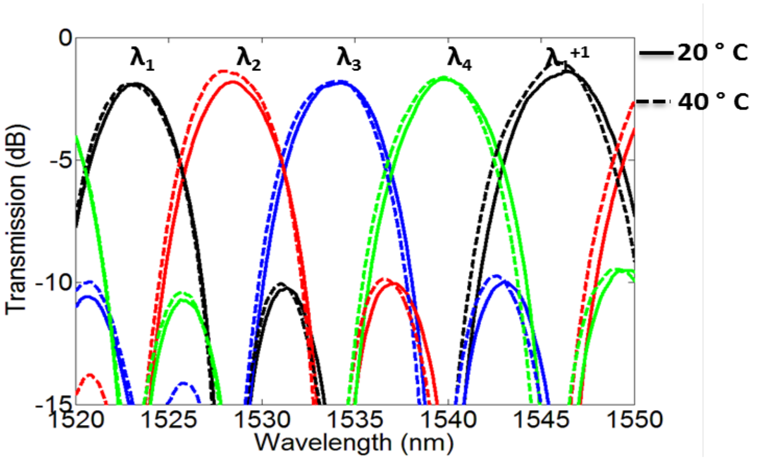

Figure 4.15: Measured normalized transmission of 4-channel athermal demultiplexer at 20 °C *and* 40 °C

sensitivity of the demultiplexer is less than 10 pm/K over the entire C-band. The same device without thermal compensation would shift 80 pm/K, hence we show an 8-fold improvement in thermal tolerances. The additional insertion loss comes from the narrow waveguide where the mode is pushed out of the waveguide core and hence suffers from higher scattering losses. The loss and footprint can further be improved by keeping the narrow waveguide only in the straight sections, while for the bends the 450 nm wide waveguides could be used. We can then use the tighter bends instead of $20\mu m$ ones. But, in that case there will be two additional tapers in each arm of the MZI which would increase the size and possibly the loss also, so there is a trade off in this design.

4.6 All-Silicon Athermal Arrayed Waveguide Gratings

Arrayed waveguide gratings (AWG) face the similar problem of temperature dependence like other wavelength filters on SOI. In lower contrast material like silica AWG suffer much less from this problem due to its lower TO coefficient. Their are several demonstrations of athermal silicon AWG with polymer cladding on top similar to the one for ring resonators [15, 16]. However, they face the similar CMOS compatibility issues. In order to apply the same passive compensation techniques to AWGs, we can treat them as a a set of MZIs connected in parallel. The schematic of the athermal AWG is shown in Fig. 4.16.

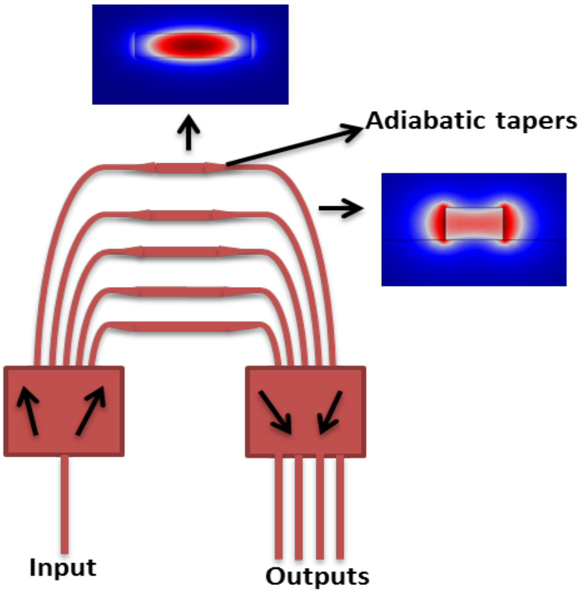

Figure 4.16: Schematic of all-silicon athermal AWG

4.6.1 Design and Simulation

In an AWG, light is coupled in a waveguide array by the star coupler. The lengths of the individual waveguides in this array increase by fixed increments so any thermal drift causes light to acquire a different additional phase. Therefore, in order to make the AWG output athermal, we need to compensate for the thermal drift in the waveguide array. To achieve this compensation, we use individual waveguides with two widths, unlike in a conventional AWG where all the waveguides have the same width over their entire length. As shown in Fig. 4.16, the AWG delay lines are combination of two different waveguides, one with wider width w_0 and other with narrow width w_1. Due to the combination of two waveguides, the phase matching condition at the center wavelength λ becomes:

$$\frac{2\pi}{\lambda}n_{w0}(l_1+(i-1)\Delta l)+\frac{2\pi}{\lambda}n_{w1}(p_1-(i-1)\Delta p) = \frac{2\pi}{\lambda}n_{w0}(l_1+i\Delta l)+\frac{2\pi}{\lambda}n_{w1}(p_1-i\Delta p)+2m\pi \tag{4.18}$$

where n_{w0}, n_{w1} are the effective refractive indices of the waveguide and l_1, p_1 denote the outermost path length when $i = 1$. As we can see the narrow waveguide length gradually decreases with length Δp while the wider waveguide increases with the length Δl.

From Eq.(4.18) we get:

$$m\lambda = n_{w1}\Delta p - n_{w0}\Delta l \tag{4.19}$$

The athermal condition becomes:

$$\frac{d\lambda_m}{dT} = \frac{1}{m}(\Delta p\frac{dn_{w1}}{dT}\Delta l\frac{dn_{w0}}{dT}) \tag{4.20}$$

where m is the filter order. When we take the dispersion into account Eq. (4.20) is modified in a similar way as it is for athermal MZI Eq.(4.7-4.8). The target is to minimize $\frac{d\lambda_m}{dT}$. The modified equation taking the dispersion into account becomes:

$$\frac{d\lambda_m}{dT} = \frac{\lambda}{n_{gw0}\Delta p - n_{gw1}\Delta l}.(\Delta p\frac{dn_{w0}}{dT} - \Delta l\frac{dn_{w1}}{dT}) \tag{4.21}$$

which is quite similar to Eq.(4.13). Similarly the lengths Δp and Δl can be calculated for any given FSR becomes:

$$\Delta p = \frac{\lambda^2}{(n_{gw0} - n_{gw1}\frac{TO_1}{TO_2})FSR} \tag{4.22}$$

$$\Delta l = \frac{\lambda^2}{(n_{gw0}\frac{TO_2}{TO_1} - n_{gw1})FSR} \tag{4.23}$$

where n_{gw0}, n_{gw1} are the group indices and $TO_1 = \frac{dn_{w1}}{dT}$, $TO_2 = \frac{dn_{w0}}{dT}$ are corresponding TO coefficients of the waveguides.

The device is designed for four channels with 1000 GHz (8 nm) channel spacing. The absolute path length of the narrow waveguide (Δp) is 96.15 μm and wider waveguide (Δl) is 76 μm respectively. The device design layout is done in the IPKISS parametric design framework from Luceda photonics [17]. The device layout is shown in the Fig. 4.17.

4.6.2 Fabrication and Measurements

The device is fabricated in IMEC's standard passive platform which is described in the chapter 2. The device uses 300 nm and 800 nm wide, fully etched 220 nm thick silicon waveguides with oxide as top cladding. The fabricated device is shown in Fig. 4.18. The bend radius in the delay lines are kept as 20 μm to avoid reflection and losses due to narrow waveguides. 5 μm long adiabatic tapers are used for smooth mode transition from 800 nm wide waveguide to 300 nm waveguide. The device is designed for TE polarization. The number of delay lines is kept as 16. If we increase the delay line the imaging is better and hence the demultiplexer has a better roll-off. It is explained in the flat band AWGs in the chapter 2. For thermal shift comparison, we have fabricated a standard silicon AWG next to our proposed athermal AWG with 800 GHz of channel spacing.

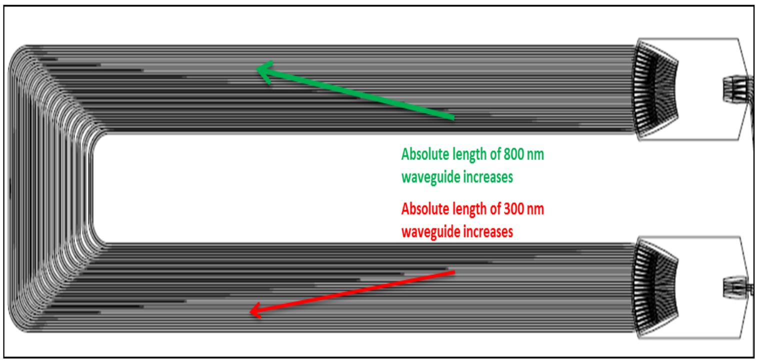

Figure 4.17: Design layout of all-silicon athermal AWG. The absolute length of wider section decreases at the outermost section while the narrower section length increases. The wider waveguide is 800 nm wide and the narrower section is 300 nm.

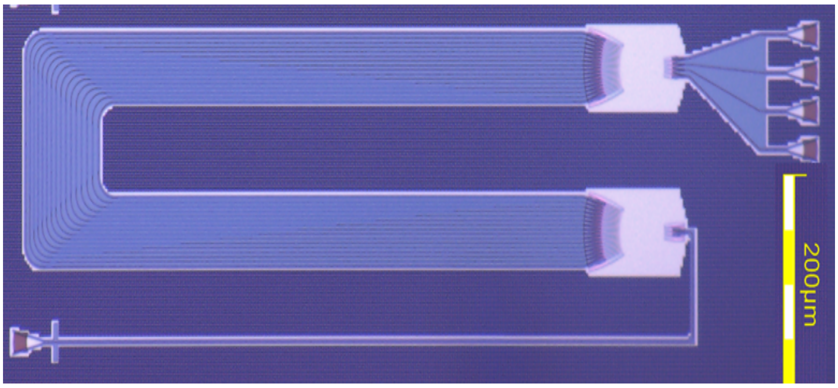

Figure 4.18: Fabricated all-silicon four channels athermal AWG

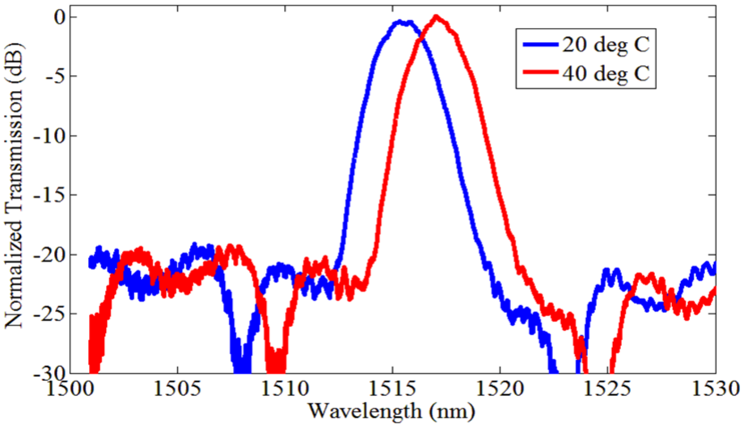

Figure 4.19: Normalized one channel response of standard silicon AWG at temperatures 20 °C *and* 40 °C.

The device is measured using CW Agilent laser with input power of 4 mW. The measurement setup is explained in Fig. 4.10. The chip is kept at thermally controlled chuck as explained in the previous section. All the channels are individually aligned with respect to the straight waveguide sitting next to the waveguide to get the maximum transmission.

The normalized transmission measured at two different temperatures 20 °C and 40 °C for one for normal silicon AWG and our athermal AWG are shown shown in Fig. 4.19 and Fig. 4.20 respectively.

The measured and normalized all four channels are shown in Fig. 4.21. The fourth channel is worst performing with a thermal shift less than 20 pm/K while the first one is best with shift less than 5 pm/K. The insertion loss between the channels varies between 3.5 and 4.8 dB. The high insertion loss is due to the narrow waveguides. The measured best channel cross talk is almost -9 dB while the worst one is just -6 dB. The reason for this low cross talk is due to the phase errors which caused by narrow waveguides.

The measured wavelength shift with temperature for standard silicon AWG is more than 80 pm/K as expected while the measured average wavelength shift for our proposed all-silicon athermal AWG is less than 10 pm/K.

4.7 Conclusion and Discussion

In this chapter we have proposed a novel design based on passive compensation technique for silicon spectral filters. We have successfully demonstrated several all-silicon athermal filters e.g. MZI, four channel demultiplexer and AWGs based on this technique. Although this method works well, yet it also comes with a

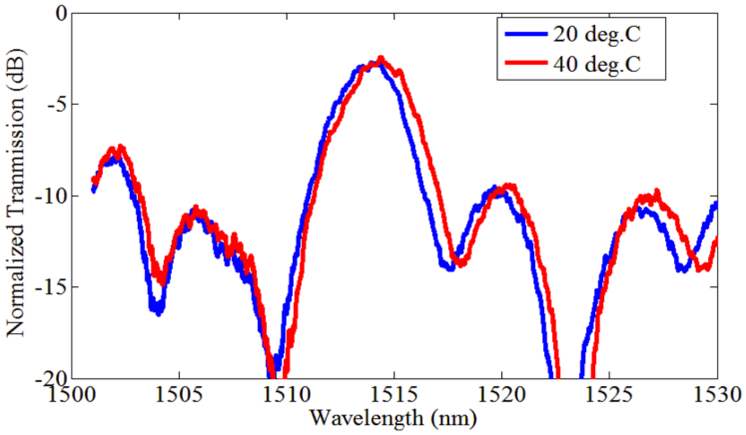

Figure 4.20: Normalized first channel response of all silicon athermal AWG at temperatures 20 °C *and* 40 °C

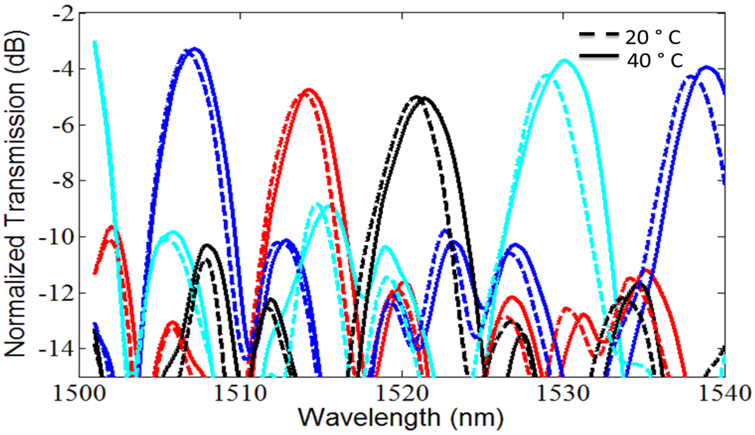

Figure 4.21: Normalized all four channels of all silicon athermal AWG at 20 °C *and* 40 °C

Reference	Device	Av. IL(dB)	Av. XT (1dB)	Footprint
CEA Leti [18]	Cascaded MZIs (O-band)	4	-9	1000×1000 μm^2
UGhent-Imec	Cascaded MZIs (C-band)	2	-10	550×250 μm^2

Table 4.1: 4-channel athermal demux

trade-off of high insertion loss and low cross talk especially in the athermal AWG caused by to the narrow waveguides. The performance of the AWG can certainly be improved with a better fabrication process e.g. by fabricating in a 300 mm p-line that has much better control of linewidths and sidewall roughness.

The comparison with one of the recent demonstrations from CEA-Leti is shown in the table 4.1. The design from CEA-leti [18] is centered at O-band, although the channel spacing 5 nm similar to our case. They have used 300 nm thick silicon in their processing line. The possible reason for our better performance is the small delay lengths as compared to them and better design methodology and processing. The crosstalk and insertion loss is also much better compared to them.

If we compare the our all silicon athermal AWGs with the polymer cladding athermal AWGs [16], the performance is not comparable due to high phase errors which results in high insertion loss and low crosstalk.

The other issue is a larger footprint of the devices because the compensation is mainly based on the difference in the TO coefficients of the waveguides. In the next chapter, we show how by using TM polarization one can further reduce the footprint further.

References

[1] Pieter Dumon, Roman Kappeler, Daniel Barros, Iain McKenzie, Dominic Doyle, and Roel Baets. *Measured radiation sensitivity of silica-on-silicon and silicon-on-insulator micro-photonic devices for potential space application*. Proc. SPIE, 5897(10):58970D–58970D–10, July 2005.

[2] Jie Teng, Pieter Dumon, Wim Bogaerts, Hongbo Zhang, Xigao Jian, Xiuyou Han, Mingshan Zhao, Geert Morthier, and Roel Baets. *Athermal Silicon-on-insulator ring resonators by overlaying a polymer cladding on narrowed waveguides*. Opt. Express, 17(17):14627–14633, Aug 2009.

[3] Feng Qiu, Andrew M. Spring, Feng Yu, and Shiyoshi Yokoyama. *Complementary metaloxidesemiconductor compatible athermal silicon nitride/titanium dioxide hybrid micro-ring resonators*. Applied Physics Letters, 102(5), 2013.

[4] Biswajeet Guha, Jaime Cardenas, and Michal Lipson. *Athermal silicon microring resonators with titanium oxide cladding*. Opt. Express, 21(22):26557–26563, Nov 2013.

[5] Stevan S. Djordjevic, Kuanping Shang, Binbin Guan, Stanley T. S. Cheung, Ling Liao, Juthika Basak, Hai-Feng Liu, and S. J. B. Yoo. *CMOS-compatible, athermal silicon ring modulators clad with titanium dioxide*. Opt. Express, 21(12):13958–13968, Jun 2013.

[6] Shaoqi Feng, Kuanping Shang, Jock T. Bovington, Rui Wu, Binbin Guan, Kwang-Ting Cheng, John E. Bowers, and S. J. Ben Yoo. *Athermal silicon ring resonators clad with titanium dioxide for 1.3 μm wavelength operation*. Opt. Express, 23(20):25653–25660, Oct 2015.

[7] Jock Bovington, Rui Wu, Kwang-Ting Cheng, and John E. Bowers. *Thermal stress implications in athermal TiO2 waveguides on a silicon substrate*. Opt. Express, 22(1):661–666, Jan 2014.

[8] F. Gan, T. Barwicz, M.A. Popovic, M.S. Dahlem, C.W. Holzwarth, P.T. Rakich, H.I. Smith, E.P. Ippen, and F.X. Kartner. *Maximizing the Thermo-Optic Tuning Range of Silicon Photonic Structures*. In Photonics in Switching, 2007, pages 67–68, Aug 2007.

[9] Po Dong, Wei Qian, Hong Liang, Roshanak Shafiiha, Dazeng Feng, Guoliang Li, John E. Cunningham, Ashok V. Krishnamoorthy, and Mehdi Asghari. *Thermally tunable silicon racetrack resonators with ultralow tuning power*. Opt. Express, 18(19):20298–20304, Sep 2010.

[10] Joris Van Campenhout, William M. J. Green, Solomon Assefa, and Yurii A. Vlasov. *Integrated NiSi waveguide heaters for CMOS-compatible silicon thermo-optic devices*. Opt. Lett., 35(7):1013–1015, Apr 2010.

[11] Adil Masood, Marianna Pantouvaki, Danny Goossens, Guy Lepage, Peter Verheyen, Joris Van Campenhout, Philippe Absil, Dries Van Thourhout, and Wim Bogaerts. *Fabrication and characterization of CMOS-compatible integrated tungsten heaters for thermo-optic tuning in silicon photonics devices*. Opt. Mater. Express, 4(7):1383–1388, Jul 2014.

[12] T. Goh, S. Suzuki, and A. Sugita. *Estimation of waveguide phase error in silica-based waveguides*. Lightwave Technology, Journal of, 15(11):2107–2113, Nov 1997.

[13] P. Dumon. Ultra-compact integrated optical filters in silicon-on insulator by means of wafer-scale technology, Ph.D. thesis, Ghent university, 2007.

[14] Martin Fiers, Thomas Van Vaerenbergh, Ken Caluwaerts, Dries Vande Ginste, Benjamin Schrauwen, Joni Dambre, and Peter Bienstman. *Time-domain and frequency-domain modeling of nonlinear optical components at the circuit-level using a node-based approach*. J. Opt. Soc. Am. B, 29(5):896–900, May 2012.

[15] Xiang Wang, Simiao Xiao, Weiwei Zheng, Fan Wang, Yinlei Hao, Xiaoqing Jiang, Minghua Wang, and Jianyi Yang. *Athermal silicon arrayed waveguide grating with polymer-filled slot structure*. In Group IV Photonics, 2008 5th IEEE International Conference on, pages 253–255, Sept 2008.

[16] Linghua Wang, Wim Bogaerts, Pieter Dumon, Shankar Kumar Selvaraja, Jie Teng, Shibnath Pathak, Xiuyou Han, Jinyan Wang, Xigao Jian, Mingshan Zhao, Roel Baets, and Geert Morthier. *Athermal arrayed waveguide gratings in silicon-on-insulator by overlaying a polymer cladding on narrowed arrayed waveguides*. Appl. Opt., 51(9):1251–1256, Mar 2012.

[17] `http://www.lucedaphotonics.com/`.

[18] Karim Hassan, Corrado Sciancalepore, Julie Harduin, Thomas Ferrotti, Sylvie Menezo, and Badhise Ben Bakir. *Toward athermal silicon-on-insulator (de)multiplexers in the O-band*. Opt. Lett., 40(11):2641–2644, Jun 2015.

5

Compact All-Silicon Temperature Insensitive Filter Using Splitter-Polarization Rotator Section

In this chapter, we propose a novel approach to the all-silicon athermal MZI filter presented in the previous chapter. The device achieves a reduced footprint by making use of both the TE and the TM polarization, compared to the TE-based design in chapter 4. We discuss the design, simulation, fabrication and characterization of this device, with a detailed discussion of the splitter/combiner which also acts as a polarization rotator.

The device presented in this chapter is also the subject of a patent application [1].

5.1 Introduction

As discussed in chapter 4, the spectrum of an interferometric device such as a Mach-Zehnder interferometer (MZI) can be made temperature insensitive by combining wide and narrow waveguides in different arms. In this technique, the two arms of the MZI have different thermo-optic (TO) coefficients which directly depend upon the confinement of the propagating mode in the silicon core. By choosing appropriate arm lengths, the temperature dependence of both the arms can be made to cancel each other out. However, this technique increases the device footprint considerably [2]. To reduce the footprint, the difference in the thermo-optic (TO) coefficient between the two arms should be as large as possible. It is possi-

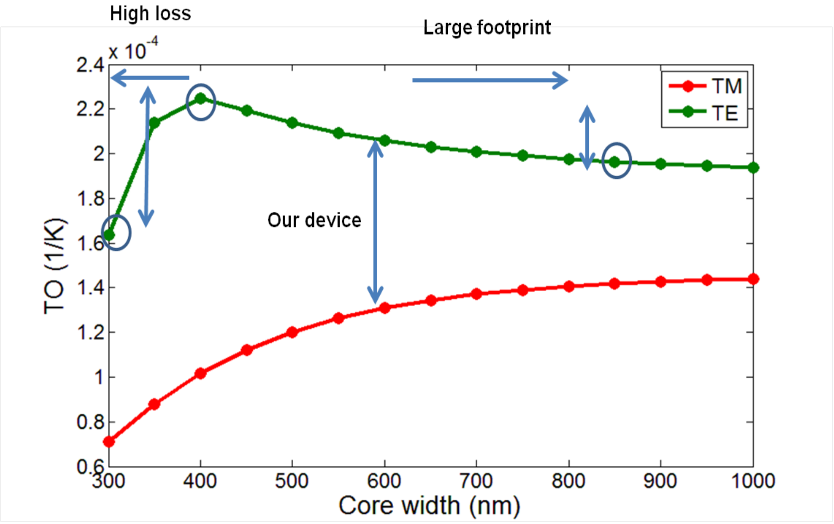

Figure 5.1: Simulated TO coefficients of TE and TM modes of SOI waveguide as a function of core width at a wavelength of 1550 nm.

ble to achieve this by using a very narrow waveguide in one arm but the narrow waveguides introduce a high propagation loss [3]. To deal with this issue we propose to use the TM polarization in one arm and TE in the other [1, 4, 5]. Since the TM mode is much less confined in the silicon core than the TE mode, this results in a lower TO coefficient. The loss is also lower since the TM mode does not have high field intensities on the rough sidewalls. By exploiting both polarizations of the waveguide, we can achieve similar temperature insensitivity, but at one third of the footprint and lower insertion loss.

Fig. 5.1 shows the simulated TO coefficient of the TE and TM modes as a function of core width for a strip waveguide at a wavelength of 1550 nm. If we want to make an athermal MZI using the same polarization for e.g. TE only then:

1. Combination of narrow and nominal waveguide width ends up with higher propagation losses and the device is more prone to fabrication errors due to the width of the narrow waveguide.

2. Combination of nominal and wider waveguide width ends up with 6 times larger footprint due to the very small difference in the corresponding TO coefficients.

   In our proposed device we use both TE and TM polarization that have a large difference between their TO coefficients and thus a small footprint device is possible. The wider waveguides ensure low-loss and more tolerant behavior to the fabrication variations.

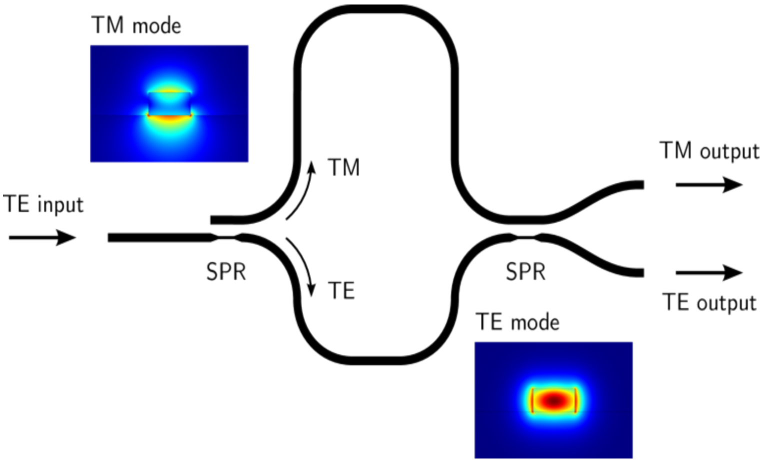

Figure 5.2: Schematic of the proposed temperature insensitive filter with TM and TE mode profile

5.2 Method

The schematic of this dual-polarization MZI is shown in the Fig. 5.2. In this design, TE polarized light is coupled in a waveguide from the fiber grating couplers. This waveguide is then connected to a *splitter / polarization-rotator* (SPR) which is capable of not only splitting the light in two waveguides but also rotate the polarization in one of the waveguides. These waveguides (one containing TE polarized light and another containing TM polarized light) now form the two arms of the MZI. Afterwards these two arms are joined together using a second SPR. The SPR splits the power into equal halves to maximize the extinction ratio of the MZI. The SPR also allows to have both TE and TM polarization at the output of the MZI. One output port gives the TE mode, while the complementary port gives the TM mode. The power spectra of both outputs are in antiphase as is typical for an MZI.

5.3 Splitter Polarization Rotator

The schematic of the SPR and cross-section are shown in the Fig. 5.3. The geometry of the SPR is similar to a conventional directional coupler, but the waveguides have a different width [6, 7]. We have employed air as a top cladding in order to break the vertical symmetry and thus induce an efficient cross polarization coupling. The widths of the two waveguides are chosen in such a way so that the effective refractive index (n_{eff}) of the fundamental TM mode in waveguide 1 is equal to n_{eff} of the fundamental TE mode in waveguide 2. This procedure is called phase matching, and is a requirement

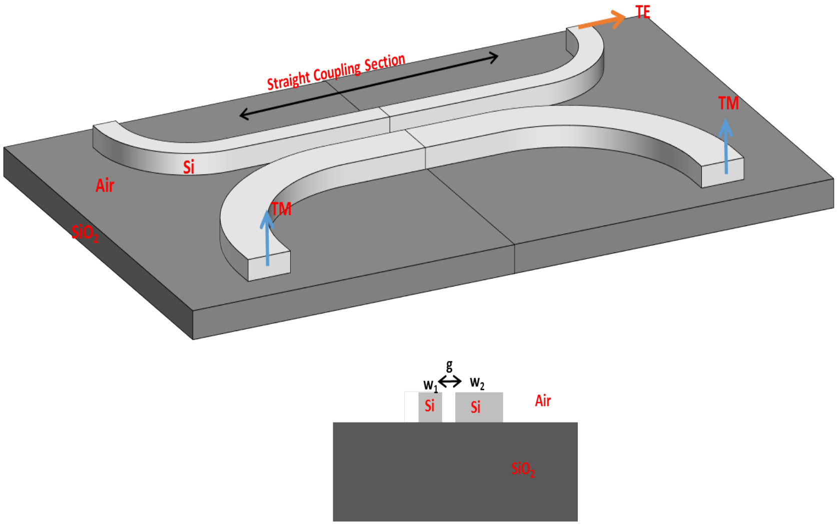

Figure 5.3: Schematic structure of the splitter and polarization rotator. (a) three dimensional model; (b) x-y cross section

for efficient and reproducible coupling. Fig. 5.4 shows the variation of n_{eff} with the core width of an SOI photonic wire of thickness 220 nm for both the TE and the TM mode. The arrow shows the phase matching condition, $n_{eff,TE} = n_{eff,TM} = 1.66$ at a simulated TE width of 320 nm and TM width of 600 nm.

We have performed the simulation of the SPR using the eigenmode propagation tool FIMMPROP by Photon Design, which solves for the propagation of the optical field.

Fig. 5.5 shows the simulation of the mode power coupling between the fundamental TE and the fundamental TM mode at the input and output respectively. The optimal coupler length (L_c) for an equal power splitting between the fundamental TE and fundamental TM mode is found to be around 10 μm.

Fig. 5.6 shows the full wave simulation of the SPR for these widths and coupling length. The gap between the waveguides is 200 nm. The TE mode from the narrow waveguide is fully coupled and converted to the TM mode in the wider waveguide. Similarly, a TM mode injected from the wider waveguide couples completely to the TE mode in the narrow waveguide. However, if the input is TE mode in wider waveguide, it will pass freely across the device without coupling. In our case, we only want the coupler to split the power equally in both the output waveguides, so instead of the full beating length, we choose the length to be only (L_c). In principle, the SPR length can be reduced by decreasing the gap to 100 nm but this makes

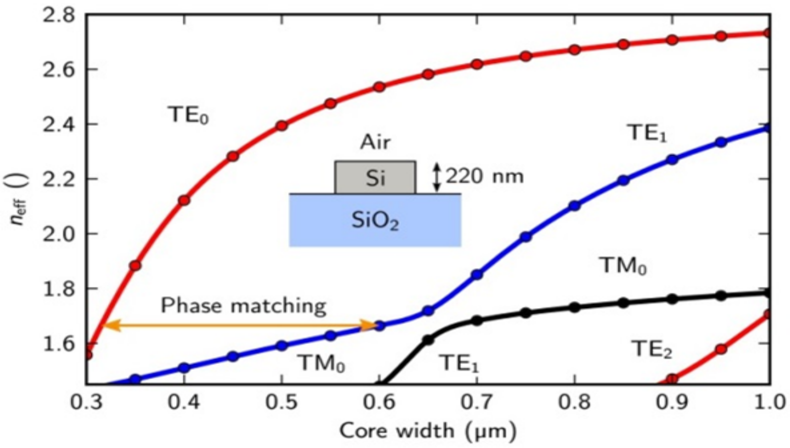

Figure 5.4: n_{eff} variation with waveguide width of an SOI waveguide with air cladding (inset) showing a phase matching condition at 1550 nm

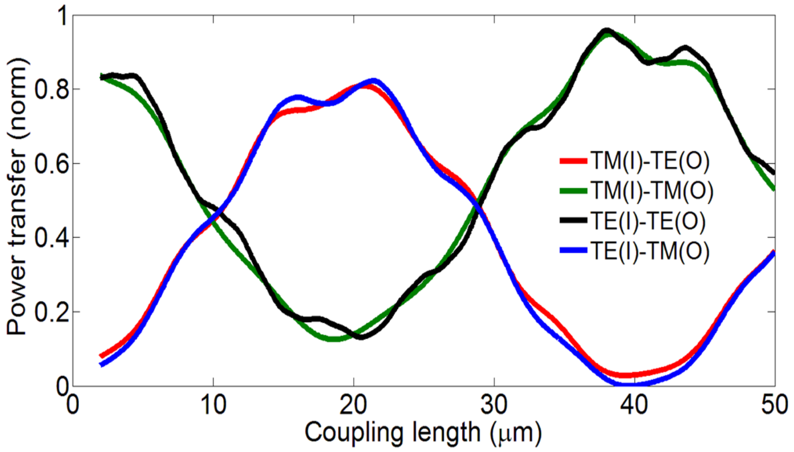

Figure 5.5: Simulated mode beating in an SPR from one mode to another as a function of coupling length showing the full mode conversion at 1550 nm. I and O represents the input and output port of an SPR

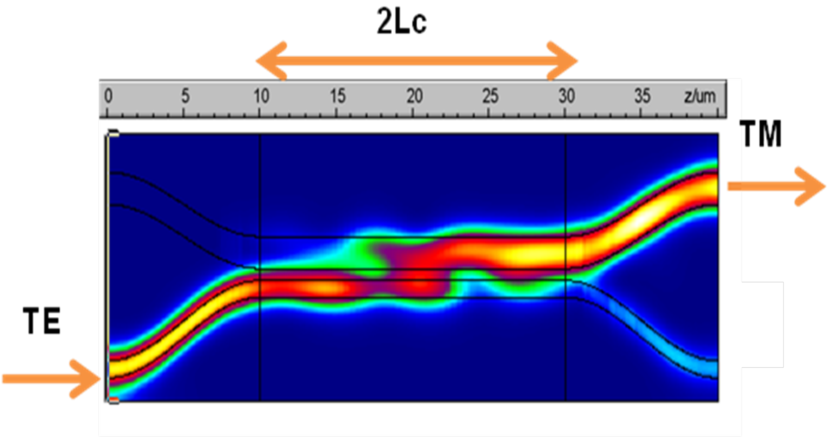

Figure 5.6: Intensity profile for the calculated cross coupling length from the input TE mode to the output TM mode at 1550 nm

the device less tolerant to fabrication variations and the device would also violate the design rule for 130 nm node of the 200 p-line of imec [8].

The narrow TE waveguide in the SPRs is tapered to a 450 nm wide waveguide and connected to the fiber grating couplers. We keep the MZI arm width at 600 nm wide because it reduces loss, phase errors, and the introduced phase is also more robust to fabrication tolerances. Including even broader waveguides in this design would not affect the device footprint much, as opposed to athermal MZIs with a single polarization where the device size strongly depends on the waveguide widths, as shown in the Fig. 5.1. For TE-TE athermal MZIs, the device size would become unacceptably large for larger waveguide widths. To connect waveguides with different cross sections, tapers need to be included. Only when the taper is sufficiently long, the mode is adiabatically converted between different waveguides, and no higher order waveguide modes or radiating modes are excited. As can also be deduced from this figure, the difference in TO coefficients could be made even larger by using a 450 nm wide waveguide in the TE arm, making the device even more compact.

5.4 Design

The modified FSR for the proposed device is given by:

$$FSR = \frac{\lambda^2}{n_{g,TM}.L_{TM} - n_{g,TE}.L_{TE}} \tag{5.1}$$

where $n_{g,TM}$, $n_{g,TE}$ and L_{TM} , L_{TE} correspond to the group index and the length of TM and TE arm waveguides guiding the TE and TM polarization, respectively. This equation is similar to Eq. 4.11 but, now it is replaced with TE and TM mode arms.

As can be derived from Eq. (4.13), in an athermal MZI, we would have ($\frac{d\lambda_m}{dT} = 0$), with TE and TM polarizations obtained when both arm lengths are related by:

$$\frac{L_{TE}}{L_{TM}} = \left.\frac{TO_{TM}}{TO_{TE}}\right|_{\lambda_0,\, T_0} \tag{5.2}$$

Here, T is the temperature and TO is the thermo-optic coefficient of the corresponding arms. For a particular waveguide geometry, wavelength λ_0, and temperature T_0, the arm lengths are chosen in such a way that the above condition is satisfied. Because this condition depends on temperature and wavelength, it leads to a zero spectral shift only for a certain temperature, and wavelength. Also, the TO coefficient depends on the core width, height, and sidewall slope, which are prone to fabrication tolerances. In good approximation, the TO coefficient can be assumed to be temperature independent. Taking into account the athermal condition, the thermal sensitivity of the spectrum position becomes:

$$\frac{d\lambda_m}{dT} = \frac{TO_{TM} \left.\frac{TO_{TE}}{TO_{TM}}\right|_0 - TO_{TE}}{n_{g,TM} \left.\frac{TO_{TE}}{TO_{TM}}\right|_0 - n_{g,TE}} \tag{5.3}$$

It follows from Eq. (5.2) that L_{TM} is larger than L_{TE} because TO_{TE} is larger than TO_{TM}, and for any core width. Combining Eq. (5.1) and Eq. (5.3) gives the required arms lengths to have an athermal MZI with a particular FSR is given by:

$$L_{TE} = \frac{\lambda^2}{\left(n_{g,TM}\frac{TO_{TE}}{TO_{TM}} - n_{g,TE}\right)\Delta\lambda_{FSR}}, \tag{5.4}$$

$$L_{TM} = \frac{\lambda^2}{\left(n_{g,TM} - n_{g,TE}\frac{TO_{TM}}{TO_{TE}}\right)\Delta\lambda_{FSR}} \tag{5.5}$$

For simulation, tapers can be approximated by a staircase profile which can be seen as a concatenation of short-length waveguides with increasing or decreasing widths. When taking enough staircase sections, the summation of all tapers will converge to an integral of the propagation. Using this lumped approximation, tapers are easy to add to a circuit simulation. When they are included in the MZI arms, the above equations for the required arm lengths need to be changed in such a way that the athermal point and FSR remain the same after the inclusion of the tapers. The required TM arm length, excluding the lengths of the tapers, becomes:

$$L_{1,d} = \frac{\frac{\lambda^2}{\Delta\lambda_{FSR}} - P}{n_{g,1,d} - n_{g,2,d}\frac{TO_{1,d}}{TO_{2,d}}}, \tag{5.6}$$

where the term P includes the effect of the tapers, which is given by

$$P = \sum_t n_{g,1,t}L_{1,t} - \sum_t n_{g,2,t}L_{2,t} - \frac{n_{g,2,d}}{TO_{2,d}}\left(\sum_t L_{1,t}TO_{1,t} - \sum_t L_{2,t}TO_{2,t}\right). \tag{5.7}$$

The summations are performed over the different staircase sections constituting the taper. Subscripts 1 and 2 denote the TM and TE arm, respectively; and subscript d denotes the regular waveguide connected to the tapers. The expression for the TE arm is similar. An athermal MZI is obtained as follows. We assume that the desired arm widths (e.g. each 600 nm) and the widths of the SPR waveguides are known. First, the tapers are divided in sections of constant width, which allows to calculate P. Then, for a specified FSR, the arm lengths are calculated. The position of the filter spectrum can be modified in the design by slightly changing the arm widths or arm lengths. To have minimum and maximum transmission at the output ports, at a certain wavelength λ_0, the width and/or length of the waveguides need to be changed in such a way that the filter order $m(w, L)$ is an integer or half-integer. The calculation of m is the same as in Eq. (4.5), but when tapers are included, it also includes a summation over the taper sections. For example, for a transmission peak at the cross port, m needs to be an integer and the corresponding width w for fixed arm lengths is found with the following optimization

$$\underset{w}{\arg\min}\left(m(w, L_0, \lambda_0) - \text{round}(m(w_0, L_0, \lambda_0))\right), \tag{5.8}$$

where w_0 and L_0 are the initial width and length of the waveguides. It is sufficient to change the width of one arm. The optimization of the length for a fixed width is similar. The change in width or length also slightly changes the FSR. This can be avoided by performing an iteration between the calculation of the required arm lengths for a certain geometry and FSR, and the optimization for waveguide width. Because of a small change in width or length, the change in FSR is also small, and often an iteration is not needed.

Our demonstration device is designed for FSR of 9 nm. The width of TE and TM mode waveguide is kept as 600 nm wide each to achieve a low loss and small phase errors. Also, by using these widths a very compact filter can be realized which is due to the large difference in their corresponding TO coefficients difference, as shown in the Fig. 5.1.

5.5 Fabrication

The device has been fabricated in the imec 200 mm CMOS pilot line, using silicon-on-insulator wafers with 220 nm of silicon and 2 μm of buried oxide. The details of this process have already been discussed in chapter 2. The fabricated device, one of the test SPR structures and its cross which are fabricated separately as shown in Fig. 5.7 and Fig. 5.8, respectively.

The input TE-polarized light passes through the SPR that splits and converts half of the power into TM polarization. The TM light goes to the upper arm, while the remaining half of the input power remains in the lower arm as the TE polarized light. Finally, both polarizations combine at the MZI output using a similar SPR as a combiner. The device also includes adiabatic tapers before and after the SPR section. The need for an adiabatic taper is to prevent coupling between the fundamental mode and the higher order modes.

Compact curved grating couplers designed for operation in the 1550 nm wavelength range are added to couple light in and out of the device [9]. Depending on the arm, a coupler for either the TE or the TM polarization is used. The length of designed TM arm of the MZI is 213.25 μm which is longer than TE arm of 139.25 μm. It is due to the lower TO coefficient of TM mode (see Eqs. (5.2)-(5.5)).

The fabricated length of the SPR is 10 μm and the gap is 190 nm. The width of the SPR waveguides is 560 nm and 310 nm respectively, as measured from a FIB cross section image. The fabricated width of both the upper TM arm and lower TE arm is 560 nm. Adiabatic tapers in the TE arm are shown in the inset of Fig. 5.7. Since the upper arm guides the TM mode, larger bends with a radius of 25 μm are used in the design for the lower radiation loss. In the upper arm of the device there are no tapers as the width of the upper arm and the SPR waveguide width is the same. We have also incorporated separate test structures for the SPR with a sweep of the coupling length and widths. The footprint of the device is $188 \times 125 \mu m^2$.

5.6 Measurements and Analysis

All the devices are characterized in *continuous wave* (CW) regime. The measurement set-up consists of a CW laser source, followed by a polarization controller, the sample to be characterized, and a power meter and

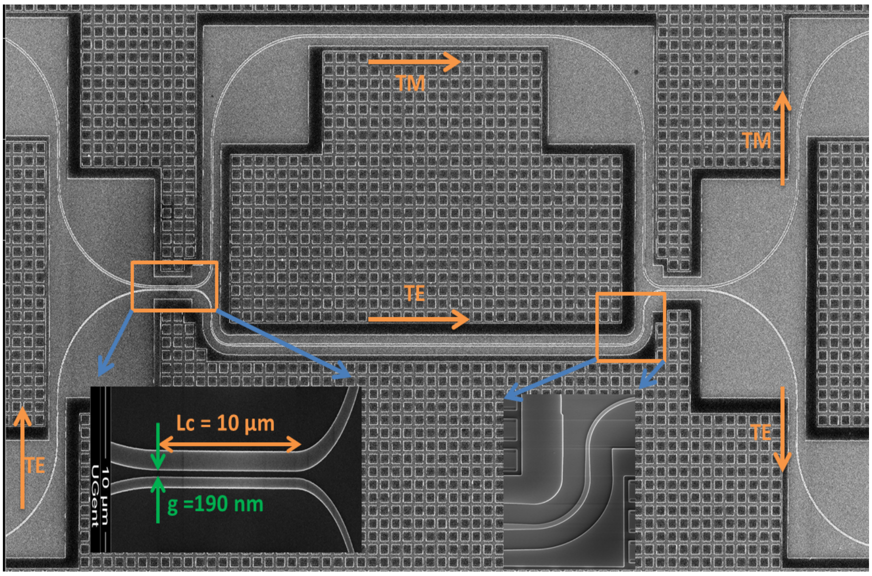

Figure 5.7: SEM image of fabricated athermal MZI filter with zoomed in SPR and waveguide tapering in the lower arm

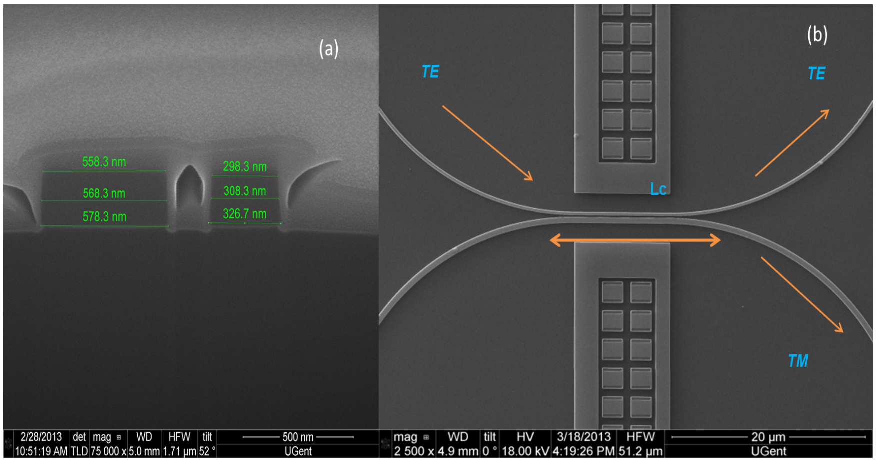

Figure 5.8: (a)SPR cross section and (b) SPR test structure showing input TE mode, coupling length and outputs

optical spectrum analyzer as mentioned in Fig. 2.13. The fiber tails, guiding the light in and out of the grating couplers, are mounted under a small angle ($\sim 10^{\circ}$) from the vertical. After alignment and identification of the components, the spectrum of the components is measured automatically. Before starting the measurements, the polarization controller is adjusted in such a way that there is only TE or TM polarization at the input of the component, depending on the need. As the surface grating couplers are optimized for a certain polarization, the correct input polarization is obtained by changing the polarization so that the output power is maximum at a certain component, e.g. a reference waveguide. This polarization is maintained during the measurement of all components.

To determine the thermal influence, the spectrum of the components is measured at different temperatures. This is done by fixing the chip on top of a thermally controlled chuck containing a resistive heater and temperature sensor as shown in Fig. 4.10. Between the heater and the set-up is a thermal insulator to protect the set-up and to have a uniform temperature profile on the heater. Before the temperature is changed, the fibers need to be lifted, otherwise they can make contact with the substrate due to thermal expansion, which can damage the fiber tip. After each change in temperature, the set-up needs to stabilize for a sufficiently long time. Changes in temperature result in a slowly vibrating fiber. Once the position of the fiber is stable, the chip needs to be realigned because of the thermal expansion. Once the chip is realigned, a new sweep is performed, with a 5 pm step.

The measured spectrum includes the transmission of the MZI, and also the transmission of the input and output grating couplers. In order to obtain only the spectrum of the device under test, the measured spectrum is normalized. For a component with TE input and output, and transmissions expressed in dB, the spectrum is normalized by subtracting the transmission of the reference waveguide from the total transmission. The reference waveguide has the same grating couplers as the component, but the component itself is replaced by a single wire waveguide. When input and output have a different polarization, the normalization is done as

$$T_{norm,dB} = T_{tot,dB} - \frac{T_{ref,s,dB} + T_{ref,p,dB}}{2}, \tag{5.9}$$

where $T_{ref,s,dB}$, and $T_{ref,p,dB}$ are the transmission of the TE and TM reference waveguides expressed in dB.

5.6.1 Parameter Extraction

It is instructive to compare the group index and the TO coefficient used in the simulations with the values extracted from the measurements. The extracted optical parameters can be fed back to the circuit simulator to obtain designs

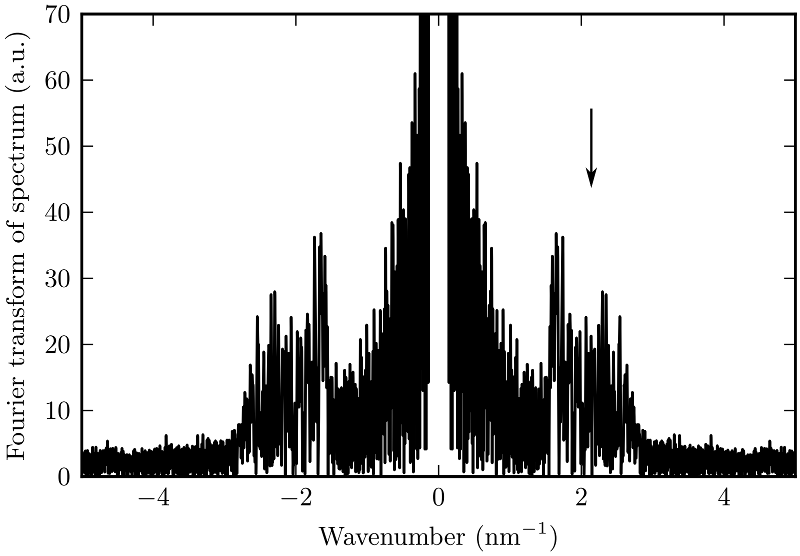

Figure 5.9: Fourier transform of transmission spectrum.

with a well predicted behaviour. The group index can be retrieved from the minima and maxima of the measured transmission spectrum. Because the minima points are least affected by Fabry-Perot interference fringes, generally only these values are taken into account. These data points, however, are only a fraction of the whole spectrum. It is better to fit the entire transmission spectrum to an analytical model of the MZI, as this will use all the available information and result in more accurate results.

When looking in detail at the transmission spectrum of the MZI, we notice Fabry-Perot interference fringes. Those fringes are due to reflections at the SPRs and grating couplers. The Fourier transform of a transmission spectrum is shown in Fig. 5.9. The side lobes visible in the Fourier transform are due to the ripple in the transmission spectrum. These ripples can be filtered out of the spectrum to facilitate optical parameter extraction.

By using a transmission matrix description, the MZI can be modeled by the power transmission to the cross or bar port. The power transmission to cross port is

$$P_{cross} = K_{cross}(\kappa, \tau, \alpha L) + 4\kappa_1\kappa_2\tau_1\tau_2\,\mathrm{e}^{-(\alpha_1 L_1+\alpha_2 L_2)}\cos^2\left(\frac{\Delta\phi}{2}\right), \tag{5.10}$$

where κ and τ are the self coupling and the cross coupling coefficients; α is the attenuation coefficient; and $\Delta\phi$ is the phase difference between both the arms. The power transmission to the bar port is in antiphase given by

$$P_{bar} = K_{bar}(\kappa, \tau, \alpha L) + 4\kappa_1\kappa_2\tau_1\tau_2\,\mathrm{e}^{-(\alpha_1 L_1+\alpha_2 L_2)}\sin^2\left(\frac{\Delta\phi}{2}\right). \quad (5.11)$$

When we assume $a = \mathrm{e}^{-\alpha_1 L_1} = \mathrm{e}^{-\alpha_1 L_1}$, we get

$$K_{cross}(\kappa, \tau, \alpha L) = a^2\left(\kappa_2^2\tau_1^2 + \kappa_1^2\tau_2^2 - 2\kappa_1\tau_1\kappa_2\tau_2\right), \quad (5.12)$$

$$K_{bar}(\kappa, \tau, \alpha L) = a^2\left(\kappa_1^2\kappa_2^2 + \tau_1^2\tau_2^2 - 2\kappa_1\tau_1\kappa_2\tau_2\right). \quad (5.13)$$

To extract the group index and the TO coefficient, it is assumed that the effective index is of the form

$$n_{eff} = n_0 + n_1\Delta\nu + n_2\Delta T + n_3\Delta T\Delta\nu, \quad (5.14)$$

so that the group index and the TO coefficient are linearly dependent on frequency as

$$n_g|_{T_0} = n_{g,0} + n_{g,1}\Delta\nu \quad (5.15)$$

$$TO = TO_0 + TO_1\Delta\nu \quad (5.16)$$

If the amplitude of the power transmission is assumed to be a second order polynomial, then the fitting equation is

$$P(\nu, T) = (a_0\nu^2 + a_1\nu + a_2)\cos^2\left(a_3\nu^2 + a_4\nu + a_5\nu T + a_6\nu^2 T + a_7\right) + a_8 \quad (5.17)$$

This is a two dimensional fitting problem. The term a_7 takes into account imperfections in the model. Coefficients a_3 to a_6 take into account the frequency and temperature dependence of the effective index; and a_8 takes into account the non-infinite extinction ratio due to deviations in the coupling coefficients. The thermal behaviour of the coupling coefficients can also be included by adding temperature dependent terms in the amplitude factor. We fit the measurements to this model with a least squares optimization algorithm. The extracted parameters from the transmission spectra of one output port can be compared with the extracted parameters from the other output port, or the transmissions of both ports can be fed into the fitting algorithm together in order to increase the number of data points.

The least squares optimization algorithm has the tendency to converge in local minima. Therefore, it is important to provide a good initial guess of the fitting coefficients. The fitting algorithm is structured as follows. First the peaks and troughs of a measured spectrum are searched for. From the maxima, an initial guess of the coefficients in the amplitude factor is made. This is done by fitting a second order polynomial through these maxima. An initial guess of the period is found from the distance between two successive minima. The fitting algorithm returns the extracted parameters, which are fed back into fitting algorithm as initial guess and the fitting is repeated. This gives a more reliable result.

From the fitted parameters, the group index, TO coefficient, and the thermal sensitivity are retrieved by matching the coefficients in the fitting formula with the coefficients in the power transmission formula. From the amplitude factor, the frequency dependent behaviour of the coupling coefficients can be extracted. The temperature sensitivity of the spectrum as a function of the fitting coefficients is

$$\frac{d\lambda}{dT} = \frac{a_5\lambda^2 + a_6 c\lambda}{a_4\lambda + a_5\lambda T + 2a_6 cT + 2a_3 c}, \tag{5.18}$$

where c is the speed of light in vacuum. The temperature dependent group index and the TO coefficient extracted from the effective index (5.14) are

$$\begin{aligned} n_g &= n_0 + n_1\nu_0 + (n_2 + n_3\nu_0)\Delta T + 2(n_1 + n_3\Delta T)\Delta\nu, && (5.19)\\ TO &= n_2 + n_3\Delta\nu. && (5.20) \end{aligned}$$

For the conventional MZIs, the group index extraction method is mentioned in chapter 2. To find the TE and TM group index of MZIs with different polarizations, we need to perform a fitting with at least two MZIs with different arm lengths but with the same geometry of the waveguide cross section. The coefficients in the fitting equation are of the form $n_{i,1}L_1 - n_{i,2}L_2$.

5.6.2 Measurement and Designed Device Analysis

The designed, measured and simulated results of the device transmission and the associated thermal drift during the wavelength sweep are shown in Fig. 5.10. The device has been designed to be athermal at a central wavelength of 1540 nm as shown in Fig. 5.10(a). The measured normalized transmission at 30 °C, 50 °C and 80 °C is plotted in Fig. 5.10(c). The simulations of the designed device have been performed with the circuit simulator Caphe from Luceda Photonics [10]. Waveguide tapering is also included in the simulation, taking into account the changes in the mode confinement and the TO coefficient. The TE arm widths used to obtain the simulated spectra in Fig. 5.10(b) are (532, 461, and 322) nm. This is a deviation of maximally 5% compared to the measured widths. The tapers connecting wider and narrower waveguides are simulated as a cascade of discrete waveguide sections. In a first approximation, the effective index can be assumed to have a linear wavelength dependency, or similarly, the group index can be assumed to be constant. Although, when full dispersion behaviour is taken into account, as is done in this section, yet the simulated spectrum is more consistent with the measured one. The splitting ratio of the couplers in the simulation is taken as 50:50. This matches well with the simulations of the device with the actual (fabricated) geometry, as obtained from the cross-section.

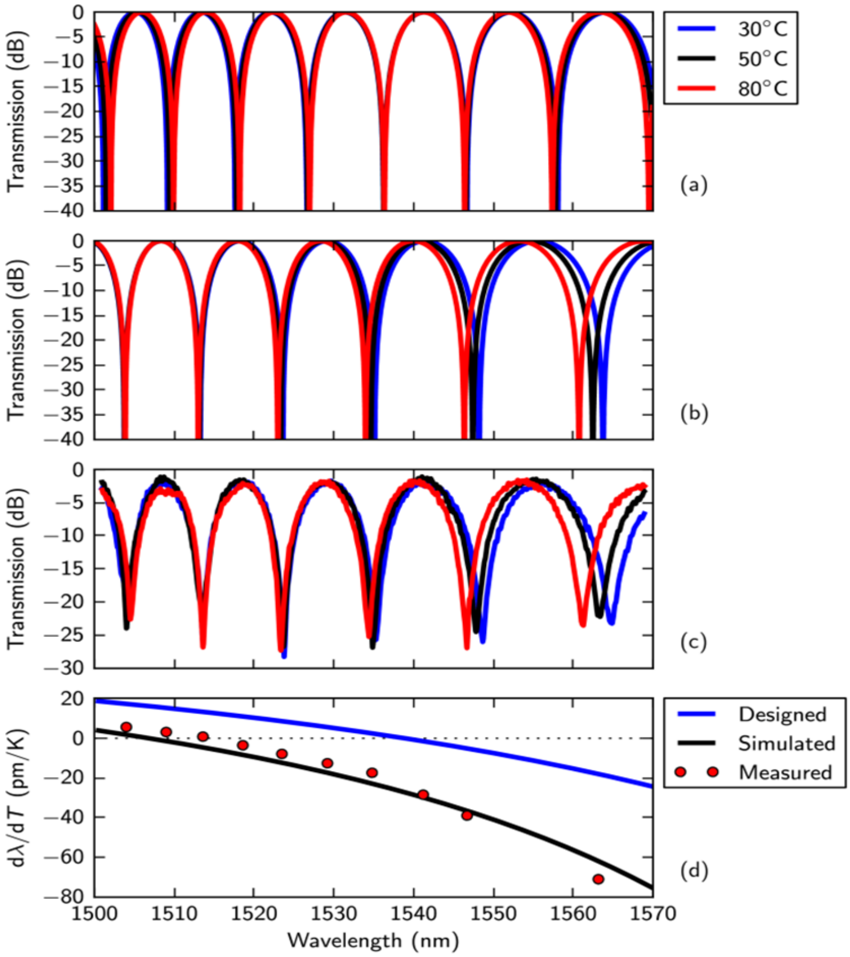

Figure 5.10: (a) Transmission of designed device to be athermal at center wavelength of 1540 nm, (b) simulated transmission of fabricated device, after taking cross section, and (c) measured transmission of fabricated device at three different temperatures. (d) Thermal sensitivity of (a), (b) and (c), the a-thermal region shifted by 20 nm due to fabrication variations.

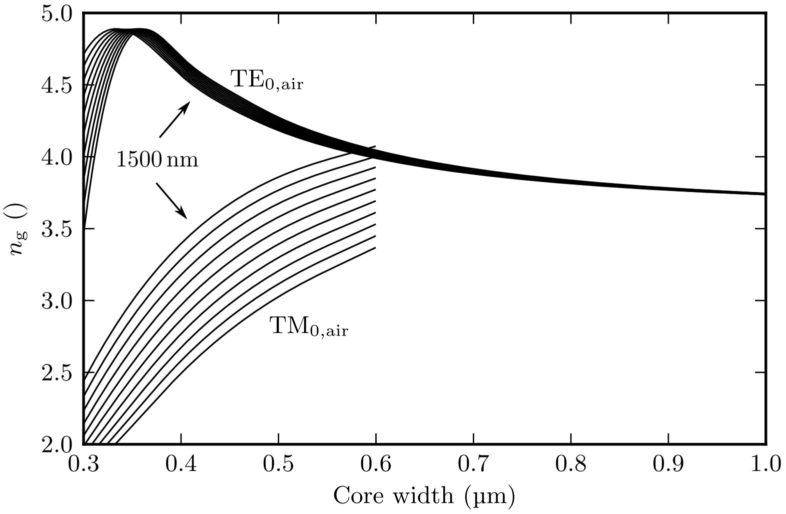

Figure 5.11: Group index as a function of core width for different wavelengths $\lambda = (1500, \ldots, 1600)$ *nm.*

The measured thermal sensitivity of the device is less than 8 pm/K over 30 nm of wavelength range and is shown in Fig. 5.10(c). The measured FSR of the device changes from 9.5 nm at the lower wavelengths to 13.5 nm at the longer wavelengths. This is due to the large wavelength dependence of the group index of the TM mode. When a constant group index is assumed, the FSR is constant in frequency. Looking at the graph in Fig. 5.11, which shows the group index for wavelengths between 1500 nm and 1600 nm, we see that the group index of the TM mode cannot be considered as constant with respect to wavelength. For decreasing wavelength, the group index of the TM mode increases.

Because of the change in the waveguide dimensions during fabrication, the athermal region of the device shifts from 1540 nm to 1515 nm. Fig. 5.10(d) shows the thermal sensitivity of the device for the original design, the fabricated design, and the post-fabricated simulation based on the cross section data. The measured sensitivity points are obtained from the transmission minima of both the cross and bar port. Also the sensitivity extracted from the fitted transmission is included. For this, the transmission spectra at 4 temperatures (including 65 °C) are fitted with respect to temperature and wavelength. For higher wavelengths, the fitted sensitivity matches well with the sensitivity obtained from the spectral minima. At lower wavelengths, there is less overlap between the fitted and measured spectra but the difference between both obtained sensitivities is higher. The simulation of $\frac{d\lambda}{dT}$ is obtained by using Eq. 5.3 which also takes into account the tapers. When

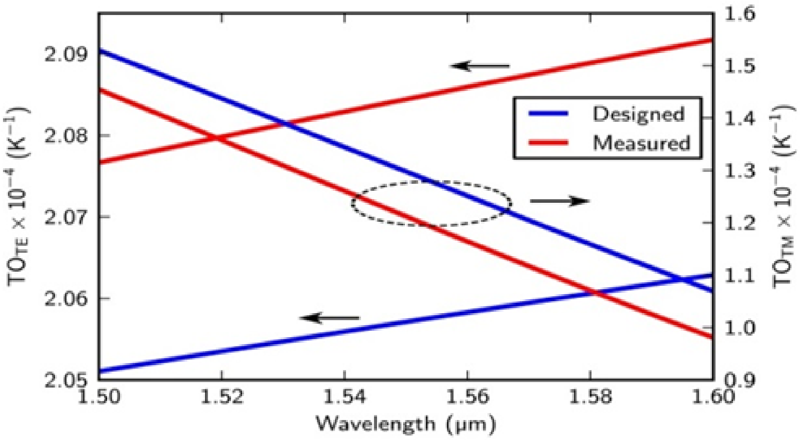

Figure 5.12: Thermo-optic coefficients of TE and TM mode waveguides for the designed and the measured waveguide widths

using the same geometry and effective indices of the waveguide sections, the result of this equation is virtually identical with the sensitivity extracted from the spectra simulated with Caphe.

Furthermore, there is also a deviation of 5% between the measured width and simulated width to obtain a simulated spectrum close to the measured one. The uncertainty of SEM measurements is 3%. When the waveguide widths obtained by SEM measurements are used in the simulations, an athermal wavelength at 1521 nm would be expected. The component is designed for a wavelength of 1531 nm which takes into account the waveguide offsets provided by imec. The discrepancy between the measurements and the simulation using the waveguide widths from the SEM measurements is due to the mismatch between the actual optical parameters and the parameters used in the circuit simulator.

It is also found that the TO coefficients are quite wavelength dependent and therefore the device spectrum is red shifted with the increasing temperature for the wavelengths lower than the athermal point, while at longer wavelengths the spectrum is blue shifted. The TO coefficients for the TE and the TM mode of the designed and measured waveguide widths are shown in Fig. 5.12. It means for wavelengths larger than the athermal point, $\frac{d\lambda_m}{dT}$ is negative, while it is positive for wavelengths smaller than the athermal point.

We have also characterized the SPR separately. The transmission spectrum of the SPR for cross coupling is shown in Fig. 5.13 for varying coupling lengths. It shows that the coupling length of 10 μm is the closest to the desired 3 dB of power transfer from the input to the TM mode in the other arm.

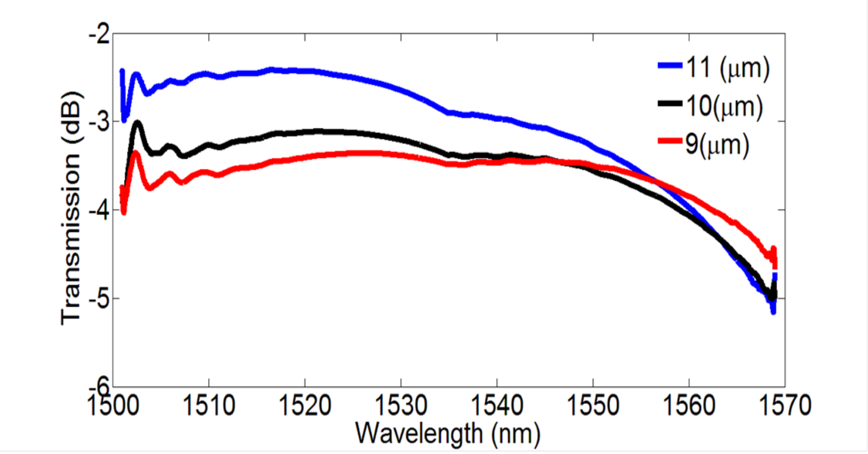

Figure 5.13: Measured transmission of the SPR test structure for different coupling lengths

The variation of 1 μm from this length shows a 0.5 dB variation in transmission in the lower wavelength side of the spectrum. The coupler design is sufficiently tolerant so that a width variation of couple of nanometers in fabrication will not have a detrimental impact. The good splitting ratio also translates into a high extinction ratio of over 25 dB in the measured MZI.

5.7 Footprint Comparison and Sensitivity

When an MZI is optimized only for minimum arm lengths, the arms should have a uniform width over their whole length. Table 5.1 gives an overview of the device footprint of athermal MZIs with the same, or with different modes in each arm, whether or not optimized for minimum arm lengths. The arm widths for the optimization are taken in the interval $[350, 1000]$ nm.

A figure of merit for the device footprint of the designed MZIs is the length of the longest arm normalized with respect to the arm length difference of a conventional MZI:

$$\Delta L = \frac{\lambda^2}{n_g FSR} \tag{5.21}$$

For an athermal TE-TM configuration, the length of the TM arm is longer than the TE arm length because of the athermal condition is $\frac{L_{TM}}{L_{TE}} = \frac{TO_{TE}}{TO_{TM}}$. It is larger than 1, as TO_{TE} is larger than TO_{TM} in the core width range of interest.

Mode arm 1 – Mode arm 2	w_1 (nm)	w_2 (nm)	$\frac{L_2}{\Delta L_{conv}}$ ()	Optimized for
TE – TE	350	1000	6.91	Minimum arm length
TM – TM	350	1000	5.90	Minimum arm length
TE – TM	1000	350	2.90	Minimum arm length
TE – TM	450	450	3.31	–

Table 5.1: Comparison of device footprint between athermal MZIs with the same, or with different polarizations in both arms.

When the optimum widths are compared with the graph of the TO coefficients, it can be seen that the device footprint is minimum when the difference in the TO coefficients is largest. For TE or TM polarizations, the difference in TO coefficients is largest for a very small and a very large waveguide width. For TE and TM polarizations, the difference in TO coefficients is larger while the device footprint is smaller compared to waveguides with only TE or TM polarizations.

Compared to a TE-TM MZI, the thermal sensitivity of a TE-TE MZI can be small over a large wavelength range. A small sensitivity over a large wavelength range is obtained when the TO coefficient of the mode in the second arm has the same wavelength dependence as the TO coefficient of the mode in the first arm scaled by a factor $\left.\frac{TO_2}{TO_1}\right|_0$. The difference between both TO coefficients also needs to be as large as possible to obtain an acceptable device footprint. However, as can be seen in Fig. 5.14, the TO coefficients of the TE and TM modes do not follow the same slope for any combination of waveguide widths of interest. The factor $\left.\frac{TO_2}{TO_1}\right|_0$ is different from one which makes the wavelength dependent sensitivity higher. This explains that an athermal MZI based on TE and TM polarizations has a smaller athermal wavelength range than an athermal MZI with only TE polarization.

5.8 Applications

5.8.1 Sensing

Simulations are performed to test the sensing capabilities of the dual polarization MZI. Because we use two polarizations that have a very different overlap with the upper cladding, the MZI device can be used as a sensor without the need of a protective overcladding or selective sensing window

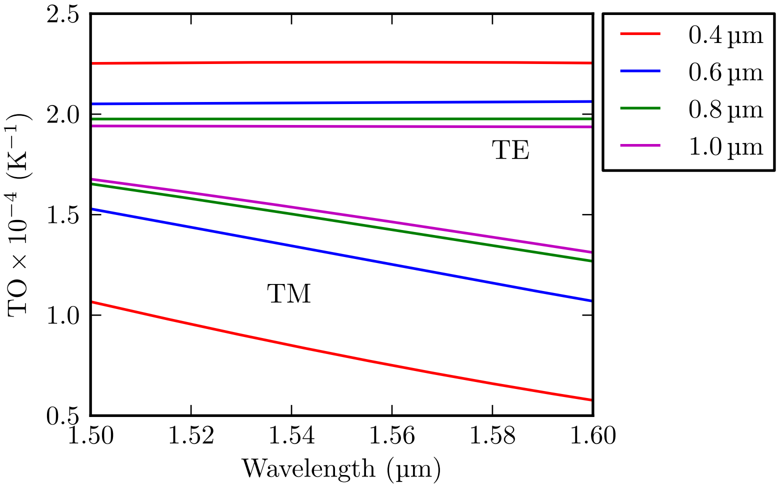

Figure 5.14: TO coefficients of TE and TM polarization at different waveguide widths for air top-cladding.

on one of the arms. We assume that the device is covered with a liquid layer of certain refractive index which varies from 1.31 to 1.35 [11]. We also assume that the TO coefficient of the aqueous solution is the same as that of DI water [12]. We have simulated the wavelength shift of the constructive interference in three situations: both arms exposed to the same cladding change, and the TE arm and TM arm separately. This has been simulated for two different temperatures of 20 °C and 50 °C respectively. The absolute athermal wavelength would shift because of the different cladding index (fluid instead of air) but it is still within the C-band.

Fig. 5.15 shows the response of the sensor. When we increase the cladding index n_c on the TE arm only, we get a blue-shifted wavelength response. When we apply the same for the TM arm only, we get a much stronger shift, but towards the longer wavelengths. When the cladding of the entire device is changed, the net response is red-shifted to a somewhat lesser degree. The resonance wavelength shifts linearly with cladding the refractive index change. The responsivity of 635 nm/RIU is observed in simulation which corresponds to a three-fold improvement when compared to a pure TE waveguide. Moreover, the sensor response is temperature independent, and the fact that the entire sensor can be exposed to the analyte which can simplify the fluidic design and fabrication. The sensor simulations provided are indicative figures and the device can be improved drastically by designing as a dedicated sensor. The key observation is that the temperature changes do not affect the performance of the sensor.

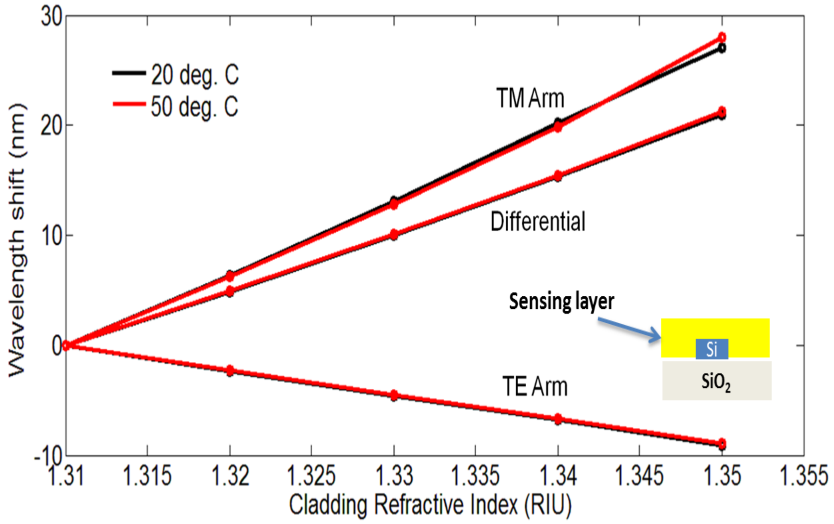

Figure 5.15: Simulated shift in the resonant wavelength of the separate arms TM, TE and device (differential) with cladding refractive index variation in refractive index unit (RIU) at two different temperatures.

5.9 Conclusion and Discussion

In this chapter, we have demonstrated a compact temperature insensitive MZI filter using a splitter and polarization-rotating section. The measured result shows that the temperature insensitivity is less than 8 pm/ K over a wavelength range of 30 nm.

The footprint of the device is one-third of the single-polarization athermal MZI filter and we show how it can be further reduced. The novel concept gives a number of flexibility to the designer in terms of choosing waveguide widths with different polarizations without significantly changing the performance of the athermal filter.

Simulated results show that the device can also be useful for bio-sensing applications on chip where thermal sensitivity is an issue. These devices can be integrated together to make efficient and compact athermal higher-order filters and de-multiplexers.

This wavelength of operation can be further improved [13]. In this paper authors have extended our work and performed the second order thermal compensation and stabilized the FSR. Instead of using the fundamental TE, they have used first order TE mode in other arm of the MZI.

References

[1] S. Dwivedi and W. Bogaerts. *Integrated photonic devices with reduced sensitivity to external influences*, July 7 2015. US Patent 9,075,251.

[2] Mutsunori Uenuma and Teruaki Motooka. *Temperature-independent silicon waveguide optical filter*. Opt. Lett., 34(5):599–601, Mar 2009.

[3] Biswajeet Guha, Alexander Gondarenko, and Michal Lipson. *Minimizing temperature sensitivity of silicon Mach-Zehnder interferometers*. Opt. Express, 18(3):1879–1887, Feb 2010.

[4] S. Dwivedi, H. D'heer, and W. Bogaerts. *Maximizing Fabrication and Thermal Tolerances of All-Silicon FIR Wavelength Filters*. Photonics Technology Letters, IEEE, 27(8):871–874, April 2015.

[5] S. Dwivedi, H. D'heer, and W. Bogaerts. *A compact temperature insensitive filter using splitter polarization-rotating section*. In Group IV Photonics (GFP), 2013 IEEE 10th International Conference on, pages 29–30, Aug 2013.

[6] Liu Liu, Yunhong Ding, Kresten Yvind, and Jørn M. Hvam. *Silicon-on-insulator polarization splitting and rotating device for polarization diversity circuits*. Opt. Express, 19(13):12646–12651, Jun 2011.

[7] Daoxin Dai and John E. Bowers. *Novel concept for ultracompact polarization splitter-rotator based on silicon nanowires*. Opt. Express, 19(11):10940–10949, May 2011.

[8] Philippe P. Absil, Peter Verheyen, Peter De Heyn, Marianna Pantouvaki, Guy Lepage, Jeroen De Coster, and Joris Van Campenhout. *Silicon photonics integrated circuits: a manufacturing platform for high density, low power optical I/O's*. Opt. Express, 23(7):9369–9378, Apr 2015.

[9] F. Van Laere, T. Claes, Jonathan Schrauwen, S. Scheerlinck, W. Bogaerts, D. Taillaert, L. O'Faolain, D. Van Thourhout, and R. Baets. *Compact Focusing Grating Couplers for Silicon-on-Insulator Integrated Circuits*. Photonics Technology Letters, IEEE, 19(23):1919–1921, Dec 2007.

[10] `http://www.lucedaphotonics.com/`.

[11] Katrien De Vos, Irene Bartolozzi, Etienne Schacht, Peter Bienstman, and Roel Baets. *Silicon-on-Insulator microring resonator for sensitive and label-free biosensing*. Opt. Express, 15(12):7610–7615, Jun 2007.

[12] Young Ho Kim, Seong Jun Park, Sie-Wook Jeon, Seongmin Ju, Chang-Soo Park, Won-Taek Han, and Byeong Ha Lee. *Thermo-optic coefficient measurement of liquids based on simultaneous temperature and refractive index sensing capability of a two-mode fiber interferometric probe*. Opt. Express, 20(21):23744–23754, Oct 2012.

[13] Peng Xing and Jaime Viegas. *Broadband CMOS-compatible SOI temperature insensitive Mach-Zehnder interferometer*. Opt. Express, 23(19):24098–24107, Sep 2015.

6

Maximizing Fabrication and Thermal tolerances of All-Silicon FIR wavelength filters

In the chapters (4-5) we have proposed and demonstrated a passive compensation of all silicon wavelength filters. In this chapter, we extend this concept, and explore the possibility of fabrication tolerances along with thermal tolerances.

6.1 Introduction

One of the most pronounced weaknesses of silicon nanophotonics is the need of extremely precise fabrication, especially for passive wavelength filter devices. The high index contrast and submicron waveguide dimensions would translate any change in waveguide width and height into a substantial change in the effective refractive index [1].

The fabrication processes have considerably improved with the availability of advanced lithographic and etching techniques. The major fab-lines move from 200 mm to 300 mm where the line-width variation is already in the order of a few nanometers [2–4] and the loss of typical single mode strip waveguides are less than a 1 dB/cm. However, these final few nano-meter precision still poses a very difficult issue for the accuracy of wavelength filters.

Fabrication variations can be actively compensated (e.g. with thermal tuning), but this drives up the power consumption and complicates the device with active control circuitry. Pre-fabrication or post-fabrication trimming of the components can be used to correct the effects of the last nanometer fabrication offsets. However, it comes with a significantly increased cost of the whole fabrication process [5, 6].

In this chapter, we demonstrate a technique to make a wavelength filter tolerant to linewidth variations by design, without changing the fabrication process itself. We show that it is indeed possible to get a fabrication tolerant MZI filter by using different mode confinement in the arms of the filter. Also, since simultaneous fabrication and thermal tolerances are needed to make the SOI platform truly robust, we extend the technique and show that it can used to make the circuit tolerant both to linewidth variations and ambient temperature fluctuations. Simulations show that the technique can be used for higher order filters with multiple channels.

6.2 Proposed Method

The wavelength sensitivity expression of any FIR filter is given in Eq. 4.2 as mentioned in chapter (4).

The wavelength shift of an MZI is around 1 nm and 1.4 nm for 1 nm change in the waveguide width and thickness, respectively. These variations hold good for all waveguide based FIR filtering devices on SOI.

To compensate the wavelength sensitivity due to the fabrication variations, we introduce design variations such as different waveguide width in each arm as mentioned in section 4.3. The modified expression for the sensitivity then becomes the modified form of Eq. 4.13:

$$\frac{d\lambda}{dX} = \frac{\lambda}{n_{g1}.L_1 - n_{g2}.L_2}.(\frac{dn_{eff1}.L_1}{dX} - \frac{dn_{eff2}.L_2}{dX}) \tag{6.1}$$

which we try to minimize. This is a first-order approximation. Here, X can be the waveguide width w, height h instead of temperature T or any other influence. We assume here that the influence affects the entire device uniformly. λ_m is the wavelength of operation, and n_g is the group index.

For a device tolerant to width variations, the condition for zero sensitivity at wavelength and for a given free spectral range (FSR) becomes:

$$\frac{L_1}{L_2} = \left.\frac{\frac{\partial n_{eff,2}}{\partial w}}{\frac{\partial n_{eff,1}}{\partial w}}\right|_{\text{geometry}, \lambda_0, T_0} . \tag{6.2}$$

For the filter to be width tolerant, the length ratio of the arms should be inversely proportional to the sensitivity of the effective index of the waveguides of the arms. Here, we assume that the linewidth change induced by the fabrication process is similar to the waveguides in the two arms. This is generally true if the linewidth change is caused by global or long-range effects, such as lithographic dose variation or a change in etch rate, and the device is sufficiently compact.

To make the device fabrication as well as thermally tolerant, we introduce orthogonal polarizations (TE and TM) in the two arms of the filter as mentioned in chapter 5. The details of thermal compensation of a similar kind of device are explained in section 5.2. For thermal tolerance, the wavelength sensitivity with respect to temperature $\frac{d\lambda}{dT}$ becomes zero and Eq. 6.1 should satisfy:

$$L_{TM}\frac{dn_{eff,TM}}{dT} = L_{TE}\frac{dn_{eff,TE}}{dT} \tag{6.3}$$

where L_{TM}, L_{TE} and $\frac{dn_{eff,TM}}{dT}$, $\frac{dn_{eff,TE}}{dT}$ are the length of the TM, TE arm and their corresponding waveguide TO coefficients. Thus, the combined condition of being tolerant to width and temperature at wavelength λ_0 and at temperature T_0 for a given FSR becomes:

$$\frac{L_1}{L_2} = \left.\frac{TO_2}{TO_1}\right|_0 = \left.\frac{\frac{\partial n_{eff,2}}{\partial w}}{\frac{\partial n_{eff,1}}{\partial w}}\right|_0, \tag{6.4}$$

The width sensitivity of an athermal MZI is given by:

$$\frac{d\lambda_m}{dw} = \lambda\,\frac{\frac{\partial n_{eff,1}}{\partial w}\left.\frac{TO_2}{TO_1}\right|_0 - \frac{\partial n_{eff,2}}{\partial w}}{n_{g,1}\left.\frac{TO_2}{TO_1}\right|_0 - n_{g,2}} \tag{6.5}$$

Physically, it means that a variation in width or temperature gives an identical change in phase in each arm. The simulated contour plot of the sensitivity of the spectral position to the width for an athermal MZI is shown in Fig. 6.1 with respect to TE and TM core widths. The simulation shows that there is a region where the sensitivity due to line width variations of waveguide is minimized.

The robustness of the design to width tolerances is experimentally verified by deliberately varying the core width over several designs. In these designs, core width of both arms is equally and uniformly varied over the waveguides, as this is in close approximation to variations introduced by lithographic processes. The tolerance to height variation can be tested by

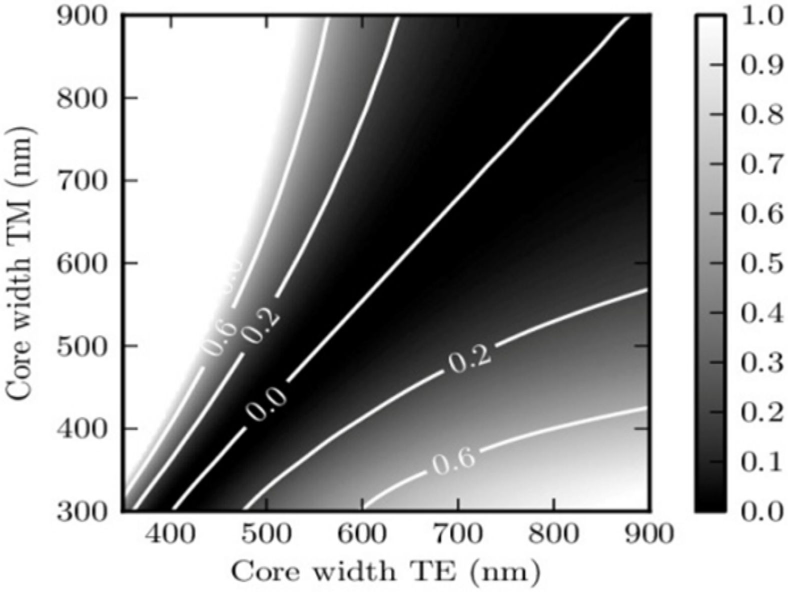

Figure 6.1: Contour plot of $(\frac{d\lambda}{dw}^2)$ *of proposed filter at* $\lambda = 1550\ nm$ *and at T* = $20\,^{\circ}\mathrm{C}$

etching the chip anisotropically. The selective etching of silicon is also possible via wet etching with solvent like KOH. In this way the height of the waveguides are uniformly reduced, while the widths are kept constant. The oxide around the waveguide will also be etched, but most of the optical mode is not situated in this region. Therefore, it will not significantly affect the effective refractive index and thus the tolerant behaviour. However, this method still needs an experimental validation.

This method can be further generalized to width, height and temperature. A filter which is tolerant to all the three parameters could be constructed by using arms with different polarizations which consist of multiple sections with different widths. If we want to compensate more variables, we need to add more free parameters i.e more waveguide sections. The equations describing the sensitivity, will now include a summation over the different arm sections:

$$\frac{d\lambda_m}{dX} = \frac{1}{M}\left(\sum_i L_{1,i}\frac{\partial n_{eff,1,i}}{\partial X} - \sum_i L_{2,i}\frac{\partial n_{eff,2,i}}{\partial X}\right) \tag{6.6}$$

where

$$M = \frac{\sum_i n_{g,1,i}L_{1,i} - \sum_i n_{g,2,i}L_{2,i}}{\lambda} \tag{6.7}$$

When a component has to be athermal, and tolerant to width and height at the same time, then $\frac{d\lambda_m}{dT} = \frac{d\lambda_m}{dw} = \frac{d\lambda_m}{dh} = 0$, has to be fulfilled in the temperature and wavelength region of interest. This is to be solve a linear system with multiple variables. It can also be treated as multiobjective optimization problem.

In this work, we focus on compensation of linewidth variations (primarily caused by etching and lithography) and ambient thermal fluctuations.

6.3 Fabrication Tolerant MZI filter

6.3.1 Design and Fabrication

The schematic of the filter is shown in Fig. 6.2 which is similar to the one mentioned in the Fig. 4.5 but now the design optimization is to minimize the wavelength shift due to width variation i.e. $\frac{d\lambda}{dw}$ instead of thermal variation.

The width sensitivity of the strip waveguide of thickness 220 nm with varying core width at wavelength of 1550 nm is shown in Fig. 6.3. In order to use the optimum widths for the tolerant design we take the decision based on the strategy shown in Fig. 6.3 i.e.

(a) Combination of narrow (w_1) and nominal waveguide (w_2) width ends up either with higher propagation losses and the device is more prone to fabrication errors due to the width of the narrow waveguide.

(b) Combination of nominal (w_2) and wider waveguide (w_4) width ends up with the long adiabatic tapers. In the absence of the long tapers, there is a possibility of excitation of higher order modes.

(c) Keeping both the above points in mind we have chosen to pick the widths (w_2) wide and (w_3) for our design as shown in the Fig. 6.3.

We have designed the devices using the IPKISS parametric design framework from Luceda Photonics. The fabricated MZI filter SEM image is shown in Fig. 6.4.

The filter uses a shallow-etch multimode interference coupler (MMI) as a 50/50 1×2 power splitter, and the same is used as a combiner for a broadband operation. To demonstrate the width tolerant behavior given in Eq. 6.2 the designed width of upper and lower arms is 600 nm ((w_3) and 400 nm (w_2) wide respectively. Their corresponding lengths are 172μm and 45 μm which is designed for 5 nm of FSR.

The devices are fabricated in Imec's standard passive platform. This process uses 200 mm SOI wafers with nominally 220 nm of silicon and 2 μm of buried oxide. The details of this process have been discussed in chapter 2. To demonstrate the tolerant behavior we replicate the device with deliberate relative variations in the line-width in both arms

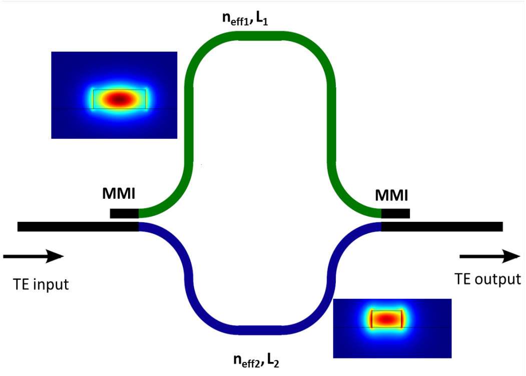

Figure 6.2: Schematic of MZI filter with different waveguide width in each arm

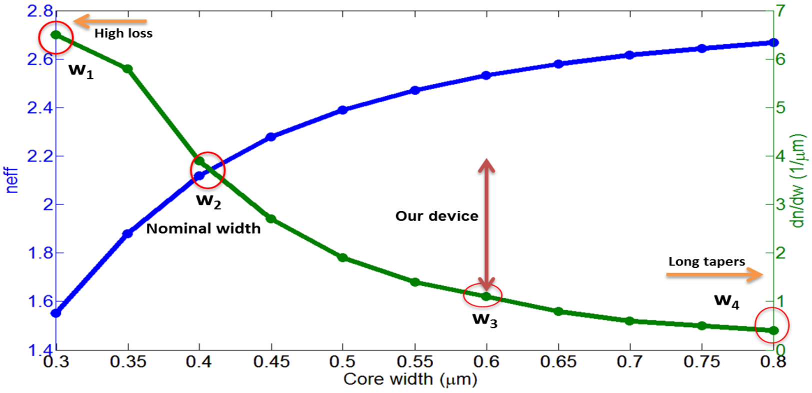

Figure 6.3: Effective refractive index and its sensitivity of strip waveguide of thickness 220 nm with varying core width at wavelength of 1550 nm

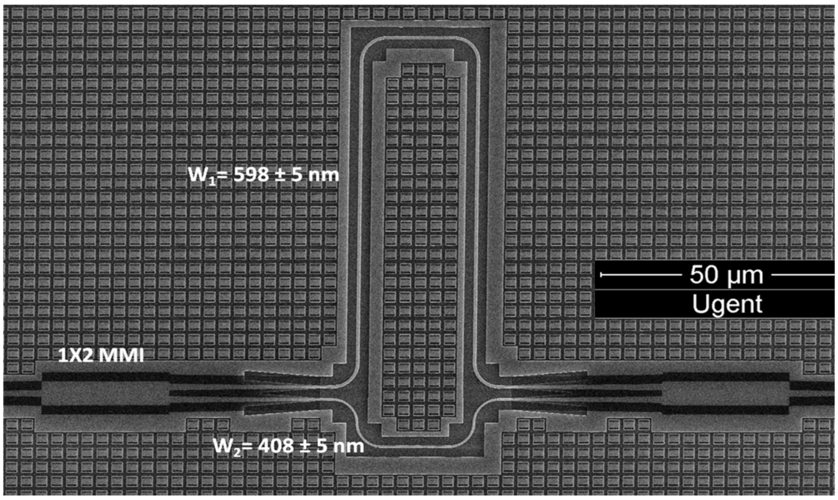

Figure 6.4: SEM image of fabricated MZI filter with shallow etch MMI

over a 20 nm range [1]. A ±10 nm absolute line width variation can be considered as controllable for an optimized, stabilized fabrication process.

6.3.2 Measurements and Analysis

The measured thickness of the silicon waveguide in the presented devices is 218±3 nm. The measured arm width (from SEM inspection) is approximately 598 ± 5 nm in the upper arm and 408 ± 5 nm in the lower arm, as shown in Fig. 6.4. The eigenmode simulations have been performed using COMSOL which gives the waveguide's effective refractive index and its wavelength dependence [7]. These simulations are fed into the circuit simulator Caphe from Luceda Photonics [8, 9]. The simulated spectra of the conventional MZI with ± 2 nm width variation is shown in the Fig. 6.5(a).

The experimental measurements are shown in Fig. 6.5(c). The devices show an extinction ratio of more than 25 dB and an insertion loss of less than 0.3 dB throughout the C band. The measured FSR of the filter is around 5 nm which matches with the designed one. The circuit simulations were performed with the SEM measured widths and also incorporate the tapers as explained in the section 5.4. The fitted spectrum corresponding to the measured widths taken from SEM is shown in Fig. 6.5(b). The measured spectra match very well with the circuit simulation.

The extracted and simulated sensitivity to line-width $\frac{d\lambda}{dw}$ is shown in

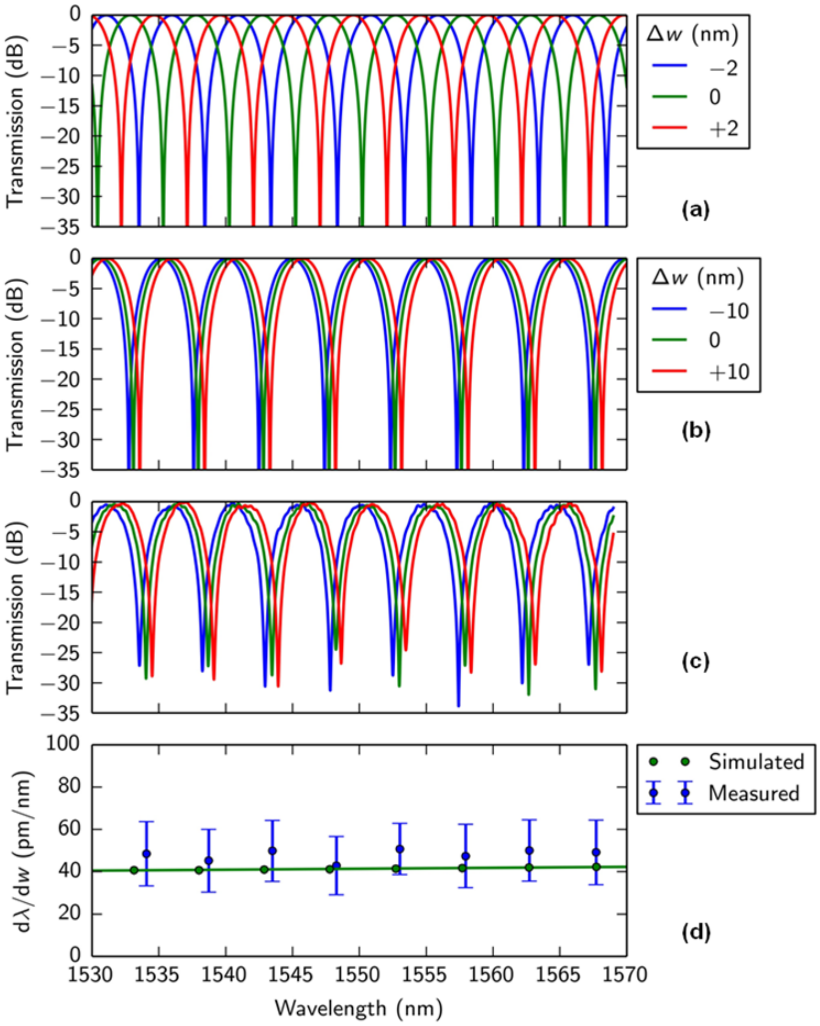

Figure 6.5: (a) Simulated spectra of a conventional MZI for 0, -2 and +2 nm width offset. (b) Simulated spectra of the optimized design for 0, -10 and +10 nm width offset (c) Normalized measured transmission and (d) $\frac{d\lambda}{dw}$ *variation with wavelength.*

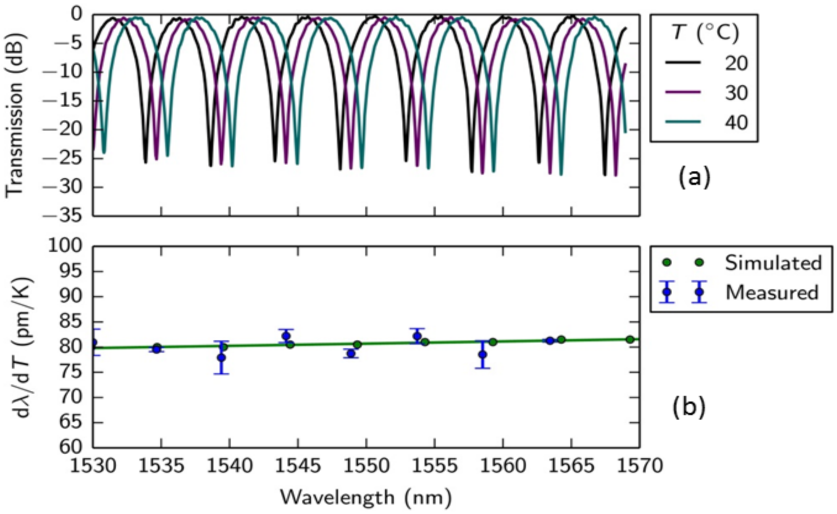

Figure 6.6: (a) Measured transmission of fabrication tolerant filter at $T = 20\,^\circ\mathrm{C}$, $30\,^\circ\mathrm{C}$ *and* $40\,^\circ\mathrm{C}$, *(b) thermal sensitivity* $\frac{d\lambda}{dT}$ *variation simulated and measured*

Fig. 6.5(d). The measured width sensitivity is reduced from 1 nm/nm to less than 60 pm/nm over the entire spectrum with standard deviation of about 15 pm/nm which is measured over four devices with deliberate width offsets of ±5 nm and ±10 nm. These measured devices are positioned close together on the chip to minimize non-intentional relative linewidth variations, which can be assumed to be of the order of 1 nm [1]. If we compare the footprint of the device with respect to the longer arm length with a conventional MZI filter as mentioned in Eq. 5.21, it is only 1.5 times longer. On the other hand, the width sensitivity has improved almost by 20 times compared to the conventional one.

We have also measured the thermal behavior of this filter. To determine the thermal influence, the spectrum of the components is measured at different temperatures. This is done by fixing the chip on top of a thermally controlled chuck containing a resistive heater and temperature sensor as explained in detail in the section 5.6. The setup is shown in Fig. 4.10.

Measured spectra at different temperatures are shown in Fig. 6.6(a) and the corresponding thermal sensitivity is shown in Fig. 6.6(b) respectively. Thermal measurement of the device shows that it behaves similar to a standard MZI with 80 pm/K of shift. Thus, the measurement shows that we have to incorporate some extra degree of freedom to make a filter tolerant to both fabrication variations and thermal fluc-

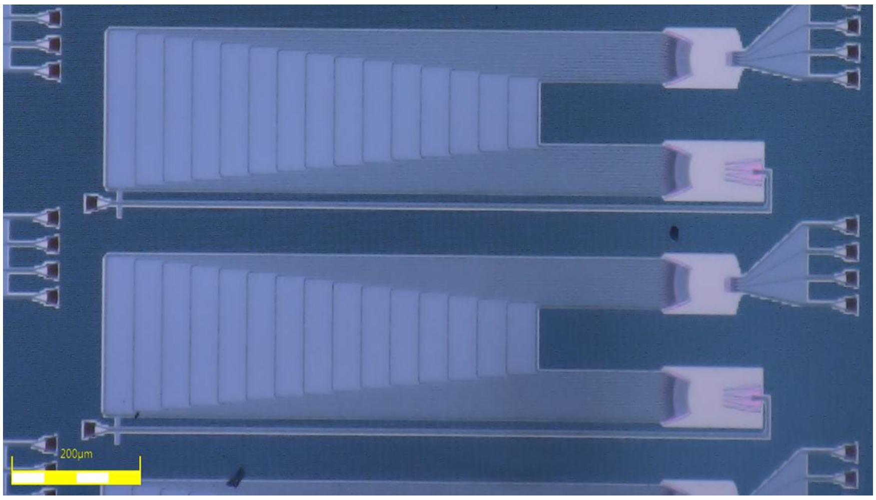

Figure 6.7: Camera image of AWG with deliberate width variation of 20 nm

tuations.

6.4 Fabrication Tolerant AWG

The concept of width tolerant MZI can be extended to the AWG as well. We have designed AWG for 200 GHz channel spacing. The concept is similar as athermal AWG as discussed in the section 4.6, but here we have optimized for the width tolerance. Each delay is a combination of 800 nm and 450 nm waveguides. We have provided a deliberate width variation of 20 nm to demonstrate the concept.

The fabricated device is shown in the Fig. 6.7.

The measured normalized single channel transmission is shown in Fig. 6.8.

The channel transmission of all the four channels with nominal width and a variation of 20 nm are shown in Fig. 6.9.

The measured response shows that the width tolerance of the AWG is improved by 10 times from 1 nm/nm to 100 pm/nm. All the channel shows insertion loss better than 6 dB and cross talk more than -15 dB. These parameters can be further optimized.

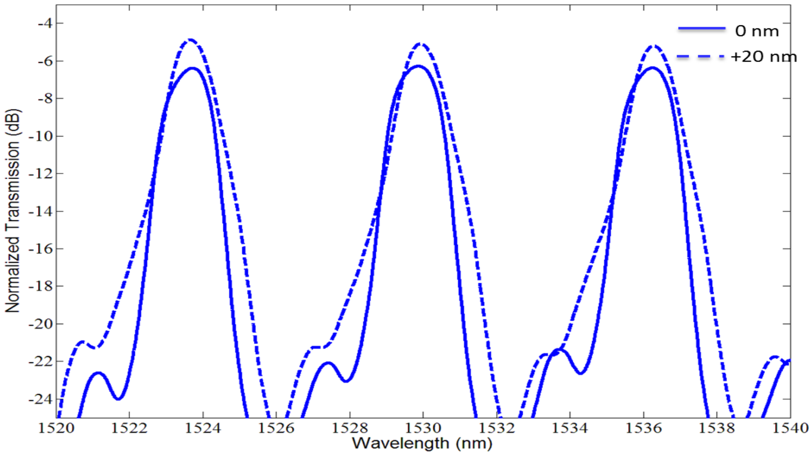

Figure 6.8: Normalized and measured single channel response of the two AWGs, one with nominal width and another with linewidth variation of 20 nm

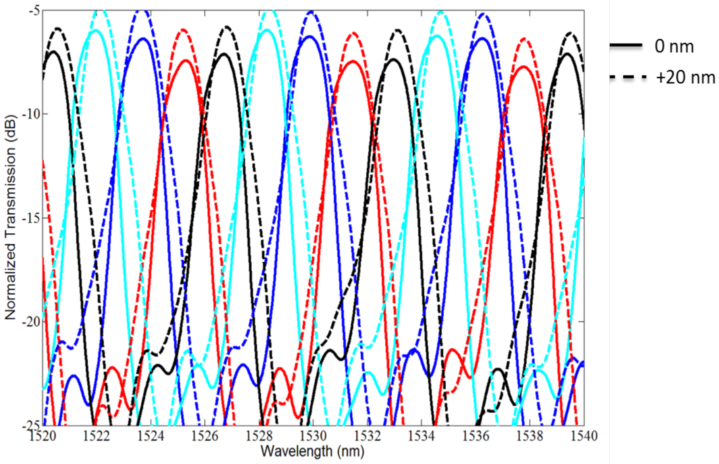

Figure 6.9: Normalized and measured of all four channels response of the two AWGs, one with nominal width and another with linewidth variation of 20 nm

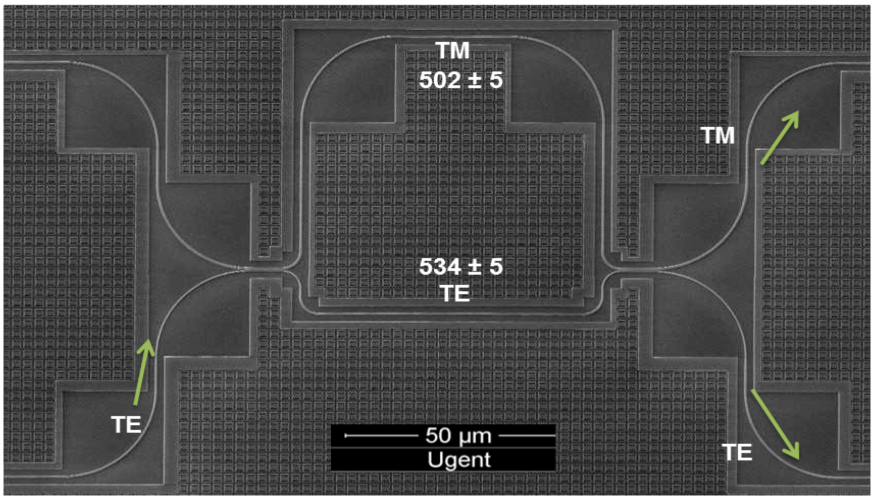

Figure 6.10: SEM image of fabricated MZI filter with SPR

6.5 Fabrication and Thermal Tolerant MZI

6.5.1 Design and Fabrication

To demonstrate both linewidth and thermal tolerance in the same device, we should minimize the temperature dependence for devices on the minimum curve of the linewidth sensitivity (i.e. the zero diagonal in Fig. 6.1). The device schematic is similar to one showed in Fig. 5.2.

We find this condition for a TM and TE nominal width of 490 nm and 522 nm, respectively. The filter is designed for an FSR of 10 nm. The corresponding TM and TE arm lengths for the designed FSR are 180 μm and 87μm, which are calculated by using the condition in Eq. 6.4. In order to check the fabrication tolerant behavior, we replicate the device with deliberate relative variations in the line-width in both arms over a 20 nm range similar to the one we mentioned in previous section 6.3.1.

The device is fabricated with the similar CMOS process and on the same chip and fabrication run as mentioned in the section 6.3.1. The SEM picture of the fabricated device with nominal width is shown in Fig. 6.10. The device uses a splitter polarization rotator (SPR) which splits the light into two equal parts and at the same time rotates the polarization in one arm as already explained in the section 5.3.

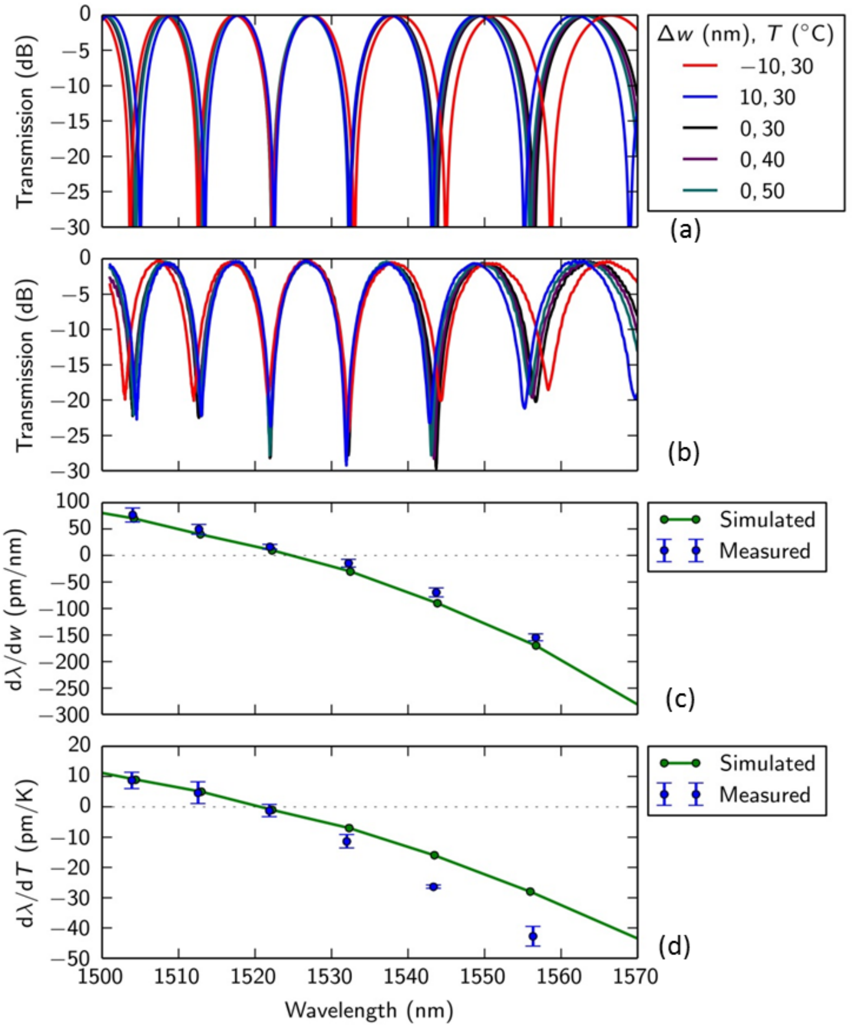

Figure 6.11: (a) Simulated spectra of optimized design for 0, -10 and +10 nm width offset and at $T = 30\,^{\circ}\mathrm{C}$ *and* $40\,^{\circ}\mathrm{C}$ *and* $50\,^{\circ}\mathrm{C}$*, (b) normalized measured transmission, (c) width sensitivity* $\frac{d\lambda}{dw}$ *and (d) thermal sensitivity* $\frac{d\lambda}{dT}$ *simulated and measured*

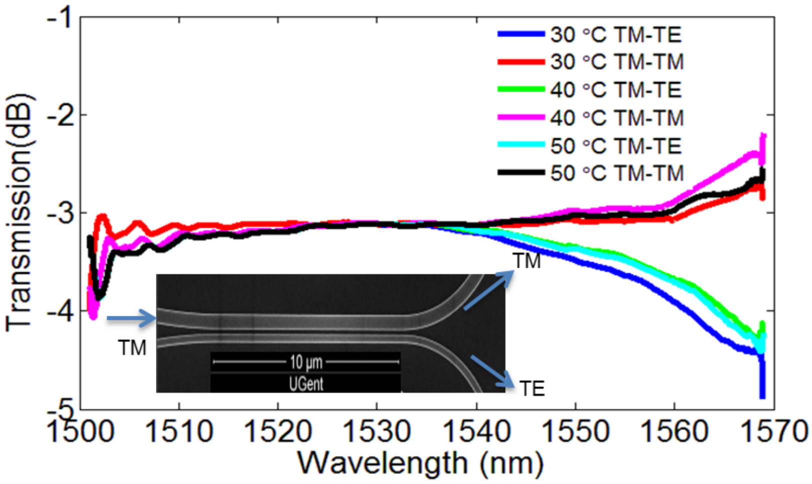

Figure 6.12: Bar and cross port measured transmission of SPR at different temperatures. SEM image of SPR (inset)

6.5.2 Measurements and Analysis

The measured SEM width of the fabricated device is 502±5 nm in TM arm and 534±5 nm in a TE arm. The Eigenmode simulations of these waveguides have performed using COMSOL which gives waveguide effective refractive index and its wavelength dependence (the detailed modelling can be found in chapter 2). These values were passed to the circuit simulator Caphe from Luceda Photonics. The simulated transmission spectra using the device parameters from SEM are shown in Fig. 6.11(a). Tapers are included in a similar fashion as explained in the section 5.4.

To determine the thermal influence, the device is measured at three different temperatures , i.e. 30 °C, 40 °C and 50 °C on a nominal-width device. This is done by fixing the chip on top of a thermally controlled chuck containing a resistive heater and temperature sensor as explained in detail in the section 5.6. The setup is shown in Fig. 4.10. The transmission measurement is performed on varying width devices of ±10 nm at 30 °C. The five (three widths and three temperatures: one is common) normalized measured transmission spectra are shown in Fig. 6.11(b). The fabrication and thermal insensitive point are situated around 1525 nm.

The measured device shows a width sensitivity of less than ±65 pm/nm with a standard deviation of about ±15 pm/nm measured over four devices with width offsets of ±10 nm and ±20 nm. The measured thermal sensitivity is less than ±15 pm/K with a standard deviation of about 3 pm/K over the wide wavelength range of 40 nm from 1501 to 1540 nm. The simulated and measured width as well as the thermal sensitivity are shown in the Fig. 6.11(c) and Fig. 6.11(d) respectively. The simulated spectra match very well with the measured device which confirms the accuracy of the circuit model.

The width sensitivity changes from positive to negative on the different sides of the insensitivity point. A similar behavior can be seen while varying the temperature of the device. This phenomenon is due to the n_{eff} variation with w ($\frac{dn_{eff}}{dw}$) and T ($\frac{dn_{eff}}{dT}$) for TM waveguide with increasing wavelength. This variation changes at much faster rate than in the TE waveguide. If we compare the response with the width tolerant device shown in Fig. 6.5, the wider waveguide is always red shifted over the entire wavelength range and width sensitivity is much flatter.

We have characterized the SPR separately for completeness of the measurements since these devices have been fabricated in a different fabrication run compared to the one which is fabricated and measured in the section 5.6.2.

The measured transmission of the SPR at different temperatures is shown in Fig. 6.12. The SPR is designed for equal power splitting in C-band, but we do see a deviation from that value for longer wavelengths. This will not significantly affect the athermal/width tolerant behavior, but it will result in a lower extinction ratio of the MZI.

6.5.3 Footprint Analysis

The device is fairly compact due to large difference in TO coefficients between the arms, as shown in the Fig. 5.1. Fig. 6.13 displays the ratio of the required longest arm length of the presented fabrication and thermal tolerant MZI, to the arm length difference of a conventional MZI with a core width of 450 nm. The required longest arm length is 3.2 times longer than the conventional MZI. The comparison is made with the demonstrated filter which is designed for FSR of 10 nm.

6.6 Higher Order Filters

The next step is to use these presented integral components to build higher order filters for different WDM applications.

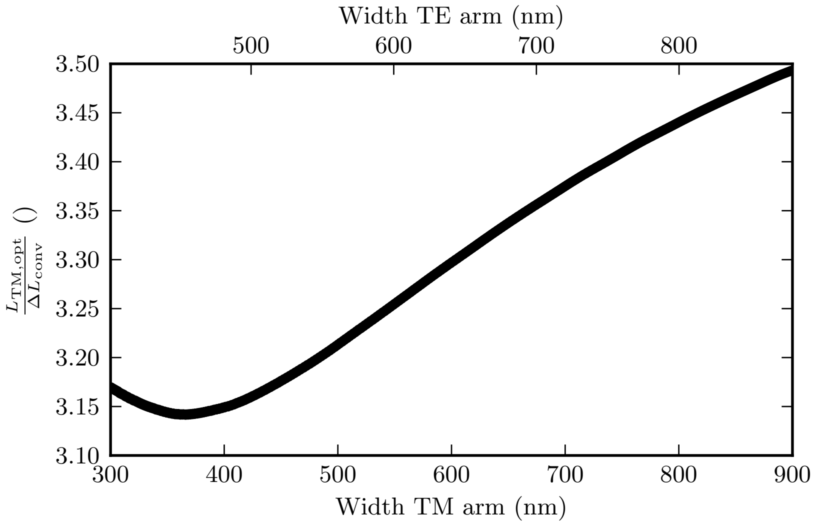

Figure 6.13: Longest arm of the fabrication and thermal tolerant MZI, normalized to the arm length difference of a conventional MZI with a core width of 450 nm.

6.6.1 Fabrication and Thermal Tolerant Demultiplexer

A schematic of a four channel de-multiplexer is shown in Fig. 6.14(a). The design is based on the width and thermal tolerant MZI filter. The designed channel spacing is 6.4 nm. The length of the TE and TM arms for the first stage which is designed for an FSR of 12.8 nm is 74.4μm and 162.9μm respectively.

The lengths of the arms become half in second stage since the FSR of each MZI needs to be doubled. The power coupling coefficient of directional coupler is 0.5 which is similar to the SPR explained in the previous section. The simulated circuit transmission at three different widths of (0,-10, 10) nm and at temperature of 30 °C and 50 °C is shown Fig. 6.14(b). The simulated width and thermal sensitivity for this filter are found to be 30 pm/nm and 8 pm/K respectively.

6.6.2 Fabrication and Thermal Tolerant Flat Band Filters

Another approach to making fabrication and thermal tolerant FIR filters is to combine the approach of passive compensation and flatten the pass-bands as demonstrated in chapter 3.

The normal flat band designs based on the cascaded MZI filters are shown in the section 3.4. If we want to include the fabrication tolerant behavior in this design then the schematic is modified and shown

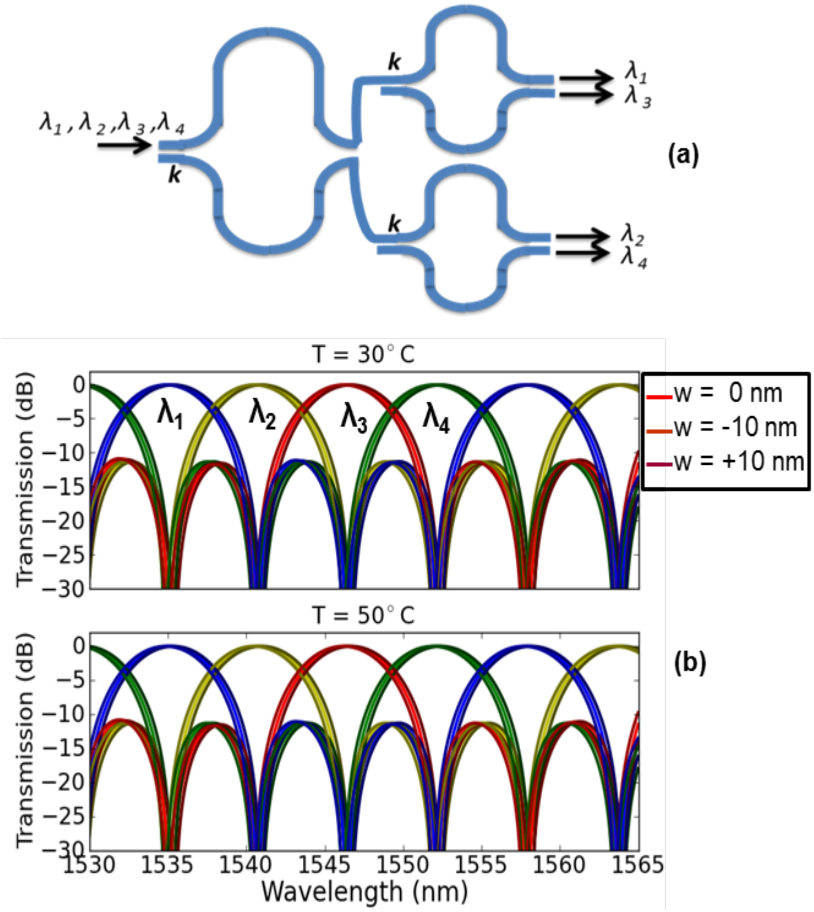

Figure 6.14: (a) Schematic of two stages filter 4 channel de-multiplexer with k=0.5, (b) simulated transmission of filter at $T = 30\,^\circ\mathrm{C}$, $50\,^\circ\mathrm{C}$ *and with width variation of (-10,0,+10)nm*

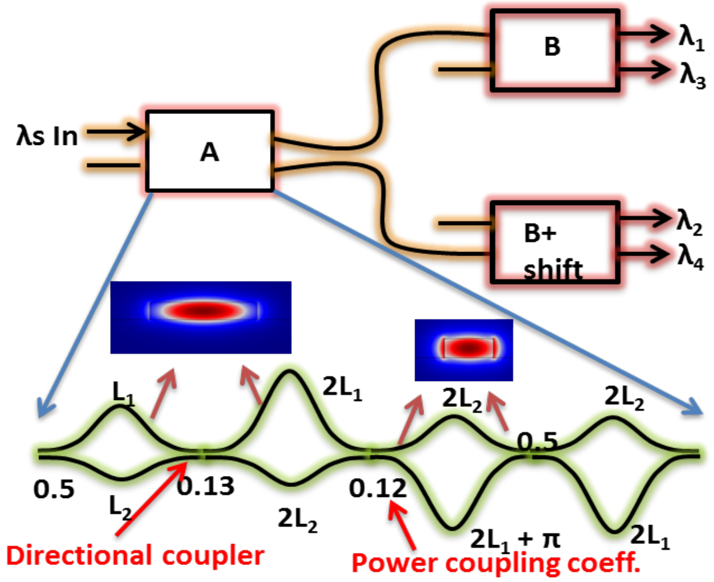

Figure 6.15: Block diagram filter of 2-stage 4-channel cascaded mzi lattice filter. In block A the coupling coefficients are mentioned and now delay line comes from different waveguide widths w_1 and w_2 with corresponding lengths L_1 and L_2

in Fig. 6.15. It is to be noted that in this case, we are using the TE polarization in both the arms.

The de-multiplexer is designed for 5 nm of channel spacing; which implies that every MZI of the first and second stages has an FSR of 10 nm and 20 nm respectively. The waveguide widths of the the two arms, w_1 and w_2, are 800 nm and 450 nm respectively.

The corresponding lengths are calculated based on the Eq. (6.1-6.2). The lengths of the 800 nm and the 450 nm waveguide arms of the first stage (which is designed for an FSR of 10 nm) are 76μm and 14μm respectively.

The simulated circuit transmission at width variations of 20 nm is shown in the Fig. 6.16. The tapers, waveguide width sensitivity and wavelength dependence of directional couplers are taken into account. The directional couplers are designed in the 450 nm wires only. The simulated spectra show that the width tolerance is improved by 20 times i.e. less than 50 pm/nm if we compare with the normal de-multiplexer shift of 1 nm/nm. Also, due to 60% of the pass-band is flat this de-multiplexer is already thermally robust upto $\pm 15\,^{\circ}$C. These devices are still in fabrication.

We can also combine the flat band approach with passive compensation

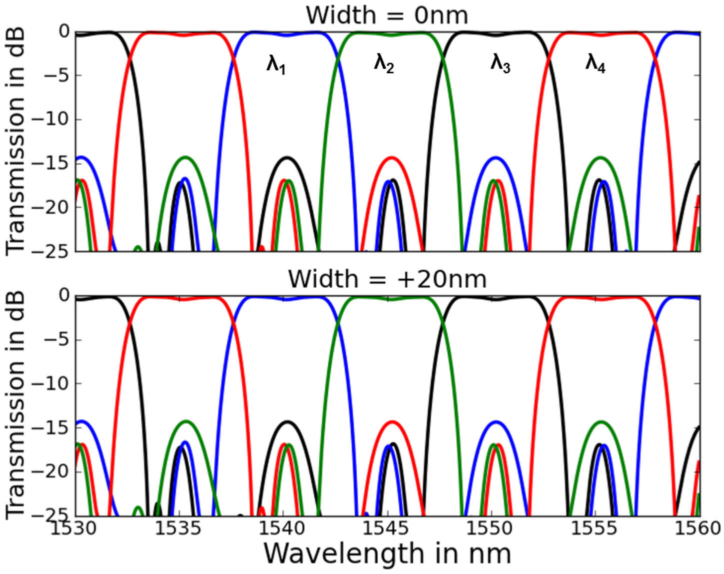

Figure 6.16: Circuit simulation of spectral shift of fabrication insensitive 4- channel flat band de-multiplexer

technique to make the de-multiplexer thermally robust. This method can certainly improve the performance of the CWDM for 100 GbE at O-band demonstrated in chapter 3.

If we use combination of wide and narrow waveguide widths for every MZI, then we can make it athermal as already demonstrated in the section 4.5. Similarly, if we combine two different waveguide widths in every MZI of the CWDM mentioned in section 3.9, the thermal robustness can be further improved. In order to achieve this goal, we have first simulated the TO coefficients of the waveguide at O-band using FEM solver COMSOL [7]. The simulated TO coefficient of the SOI waveguide with thickness of 220 nm with increasing width at O-band of center wavelength 1310 nm is shown in Fig. 6.17.

The simulated circuit transmission is shown in Fig. 6.18. Every MZI is made of combination of 250 nm wide and 380 nm wide waveguides in either arms. The simulated TO coeff. are $1.62 \times 10^{-4}\ K^{-1}$ and $2.02 \times 10^{-4}\ K^{-1}$ as shown in the Fig. 6.17. The corresponding lengths of the MZI arm with width 250 nm wide waveguide and 300 nm wide waveguide are $41.17\mu m$ and $33.0\mu m$ respectively. These lengths are calculated for an FSR of 40 nm (1st stage) from the given Eq. 4.13. The tapers are designed in such a way that they cancel out each others effects. The directional couplers are kept in the 380 nm wide waveg-

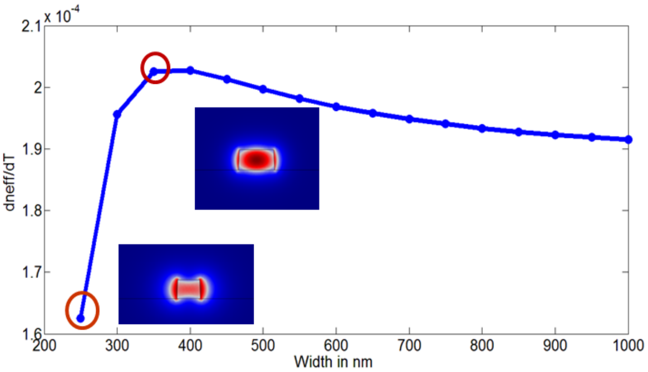

Figure 6.17: Simulated TO coefficients of the SOI waveguide at 1310 nm and in showing the mode profile of 250 nm and 380 nm wide waveguides

uide. The circuit simulation has included the wavelength and thermal dependence of the waveguide and the directional couplers.

The passive compensation comes with a cost of footprint and typically the longest arm is 4 times longer than the conventional fabricated CWDM de-multiplexer demonstrated in section 3.8. The thermal tolerance increases by almost 10 times i.e. less than 8pm/K over the entire 80 nm band when compared with the normal de-multiplexer demonstrated in chapter3. Narrow and long waveguides increase the phase errors and hence reduce the cross talk and increase the insertion loss of the designed device. The simulated cross talk is around 25 dB and insertion loss is -1.2 dB.

All the circuit simulations for the de-multiplexers have been performed using the circuit solver Caphe from Luceda photonics [9].

6.7 Conclusion and Discussion

We have proposed and demonstrated a technique to make tolerant all-silicon FIR filter devices. The measured results show a reduced linewidth sensitivity of less than 60 pm/nm over a wide band which is a 20-fold improvement over the conventional devices. This concept can be extended to fabrication tolerant AWGs, in which, instead of using similar delay line, one has to use the differential delay line. This method is conceptually similar to one demonstrated for athermal AWGs in section 4.6.

A very short demonstration of fabrication tolerant AWGs are provided but, it required further investigation to optimize the parameters. Also, the phase errors are an important issue here and need to be taken into

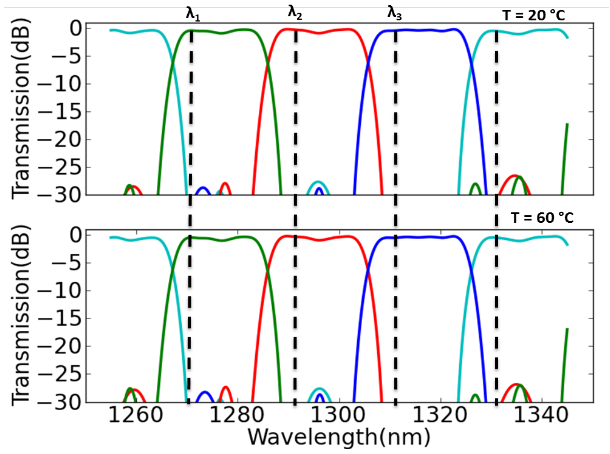

Figure 6.18: Simulated spectral shift of thermally insensitive demultiplexer at 20 °C *and* 60 °C

account. As best of our knowledge this is a first demonstration of the fabrication tolerant MZIs and AWGs.

We have also demonstrated a width and thermal tolerant compact device with width sensitivity less than ±65 pm/nm and thermal sensitivity smaller than ±15 pm/ K over 40 nm of wavelength range.

Hence, this proves the concept of passive compensation over a number of devices where the improvement can be done at the design level itself without altering the fabrication process.

Various simulations show that these filters can cater to the needs of fundamental issue of highly sensitive SOI platform and serve the purpose in various applications like WDM, bio-sensing, microwave photonics and many others.

References

[1] S.K. Selvaraja, W. Bogaerts, P. Dumon, D. Van Thourhout, and R. Baets. *Subnanometer Linewidth Uniformity in Silicon Nanophotonic Waveguide Devices Using CMOS Fabrication Technology*. Selected Topics in Quantum Electronics, IEEE Journal of, 16(1):316–324, Jan 2010.

[2] Frederic Boeuf, Sebastien Cremer, Enrico Temporiti, Massimo Fere', Mark Shaw, Nathalie Vulliet, bastien orlando, Delia Ristoiu, Alexis Farcy, Thierry Pinguet, Attila Mekis, Gianlorenzo Masini, Peng Sun, Yuemeng Chi, Herve Petiton, Sebastien Jan, Jean-Robert Manouvrier, Charles Baudot, Patrick Le-Maitre, Jean Francois CARPENTIER, Laurent Salager, Matteo Traldi, Luca Maggi, Danilo Rigamonti, Chiara Zaccherini, Carolina Elemi, Bernard Sautreuil, and Luigi Verga. *Recent Progress in Silicon Photonics R&D and Manufacturing on 300mm Wafer Platform.* In Optical Fiber Communication Conference, page W3A.1. Optical Society of America, 2015.

[3] Tohru Mogami, Tsuyoshi Horikawa, Keizo Kinoshita, Hironori Sasaki, Ken Morito, and Kazuhiko Kurata. *High-performance optical waveguide devices using 300 mm Si photonics platform.* Microelectronic Engineering, pages –, 2015.

[4] S.K. Selvaraja, P. De Heyn, G. Winroth, P. Ong, G. Lepage, C. Cailler, A. Rigny, K.K. Bourdelle, W. Bogaerts, D. Van Thourhout, J. Van Campenhout, and P. Absil. *Highly uniform and low-loss passive silicon photonics devices using a 300mm CMOS platform.* In Optical Fiber Communications Conference and Exhibition (OFC), 2014, pages 1–3, March 2014.

[5] Shankar Kumar Selvaraja, Wim Bogaerts, Dries VanThourhout, and Marc Schaekers. *Thermal trimming and tuning of hydrogenated amorphous silicon nanophotonic devices.* Applied Physics Letters, 97(7):–, 2010.

[6] J. Schrauwen, D. Van Thourhout, and R. Baets. *Trimming of silicon ring resonator by electron beam induced compaction and strain.* Opt. Express, 16(6):3738–3743, Mar 2008.

[7] `http://www.comsol.com/`.

[8] Martin Fiers, Thomas Van Vaerenbergh, Ken Caluwaerts, Dries Vande Ginste, Benjamin Schrauwen, Joni Dambre, and Peter Bienstman. *Time-domain and frequency-domain modeling of nonlinear optical components at the circuit-level using a node-based approach.* J. Opt. Soc. Am. B, 29(5):896–900, May 2012.

[9] `http://www.lucedaphotonics.com/`.

7

Conclusion and Future Perspectives

7.1 Conclusion

As we have elaborated throughout this work, the control of tolerances is essential in any technological process and device. During the course of this work we have made a number of important contributions towards developing an all silicon design based approach in realizing fabrication and temperature tolerant, and power efficient silicon photonic integrated circuits. We have been able to show that smart design approach can solve some issues of the SOI platform which were thought to impose an inherent limitation on the functionality of the photonic components and circuitry. The important contributions and achievements of this work are summarized below:

i. We have proposed and demonstrated a method for measuring the refractive index of highly dispersive SOI waveguides. This is an important step forward in the characterization of the integrated waveguide devices, because hitherto it was only possible to accurately characterize the group index. By combining 3 MZIs of lower and higher order we can extract the wavelength and temperature dependent effective index and the group index unambiguously, and also obtain an estimate for the local variability of the effective index. The demonstrated method does not perturb the waveguide of local pattern density, which is essential in a high-contrast waveguide platform such as silicon photonics.

ii. We have proposed and demonstrated a low loss robust demultiplexer which is based on cascaded MZIs with a 20 nm channel spacing in the O-band. By engineering the channel pass band we showed that the device can handle the temperature variations up to 100 °C and wafer-level waveguide dimensional variations. This device is a critical demonstration for the SOI platform because it can be integrated with uncooled lasers in CWDM systems and hence provide a low cost high speed 100GbE and 400GbE solution for short reach interconnects.

iii. We have proposed and demonstrated a passive compensation design technique of various FIR filters like MZIs and AWGs and have shown an improvement in thermal tolerances by 10 times and linewidth variations by 20 times.

iv. We have also shown compact and low loss, athermal, and fabrication tolerant devices by exploiting the different polarizations.

Combining the flat band approach and passive compensation technique one can further improve the performances of the de-multiplexers which are critical for on chip optical interconnects. Overall in an optical link, the power consumption due to thermal tuning and control elements can be as high as 20% of the total power consumption and by having thermally tolerant designs one can significantly reduce the power budget of the overall system. We have thus shown several proof-of-principle components which clearly demonstrate the potential of smart design approaches to overcome fundamental limitations of silicon photonics.

7.2 Current and future perspectives

The basic components have been investigated, therefore the future work lies in further improving the performance and use them in an actual product demonstration, such as in a 100 GbE link for short reach interconnects. It would include an on-chip heterogeneously integrated III-V-on-SOI directly modulated high speed laser or off-chip lasers modulated by on-chip silicon modulators, multiplexer on the transmitter side and de-multiplexer and germanium photo-diodes on the receiver side. This is similar to the 100 GbE link we showed in simulation. The individual components mentioned have already been demonstrated and few designs for demultiplxer connected with photodiodes are already undergoing fabrication and will soon be ready for characterization. The multiplexers with electro-absorption modulators are also undergoing fabrication. This work is in collaboration with imec. On the transmitter side design has been sent for fabrication in which the directly modulated III-V-on-SOI laser will be present at the input of the de-multiplexer carrying 10 to 25 Gbps data in each channel.

The performance of these devices (especially athermal AWGs) can certainly be improved by using better fabrication techniques like those being developed on a 300 mm p-line instead of the 200 mm process, where the roughness is much better controlled.

Other approach to improve the performance of athermal AWG could be to use a combination of TE and TM mode waveguide in each delay line with the help of two low loss polarization rotators. In this AWG the TE light which is coming from the input star coupler is first converted to TM by the first polarization rotator and then converted back to TE before the output grating coupler by the second polarization rotator. The principal of operation is an extension of TE-TM MZI and now the AWG delay lines are short due to the large TO coefficient difference between the two modes. The most critical part of this demonstration is a low loss polarization rotator otherwise this will add up to the insertion loss of the AWG. So there is a need for robust and low loss polarization rotator in SOI. The other advantage of using TM mode in AWG is lower phase errors that would improve the crosstalk figure of the AWG.

The another basic component which needs some smart design optimization is a directional coupler that can operate over wider bandwidths typically (80 to 100 nm) for a given coupling coefficient. The robustness in directional couplers are critical for other filters like ring resonators as well.

In this work we have discussed mainly FIR filters. It would be interesting to extend the passive compensation technique to IIR filters (e.g. ring resonators) as well. The present techniques don't yet solve the thermal drift issue of self interfering devices.

It is worth mentioning that the techniques described in this thesis can be applied to other waveguide platforms operating at different wavelengths or even SOI at different wavelengths. One particular region of interest is the mid-IR wavelength (3-12)μm where SOI waveguides could be used till 4 μm wavelength and beyond that GE-on-Si takes over. This wavelength range is appealing because of specific and much stronger absorption lines of many gases and liquids. Recently there has been interest in miniaturizing the sensing systems using integrated waveguides circuits.

Any spectroscopic system requires WDM components and if they suffer from fabrication and thermal drifts, then predicting the behavior of the system becomes difficult. Implementing our techniques would improve the performance of existing passive components operating in the mid-IR wavelength regime. One particularly interesting example is that of an athermal AWG. As we saw in this thesis that the athermal

AWG suffers from high cross talk which arises because of the higher phase errors from the longer delay arms. There has been a demonstration of an AWG based on Ge-on-Si which although has a much higher side wall roughness, already shows a cross talk of 18 dB at 5.3 μm because of the waveguide geometry there is very less influence of the side wall roughness. If we make an athermal AWG in Ge-on-Si, then there is a high chance that the device would show similar cross talk levels while improving the thermal behavior.

Of course each of these topics would require a significant research effort in their own right. This shows that the future research potential of tolerant silicon waveguide based devices is large and may inspire a lot of new exciting applications. Also, the presented method are equally useful for the other material platforms e.g. Ge-on-Si for mid-IR wavelength and silicon nitride for visible wavelengths.